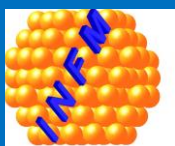
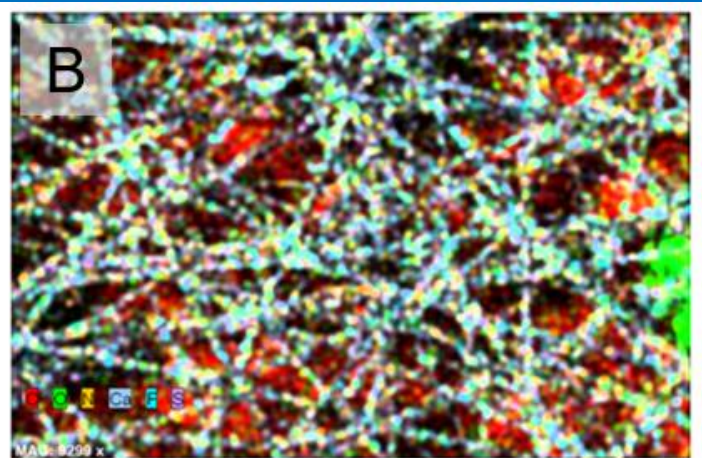
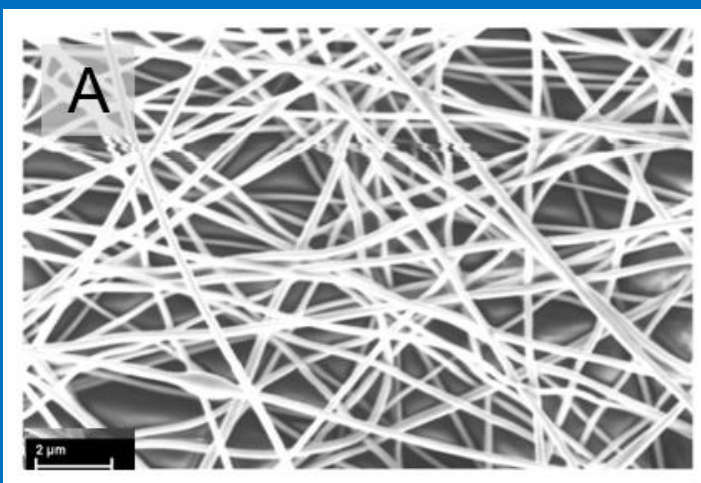
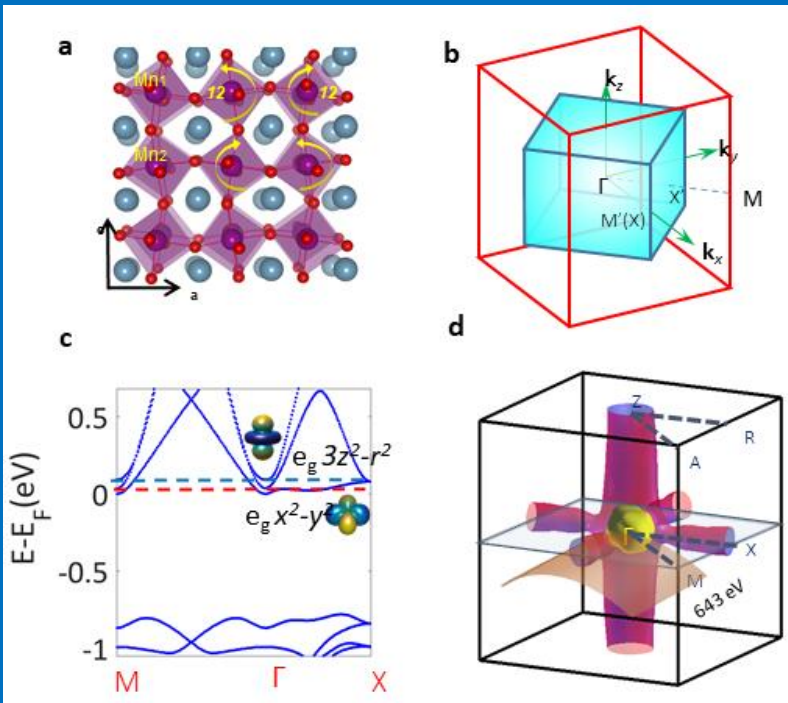


**National Institute of
Materials Physics**

ANNUAL REPORT

2020

**Ministry of Research,
Innovation and
Digitalization**



**NATIONAL INSTITUTE OF MATERIALS PHYSICS
BUCHAREST-MAGURELE**

Atomistilor Str. 405A, P.O. Box MG-7, 077125 Magurele-Ilfov, Romania

Phone: +40(0)21 3690185, Fax: +40(0)21 3690177, email: director@infim.ro, <http://www.infim.ro>

Contents

Laboratories and groups.....	3
Laboratory 10 „Multifunctional Materials and Structures Laboratory”	4
Laboratory 20 „Magnetism and Superconductivity”	9
Laboratory 30 „Nanoscale Condensed Matter”	12
Laboratory 40 „Optical processes in nanostructured materials”	16
Laboratory 50 „Atomic Structures and Defects in Advanced Materials (LASDAM)”	18
Materials modeling, preparation and characterization	21
Amplitude-based approach for complex dielectric permittivity retrieval in terahertz time-domain spectroscopy.....	22
Negative capacitance regime during polarization switching in epitaxial PbZr _{0.2} Ti _{0.8} O ₃ thin films	25
Structural and magnetic properties of La _{1-x} A _x MnO ₃ (A = K; Ba) synthesized by flash combustion method	28
Inorganic cation Eu or Sb as dopants of perovskite films.....	31
Web-like architectures based on metal oxides by biomorphic mineralization or functionalization of eggshell membrane (ESM).....	34
(Ba,Sr)TiO ₃ solid solutions sintered from sol-gel derived powders: An insight into the composition and temperature dependent dielectric behavior.....	37
Charge transfer reaction mechanisms in epoxyketone and boronated peptides at glassy carbon and boron doped diamond electrodes.....	40
MAX Phases for Chemoselective Hydrogenation of 4-nitrostyrene.....	43
Electron-polaron dichotomy of charge carriers in perovskite oxides	46
<i>In situ</i> resistance hysteresis assessment correlated with surface science studies for graphene-like carbon layers deposited on atomically clean ferroelectric surfaces	49
Polarization-dependent magnetism of the Ni/BaTiO ₃ interface	52
Quantum dot exciton dephasing by Coulomb interaction: A fermionic analog of the independent boson model.....	55
Robust conductance zeroes in graphene quantum dots and other bipartite systems	58
Switching the electron-vibron coupling in hybrid quantum systems.....	62
New optical evidence concerning the cationic photopolymerization of the SU8 photoresist and its composites with carbon nanotubes	64
Optical properties of composites based on graphene sheets functionalized with macromolecular compounds	67
Photoluminescence studies concerning the photodegradation of drugs	70
Electron Paramagnetic Resonance and Microstructural Insights into the Thermal Behavior of Simonkolleite Nanoplatelets	73
On the atomic structure of the high-temperature precipitates in Ni-base superalloy VDM 780 Premium	76
References	78

Atomic resolution analytical TEM study of chemical ordering in BaLnCo ₂ O _{6-δ} double perovskites for electrochemical applications	79
EPR insight into the magnetic interactions driving anisotropic growth of Si-doped hematite nanocrystals	82
Second magnetization peak, rhombic-to-square Bragg vortex glass transition, and intersecting magnetic hysteresis curves in overdoped BaFe ₂ (As _{1-x} P _x) ₂ single crystals	85
Magnetic Phase Evolution in Novel FePt and FeMnPt Nanocomposite Magnets.....	88
Unidirectional magnetic anisotropies in 0D and 1D nanostructures	91
Towards applications.....	94
Removal and Oxidation of As (III) from Water Using Iron Oxide Coated CTAB as Adsorbent	95
Photodetecting behavior of individual CuO-ZnO core-shell nanowires with p-n radial heterojunction	98
Ionophore-Nafion™ modified gold-coated electrospun polymeric fibers electrodes for determination of electrolytes	101
Electrospun conductive gold covered polycaprolactone fibers as electrochemical sensors for O ₂ monitoring in cell culture media	104
The use of degenerated TiO ₂ semiconductors modified with Ni and Zn in the photocatalytic water splitting reaction.....	107
Synergetic effect of Ni species and undoped SnO ₂ manuscript in oxygen evolution reaction	110
The cytotoxicity of ZnO–CdS composites and of AgZnONPs biocomposites on human fibroblast cells...	113
Organic heterostructures with hybrid and nanostructured active layer	116
Low temperature CO sensing under infield conditions with In doped Pd/SnO ₂	119
GeSn-based structures by magnetron sputtering deposition for short-wave infrared photonics.....	122
SiGe nanocrystals-based photosensors with high sensitivity from visible to short-wave infrared for detection of slippery road conditions	125
SiGe-TiO ₂ films and multilayers based on SiGe nanocrystals in TiO ₂ with extended SWIR photosensitivity	128
Advanced local investigations and manipulations of nanostructures using Scanning Tunneling Microscopy	131
Novel boron carbide based composites with special mechanical properties	134
Bulk MgB ₂ for superconducting magnet and shielding applications.....	137
Optimization of Fe oxide based nanoparticles for bio-medical and catalytic applications.....	140
Temperature dependence and defect related structure, photoluminescence, (ferro)magnetism and ammonia sensitivity of undoped nanocrystalline ZnO	143

Laboratories and groups

Laboratory 10 „Multifunctional Materials and Structures Laboratory”

Group name: Functional nanostructures

Group leader: Dr. Ionut-Marius Enculescu, Senior Researcher rank 1 (encu@infim.ro)

Personnel: 7 SR 1, 2 SR 2, 6 SR 3, 3 SR, 13 RA, 1 technician (SR stand for Senior Researcher; RA stand for Research Assistant)

Main research directions

The group deals with nanostructures and nanostructured materials preparation and development of applications. Both chemical/electrochemical (chemical bath deposition, electrochemical deposition with and without a template, chemical vapor deposition) and physical (sputtering, thermal evaporation in vacuum, electrospinning and forcespinning) methods are employed for nanostructures and nanostructured materials preparation. Different types of materials are used, including here metals, metal oxides, organometallic compounds and polymers. The nanostructures developed by this approach are used as building blocks for different types of functional devices (transistors or diodes, biosensors, actuators).

- Nanostructures and devices based on nanostructures – physical and chemical methods are employed for preparing nanostructures. Electrochemical or chemical deposition is used for preparing nanowires of zinc oxide with diameters down to 10 nm. Thermal oxidation of metal foils is used for obtaining metal oxide nanowires with diameters down to 20 nm. Further, the nanowires can be employed as building blocks for electronic devices such as diodes and transistors using microlithographic (photolithography and electron beam lithography). Devices complexity can be employed (e.g. core shell devices can be fabricated) by covering the nanowires with thin films employing methods such as sputtering or thermal evaporation. Chemical vapor deposition is employed for preparing thion nanostructured films such as metallic oxides or graphene.
- Materials for applications in optics, optoelectronics and photonics for devices which include diodes and transistors for light emitting applications, glasses or modular composition fibers for photonic applications.
- Biosensors and biomedical devices based on nanostructures or on devices containing nanostructures as building blocks.

Nanostructures and nanostructured materials can be exploited successfully in biosensors, mainly due to the high specific surface but also due to other specific functionalities induced by the low dimensionality. Electrochemical sensors are developed based on nanostructured materials and are functionalized with different types of biomolecules in such a way in which both the desired sensitivity and selectivity are obtained. In this context different types of substrates and configurations of functionalization are investigated with the goal of optimizing devices' performances. Novel applications are taken into account including wearable sensors for physiologic parameters monitoring.

- Submicrometer fibres; biomimetic devices based on microfiber web electrodes. In our group methods of fabricating polymer submicrometric fibers were developed namely: electrospinning and forcespinning. By further functionalization transparent and flexible electrodes based on metal covered polymer fiber webs are obtained. These electrodes can be applied on a wide range of substrates including here materials such as textiles and paper and can become the functional element of devices such as biosensors or for applications such as artificial muscles. Functionality can be increased by covering with electroactive polymers, leading to devices with highly superior performances when compared to classic architectures.
- Biocompatible materials represent another research direction of the group, several approaches being developed, including both biopolimeric fibers (collagen or cellulose), natural membranes (egg shell membrane) or nanostructured materials such as hydroxiapatite.

Further functionalization includes covering with different compounds or nanostructures or doping and leads to multiple fields of applications, the main one being that of medical devices.

The research directions presented in the group are mostly interconnected for developing devices with direct applications. Equipment for fabricating fibers by means of electrospinning and forcespinning were designed and developed in the group with the support of the engineers from the application department.

Relevant infrastructure

The groups' activity is based on several chemistry and electrochemistry laboratories dedicated to different types of applications. For obtaining the desired nanostructures or nanostructured materials several chemistry and electrochemistry laboratories are used including specific equipment such as chemistry hoods, ovens, potentiostats and so on.

Clean room equipment is essential for devices fabrication:

- Electron beam nanolithography equipment with Raith Elphy systems with laser interferometers and Hitachi S3400 and Zeiss Merlin Compact electron microscopes;
- EVG 620 NT equipment with nanoimprint capabilities;
- CVD equipment for preparation of carbon based nanostructures;
- CVD equipment for semiconducting materials deposition;
- Laboratory for optical characterization including UV – vis absorption spectrometers (Carry 5 and Perkin Elmer 35), photoluminescence spectrometers (Edinburgh and Perkin Elmer LS55), near field photoluminescence microscope, plasmonic resonance spectrometer with potentiostat;
- Liquid chromatography equipment with mass spectroscopy;
- Laboratory for biocompatibility testing including cell culture, flux cytometry, fluorescence microscope.

Services

- Scanning electron microscopy characterization of materials (micromorphology, composition)
- Optical characterization by means of optical spectroscopy
- Development of equipment for producing micrometric and submicrometric fibers by means of electrospinning and forcespinning;

Group name:

Group of Complex Heterostructures and Oxide Materials with Perovskite structure (CHetOMaP)

Group Leader: Dr. Lucian Pintilie, Senior Researcher rank 1 (pintilie@infim.ro)

Team:

CHetOMaP group has, at present time, 38 members, 35 with permanent contract and 3 with short term contracts. From the 35 members with permanent contracts, 6 are Senior Researchers rank1 (SR 1), 3 are Senior Researchers rank 2 (SR 2), 11 are Senior Researchers rank 3 (SR 3), 4 are Senior Researchers (SR), 5 are Junior Researchers (research assistants or RA), and 5 are sub-engineers or technicians. There are 24 holders of PhD title, 4 PhD students and 1 PhD supervisor.

Main research topics:

- **ferroelectric materials and related structures for electronic, optoelectronic and sensing applications** (including non-volatile memories, UV and IR detectors, piezoelectric devices);
- **materials and structures for photovoltaic conversion and light/particle detection** (including perovskite solar cells and Si particle detectors);
- **bio-compatible materials and other materials with potential applications in medicine or life sciences.**

Relevant infrastructure:

The Group has an extensive infrastructure, covering various methods of material preparation, thin film deposition, and complex physico-chemical characterization. Among the important infrastructures one can mention:

- PLD (pulsed laser deposition) work station with (fig. 1): 2 deposition chambers, each with 4 target carousels, sample heater up to 1000 K, fluence control, vacuum system and control of working gases pressure; one chamber has RHEED high pressure; a KrF excimer laser with 248 nm wavelength, 10 Hz repetition rate and maximum 700 mJ energy. One chamber is used to deposit ferroelectric layers from materials with a perovskite structure and other simple metal oxides (ZnO, HfO₂), and the other chamber is used to deposit superconductor materials.
- Matrix assisted pulsed laser deposition (MAPLE): 1 deposition chamber with 2 frozen and 2 solid targets; sample holder heated up to 800 K; a KrF excimer laser with 248 nm wavelength, 10 Hz repetition rate and maximum 700 mJ energy. This machine is used, for example, to deposit nanoparticles from frozen suspensions in a dielectric matrix.
- RF sputtering equipment (with 4 confocal magnetron sputtering for 2 inch targets, and 1 central magnetron sputtering with 3-inch target, see figure 2).
- Chemistry laboratory, with various spin-coaters, annealing furnaces, glove boxes and other laboratory equipment for preparation of nanopowders and thin films.
- X-ray diffraction equipment for thin films (XRD) from Rigaku (figure 3), and other two older machines from Bruker, one for powders and one for thin films. These are used for structural characterization, allowing identification of crystalline phases, crystalline strain, quality of epitaxy, etc.

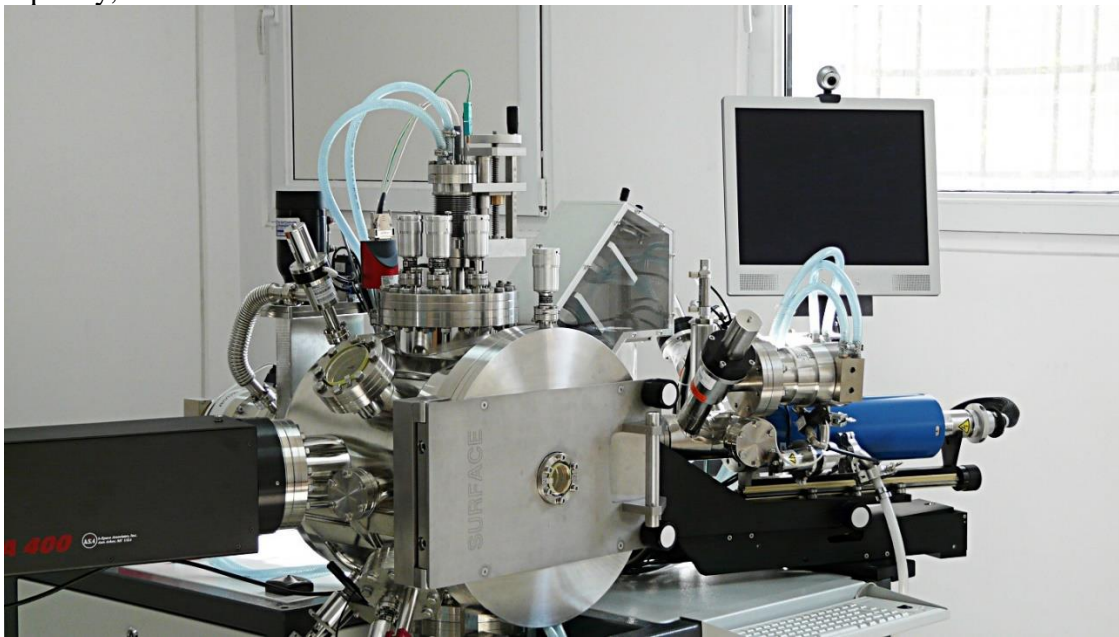


Fig. 1 PLD work station-the chamber for deposition of ferroelectric thin films (from Surface GmbH).

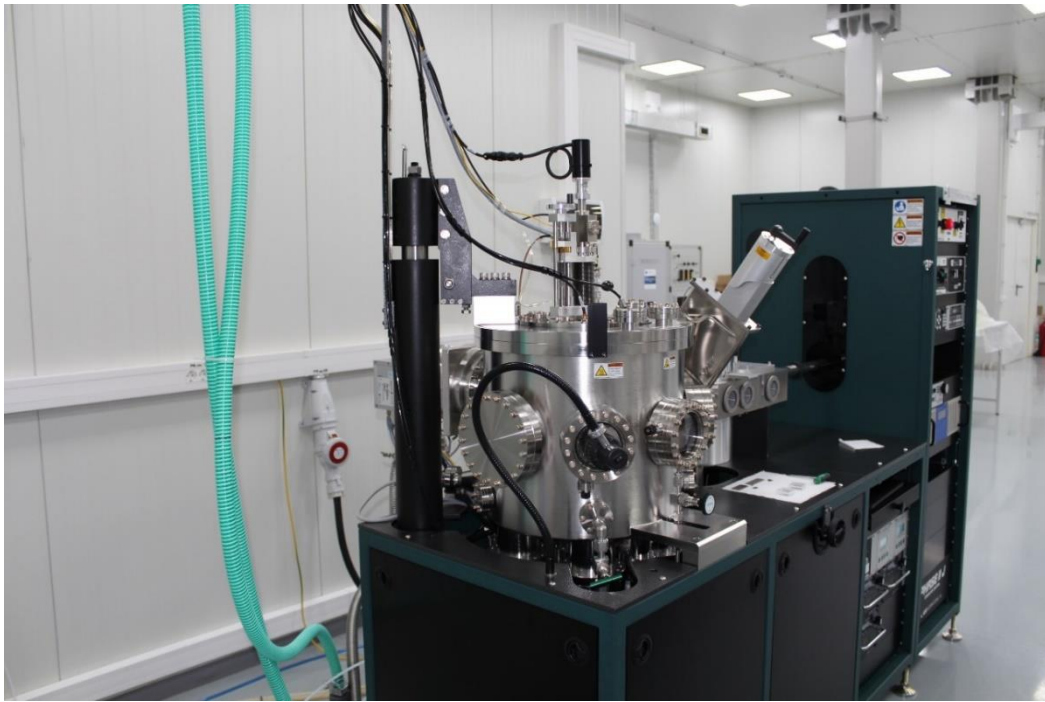


Fig. 2 RF magnetron sputtering equipment from Aja International Inc.



Fig. 3 XRD equipment for thin film characterization, produced by Rigaku.

- Laboratory for electrical measurements (see figure 4), including: 2 Lake Shore cryo-probers, one with vertical magnetic field up to 2.5 T, and one with horizontal magnetic field up to 1.5 T, each has at least 3 micro-manipulated arms with contact needles allowing electrical measurements from liquid helium to 425 K with various electric fields and illumination conditions; several closed cycle cryostats for measurements between 10 K and 400 K; DLTS system for trap investigation; set-up for pyroelectric measurements; ferritester from AiXACCT; various instruments to measure low currents, high resistance; RLC bridges. This lab is used to perform complex investigation of the electrical properties (hysteresis loops, C-V and I-V characteristics, impedance spectroscopy; thermally stimulated currents, etc.).
- Laboratory for testing solar cells, with 1 SUN solar simulator and other accessories.

- Laboratory for characterization of materials for microwave devices, as well as laboratory models of microwave devices, including: 1) Vector Network Analyzer PNA 8361° from Agilent (0,01 - 67 GHz) for two-ports complex S parameters. The instrument is also used for material characterization. It uses electronic calibrator Agilent N4694-60001 in range 10 MHz – 67 GHz. For access, 1.9 mm, 2.9 mm, 2.4mm, 3.5 mm, SMA or N connectors or adaptors are used. 2) Vector Network Analyzer PNA-X N5245A from Agilent (0,1 – 50 GHz stand-alone) with 4 ports and dual sources. It allows measurements of such non-linear parameters as the X parameters. By using the millimeter wave extensions, the system covers a wide frequency band up to 500 GHz, unique in South-Eastern Europe. Each extension pair allows the measurement of two-ports parameter of waveguide devices. The millimeter wave extensions are from OML (N5260A V10 VNA2, WR-10, 75-110 GHz; N5260A V06 VNA2, WR-06, 110-170 GHz; N5260A V05 VNA2, WR-05, 140-220 GHz; N5260A V03 VNA2, WR-03, 220-325 GHz; N5260A V02.2 VNA2, WR-02.2, 325-500 GHz). 3) Anechoic chamber with internal dimensions 3040 mm x 4100 mm x 2800 mm. 4) Microprobe station for direct on wafer measurements of two-ports in the frequency range 0.1 - 67 GHz by using probes GSG with 150 μ m si 100 μ m pitch. 5) TDS THz spectrometer from Aispec
- Laboratory for optical spectroscopies including a spectroscopic ellipsometer and FTIR.

The group has access to other infrastructures located at NIMP, through collaborative research activities, such as: TEM and SEM equipment; XPS characterization (including at Elettra Synchrotron Trieste); magnetic measurements (SQUID, PPMS); other optical spectroscopies (Raman, UV-Vis-NIR, luminescence); cleanroom facility; small bio-laboratory for testing bio-materials.



Fig. 4 Laboratory for electrical characterization of dielectric, ferroelectric and semiconductor materials and related structures.

Services:

- Material preparation (bulk ceramics, thin films deposition by various techniques)
- Trap investigation by DLTS and TSC
- Electric characterization of materials on a wide temperature range, under electric and magnetic fields
- Investigation of pyroelectric properties
- Fabrication and characterization of perovskite solar cells
- Characterization of microwave, millimeter waves and Terahertz materials and devices
- Biocompatible coatings for implants
- Realization and characterization of catalytic materials
- AFM/PFM characterization

Laboratory 20 „Magnetism and Superconductivity”

Group name: Electronic Correlations, Magnetism and Superconductivity (recently formed by joining the former group of Electronic Correlations and Magnetism and the group of Superconductivity)

Group leader: Dr. Victor Kuncser, Senior Researcher rank 1 (kuncser@infim.ro)

Personnel: 5 Senior Researchers ranka 1 (Research Professor), 5 Senior Researcher rank 2, 9 Senior Researchers rank 3, 4 Scientific Researchers, 6 Research Assistant, 1 engineer for technological development and 3 technicians. Except for the scientific activity, the group is also involved in educational and training activities. There are 3 PhD advisers coordinating 2 to 3 PhD students yearly as well as master and undergraduate students performing their scientific training.

Main research directions

Envisage fundamental and applied research in the field of magnetic and magneto-functional materials for actuator and sensoristic applications as well as in the field of superconductivity, mainly targeting materials with superconducting properties with potential for practical applications. The research process covers all stages, from preparation (bulk materials, thin films or nanostructures) to structural and electronic characterization, completed with a deep analysis of the magnetic and respectively superconducting properties.

Related to the magnetic behavior, mainly the functionalities mediated by magnetic reconfiguration controlled by temperature, magnetic and electric fields, applied or from interface interactions, are envisaged. The research is focused especially on the study of 0D,1D and 2D nanostructures. In the case of magneto-functional structures, magnetic systems of nanoparticles, thin films and multilayers, materials for colossal magnetoresistance (CMR), giant magnetoresistance (GMR) and tunnelling magnetoresistance (TMR), soft and hard magnetic materials, Heusler compounds with spin polarization, heterogeneous multiferroic systems, magneto-caloric materials, diluted magnetic oxides/semiconductors, thermo-electric systems, etc. are envisaged. In addition, bulk materials, advanced hybrid systems and composites / nanocomposites destined to operate in extreme conditions such as the ones in fusion and fission reactors, particle accelerators and in space, are investigated. Interactions at the interface and functionalities induced by them in nanostructured hybrid systems such as soft magnet / hard magnet (exchange-spring), ferromagnet/antiferromagnet (exchange-bias), ferromagnet-ferroelectric (magneto-electric coupling) represent another field of interest related to fundamental and applicative aspects of smart multi-functional systems. In specific cases, the experimental studies are completed by theoretical studies approaching electronic configurations based on Density functional theory (DFT) and magnetic configurations based on finite-element simulation programs.

Related to the superconducting behavior, studies of vortex matter, dynamics and pinning and nano-engineering of artificial pinning centres for high-magnetic field applications are envisaged. Exploration of fields of applicability of these materials and related ones considering, beyond superconductivity, other that may be important for applications, such as mechanical, biological, optical are also considered. The studied materials are mainly cuprate high temperature superconductors Y (rare earth) $\text{Ba}_2\text{Cu}_3\text{O}_7$ (RE123) with nano-engineered pinning centres, Bi- and La-based superconducting cuprates, MgB_2 (with various additions for increasing pinning properties), iron-based pnictide and chalcogenide multicomponent superconductors and low temperature (classic) metallic and intermetallic superconductors. Other materials of interest are CeO_2 , SrTiO_3 , LiPdPtB , PdO , boron/carbide composites, selected steels, and archaeological ceramic materials. Most of the materials are obtained in the laboratory in various morphologies: powders, polycrystalline bulk samples, single crystals, wires/tapes, nanostructures, heterostructures and nanocomposites. The group uses advanced techniques for obtaining or processing materials: conventional powder synthesis in controlled atmosphere, cryochemistry or energy milling, crystal growth in flux or by melting zone,

growth of thin films by laser ablation, sintering by Spark Plasma, lamination, arc melting, etc. Advanced analysis of superconducting properties aims in particular to determine vortex phase diagrams vortex dynamics and vortex pinning. Temperature dependence of magnetization and resistivity, isothermal hysteresis magnetization and magnetic relaxation, current-voltage characteristics, bulk pinning force and pinning potential etc. are analysed within the existing theoretical models or using recognized practical and theoretical methodologies developed by some members of the group, for example pinning potential determined from frequency-dependent AC susceptibility response, or the use of normalized magnetic relaxation rate to determine the cross-over between elastic and plastic vortex creep, and various field-m and temperature-dependent creep exponents.

Relevant infrastructure

Among important research equipment, considering preparation facilities as well as characterization ones, the following can be listed: spark plasma sintering, hot press sintering, microwave sintering and melt spinning equipment, nanoparticle preparation systems by hydrothermal / solvothermal synthesis in autoclave and centrifugation for separation by sizes), RF/DC sputtering deposition system for magnetic thin films and multilayers with 4 sources and base pressure in the range of 10^{-9} mbar, facility for inducing thermal transfer in radiofrequency magnetic field to determine specific absorption rates in dispersed nanoparticle systems, thermogravimetric and differential scanning calorimetry systems, Vibrating Sample Magnetometry system in magnetic fields up to 9 Tesla, Mossbauer spectrometers with different accessories to perform measurements at variable temperatures (4.5 K –1000 K) and in applied fields, via the detection of gamma radiation / X- rays / conversion electrons (the only group in Romania active in Mossbauer Spectroscopy), complex system for measurements of physical properties (PPMS) with magnetic fields up to 14 Tesla and a SQUID type magnetometer working in 7T down to 2K from Quantum Device with the corresponding facility for liquid He production (18 l /24 h). Magnetic texturing of thin films is investigated by vectorial MOKE magnetometry. For high temperature domain, the laboratory possesses a Laser Flash Analyzer system that allows the determination of thermal diffusivity, specific heat and thermal conductivity of the volume materials or multilayers (3 layers, including liquids) in the range 25-1100 C, a dilatometer (Netzsch 402 C, 2015) to determine thermal expansion coefficients (25-1600 C) and an equipment (Netzsch, Nemesis 2015) to determine electrical conductivity and Seebeck coefficient (25-800 C). In order to determine the composition in bulk / powder systems, an X-ray fluorescence device is available, while for very low concentrations/quantities the group possesses an inductively coupled plasma mass spectrometer (ICP-MS), with an extension for thin film analysis by laser ablation (LA), the last one being acquired in 2019, in collaboration with Laboratory 10. Mechanical properties are determined in quasistatic regime up to 1700 °C, using a recently-acquired equipment (INSTRON).



ICP-MS with LA for thin films (upper left), Mossbauer spectrometers with closed circuit He cryostats (lower left) and SQUID device – Quantum Design, of high sensitivity (middle). Spark plasma sintering plant (FCT Systeme GmbH) used to obtain high density bulk materials (right).

Available services

- Preparation of metallic and intermetallic compounds in the geometry of thin films, ribbons or bulk,
- synthesis of materials that are important for applications using state-of-the-art powder metallurgy techniques,
- lyophilisation from frozen materials,
- treatment of powders and thin films at high pressures and temperatures in non-corrosive gas atmosphere (hydrogen, nitrogen, methane, carbon dioxide, helium) and measurement of the formation kinetics and thermodynamics of the materials obtained by gas-solid reaction,
- high sensitivity magnetometry to characterize the magnetic properties of the elements (bulk, powders and nano-powders, ribbons and nanocomposites, 0-, 1- and 2-dimensional nanostructures),
- characterization of the thermodynamic and transport properties (thermal, electric) of the materials in a large temperature domain,
- determination of the Debye temperature, specific heat and entropy variation of solid materials in the temperature range of 2-300 K and in a magnetic field between 0 and 14 T,
- determination of thermal conductivity of solid materials in the temperature range of 2-300 K and in a magnetic field between 0 and 14 T,
- complex characteristics and specific properties of materials with iron evidenced by powerful nuclear gamma resonance investigation methods (Mossbauer spectroscopy),
- specific temperature-dependent properties evidenced by modern differential thermal analysis methods, differential calorimetry and mass spectrometry,
- atomistic simulation within the density functional theory (DFT) of the materials for advanced applications and finite element micromagnetic modelling,
- preparation / processing by various techniques of powders, single-crystals, thin films / heterostructures / nanostructures, bulks, composites;
- magnetic and transport measurements on superconducting materials;
- analysis of experimental data obtained on superconductors with the determination and modeling of critical parameters (critical temperature, critical current density, irreversibility field, pinning force and pinning mechanisms, trapped field, vortex pinning energies, Debye temperature, and others)
- mechanical measurements in quasistatic regime up to 1700 °C (bending / compression of hard materials);
- analysis of mechanical properties and correlation with fractography aspects;
- targets fabrication for thin layer deposition.

The group also develops materials and technologies for a number of applications: superconducting thin layers and coated conductors from high critical temperature cuprates containing nano-engineered pinning centres; superconducting MgB₂ wires/tapes in metallic sheath; MgB₂-based magnetic storage devices, magnetic concentrators and magnetic shieldings; MgB₂-based powders, coatings and bulks for biomedical applications; boron-based super-hard materials for tools and extreme high temperature applications, integrated multifunctional devices.

Laboratory 30 „Nanoscale Condensed Matter”

Group name:

Theoretical Physics

Group leader: Dr. Valeriu Moldoveanu, Senior Researcher rank 1 (valim@infim.ro)

Personnel: 8 permanent positions (2 SR 1, 1 SR 2, 2 SR 3, 1 SR, 2 AR).

Research topics:

- A. *Topological features of 2D materials and transport properties of 2D lattices.*
- B. *Open quantum emitters and nano-electromechanical systems.*

Group name

Group of Surface and Interface Science

Group leader: Dr. Habil. Cristian Mihail Teodorescu, Senior Researcher rank 1 (teodorescu@infim.ro)

Personnel:

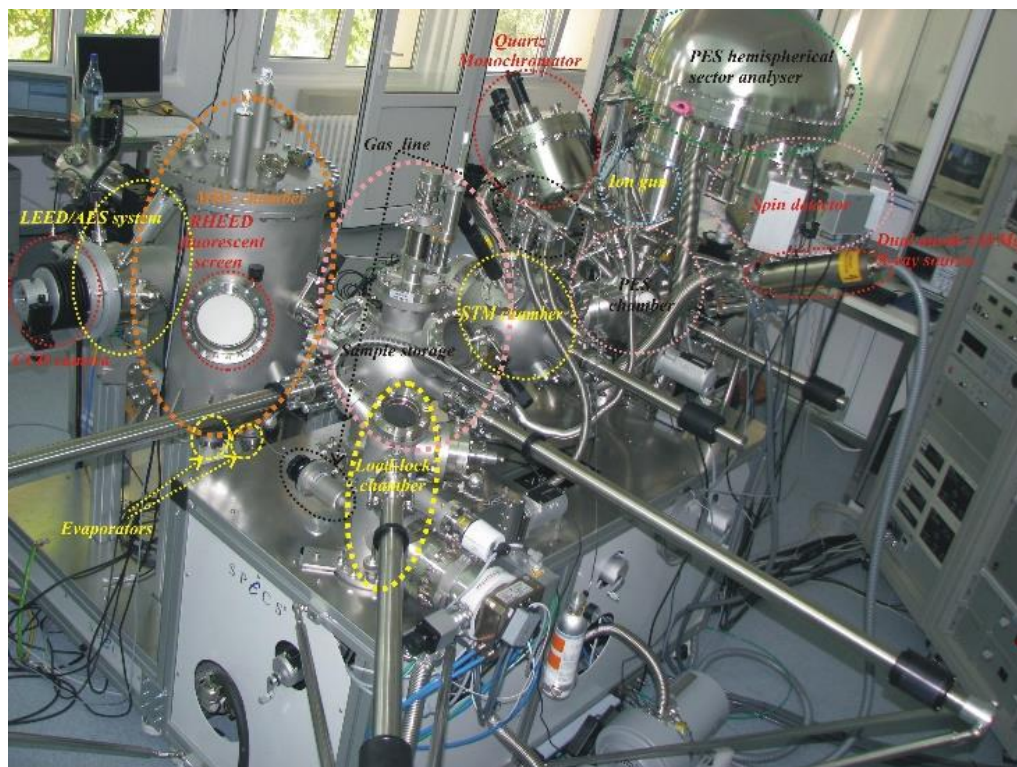
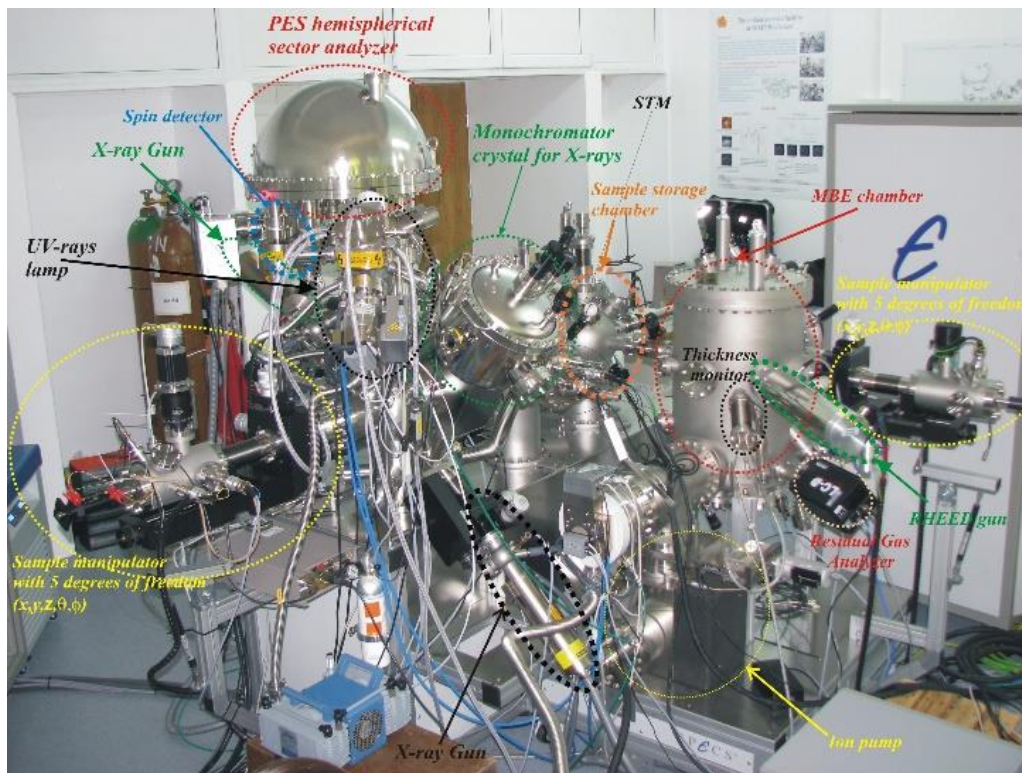
1 SR 1, 5 SR 2, 7 SR 3, 4 SR, 5 RA, 1 Engineer, 3 Technicians.

Main research topics:

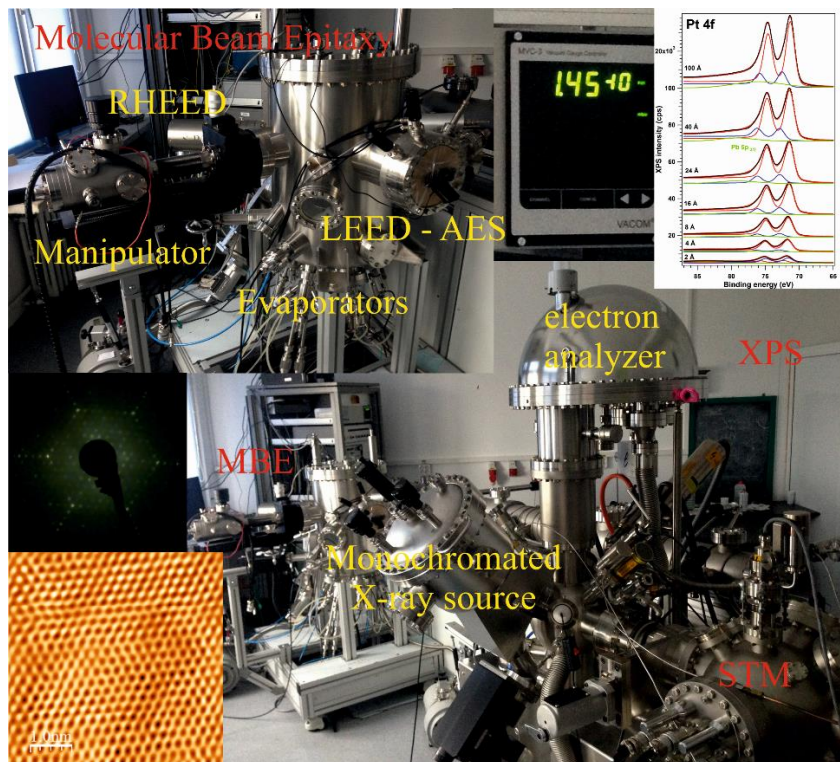
surface science, ferroelectrics, catalysis, magnetic materials, epitaxy

Experimental setups:

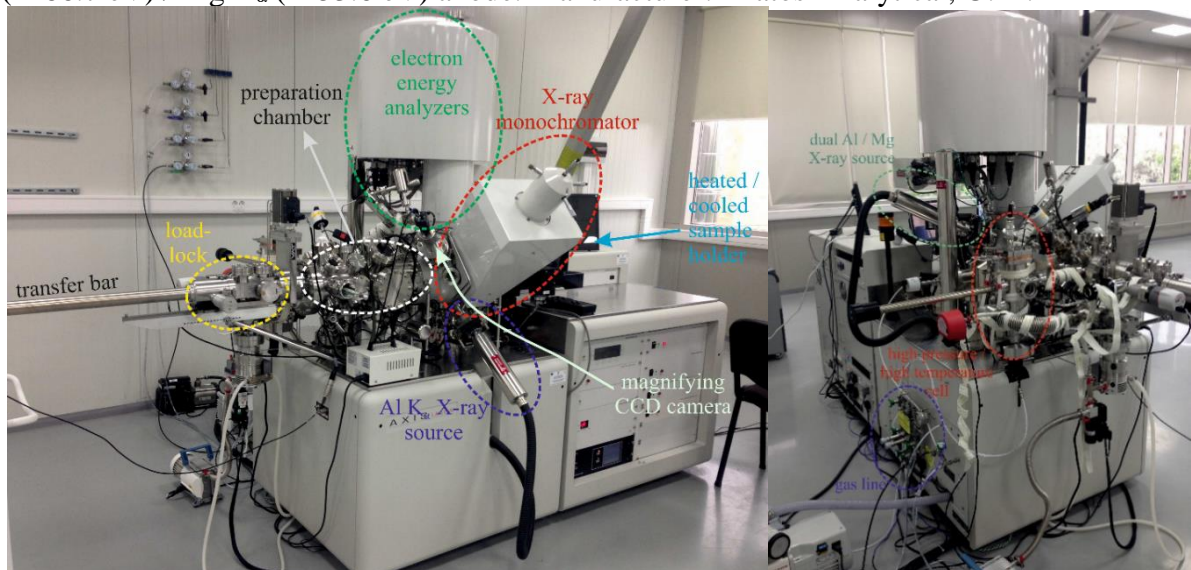
- Experimental surface science setup, comprised by: (i) molecular beam epitaxy, with in situ analysis by low energy electron diffraction (LEED), reflection high energy electron diffraction (RHEED), Auger electron spectroscopy (AES), sample preparation by ion sputtering, annealing, plasma source, Knudsen cells, electron bombardment evaporators, residual gas analysis; (ii) an installation for scanning tunneling microscopy and spectroscopy (STM–STS), at variable temperature; (iii) an installation for angle- and spin-resolved photoelectron spectroscopy, allowing X-ray photoelectron spectroscopy (XPS), photoelectron diffraction (PED, XPD), angle-resolved ultraviolet photoelectron spectroscopy (ARUPS) also with spin resolution. Actually, this cluster is delocalized on the SuperESCA beamline at the Elettra synchrotron radiation facility in Trieste, Italy and is available for external users, feed with synchrotron radiation with continuous spectrum with energy between 90–1200 eV. Outside the beamtime allocated by Elettra, photoemission can still be performed by using monochromated Al K α (1486.7 eV)/ Ag L α (2984.3 eV) radiation and high power UV lamp (300 W) with He I (21.2 eV) and He II (40.8 eV) radiation. Manufacturer: Specs, Germany.



- Experimental cluster comprising (i) a molecular beam epitaxy (with *in situ* LEED, RHEED and AES analyses), sample preparation (sputtering, annealing, Knudsen cells, e-beam evaporators), residual gas analysis, gas cabinet; (ii) a chamber for scanning tunneling microscopy and spectroscopy (STM – STS); (iii) chamber for photoelectron spectroscopy (XPS, UPS). Available excitation sources: monochromated Al K_{α} radiation (1486.7 eV), dual Al K_{α} (1486.7 eV) / Mg K_{α} (1253.6 eV) anode, UV lamp with He I (21.2 eV) radiation. Manufacturer: Specs, Germany.



- Automated installation for XPS with spatial resolution (2 μm) coupled to a reaction cell for online studies of surface reactions at high temperatures and pressures (1000 $^{\circ}\text{C}$, 4 bar), with gas cabinet with 4 ways. Excitation sources: monochromated Al K_{α} (1486.7 eV), dual Al K_{α} (1486.7 eV) / Mg K_{α} (1253.6 eV) anode. Manufacturer: Kratos Analytical, U. K.



- Installation for low energy electron microscopy (LEEM) and photoemission electron microscopy (PEEM). Available techniques: (i) dark or bright field LEEM with 4 nm lateral resolution; (ii) PEEM using excitation with Hg lamp or with UV lamp with He I and He II radiation, lateral resolution 15 nm; (iii) mirror electron microscopy; (iv) micro-LEED (with μm lateral resolution); k -space mapping with sub-micrometer lateral resolution (vi) Possibility to follow in real time LEEM, PEEM, MEM, LEED during thermal treatment, ion bombardment, thin film growth. Manufacturer: Specs, Germany.
- Setup for laboratory extended X-ray absorption fine structure (EXAFS). Excitation: Mo $K_{\alpha 1}$ (17479.34 eV), W $L_{\alpha 1}$ (8397.6 eV), power 3 kW (40 kV, 75 mA); monochromators Ge(220),

- Ge(400), Ge(840); detectors: proportional or scintillators, measurements in transmission or fluorescence, simulation and analysis software. Manufacturer: Rigaku, Japan.
- Chemistry laboratory, with basic instrumentation: glassware, balances, ultrasonic shafts, vortex, water distillation, pressure reactors, heating and stirring systems, photocatalytic reactions, vacuum stove (Memmert), rotvapor (Heidolph), etc. Dedicated to catalyst preparation and performance evaluation for oxidation, hydrogenation, coupling reactions etc. The laboratory is assisted by: (a) Analytical methods for chemical compound identification (gas chromatography coupled to mass spectroscopy GC-MS QP2010 Ultra, manufactured by Shimadzu, Japan). This equipment uses two injectors, two detectors (MS and BID), pressure valve for real time analysis, auto-sampler, detects gaseous compounds or volatile liquids. (b) Analysis system for materials characterization, using cumulative characterization techniques, such as temperature programmed desorption, reduction or oxidation (TPD, TPR, TPO), pulsed chemisorption, nitrogen physisorption (Brunauer-Emmett-Teller BET) for pore size analysis. (c) Raman spectroscopy (AvaRaman 532) and UV-Vis-NIR spectro-photometry (AvaSpec-ULS 2048 L-RS-USB2) used for reaction follow-up, product identification, detection and characterization of nanoparticles in suspension. Irradiation sources: 532 nm laser for Raman spectroscopy and Xe source with emission 200 – 1100 nm, for the UV-Vis-NIR spectro-photometer. The latter is equipped with an integrating sphere with 80 mm internal diameter and flux cell analysis with transverse Swagelok feedthroughs and two collimating lenses UV-Vis-NIR; maximum temperature 80 °C, maximum pressure 10 bar.

Services provided:

- Photoelectron spectroscopy-based techniques: X-ray photoelectron spectroscopy (XPS) and diffraction (XPD), ultraviolet photoelectron spectroscopy (UPS), angle-resolved UPS (ARUPS), spin-resolved ARUPS.
- Auger electron spectroscopy (AES) and diffraction (AED).
- Low energy electron diffraction (LEED) and reflection high energy electron diffraction (RHEED) characterization of surfaces.
- Scanning tunneling microscopy (STM) and spectroscopy (STS) at variable temperature.
- Sample depth profiling by ion sputtering assisted by XPS or AES.
- Surface cleaning and synthesis of epitaxial thin films by molecular beam epitaxy (MBE).
- Thermally-programmed desorption of molecules from surfaces by residual gas analysis (RGA).
- Low energy electron microscopy (LEEM) and photoemission electron microscopy (PEEM), micro-LEED and micro-ARUPS.
- Extended X-ray absorption fine structure (EXAFS).
- Positron annihilation-induced Auger electron spectroscopy (PAES).

Laboratory 40 „Optical processes in nanostructured materials”

Group name

Group of Optical Processes in Nanostructured Materials

Group leader: Dr. Mihaela Baibarac, Senior Researcher rank 1 (barac@infim.ro)

Personnel:

3 SR 1, 6 SR 2, 3 SR 3, 6 SR, 14 RA and one technician.

The main research directions:

- optical properties of composite materials based on macromolecular compounds and carbon nanoparticles (graphene, including graphene oxide and reduced graphene oxide, carbon nanotubes, fullerene) and phosphorene, respectively, for applications in the field of eco-nanotechnologies, health and energy storage (supercapacitors, rechargeable batteries)
- optical properties of the inorganic micro/nano-particles for applications in the field of heritage and optoelectronic.

The relevant infrastructure:

- an UV-VIS-NIR spectrophotometer, Lambda 950 model, from Perkin Elmer;
- a FTIR spectrophotometer, Vertex 80 model, from Bruker,
- a FTRaman spectrophotometer, RFS 100 S model, from Bruker;
- a Fluorolog FL-3.2.2.1 model with upgrade for the NIR range, from Horiba Jobin Yvon,
- a triple Raman spectrophotometer T64000 model, from Horiba Jobin Yvon, equipped with the lasers for the excitation in visible range;
- a FTIR imaging microscope SPOTLIGHT 400 from Perkin Elmer,
- a thermoluminescence reader Harshaw TLD 3500,
- a system for photoconductivity and I-V characteristics;
- a Scanning Near Field Optical Microscope (Multiview 4000 SNOM/SPM system from Nanonics) coupled with Atomic Force Microscope (AFM),
- Fluoromax 4P with quantum efficiency and colorimetry options, for luminophores characterization,
- system to measure surface/interfacial tension, contact angle and density;
- Langmuir-Blodgett instruments, KSV 2000 system and KSV 5003 model;
- a potentiostat/galvanostat, Voltalab 80, from Radiometer Analytical;
- multi-channel potentiostat/galvanostat, Origaflex model, from Origalys;
- equipment for deposition by vacuum evaporation of organic materials;
- broadband dielectric spectroscopy system from Novocontrol;
- an infrared spectro-microscope, Carry 600, from Agilent Scientific;
- a surface plasmons resonance (SPR) equipment from Reichert;
- Hybrid Magnetron Sputtering – Pulsed Laser Deposition equipment for thin films and
- Physical Vapor Transport equipment for transition metal dichalcogenides.

Services:

The economic contract with S.C. Intelectro Iasi S.R.L. which is aimed at highlighting the physico-chemical properties of nanostructured inks, the main analyzes being performed by UV-VIS and IR absorption spectroscopy, Raman scattering and viscosimetry.



Surface Plasmon Resonance equipment from Reichert



Infrared spectro-microscope, Cary 600 from Agilent Technologies



Physical Vapor Transport equipment for transition metal dichalcogenides



Hybrid Magnetron Sputtering – Pulsed Laser Deposition equipment for thin films

Laboratory 50 „Atomic Structures and Defects in Advanced Materials (LASDAM)”

Group name:

Atomic Structures and Defects in Advanced Materials

Group leader: Dr. Corneliu Ghica, Senior Researcher rank 1 (cghica@infim.ro)

Personnel: LASDAM counts 36 research and technical personnel including 22 Senior Researchers (6 SR 1, 5 SR 2, 9 SR 3, 2 SR), 8 research assistants (7 PhD students, 1 MSc student) and 3 engineers and 3 technicians.

Main research topics

- Development and implementation of new techniques and methods, unique at the national and European regional level, for the advanced characterization of the physical and chemical properties of materials, with the reinforcement of the existing internationally recognized expertise.
 - In-depth study of the microstructural properties of advanced materials such as nanostructures (powders, nanowires), thin films, ceramics and special alloys using advanced techniques of analytical electron microscopy TEM/SEM including atomic resolution imaging (HRTEM, HAADF STEM), elemental mapping at atomic resolution (HRSTEM EELS), electron tomography, structural mapping (SEM-EBSD, precession electron diffraction).
 - Multifrequency and multiresonance EPR investigation of the paramagnetic point defects, either intrinsic or induced by impurities or radiations in insulators and wide-bandgap semiconductors.
- Synthesis and characterization of physical and chemical properties of new classes of advanced materials for applications of high interest at national and global level.
 - Investigation of the physical chemical mechanisms at the bottom of the detection process in nanostructured materials for gas sensing applications.
 - Thin films from advanced materials for microelectronic industry with a wide range of applicability in sectors of high impact at a global level: environment, security, space, biomedicine, food safety.
 - Interdisciplinary researches on cellular and non-cellular in vitro interactions and biomedical applications of inorganic nanomaterials and hybrid nanostructures

Main research infrastructure

Among the important research equipment we mention: aberration-corrected analytical transmission electron microscope (HRTEM/HRSTEM) provided with probe Cs corrector of the spherical aberration and EDS and EELS microanalytical facilities, allowing sub-Ångström spatial resolution and atomic elemental mapping; high-resolution analytical electron microscope for electron tomography and in-situ heating/cooling experiments; SEM-FIB dual analytical system used for morphostructural and microanalytical investigations (SEM, EDS, EBSD) as well as for the advanced materials processing at micro and nanometric scale by means of a Ga⁺ ion beam and nanomanipulators; specialized equipment for TEM/SEM specimens preparation by mechanical thinning and polishing, ion milling, electropolishing; continuous wave (cw) X-band (9.8 GHz) EPR spectrometer with variable temperature (VT) accessories in the range 80 to 500 K; cw Q-band (34 GHz) EPR spectrometer with ENDOR (Electron-Nuclear Double Resonance) and VT: 5 to 300 K accessories; pulse X-band (9.7 GHz) EPR spectrometer equipped with pulse ENDOR, pulse ELDOR (Electron-Electron Double Resonance) and VT: 5 to 300 K accessories; automatic liquid He plant completed with a helium recovery system; gas mixing station and associated electrical measurements equipment for materials testing under controlled atmosphere; specialized equipment for hydrothermal

and co-precipitation chemical synthesis; magnetron sputtering installation for thin films deposition, provided with techniques for in situ characterization such as Auger electron spectroscopy (AES), low-energy electron diffraction (LEED) and ellipsometry; installation for rapid thermal processing including rapid thermal annealing (RTA), oxidation and nitriding; horizontal furnace with 3 temperature zones for thermal treatments and physical vapour deposition (PVD); measurement chains for electrical, ferroelectric and photoelectric characterization, Hall effect and magnetoresistance measurements.



- a. Bruker EPR spectrometer in X band (9.7 GHz) in pulsed regime with ENDOR accessories;*
- b. Bruker EPR spectrometer in CW Q-band with ENDOR accessory;*
- c. Setup for electrical measurements under controlled atmosphere gas mixing station.*
- d. JEM 2100 high-resolution analytical transmission electron microscope;*
- e. Tescan Lyra III analytical SEM-FIB dual system;*
- f. Magnetron sputtering installation for thin films deposition, provided with in situ AES, LEED and ellipsometry;*
- g. Installation for rapid thermal processing (RTA, RTO, RTN), horizontal furnace with 3 temperature zones for thermal treatments and PVD;*
- h. Measurement chains for electrical, ferroelectric and photoelectric characterization, Hall effect and magnetoresistance measurements.*

The HRTEM and EPR spectroscopy facilities are included in the Central-European network of research infrastructures CERIC (<http://www.c-eric.eu/>) since its creation in 2014. NIMP-LASDAM is Romania's representing entity and partner facility in CERIC along with advanced laboratories from research institutions and universities in Austria, Croatia, Czech Republic, Hungary, Italy, Poland and Slovenia.

Types of performed scientific investigations:

Apart from the scientific research activities developed within national and European research projects, LASDAM offers a wide range of contract R&D services for the private and public sectors in Romania and abroad:

- High-resolution FEG-SEM morphological characterization of advanced materials, from nanopowders and nanowires/nanotubes to bulk ceramic or metallic materials;
- Microstructural characterization of nanostructured materials (powders, nanowires), thin films, ceramics, alloys by TEM/HRTEM and SEM;
- Chemical elemental composition measurements by EDS;
- Large area and/or local elemental mapping by SEM-EDS and STEM-EDS;
- Multifrequency EPR characterization of bulk and nanostructured insulating and semiconductor materials:
 - Determination of the nature, concentration, localization, formation mechanism and stability of the paramagnetic centers (intrinsic defects, impurities, radiation defects, radicals etc.) present in the materials;
 - Investigation of chemical transformations, structural or magnetic transitions;
 - Detection and characterization of radicals in materials with biochemical applications using EPR spin-trapping;
- Controlled simulation of toxic and explosive gas environments (CO, CH₄, NO₂, H₂S, NH₃, SO₂) for gas sensors testing and calibration; temperature-voltage calibration for the optimization of power consumption for substrates and gas sensors.
- Growth of thin films and multilayers by magnetron sputtering: dielectrics (SiO₂, TiO₂, ZrO₂, HfO₂, Al₂O₃, Si₃N₄) and semiconductors (Si, Ge, SiGe, SiGeSn);
- Rapid thermal annealing (RTA) and controlled oxidation (RTO) at temperatures within 200-1250 °C (wafers up to 3 in), heating rates up to 200 °C/s in gas flow (N₂, O₂, Ar, H₂) and thermal treatments using the horizontal furnace with 3 temperature zones up to 1200 °C in vacuum or flow of Ar, N₂;
- Electrical characterization under dark/illumination conditions, Hall effect measurements and modelling of experimental curves current-voltage (I–V) at varying temperature, in DC and AC, capacity-voltage (C–V), capacity-frequency (C–f), capacity-time (C–t), polarization-voltage (P–V), I–T and R–T; spectral characteristics of the photocurrent (I–λ) in modulated and continuous illumination; Hall measurements: V-I curves as a function of current, magnetic field and temperature.

As partners in the CERIC consortium, we perform specific TEM and EPR investigations on projects submitted by external users worldwide. The technical and scientific peer review evaluation system guarantees a competitive free access to nearly 50 multi-probe available techniques. Six teams of international external users are hosted by LASDAM in average every year, which represents a significant contribution to the increase of international visibility and scientific prestige of NIMP.

Materials modeling, preparation and characterization

Amplitude-based approach for complex dielectric permittivity retrieval in terahertz time-domain spectroscopy

L. Nedelcu,^a C. Chirila,^a L. Trupina,^a A. C. Galca,^a M. G. Banciu,^a G. Annino^b

^aNational Institute of Materials Physics, Bd. Atomistilor 405A, Magurele, Romania, 077125

^bIstituto per i Processi Chimico-Fisici, IPCF-CNR, via G. Moruzzi 1, Pisa, Italy, 56124

The terahertz science and technology have continuously evolved during the last decades from an emerging field to a mature one [1]. One of the main driving forces was the terahertz time-domain spectroscopy (THz-TDS), being successfully exploited in materials science, chemistry, security, sensing, imaging, medicine etc. [1, 2]. Development of novel materials and devices have a significant contribution to the progress of THz technology. In this regard, fundamental and applied research were performed for identification of dielectric materials with suitable properties in the THz frequency range.

Although THz-TDS measurements can be performed in transmission or reflection configuration, the transmission set-up is preferred due to the better reliability of the obtained data because the higher power of the signal. For this reason, most of the mathematical procedure was focused on the retrieval of the complex refractive index ($\tilde{n} = n + jk$) from transmission measurements. In order to extract the material parameter in THz, the reference, which is the signal measured without the sample, and the pulse through the sample pulse are measured (Fig. 1.a). The spectral information of the transient electric field is obtained by Fourier transformation of the THz pulse (Fig. 1.b).

The relative complex permittivity ($\tilde{\epsilon} = \epsilon' + j\epsilon''$) is obtained from the amplitude and phase of the THz signal, which propagates through the sample and suffers multiple reflections between the plane parallel sample surfaces. The algorithm for obtaining dielectric parameters of the material uses an iterative procedure [2].

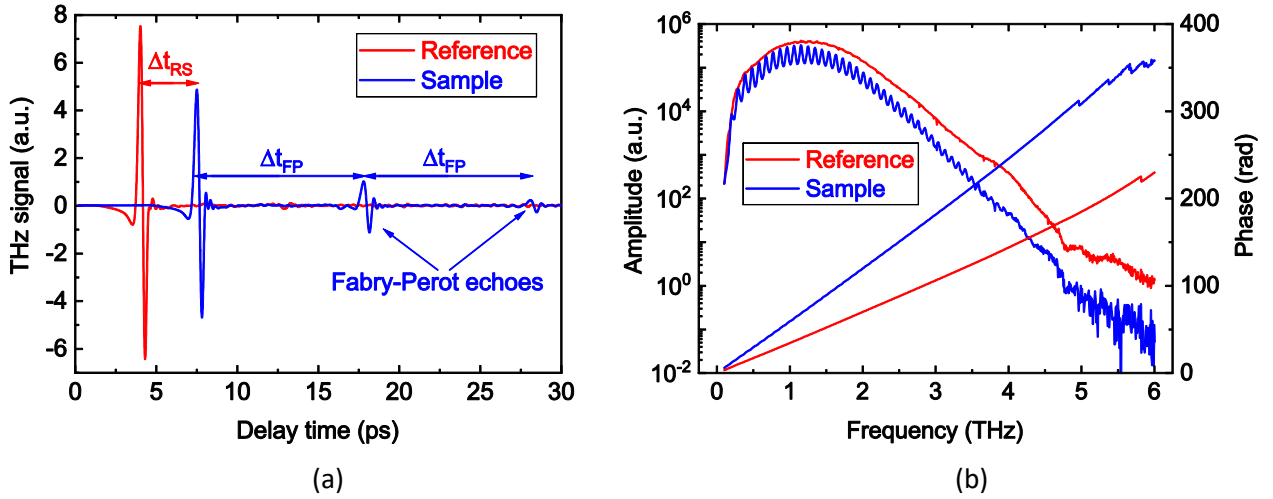


Fig. 1 Time domain (a) and Fourier-transformed (b) THz electric field.

The standard procedures are generally accurate and their accuracy increases with the increasing of the recorded Fabry-Perot echoes. On the other hand, the absorption and thickness of the sample are the decisive factors in extracting the material parameters. Assuming that the absorption is low enough to be able to perform measurements in transmission, in Fig.1.a are highlighted the delay of the pulse through the sample with respect to the reference (Δt_{RS}) and the difference between two consecutive Fabry-Perot echoes (Δt_{FP}), as follows:

$$\Delta t_{RS} = \frac{d(n-1)}{c} \quad (1.a)$$

$$\Delta t_{FP} = \frac{2nd}{c} \quad (1.b)$$

where d , n , and c are thickness, refractive index and speed of light in vacuum, respectively.

The usual scanning range of commercial spectrometers is 100-300 ps. Under certain conditions, it can reach up to 500 ps. For this reason, the sample sizes must be chosen appropriately. Supposedly, the material of interest has $n = 10$. Although this value is higher than that of polar dielectrics and underestimated for ferroelectrics, we will use it to evaluate two extreme cases:

1. $d = 1 \mu\text{m}$; for thin samples $\Delta t_{RS} = 0.03 \text{ ps}$ and $\Delta t_{FP} \sim 0.07 \text{ ps}$. The difference between the reference pulse and sample pulse is too small, the Fabry-Perot echoes cannot be separated and the spectrometer band should be at least 15 THz. Practically, it is not possible to extract the material parameters of a sample with a thickness of $1 \mu\text{m}$ and $n = 10$ by using algorithms based on the Fabry-Perot echo pulses.

2. $d = 1 \text{ mm}$; material parameters can be extracted accurately because $\Delta t_{RS} = 30 \text{ ps}$ and $\Delta t_{FP} \sim 70 \text{ ps}$. However, the thickness of the sample should not be too large because the number of Fabry-Perot echoes that can be recorded decreases due to the sample's absorption.

THz characterization of dielectric layers deposited on a substrate is demanded by research of new advanced materials. In this case, the measured sample is not homogeneous anymore, but exhibits a multilayer structure. In order to perform high sensitive measurements, appropriate low loss substrate should be considered, otherwise, the THz signal will be affected by large absorption in the substrate.

An amplitude-based approach for extraction of the complex permittivity of $\text{Ba}_{0.6}\text{Sr}_{0.4}\text{TiO}_3$ (BST) ferroelectric thick films from the THz-TDS data was developed [3]. First, the procedure requires the measurement by THz TDS of the substrate alone, before the film deposition. The dielectric parameters of the substrate are then extracted from the THz TDS data. The small variation in the substrate thickness may considerably affect the measurements, hence, the film is then deposited on that particular substrate, which was previously measured in THz. While the film deposited on the substrate is measured in THz, the transmission peaks resulted by multiple reflections in the multilayer sample are investigated. Such parameters of the peaks as position in time, amplitude, contrast and width are investigated.

Following the approach in [4], at normal incidence, the propagation of the plane wave through the two layered sample with plane parallel interfaces is described by the equation

$$t(\nu) = \frac{t_{12}t_{23}t_{31}}{(1-(r_{32}r_{31}e^{i\delta_3}+r_{21}r_{23}e^{i\delta_2})-(t_{23}t_{32}r_{21}r_{31}-r_{21}r_{23}r_{32}r_{31})e^{i(\delta_2+\delta_3)})} e^{i\left(\frac{\delta_2+\delta_3}{2}\right)} \quad (2)$$

$$\text{where } \delta_2 = \frac{4\pi}{\lambda} n_2 h_2, \delta_3 = \frac{4\pi}{\lambda} n_3 h_3, n_2 = \sqrt{\epsilon'_2 + i\epsilon''_2}, n_3 = \sqrt{\epsilon'_3 + i\epsilon''_3}, r_{ij} = \frac{n_i - n_j}{n_i + n_j}, t_{ij} = \frac{2n_i}{n_i + n_j}.$$

The indices i and j take value 1 for air, 2 for substrate, and 3 for the film, λ is the wavelength of the THz wave in vacuum and h_2 and h_3 indicate the thickness of the substrate and the film, respectively.

The transmission spectrum of the MgO substrate (T_{sub}) can be derived from the $|t(\lambda)|^2$ function, based on the eq. 2. In general, $|t(\lambda)|^2$ and T_{sub} will differ in the amplitude of the peaks and their position. The concept of the approach is to adjust the value of $\tilde{\epsilon}(\nu_{peakj})$ in order to replicate amplitude of the peak j in T_{sub} and position (ν_{peakj}), as well as its contrast, here defined as the fraction between the amplitude of the peak and the amplitude of the closest minimum. Once the agreement between experimental and analytical peak position is obtained (inset in the Fig.2.a), the algorithm is applied to the substrate loaded by the BST thick film. Due to the dielectric constant of the BST film, the transmission peaks are shifted toward lower frequencies. Moreover, due to the BST dielectric loss, the peak amplitude (transmission value) of the peaks is decreased (Fig. 2.a).

The discrete values of the complex permittivity returned from the best fit of the transmission spectrum are shown in Fig. 2.b. For MgO substrate, the obtained data were compared with those extracted by using the Teralyzer software (Menlo Systems GmbH) and the agreement was good. The

ε'_{BST} and ε''_{BST} are lower than for bulk materials but are similar to those reported for both thin and thick BST films.

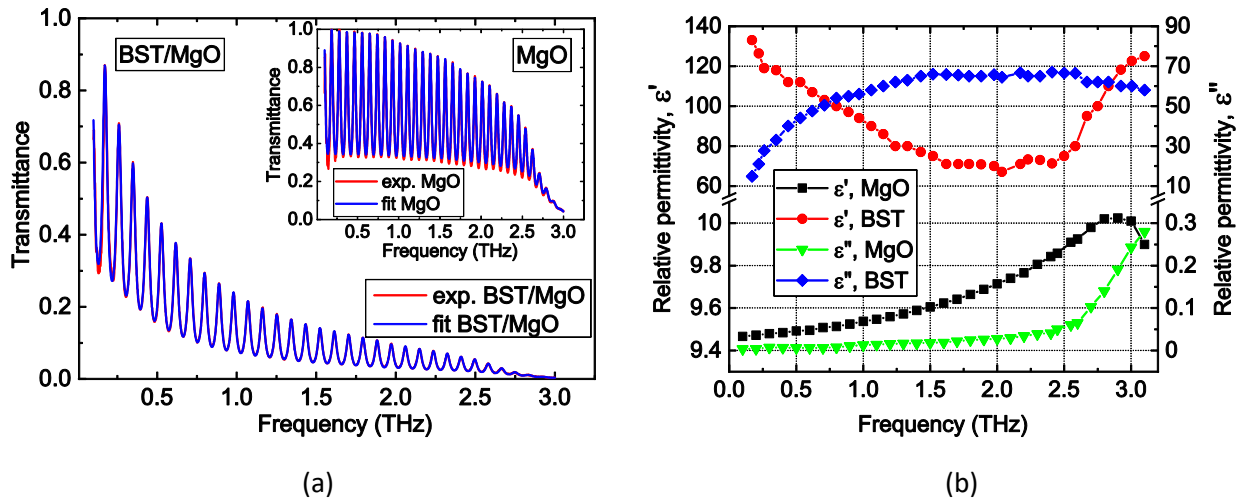


Fig. 2 Transmittance (a) and complex permittivity (b) for the 525 μm MgO substrate and 2.7 μm BST film grown on MgO.

The analysis of a number of peaks in the transmission spectrum provides information on the evolution of the BST layer dielectric parameters, which makes this procedure succeed in finding ε'_{BST} and ε''_{BST} in cases in which the standard procedures failed. Compared to conventional algorithms, the proposed approach shows an increased robustness because of two aspects:

- a) high values of the signal to noise ratio are ensured by using the local maxima of the THz transmission and
- b) the results can be checked by also using the signal phase, which was not needed for the main procedure.

References

1. S. S. Dhillon et al., *The 2017 terahertz science and technology roadmap*, J. Phys. D: Appl. Phys. **50**, 043001(2017) [<https://doi.org/10.1088/1361-6463/50/4/043001>].
2. J. Neu, C. A. Schmuttenmaer, *Tutorial: An introduction to terahertz time domain spectroscopy (THz-TDS)*, J. Appl. Phys. **124**, 231101 (2018) [<https://doi.org/10.1063/1.5047659>].
3. L. Nedelcu, G. Annino, C. Chirila, L. Trupina, A.C. Galca, M.G. Banciu, *Investigation of Ba_{0.6}Sr_{0.4}TiO₃ thick films by means of a novel THz-TDS approach*, Appl. Surf. Sci. **506**, 144807 (2020) [<https://doi.org/10.1016/j.apsusc.2019.144807>].
4. M. Born M., E. Wolf, *Principles of Optics*, Cambridge University Press, Cambridge, UK (1999).

Negative capacitance regime during polarization switching in epitaxial $\text{PbZr}_{0.2}\text{Ti}_{0.8}\text{O}_3$ thin films

Lucian Pintilie,^a Georgia Andra Boni,^a Cristina Chirila,^a Luminita Hrib,^a Luminita Hrib,^a
Lucian Dragos Filip,^a Ioana Pintilie^a

^aNational Institute of Materials Physics, Atomistilor 405A, Magurele, Romania, 077125

In recent years, one of the most investigated phenomena in ferroelectric-based structures has been the so-called negative capacitance (NC) regime. From a thermodynamic approach, NC in a ferroelectric is related to the permittivity defined as the double derivative of the free energy, which is negative in the vicinity of the zero polarization state (where the free energy has a maximum). Using a NC element in the dielectric gate of the field-effect transistors should reduce the subthreshold swing factor S below the thermodynamic limit of 60 mV per decade thus allowing for a faster transistor turn on.

Our study is based on analyzing the switching of polarization in an epitaxial thin film of PZT. The dielectric displacement, D , is defined as a function of the electric field, E , and dielectric polarization, P as:

$$D = \varepsilon_0 \varepsilon_b E + P_s \quad (1)$$

Where, ε_b is the background static dielectric constant. The total dielectric constant of the ferroelectric is thus defined as:

$$\varepsilon_f = \varepsilon_b + \frac{1}{\varepsilon_0} \frac{\partial P_s}{\partial E} \quad (2)$$

Since the derivative of polarization with respect to the electric field can be negative in Eq. (2), the total dielectric constant of the ferroelectric may become negative as well. This behavior corresponds to the NC regime.

In Fig.1a) are represented the polarization hysteresis characteristics as a function of the applied voltage recorded by applying triangular pulses with different amplitudes. A pre-polarization pulse is applied before every measurement. It can be observed that for pulse amplitudes in the vicinity of the coercive voltage, there are regions, where polarization continues to increase while the voltage decreases towards zero. This is a clear evidence of a negative capacitance regime described by Eq. 2. Indeed, in Fig.1 b) is evidenced as the specific capacitance, which is obtained as a derivative of the polarization characteristics shown in Fig.1 a), present clear negative values in the voltage range where polarization switching takes place. It should also be noted that NC has a maximum for voltages around the coercive value, which is in agreement with the fact that NC occurs in the vicinity of the zero polarization state.

Fig. 2a) displays the hysteresis current and it can be observed that the current value for the maximum voltage amplitude presents a peak when it is represented as a function of the maximum voltage pulse amplitude, in Fig. 2b). Thus in Fig. 2b) the correlation between the amplitude of NC and the current recorded during polarization switching, is presented. Considering that the voltage has a linear time dependence (for a triangular pulse) $V = \alpha t$, where $\alpha = 4fV_{max}$, the switching time can be obtained from Fig. 2b) by taking the time difference $t_2 - t_1$ (the two moments are shown by arrows in Fig. 2b)) which is estimated to be between 200 and 500ns.

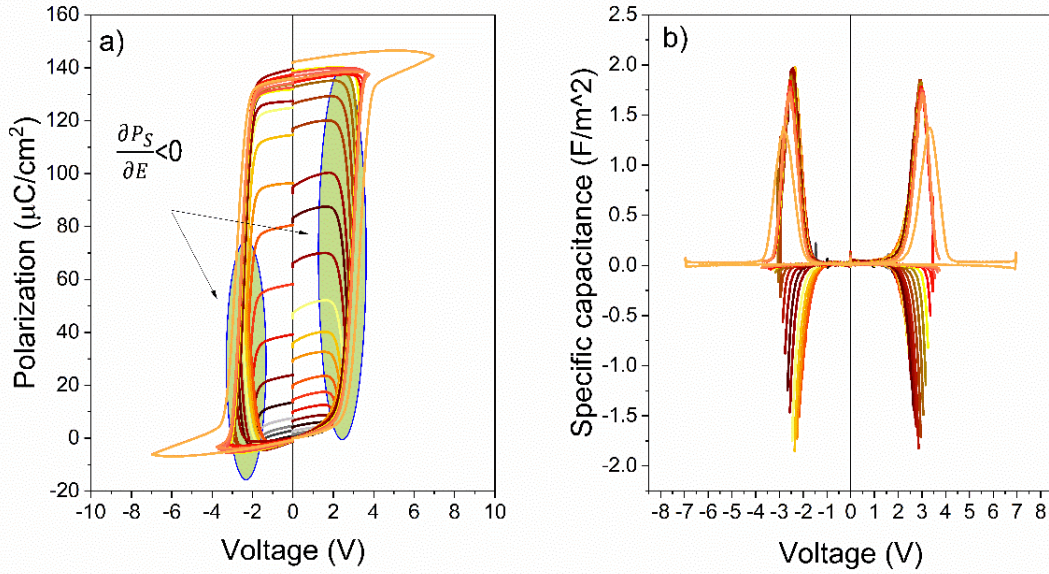


Fig. 1 a) The polarization hysteresis characteristics as the amplitude of the triangular voltage pulse is gradually increased; b) The C-V characteristics derived from the polarization hysteresis in a).

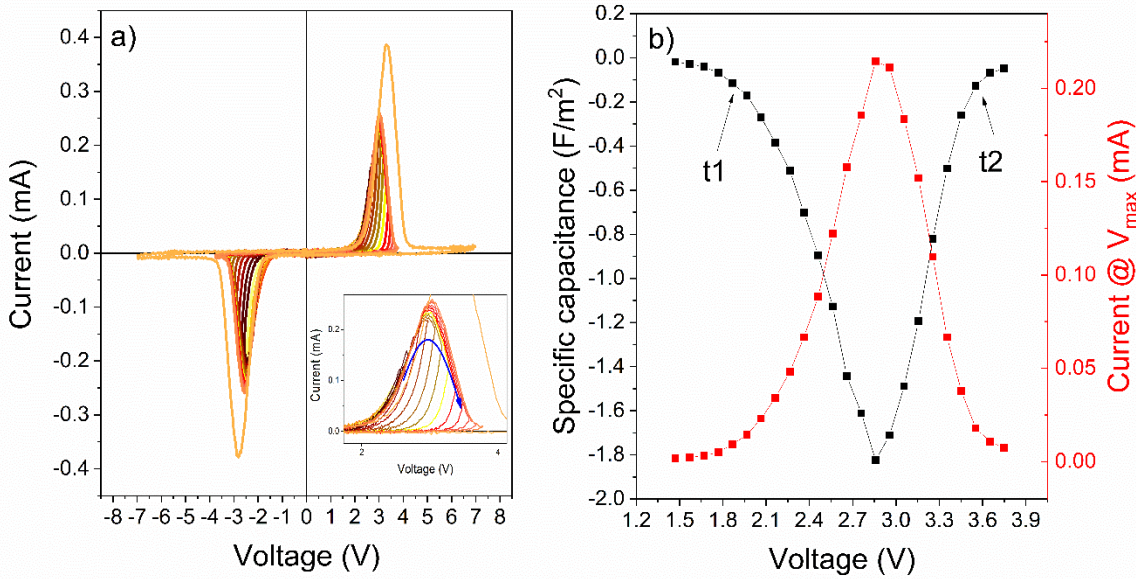


Fig. 2 a) Current hysteresis recorded at the same time as the polarization-hysteresis measurements in Fig. 1a). b) The voltage dependence of the maximum value of NC in the positive voltage range together with the voltage dependence of the current recorded at the maximum applied voltage during the hysteresis measurements.

In article [1] PFM measurements are also presented, showing the switching process at the microscopic level, revealing that during switching, there is no mix of ferroelectric domains of different orientations, the polarization switches very rapidly from one orientation to the other. These results suggest that switching occurs with no intermediate states composed of ferroelectric domains with different orientations.

This experimental evidence can be explained considering that the test structure is a metal-ferroelectric-metal and that the electrode-ferroelectric interfaces behave as Schottky-like contacts. Thus the switching process and NC regime around coercivity could be explained using the schematic representation in Fig. 3. The experiment starts from the initial state with a defined orientation of

polarization and with space charge regions at the electrodes formed to compensate the ferroelectric charges. When the applied electric field opposing the initial polarization direction, the polarization is still maintained but the width of the depletion regions starts to change as long as the voltage is under the coercive value. When the voltage is nearing the coercive value and polarization is close to zero, the depletion regions are strongly reduced and a significant flow of charges occurs. After the polarization switches direction, the depletion barriers are restored such that the new polarization state is compensated.

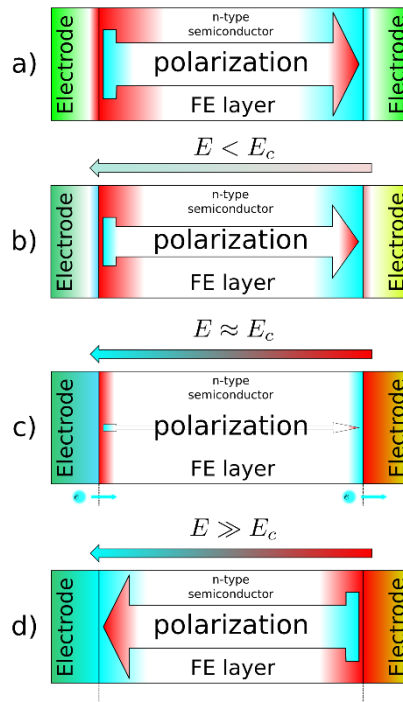


Fig. 3 a) Schematic representation of the evolution of a ferroelectric capacitor during polarization switching: a) initial state; b) an opposing electric field is applied and polarization switching is started; c) the ferroelectric nears the switching point and the incoming (left interface) and outgoing (right interface) charge transfer destabilizes the polarization charge compensation until, d) polarization switching occurs. (light blue areas are negative charges; in red- the positive charges).

References

1. L.Pintilie et al., *Polarization Switching and Negative Capacitance in Epitaxial PbZr_{0.2}Ti_{0.8}O₃ Thin Films*, PHYS. REV. APPLIED **14**, 014080 (2020).

Structural and magnetic properties of $\text{La}_{1-x}\text{A}_x\text{MnO}_3$ (A = K; Ba) synthesized by flash combustion method

Aurelian Catalin Galca,^a Sara Ait Bouzid,^b Mohamed Sajieddine,^b Abdellatif Essoumhi,^b Arpad Mihai Rostas,^a Nicusor Iacob,^a Monica Enculescu,^a Luminita Amarande,^a Iuliana Pasuk,^a Victor Kuncser,^a

^aNational Institute of Materials Physics, Atomistilor 405A, Magurele, Romania, 077125

^bSultan Moulay Slimane University, B.P 592, Beni-Mellal, Morocco, 23000

Recent attention is given to the use of perovskite oxides $\text{Ln}_{1-x}\text{R}_x\text{MnO}_3$ (Ln = rare earth element and R = monovalent metals / divalent alkaline earth metals) which exhibit a transition from ferromagnetic to paramagnetic behavior at a Curie temperature (T_C) close to ambient temperature. Thus, the exhibited magnetocaloric effect (MCE) of these oxides have attracted considerable attention being possible to be used in magnetic refrigeration and to compete with the more expensive Gadolinium (Gd), which is considered as the most efficient material in magnetic refrigeration technology.

The aim of the work [1] published in Journal of Alloys and Compounds was to investigate the La substitution with divalent (Ba) and monovalent (K) cations, especially the magnetocaloric properties of these manganites obtained by flash combustion and to provide an insightful and self-referenced analysis of LaMnO_3 , $\text{La}_0.9\text{K}_{0.1}\text{MnO}_3$ and $\text{La}_{1-x}\text{Ba}_x\text{MnO}_3$ ($x = 0.1; 0.2$). The ‘doping’ was done to increase the Curie temperature, and to modify the electronic properties of these materials.

Table 1 Crystallographic parameters of the analyzed samples extracted by using the interplanar spacing equations* and TOPAS v.3 software**. $a_H/a_C = \sqrt{2}$ is used to qualitatively compare the 2 systems.

Parameters	LaMnO_3	$\text{La}_{0.9}\text{K}_{0.1}\text{MnO}_3$	$\text{La}_{0.9}\text{Ba}_{0.1}\text{MnO}_3$	$\text{La}_{0.8}\text{Ba}_{0.2}\text{MnO}_3$
Crystal system	rhombohedral	rhombohedral	rhombohedral	cubic
Space group	R-3c	R-3c	R-3c	Pm3m
d_{244}	0.872	0.871	0.874	-
d_{2212}	0.865	0.866	0.868	-
d_{420}	-	-	-	0.874
d_{421}	-	-	-	0.853
a_C^* (Å)	3.902	3.899	3.911	3.907
a_H^* (Å)	5.519	5.514	5.531	5.525
c_H^* (Å)	13.321	13.349	13.485	-
V (Å ³)	351.378	351.479	357.253	59.638
a^{**} (Å)	5.518	5.513	5.532	3.911
c^{**} (Å)	13.321	13.349	13.391	-
V^{**} (Å ³)	351.365	351.461	355.014	59.811

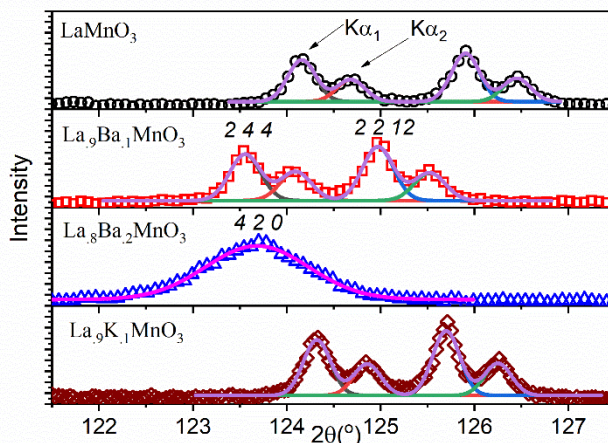


Fig. 1 XRD diffraction patterns of $\text{La}_{1-x}\text{Ba}_x\text{MnO}_3$ ($x = 0.1; 0.2$) and $\text{La}_9\text{K}_1\text{MnO}_3$ calcined at 1000°C relative to undoped sample, zoom in 2θ between 121.5 - 127.5° , where the experimental data (symbols) has been fitted with Gaussian functions (lines).

$\text{La}_9\text{Ba}_1\text{MnO}_3$ and $\text{La}_9\text{K}_1\text{MnO}_3$, crystallize in a rhombohedral structure without detectable presence of any additional phases, while $\text{La}_8\text{Ba}_2\text{MnO}_3$ has a cubic structure, the diffractogram presenting also weak peaks of secondary phases that can be observable by plotting of the recorded intensity in the logarithmic scale. Note that $\text{La}_8\text{Ba}_2\text{MnO}_3$ is in the morphotropic phase region.

The diffraction lines 244 and 2212 , and 420 , respectively for the cubic system, were evaluated (Fig. 1) to extract the cell parameters as well as the average coherence lengths (the crystallites dimensions), taking into account also the instrumental broadening. Note that at higher 2θ values, the instrumental errors are minimized, while the splitting between $K\alpha_1$ and $K\alpha_2$ lines is larger. Thus, the extracted parameters have smaller errors.

Peak shifts are observed for the $\text{La}_9\text{K}_1\text{MnO}_3$ and $\text{La}_{1-x}\text{Ba}_x\text{MnO}_3$ ($x = 0.1; 0.2$) samples compared to the LaMnO_3 reference, indicating change of the lattice parameters. The Mn^{4+} ions are produced by replacing La^{3+} with Ba^{2+} (or K^+). The ionic radius of Mn^{4+} (0.530 \AA) is smaller than that of Mn^{3+} (0.645 \AA). A higher dopant concentration leads to more Mn^{4+} , which cause a change of parent rhombohedral structure to a cubic one.

The average crystallite size of LaMnO_3 sample is 60 nm and 52 nm for $\text{La}_9\text{Ba}_1\text{MnO}_3$. The sample with cubic symmetry has a dramatic lower crystallite size of 15 nm , as indicated also by the absence of 420 splitting of $K\alpha_1$ and $K\alpha_2$ lines. For the last composition, $\text{La}_9\text{K}_1\text{MnO}_3$, the average crystallite size is 62 nm .

Electron paramagnetic resonance (EPR) spectroscopy was used to assess the transition temperature of the investigated manganites, i.e. where the ferromagnetic properties vanish. The T_C (K) values determined by EPR measurements are LaMnO_3 - 195 , $\text{La}_9\text{Ba}_1\text{MnO}_3$ - 200 , $\text{La}_8\text{Ba}_2\text{MnO}_3$ - 230 , $\text{La}_9\text{K}_1\text{MnO}_3$ 275 . Similar values have been inferred from standard magnetization measurements, the small differences being explained by different time window of each technique, as well as the method of determining the Curie temperature from magnetometry, i.e. tangent approach or first derivative.

Using the magnetic measurements, the magnetic entropy variation (ΔSM) with temperature can be represented. The maximum entropy takes place close to Curie temperature, the origin of the large ΔSM in the perovskite manganites being related to the significant variation of the magnetization near T_C . The large magnetic entropy variation and the semiconductor-metal transition generated by an external magnetic field are proof of a great coupling between spin and the lattice in the perovskites type manganites, sustained also by the change of the g -values measured with EPR. The largest magnetic entropy variation belongs to the sample doped with potassium, with a value of $5.33 \text{ J kg}^{-1} \text{ K}^{-1}$ at 4 T (the entropy change for Gd is $\sim 7.1 \text{ J kg}^{-1} \text{ K}^{-1}$ using a magnetic field of 3 T).

The relative cooling power (RCP) can be further calculated. The highest RCP value of present samples belongs to $\text{La}_9\text{K}_1\text{MnO}_3$ with a value of 159.79 J kg^{-1} (at 4 T). The RCP values at 5 T of Ba doped samples are 134.4 J kg^{-1} ($\text{La}_9\text{Ba}_1\text{MnO}_3$) and 128.75 J kg^{-1} ($\text{La}_8\text{Ba}_2\text{MnO}_3$).

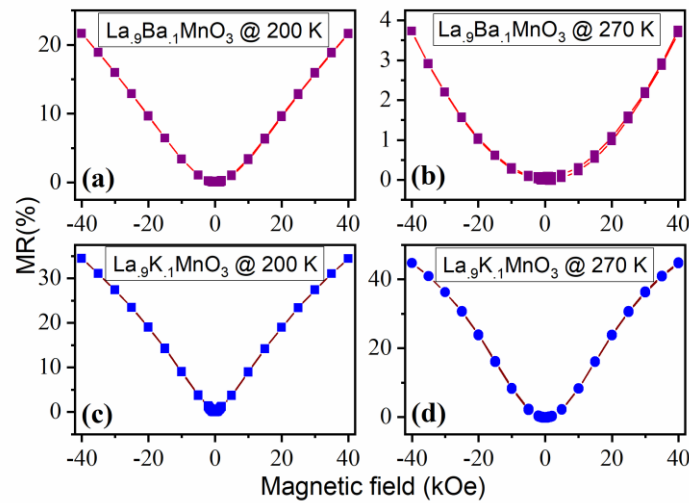


Fig. 2 Magnetoresistance versus magnetic field for $\text{La}_9\text{Ba}_1\text{MnO}_3$ at 200 K (a) and 270 K (b); $\text{La}_9\text{K}_1\text{MnO}_3$ at 200 K (c) and 270 K (d).

The magnetoresistance is calculated using the $MR = \frac{R_0 - R_H}{R_0}$ formula, where R_0 and R_H are the resistance without an applied magnetic field and under a magnetic field H . $\text{La}_9\text{K}_1\text{MnO}_3$ has the highest magnetoresistance of almost 45% at 270 K (close to its T_C), while $\text{La}_9\text{Ba}_1\text{MnO}_3$ reaches just 3.7% at 270 K and 21% at 200 K (Fig. 2).

References

1. S. Ait Bouzid et al., *Magneto-functionalities of $\text{La}_{1-x}\text{A}_x\text{MnO}_3$ ($A = \text{K}; \text{Ba}$) synthesized by flash combustion method*, Journal of Alloys and Compounds 839, 155546 (2020) [<https://doi.org/10.1016/j.jallcom.2020.155546>].

Inorganic cation Eu or Sb as dopants of perovskite films

Viorica Stancu,^a Lucia Nicoleta Leonat,^a Andrei Gabriel Tomulescu,^a Lucian Pintilie,^a Cristina Besleaga,^a Aurelian Catalin Galca,^a Florentina Neațu,^a Ștefan Neațu,^a Mihaela Florea,^a and Ioana Pintilie^a, Sarah Derbali,^b

^aNational Institute of Materials Physics, Atomistilor 405A, 077125 Magurele, Ilfov Romania

^bLaboratory of Condensed Matter Physics, Department of Physics, Ibn Tofail University, 14000 Kenitra, Morocco

Hybrid perovskites with the general formula ABX_3 have been acknowledged as one of the most interesting and challenging semiconductors for solar energy harvesting. They demonstrated exceptional semiconducting and photoelectric properties in mesoporous [1,2] and planar [3,4] solar cell architectures. The new record power conversion efficiency (PCE) value of 24.2% was achieved for small area PSCs [5]. Our study reports on altering the perovskite composition by preparing two complex perovskite compounds, $[\text{CH}_3\text{NH}_3]_{1-x}[\text{C}_3\text{N}_2\text{H}_5]_x\text{Pb}_{1-y}\text{Eu}_y\text{I}_{2.6}\text{Cl}_{0.4}$ and $[\text{CH}_3\text{NH}_3]_{1-x}[\text{C}_3\text{N}_2\text{H}_5]_x\text{Pb}_{1-y}\text{Sb}_y\text{I}_{2.6}\text{Cl}_{0.4}$ where two different dopants were simultaneously used, for the inorganic cation, europium or antimony (Eu^{3+} / Sb^{3+}) and an organic for the “A site”, imidazolium ($\text{C}_3\text{N}_2\text{H}_5^+$) [6]. Their performance was studied relative to the $\text{CH}_3\text{NH}_3\text{PbI}_{2.6}\text{Cl}_{0.4}$ composition and y was varied from 0 to 0.05. The properties of the perovskite films were investigated by characterization techniques: atomic force microscopy (AFM), X-ray diffraction (XRD), UV-Vis spectroscopy, scanning electron microscopy (SEM), and the photovoltaic parameters were determined by measuring the IV characteristics of the corresponding solar cells.

According to our study [6], the classic architecture of the standard solar cell is presented in Figure 1(a) and the cross section view of the newly studied cell is presented in Figure 1(b). The perovskite films with $y = 0$ are named as “*standard samples (Im)*” and the samples doped with europium (Eu^{3+}) or antimony (Sb^{3+}) are labeled as: *ImEu* or *ImSb* followed by a number representing the molar percentage of the corresponding doping (e.g. *ImEu1* for doping with 1% Eu, *ImSb5* for doping with 5% Sb)[6].

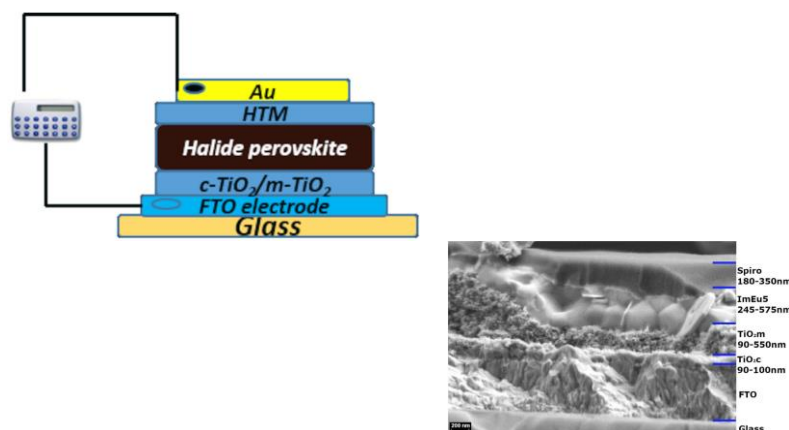


Figure 1: (a) The architecture of the theoretical perovskite solar cells and (b) the glass/FTO/TiO₂ compact and meso/MA_{1-x}IM_xPb_{1-y}B_yI_{2.6}Cl_{0.4}/HTM/Au solar cells (PSCs) architecture used in our study [6].

The crystalline structures of the studied films, characterized by XRD shows predominantly a MAPbI₃ tetragonal perovskite phase with characteristic peaks at $2\theta \sim 14.3^\circ$, 28.3° and 31.8° and an additional secondary perovskite phase of MAPbCl₃ with a peak located at $2\theta \sim 15.5^\circ$ [5,6]. The presence of IM cation, which has a larger ionic radius than MA induces the lattice expansion and the appearance of a new diffraction line at lower angles 2θ (11.1°) indicating the formation of a new phase, ImPbI₃ (IM) in competition with the standard perovskite phase containing the MA cation [7]. Low doping concentrations of Eu and Sb do not lead to any shift of the MAPbI₃ (110) peak and considering the cationic radius of Sb^{3+} of 76 pm [8] and of Eu^{3+} , 95 pm [9], compared with the 119

pm radius of Pb^{2+} considerable lattice distortions are, however, expected. The films also present a secondary phase of PbI_2 characterized by the 12.26° peak. [10,11].

Table 1. The characteristics of perovskite films calculated from the SEM images (cross section view) and AFM (scanned area $50 \times 50 \mu\text{m}$) [6]

Sample	Thickness (nm)	RMS (nm)
<i>TiO₂m</i>	-	316
<i>Standard</i>	416	206
<i>ImEu1</i>	362	115
<i>ImEu3</i>	399	123
<i>ImEu5</i>	487	105
<i>ImSb3</i>	440	107
<i>ImSb5</i>	500	78

The effect of inorganic Eu^{3+} and Sb^{3+} incorporation in the perovskite matrix on the photovoltaic properties has been investigated by current–voltage (J–V) measurements performed on the solar cells (see Figure 1a). Stancu & al [6] explains in detail the influence of doping with Sb and Eu. From figure 3(a) it is visible that the cells with higher Eu concentration present a more accentuated hysteresis effect compared with the undoped cells, pointing to a higher concentration of defects [6]. A similar effect has been also observed in the case of Sb doping in the active layer (see figure 3(b)). Still, it is interesting that the PCE decrease is not so dramatic, 3% Sb leading to only a 0.48% decrease of the PCE (that is 6% of the standard cell efficiency) which is caused by a decline in V_{oc} by 0.011 V and of the J_{sc} by 1.3 mA cm^{-2} . Further comparing these two cells, we also observe that they present similar series resistance (R_s) and FF, while the parallel resistance (R_{sh}) decreases by 9% [6]. One possible reason for the slight decrease of performance for the Sb doped perovskite is related to the active layer, which in this case contains multiple defects [6, 9, 12]. Increasing the Sb percent leads to decreased efficiency (table 2) and according to literature, cells with 100% Sb (where Pb^{2+} is totally replaced by Sb^{3+}) do not exceed 1% PCE [6,9]. Higher concentration of Sb leads to voids in the perovskite film, similar to the Eu samples.

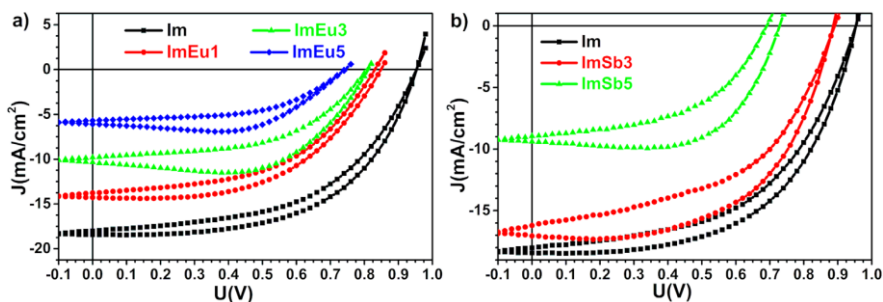


Figure 2. Photovoltaic characteristics for the PSCs doped with Eu (a) and Sb (b) (best cells) [6].

After 60 days, stability measurements show that in a low humidity environment ($<10\%$), the standard cells retain 75% of their initial efficiency, cells with Eu degrade faster (with efficiencies of only 57% to 24% from their initial PCE), cells with 3% Sb degrade slower than the standard ones (keeping over 80% of the initial PCE after 60 days). At 5% Sb doping, the cells lose half of their initial efficiency. In conclusion, europium seems to destabilize the perovskite structure compared with Sb [6].

Table 2. Average values for photovoltaic characteristics (forward and reverse) of solar cells doped with europium and antimony [6].

Conc.	Voc (V)	Jsc (mA/cm ²)	FF (%)	Rs (Ω cm ²)	Rsh (Ω cm ²)	PCE (%)
<i>Standard</i>	0.940	15.9	57	13	1834	8.24
<i>Eu1% (ImEu1)</i>	0.822	14.3	50	23	1117	5.22
<i>Eu3% (ImEu3)</i>	0.826	12.9	44	20	1172	4.08
<i>Eu5% (ImEu5)</i>	0.749	9.7	55	35	1271	2.01
<i>Sb3%(ImSb3)</i>	0.929	14.6	57	13	1667	7.76
<i>Sb5%(ImSb5)</i>	0.708	7.3	63	20	1521	3.27

The conclusion of the study is that simultaneous doping of the perovskite with imidazolium and Eu/Sb is a facile strategy to improve the PSCs in air stability of a solar cell. The partial replacement of lead with europium does not lead to increased solar cell efficiency but in the case of 3% Sb doping, an increase in stability has been observed [6]. However, partial substitution of Pb with Sb, a non-toxic element, in small amounts, helps the formation of the perovskite films with good chemical stability with only a small cost in the PCE reduction [6].

References

1. Jeon N J, Noh J H, Kim Y C, Yang W S, Ryu S and Il Seok S, *Solvent engineering for high-performance inorganic hybrid perovskite solar cells*, Nat. Mater. **13** 1–7(2014), <https://onlinelibrary.wiley.com/doi/full/10.1002/nmat.12115>.
2. Lee M M, Teuscher J, Miyasaka T, Murakami T N and Snaith H J, *Efficient hybrid solar cells based on mesostructured organometal halide perovskites*, Science (80-.) **338** 643–7 (2012) <https://doi.org/10.1038/s41578-019-0080-9>
3. Eperon G E, Stranks S D, Menelaou C, Johnston M B, Herz L M and Snaith H J, *Formamidinium lead trihalide: a broadly tunable perovskite for efficient planar heterojunction solar cells*, Energy Environ. Sci. **7** 982–8 (2014) <https://doi.org/10.1007/s12200-016-0630-3>
4. Kaltenbrunner M et al, *Flexible high power-per-weight perovskite solar cells with chromium oxide-metal contacts for improved stability in air*, Nat. Mater. **14** 1032–9 (2015) <https://doi.org/10.1063/1.453467>
5. Green M A, Dunlop E D, Hohl-Ebinger J, Yoshita M, Kopidakis N and Ho-Baillie A W Y, *Solar cell efficiency tables (Version 55)*, Prog. Photovoltaics Res. Appl. **28** 3–15 (2020) <https://doi.org/10.1021/acsami.8b20681>
6. V. Stancu, L.N. Leonat, A.G. Tomulescu & al *Influence of doping the inorganic cation with Eu or Sb on the properties of perovskite films*, Phys. Scr. **95** 075707 (2020), <https://doi.org/10.1088/1402-4896/ab90be>
7. Kim J et al, *Enhancing efficiency of perovskite solar cells by reducing defects through imidazolium cation incorporation*, Nat. Energy **3** 1–7 (2017) DOI: [10.1016/j.nature.2017.09.007](https://doi.org/10.1016/j.nature.2017.09.007)
8. Wang X, Zhang T, Lou Y and Zhao Y, *All-inorganic leadfree perovskites for optoelectronic applications*, Mater. Chem. Front. **3** 365–75 (2019) <https://doi.org/10.1039/C8QM00611C>
9. Jiang F et al, *Chlorine-incorporation-induced formation of the layered phase for antimony-based lead-free perovskite solar cells*, J. Am. Chem. Soc. **140** 1019–27 (2018) <https://doi.org/10.1021/jacs.7b10739>
10. Derbali S et al, *Exploring the effect of aliovalent substitution of Pb²⁺ by Eu³⁺ on structural, morphological and optical properties of CH₃NH₃PbI₃ perovskite films*, Phys. Scr. **95** 044003 (2020) <https://doi.org/10.1088/1402-4896>
12. Wu X, Li H, Wang K, Sun X and Wang L, *CH₃NH₃Pb_{1-x}EuxI₃ mixed halide perovskite for hybrid solar cells: the impact of divalent europium doping on efficiency and stability*, RSC Adv. **8** 11095–101 (2018) <https://doi.org/10.1039/C7RA12754E>
13. Hebig J C, Kühn I, Flohre J and Kirchartz T, *Optoelectronic properties of (CH₃NH₃)₃Sb₂I₉ thin films for photovoltaic applications*, ACS Energy Lett. **1** 309–14 (2016) <https://doi.org/10.1021/acsenergylett.6b00170>

Web-like architectures based on metal oxides by biomorphic mineralization or functionalization of eggshell membrane (ESM)

N. Preda,^a A. Costas,^a M. Beregoi,^a M. Enculescu,^a N. Apostol,^a A. Kuncser,^a I. Enculescu,^a C. Curutiu,^b F. Iordache,^c

^aNational Institute of Materials Physics, Atomistilor 405A, Magurele, Romania, 077125

^bUniversity of Bucharest, Faculty of Biology, Aleea Portocalelor 1-3, Bucharest, Romania, 060101

^cUniversity of Agronomic Sciences and Veterinary Medicine of Bucharest, Bucharest, Romania, 011464

Eggshell membrane (ESM) is an affordable, inexpensive, biocompatible, biodegradable and renewable biomaterial that offers new opportunities for designing functional web-like architectures based on metal oxides [1, 2]. Natural polymer, ESM is featured by a unique 3D porous interwoven fibrous protein network (Fig. 1) responsible for its interesting and useful properties: high porosity, large surface area, high absorption capacity and flexibility.

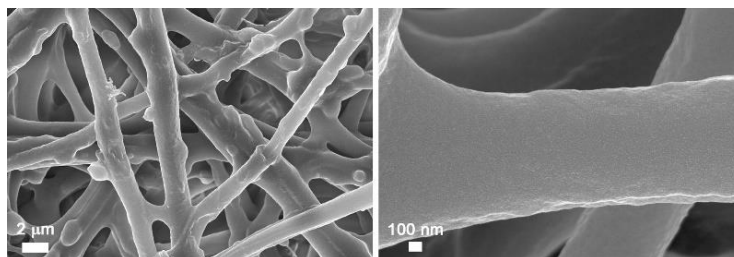


Fig. 1 FESEM images at two magnifications of the ESM.

In our studies, by biomorphic mineralization [1] or functionalization [2] of ESM, web-like architectures based on metal oxides (ZnO and CuO) were prepared (Fig. 2), further evaluating the physico-chemical and biological properties of these networks by complementary techniques such as field emission scanning electron microscopy (FESEM), EDX elemental mapping in scanning transmission electron microscopy (STEM), I-V measurements, photocatalytic activity and antibacterial activity investigations (Fig. 3, Fig. 4 and Fig. 5).

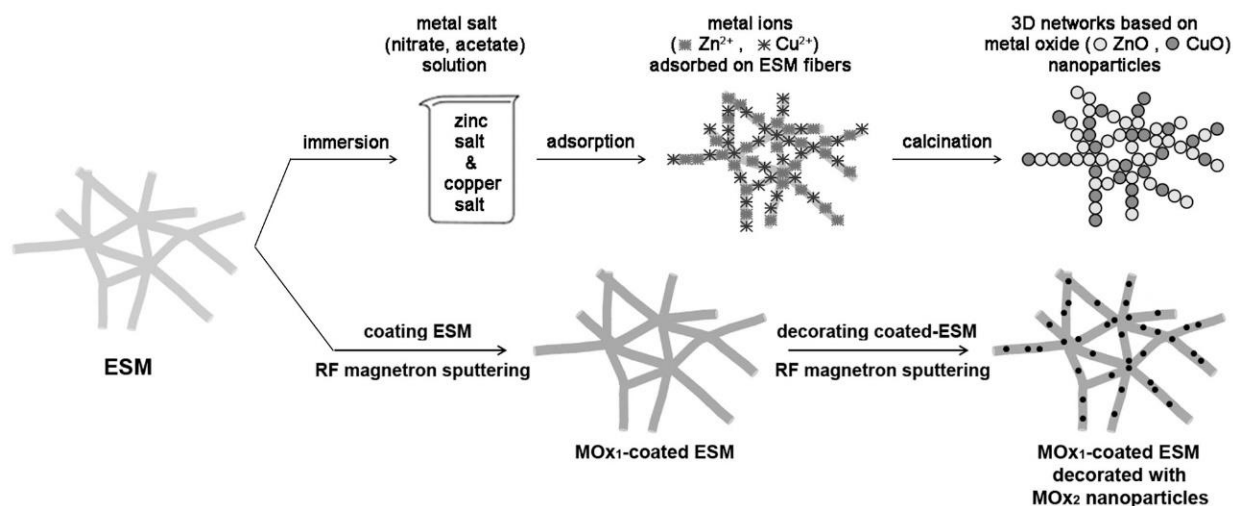


Fig. 2 Schematic illustration of the steps involved in the preparation of the web-like architectures based on metal oxides by biomorphic mineralization (up) or functionalization (down) of ESM.

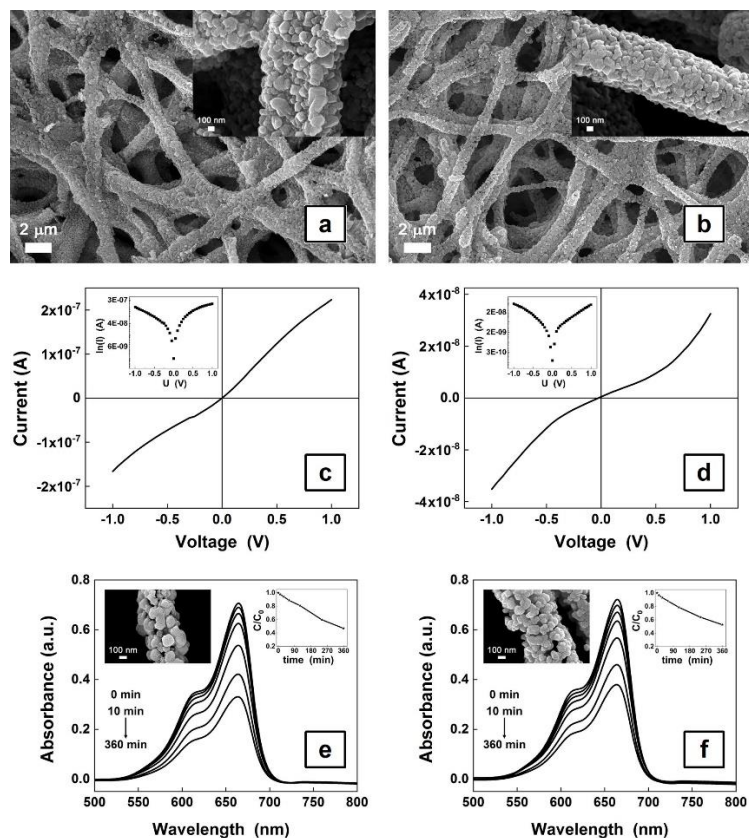


Fig. 3 (a, b) FESEM images, (c, d) I-V characteristics and their semilogarithmic representations, (e, f) Absorption spectra regarding the degradation of MB aqueous solution, the degradation profiles over time and the FESEM images after the photocatalysis experiments) of the webs based on ZnO-CuO composites prepared by ESM biomorphic mineralization using acetates (a, c, e) or nitrates (b, d, f) as metal salt precursors.

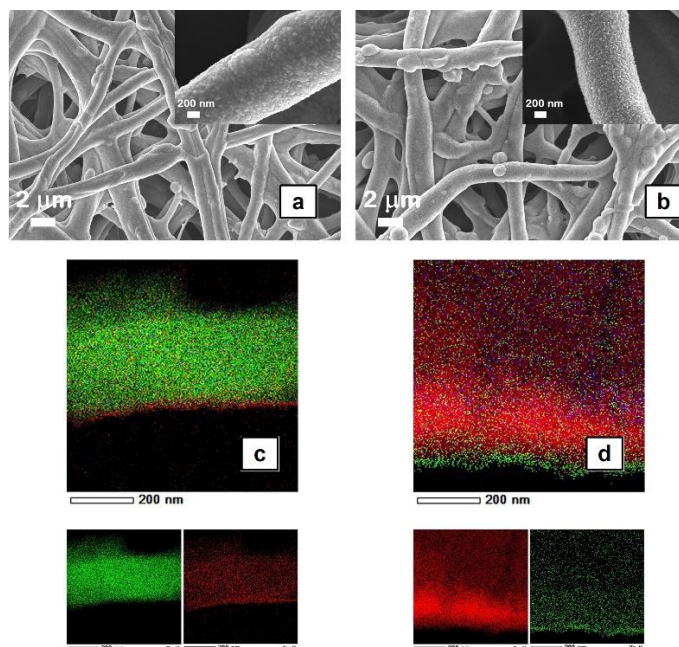


Fig. 4 (a, b) FESEM images, (c, d) EDX elemental mapping in STEM (including the spatial distribution of the Zn and Cu elements) of the webs based on ZnO-coated ESM decorated with CuO nanoparticles (a, c) or CuO-coated ESM decorated with ZnO nanoparticles prepared by ESM functionalization.

Biomorphic 3D fibrous networks based on ZnO-CuO nanostructures were prepared by a simple method consisting of the immersion of the ESM into aqueous solutions containing the metal salt precursor and subsequent calcination. The FESEM images revealed that the replicated inorganic networks are made of interconnected fibers containing metal oxide nanoparticles as building blocks.

Using Si/SiO₂ patterned with interdigitated metallic electrodes as substrates, the electrical properties of the self-contacted metal oxide networks were investigated, the transport of charges being made by percolating through the formed junctions over the Ti/Pt interdigitated electrodes. The photocatalytic tests carried on methylene blue (MB) aqueous solutions under solar simulator irradiation revealed that the metal oxide networks induce the MB photodegradation.

ESM was functionalized with inorganic materials (combination of ZnO and CuO) by RF magnetron sputtering, a straightforward deposition technique. The FESEM images emphasized that the typical 3D porous network of the ESM is successfully preserved during its functionalization, the surface of the organic fibers being coated with a continuous and uniform inorganic film. The formation of the p-n junction between the ZnO and CuO in the functionalized ESMs containing a combination of these two metal oxides, meaning ZnO-coated ESM decorated with CuO nanoparticles and CuO-coated ESM decorated with ZnO nanoparticles is evidenced by EDX elemental mapping in STEM. The change induced in the *E. coli* morphology by the antibacterial activity of the p-n junction under visible light can be observed in the FESEM images of this bacteria on the native ESM and on the CuO-coated ESM decorated with ZnO nanoparticles. Thus, on ESM, the healthy *E. coli* is featured by its characteristic shape, a rod with spherical caps, with a smooth and intact surface, while on functionalized ESM, the dead *E. coli* revealed an irregular shape due to the membrane collapse.

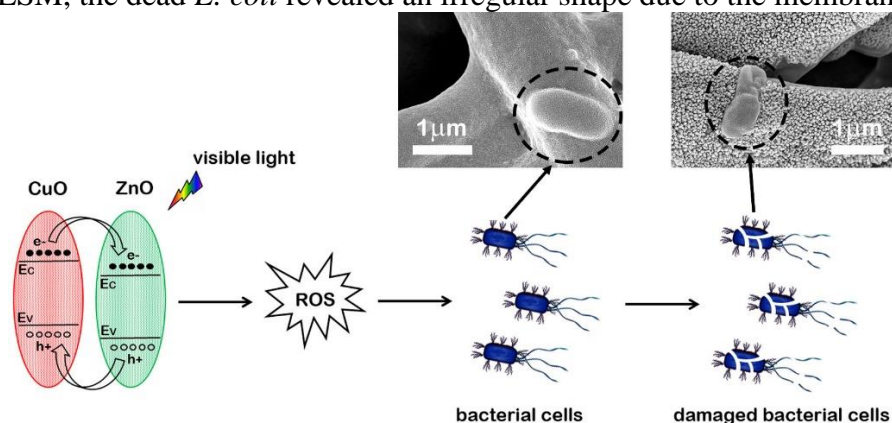


Fig. 5 Schematic representation of the enhancement of antibacterial performance under visible light in the CuO-ZnO p-n junction. The FESEM images of an *E. coli* on the native ESM and on the **CuO-coated ESM decorated with ZnO nanoparticles prepared by ESM functionalization**.

Eggshell membrane can be regarded as an interesting platform for the development of functionalized web-like architectures with potential applications in optoelectronic devices, photocatalysis, affordable wound dressing with antibacterial activity, sensing, etc.

References

1. N. Preda et al., *Biomorphic 3D fibrous networks based on ZnO, CuO and ZnO-CuO composite nanostructures prepared by eggshell membranes*, Mater. Chem. Phys. **240**, 122205 (2020) [[doi:10.1016/j.matchemphys.2019.122205](https://doi.org/10.1016/j.matchemphys.2019.122205)].
2. N. Preda et al., *Functionalization of eggshell membranes with CuO-ZnO based p-n junctions for visible light induced antibacterial activity against Escherichia coli*, Sci. Rep. **10**, 20960 (2020) [[doi:10.1038/s41598-020-78005-x](https://doi.org/10.1038/s41598-020-78005-x)].

(Ba,Sr)TiO₃ solid solutions sintered from sol-gel derived powders: An insight into the composition and temperature dependent dielectric behavior

Roxana Elena Patru,^a Constantin Paul Ganea,^a Ioana Pintilie,^a Lucian Pintilie^a, Catalina-Andreea Stanciu,^b Vasile-Adrian Surdu,^b Roxana Trusca,^b Adelina-Carmen Ianculescu,^b

^a National Institute of Materials Physics, Atomistilor 405A, Magurele, Romania, 077125

^b Department of Oxide Materials Science & Engineering, Faculty of Applied Chemistry and Materials Science, "Politehnica" University of Bucharest, 1-7 Gh. Polizu, Bucharest, Romania, 011061

Barium titanate (BT) is one of the most common and studied materials alongside its solid solutions. The composition-dependent, non-linear and hysteretic dielectric properties allow BT-based materials to bring multi-functionality suitable for a large number of microelectronics applications. In the present study, several barium strontium titanate (Ba_{1-x}Sr_xTiO₃) compositions having the ferroelectric-paraelectric phase transition located near the room temperature were investigated via broadband impedance spectroscopy [1]. Our results based on the complex analysis on the low field dielectric properties meant to elucidate the critical role played by temperature in the ferroelectric state or close to the Curie point. The Curie point of the investigated compositions was tailored by Sr addition [2], so that Ba_{1-x}Sr_xTiO₃ with x = 0.4 and x = 0.375 exhibit a paraelectric behavior at RT, x = 0.35 is facing the ferroelectric to paraelectric phase transition at RT, x = 0.325 and x = 0.3 are in the ferroelectric state at RT. The dielectric properties of BST specimens were registered by an Alpha-A Novocontrol low frequency impedance-meter system in the frequency range of 102Hz-106Hz. Data were recorded following a protocol for heating and cooling with a rate of 0.6 °C*min⁻¹ in the temperature range of -50 °C ÷ 100 °C. XRD and FE-SEM tested the purity phase and dense and uniform microstructures. Figure 1 illustrates a schematic representation of the influence of Sr concentration on the Curie point in the case of the proposed compositions. The average grain size and thermal hysteresis evolves with Sr addition following a downward trend. BST ceramics present relative density values ranged between 87 – 92% and grain sizes decrease from 15.6 μm in BST30 down to 2.1 μm in BST40.

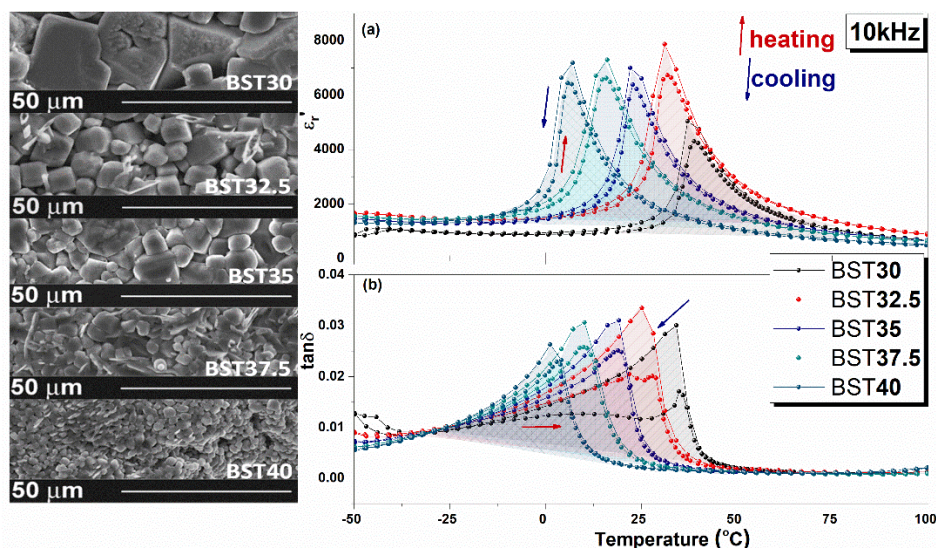


Fig. 1 BST ceramics: (a) microstructural characterization and (b) temperature dependence of the dielectric constant and the corresponding losses represented for a fixed frequency of 10kHz

All the specimens fully satisfy the classical Curie-Weiss law in the paraelectric state. The diffuseness degree and the peak broadening were determined by using a modified Curie-Weiss law based on the data measured during the different thermal cycles as a function of frequency in accordance with the Sr content.

The frequency dependence of the dielectric constant discloses particular information about the electrical polarization mechanisms and dielectric relaxations inside the BST ceramic specimens. The ferroelectric domains below the Curie point and the polar fluctuations near the Curie point caused by atoms, both stand out through dielectric anomalies in the frequency dependence of the complex dielectric constant. Figure 2 shows the frequency dependence of the complex dielectric constant at room temperature. Values of the dielectric constant in Fig. 2 (a) are specific to compositions in different phases ($x = 0.375$ and 0.4 in the cubic paraelectric, $x=0.3$ in the ferroelectric state, $x=0.325$ and 0.35 in the transition proximity) at room temperature with enhanced dielectric relaxations in the whole frequency range (b).

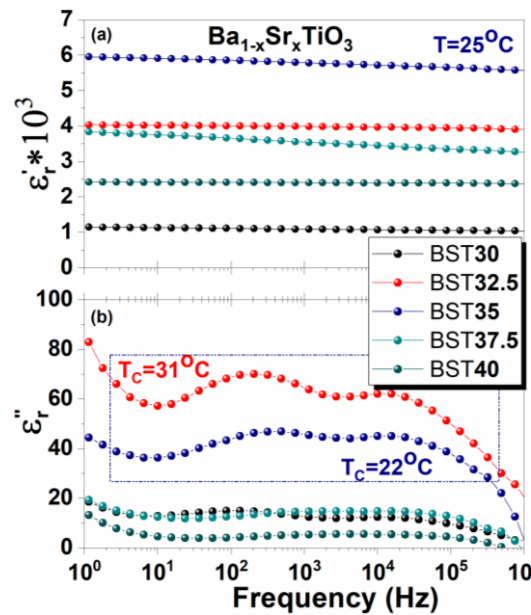


Fig. 2 The real part (a) and the imaginary part (b) of the complex dielectric constant at room temperature, as a function of frequency

Withal, the enhancement of the loss factor in low frequency range (Fig. 2. (b)) is the origin of the dc conduction and reflects accumulation of spatial charges with increased mobility in the grain boundary regions process. In grains, the ferroelectric domains alignment evolves with temperature below the Curie point, after which they completely disappear. At the boundaries and interfaces, the accumulated spatial charges are released when temperature increases highlighting thermally activated processes (07-0.77eV). The cumulative complex contributions coming from different sources were divided by performing impedance spectroscopy analysis and by fitting the experimental data to a specific equivalent circuit including two parallel R-C circuits connected in series.

Oxygen vacancies in $SrTiO_3$ donates excess of electrons, and the Ti sites trap them at low temperatures. With increasing of temperature, they become mobile and produce effects through strongly increasing the conductivity in the high-frequency region.

The interaction degree between mobile ions and the media was calculated by using the Jonscher power law on the frequency dependence of the electrical conductivity. Both the computing parameters and the circuit elements exhibit a strong temperature dependence in the transition region that can lead to further clarifications on the fundamental phenomenon responsible for conduction and relaxation processes in this type of ceramics. Figure 3 shows the Bode plots fitted using the equivalent circuit composed by a series of R-C elements.

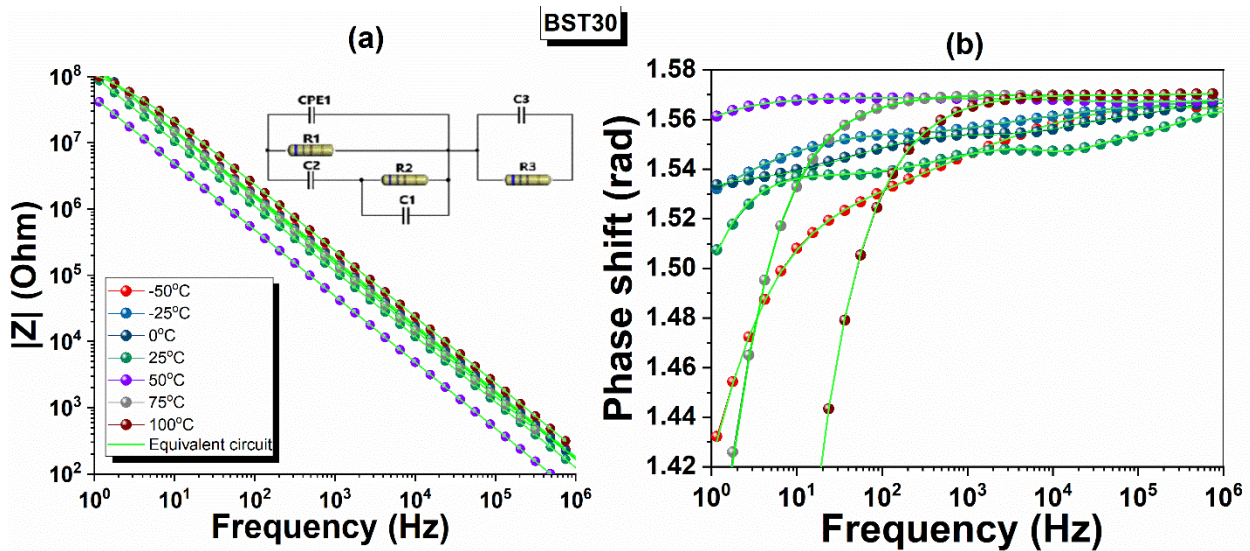


Fig. 3 Frequency dependence of the (a) complex impedance and (b) phase shift verified by the proposed equivalent circuit shown in inset of (a)

Sr addition is a powerful way to fine-tune the multifunctional properties of BT ceramics. The changing in the transition temperature comes together with a more dispersive nature of the dielectric properties when Sr concentration increases.

The work was carried out in the frame of the PCCF 16/2018 and PN-III-P4-ID-PCE-2016-0072 grants and of the PN19-03 Core Program of NIMP.

References

1. R. E. Patru, et al., *(Ba,Sr)TiO₃ solid solutions sintered from sol-gel derived powders: An insight into the composition and temperature dependent dielectric behavior*, *Ceram. Int.*, **46**, 4180-4190 (2020) [[doi:10.1016/j.ceramint.2019.10.136](https://doi.org/10.1016/j.ceramint.2019.10.136)]
2. A. Ianculescu, et al., *Intrinsic pyroelectric properties of thick, coarse grained Ba_{1-x}Sr_xTiO₃ ceramics*, *Ceram. Int.*, **42**, 10338-10348 (2016) [[doi:10.1016/j.ceramint.2016.03.152](https://doi.org/10.1016/j.ceramint.2016.03.152)]

Charge transfer reaction mechanisms in epoxyketone and boronated peptides at glassy carbon and boron doped diamond electrodes

Catarina Sofia Henriques de Jesus,^a Teodor Adrian Enache,^b Victor Constantin Diculescu^{b*}

^aLaboratory of Electroanalysis and Corrosion, Instituto Pedro Nunes, Coimbra, Portugal

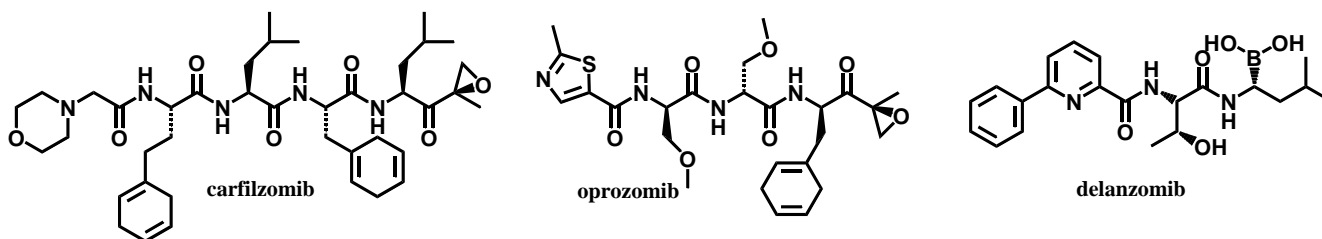
^bNational Institute of Materials Physics, Atomistilor 405A, 077125, Magurele, Romania

The regulation of protein level in eukaryotic cells represents one of the most important aspect of cell regulation. This is a fundamental process, occurs through controlled degradation, and is accomplished by the ubiquitin-proteasome system (UPS). The human UPS components are ubiquitin, a small regulatory protein, and the cytosolic proteasome 26S complex of the 20S protein subunit and 19S regulatory cap subunits. Through this regulation mechanism unfunctional/damaged proteins are marked for proteasomal degradation by being linked to ubiquitin tag of the 19S subunit and cleaved by the 20S subunit through proteolysis [1].

The dysregulation of the UPS occurs in several diseases and leads to an increased activity of the proteasome. This phenomenon results in excessive degradation of key proteins and enzymes and promotion of medical anomalies, *e.g.* the uncontrolled degradation of the tumor suppressor p53 drive to the progression of tumors [2]. Therefore, one of the standard strategy used for the control UPS dysregulation linked diseases is the inhibition of proteasome activity by target drugs. According to their mechanism of action the proteasome inhibitors may be divided into three groups: boronates, epoxyketones, and salinosporamides [3]. While the boronated inhibitor bortezomib is approved as proteasome inhibitor since 2003, the novel epoxiketones oprozomib and delanzomib are intensely examined in clinical trials, with promising results.

Understanding the physico-chemical properties of newly discovered molecules represents an important step for clarifying their mechanism of action at a biological level. Since the electrochemical methods can simulate the electron-transfer reaction that occurs *in vivo*, the electrochemical investigation of newly discovered proteasome inhibitors, carfilzomib, oprozomib and delanzomib can support the pharmacokinetic studies for understanding their mechanism of action.

The aim of this work was to investigate and elucidate the redox behavior of carfilzomib, oprozomib and delanzomib using voltammetric methods and two carbon electrode materials: glassy carbon and boron doped diamond [4].



Scheme 1. Chemical structures of A) carfilzomib, B) oprozomib and C) delanzomib.

In this context, the aim of the present study is to investigate the electron transfer properties of some newly discovered proteasome inhibitors, using voltammetric methods at glassy carbon and boron doped diamond electrodes. The investigation of the electrochemical redox mechanisms of carfilzomib, oprozomib and delanzomib, **Scheme 1**, has the potential for providing valuable insights into biological redox reactions of this class of molecules, resulting in a better understanding of physicochemical properties and their mechanisms of action at different rates and by different pathways.

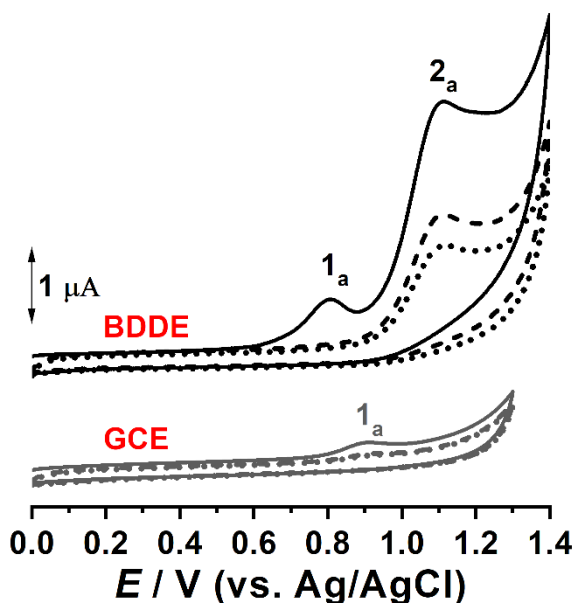


Fig 1. Cyclic voltammogram at GCE and BDDE in solution of 25 μM carfilzomib in 0.1 M phosphate buffer pH = 6.9 at $\nu = 100 \text{ mV s}^{-1}$. Adapted from [4].

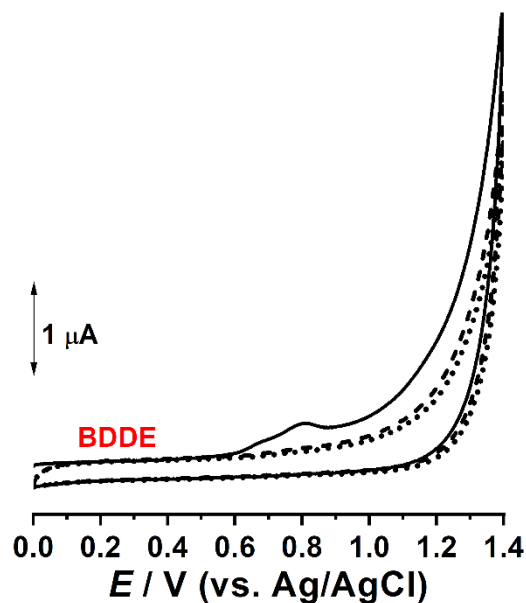


Fig 2. Cyclic voltammogram with BDDE in: 100 μM oprozomib (—) 1st, (---) 2nd and (···) 3rd scans, in 0.1 M phosphate buffer pH = 7.0 at $\nu = 100 \text{ mV s}^{-1}$. Adapted from [4]

Cyclic voltammograms recorded at the GCE for 25 μM carfilzomib in 0.1 M phosphate buffer pH 7.0 between potential limits 0.0 V and +1.40 V, at $\nu = 100 \text{ mV s}^{-1}$ revealed a single oxidation reaction, corresponding to peak 1_a at +0.90 V, **Fig 1**. By recording successive voltammograms in the same solution and without cleaning the GCE surface, a decrease of the oxidation current of peak 1_a was observed, explained by the adsorption of carfilzomib oxidation products at the GCE surface reducing the electroactive area. No additional signals were observed meaning that the oxidation products of carfilzomib are not electroactive. Increasing the negative potential limit, until -1.20 V no cathodic peaks appeared.

The cyclic voltammograms recorded at GCE for oprozomib showed no electrochemical signal. However, BDDE allowed the investigation of the electrochemical behavior of oprozomib, **Fig 2**.

The voltammograms recorded for 100 μM oprozomib revealed two oxidation peaks, at +0.67 V and +0.82 V, which disappear after successive voltammograms were recorded in the same solution, **Fig 2**, meaning that the oxidation products of oprozomib are not electroactive.

The voltammetric behaviour of 200 μM delanzomib at the GCE was investigated by cyclic voltammetry, **Fig 3**. During the voltammetric measurements a constant flux of N_2 was kept over the solution in order to avoid the diffusion of atmospheric O_2 into the delanzomib solution. On the both negative-, recorded from 0.00 V till -1.60 V, and positive-, recorded from 0.00 V till +1.40 V, going scans one charge transfer reaction per scan was observed: the reduction peak 1_c at -1.35 V and the anodic peak 1_a at +0.70 V, **Fig 3**. Recording successive voltammograms in the same solution and without cleaning the electrode surface, the anodic and cathodic peaks of delanzomib decreased with the increased number of scans due to the adsorption of redox products, which decreased the electroactive area of GCE surface. Additional experiments demonstrate that the oxidation and the reduction of delanzomib occurred independently of each other.

In addition to cyclic voltammetry experiments, the voltammetric behavior of proteasome inhibitors epoxyketones carfilzomib and oprozomib, and the boronated peptide delanzomib was also investigated using differential pulse and square wave voltammetry and the results were compared with those obtained for molecules having similar electroactive moieties [5].

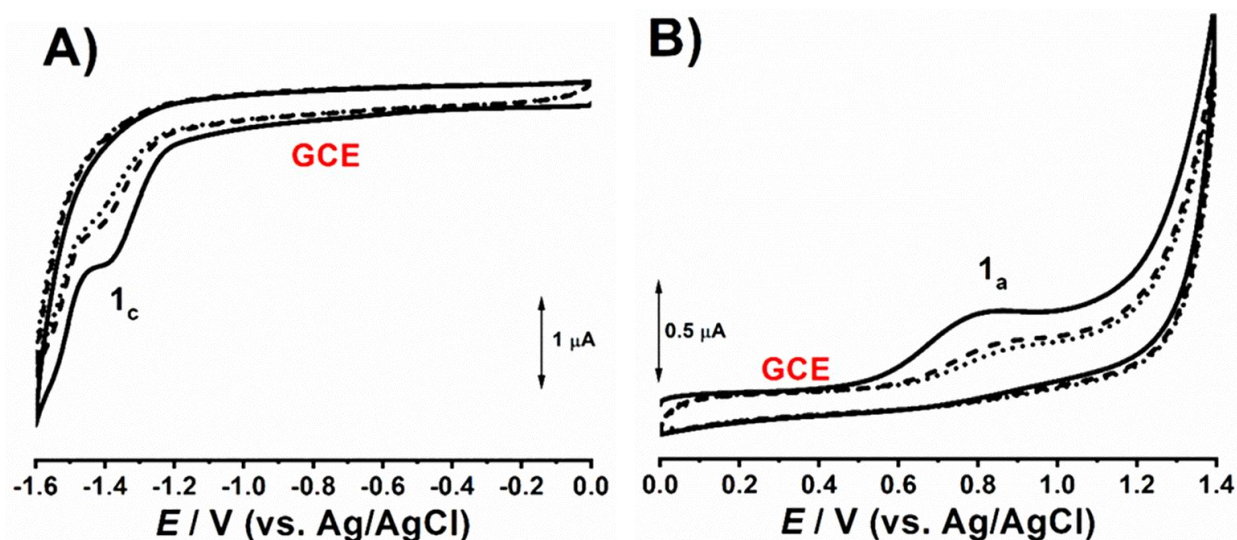


Fig 3. Cyclic voltammogram with GCE in solution of 200 μM delanzomib between: **A)** -0.00 and -1.60 V and **B)** +0.00 and +1.40 V; first, second and third scans in 0.1 M phosphate buffer pH = 6.9 at $\nu = 100 \text{ mV s}^{-1}$. Adapted from [4].

The voltammetric results indicated that the electrochemical oxidation of carfilzomib occurred at the morpholine ring with the transfer of one electron and one proton in an adsorption controlled pH-dependent mechanism.

Although the epoxyketone peptide oprozomib showed a very weak electroactivity at glassy carbon electrode, the use of boron doped diamond electrode revealed that the oxidation occurred, with the transfer of two electrons and two protons, at the thiazole moiety and the anodic charge transfer reaction lead to the formation of a sulfone.

The electrochemical oxidation of the boronated peptide delanzomib showed similar behavior at both glassy carbon and boron doped diamond electrodes. It was demonstrated that, at pH 7.0, delanzomib can be oxidized and reduced in independent reactions. The electroactive center corresponding to the oxidation was identified to be an amino group while for the reduction reaction for the phenylpyridine moiety.

References

1. Aaron Ciechanover, "The ubiquitin-proteasome proteolytic pathway", *Cell* **79** (1) 13-21 (1994)
2. B. Cao, X. Mao, "The ubiquitin-proteasomal system is critical for multiple myeloma: implications in drug discovery.", *Am. J. Blood Res.* **1**(1) 46–56 (2011)
3. Shigeki Ito, "Proteasome Inhibitors for the Treatment of Multiple Myeloma", *Cancers* **12**(2) 265 (2020)
4. de Jesus, CSH; Enache, TA; Diculescu, VC, "Charge transfer reaction mechanisms of epoxyketone and boronated peptides at glassy carbon and boron doped diamond electrodes", *J. Electroanal. Chem.* **878** (2020)
5. D.A. Golea, V.C. Diculescu, L. Tugulea, A.M. Oliveira Brett, "Proteasome inhibitor anticancer drug Bortezomib redox behaviour at a glassy carbon electrode", *Electroanalysis.*, **24** 1915-1921 (2012)

MAX Phases for Chemoselective Hydrogenation of 4-nitrostyrene

Mihaela M. Trandafir,^a Florentina Neațu,^a Ștefan Neațu,^a Andrei Kuncser,^a Elena I. Cuculea,^b Varun Natu,^c Michel W. Barsoum,^c Mihaela Florea^a

^aNational Institute of Materials Physics, 405A Atomistilor Street, Magurele, Romania, 077125

^bResearch Center for Instrumental Analysis SCIENT, Petre Ispirescu Street, no. 1, Tancabesti, Ilfov, Romania, 077167

^cDepartment of Materials Engineering, Drexel University, Philadelphia, Pennsylvania, USA, 19104

The MAX phases are early ternary transition metal carbides and/or nitrides with a layered hexagonal crystal structure¹ with unique properties, bridging the gap between metals and ceramics. MAX phase presents a bouquet of interesting properties relevant for catalysis insufficiently explored so far. Thus, we decided to investigate the catalytic properties of the MAX phases, and more importantly as a support for Pd nanoparticles, for the chemoselective hydrogenation of a functionalized nitro-compound, 4-nitrostyrene, 4-NS² (see Fig. 1). The product of interest, 4-aminostyrene, 4-AS, is an important platform molecule in organic synthesis for a variety of agrochemicals and pharmaceuticals.

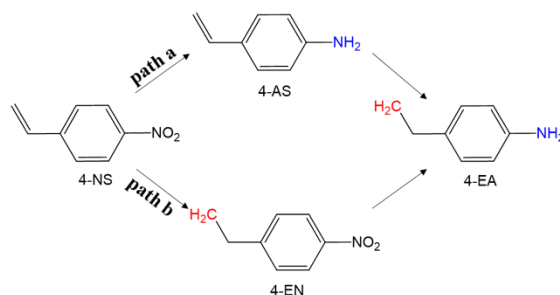


Fig. 1 Reaction pathways for hydrogenation of 4-NS².

The chemoselective hydrogenation of 4-NS was performed in the presence of the MAX phase using heptane as a solvent and hydrogen, H₂ gas, as a reducing agent. The reaction products identified were 4-AS, 4-ethylnitrobenzene (4-EN) and 4-ethylaniline (4-EA). (see Fig. 1). The experimental data and characterization of these materials are presented in detail in a recent ACS Catalysis paper (see ref. 2).

Regardless of the MAX composition powders used, as shown in top 3 entries in Table 1, we successfully hydrogenated 4-NS, with 100 % selectivity, into the product of interest, viz. 4-AS. This was a crucial result that cannot be overemphasized, since selectivity close to 100 % to 4-AS have never been achieved on such type of materials.

The addition of 0.0005 wt.% and 0.05 wt.% of Pd to Ti₃SiC₂ by impregnation increased the conversion rate to 100%, but the process was no longer selective (see Table 1). The advanced hydrogenation product, 4-EA was obtained via the formation of 4-EN (path b in Fig. 1). To determine the role of the deposition method, in this study we changed the Pd supporting method, from impregnation to deposition-precipitation (DP). Doing so improved the chemoselectivity to 4-AS, while maintaining the total conversion of 4-NS. A selectivity of 25% for 4-AS and 75% for 4-EA was thus obtained.

Changing the technique also changed the Pd content, more precisely the amount of Pd decreases from 0,00033 to 0.00014 wt. %, as the ICP analysis indicated. Such behavior was predictable, since the DP technique involves free adsorption of Pd onto the support from a higher volume solution while impregnation has the advantage of using smaller volumes that enable the deposition of higher Pd amounts onto the support and no washing step.

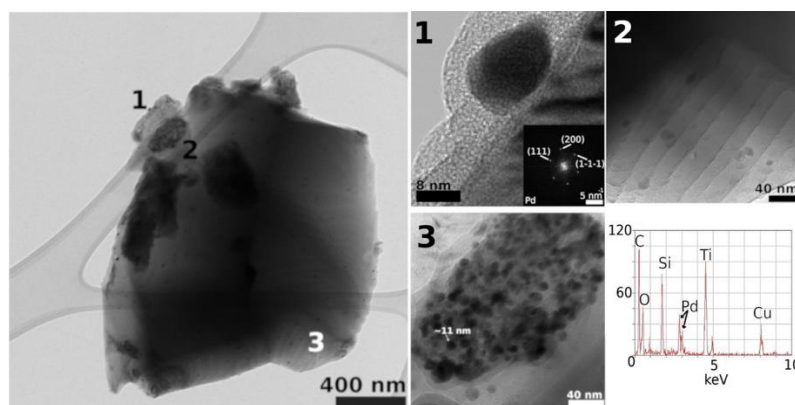
Table 1. Catalytic performance of Ti₃SiC₂-based catalysts for 4-NS conversion²

Catalyst	Conversion (%)	Selectivity (%)		
		4-AS	4-EN	4-EA
Ti ₂ AlC	0.44	100	0	0
Ti ₃ AlC ₂	0.81	100	0	0
Ti ₃ SiC ₂	3	100	0	0
0.0005 wt.% Pd/Ti ₃ SiC ₂	100	0	68	32
0.05 wt.% Pd/Ti ₃ SiC ₂	100	0	47	53
0.0005 wt.% Pd/Ti ₃ SiC ₂ _DP	100	25	0	75
Pd/Ti ₃ SiC ₂ _mix1	4	100	0	0
Pd/Ti ₃ SiC ₂ _mix2	59	73	19	8
Pd/Ti ₃ SiC ₂ _mix3	100	58	0	42
Pd/Ti ₃ SiC ₂ _mix4	100	10	0	90

Reaction conditions: 0.0134 mmol substrate; 4 mg catalyst; 3 mL of heptane; 24 h, 140 °C, 2.5 MPa H₂

In order to preserve the preferential selectivity obtained on Ti₃SiC₂ and to better control the amount of Pd, another strategy was employed, namely mechanically mixing Ti₃SiC₂ powders with those that were pre-impregnated with the Pd/Ti₃SiC₂ catalyst. The results are also listed in Table 1. The mechanically mixed Pd/Ti₃SiC₂_mix1 has the same catalytic behaviour as Ti₃SiC₂ without Pd. The reason is mostly an almost negligible (0.00002 wt.%) amount of Pd. Further increasing the Pd content, improves the catalytic conversion, but the selectivity to 4-AS decreases to 58% and 10%, respectively. Apparently, the Pd/Ti₃SiC₂_mix2 sample possesses the optimal Pd amount to reach a conversion of 100% together with a selectivity > 90% to 4-AS.

TEM images confirmed that all the samples showed similar morphology and structure (thin sheets of Ti₃SiC₂). Moreover, no changes in the MAX powders after impregnation, within TEM resolution, were evidenced. X-Ray mappings performed with a nm sized probe showed metallic Pd nanocrystals with a size in the 10 nm range in the case of 0.05 wt. % Pd doped sample (Fig. 2).

**Fig. 2** Large area TEM image of 0.05% Pd/Ti₃SiC₂ showing numbered regions of interest 1 to 3².

Moreover, we explored the catalyst stability of the most active sample by using it for 6 consecutive tests. From the results depicted in Fig. 3, it is clear that our system is stable for five reaction cycles, which represent very good results compared with data found in literature³. Deactivation starts only during the sixth reaction cycle. One possible reason for the 20% deactivation in the 6th cycle might be the partial blockage of the active centres with reaction products, as evidenced by ATR-FTIR spectroscopy and XPS.

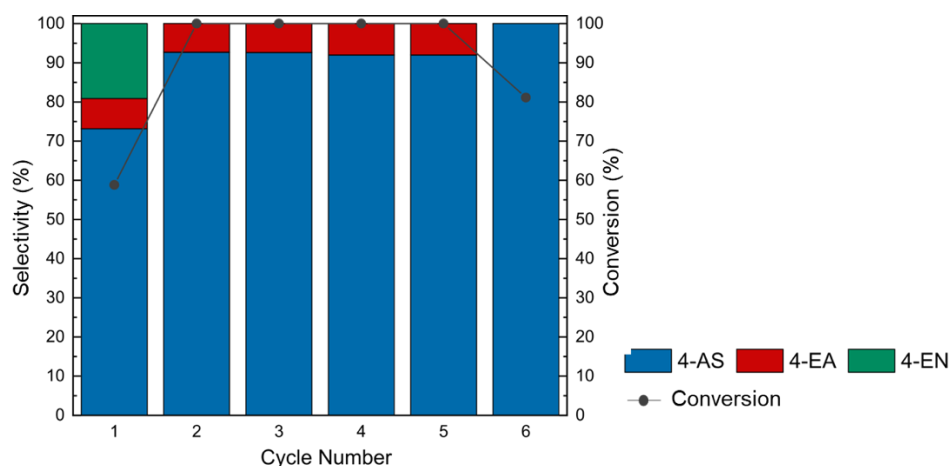


Fig. 3 Stability tests performed on Pd/Ti₃SiC₂_mix2 as catalyst for 4-NS hydrogenation, during six reaction cycles².

In conclusion, in this study we demonstrated that MAX phases are very selective materials for the transformation of 4-NS to 4-AS, with low conversion rates. We were able to maintain the very high selectivity and simultaneously increase the conversion by using low amounts of Pd. With an optimal loading of 130 ppm Pd, balanced Ti₃SiC₂, we obtained a conversion of 100% with a selectivity of 93% of 4-NS to 4-AS; higher Pd loadings result in a loss of selectivity. The role of the Pd is to dissociate/activate the H₂ gas, while the MAX phase preserves the selectivity. Pd is not an earth abundant element, and therefore the very small amounts needed together with the earth abundant and non-toxic nature of the elements in the MAX phases considered here, suggest that the cost of raw materials and/or toxicity will not be barriers to potential commercialization.

This study represents the first example where MAX phases, with low amounts of Pd, can be used as catalysts in chemoselective hydrogenation reactions. Thus, this could well be the starting point for designing a new generation of chemoselective catalysts in the hydrogenation of functionalized nitroderivatives, where the catalytic properties of the MAX phases can be exploited. Further studies are ongoing to further elucidate the mechanism of Pd reduction in-situ and to establish the right amount of Pd to reach 100% selectivity to 4-AS and total conversion.

References

1. M. W. Barsoum et al., *Synthesis and Characterization of a Remarkable Ceramic: Ti₃SiC₂*, J. Am. Ceram. Soc. **79**(7), 1953-1956 (1996) [doi.org/10.1111/j.1151-2916.1996.tb08018.x].
2. M. Florea et al., *Highly Efficient Ultralow Pd Loading Supported on MAX Phases for Chemoselective Hydrogenation*, ACS Catal. **10**(10), 5899-5908 (2020) [doi.org/10.1021/acscatal.0c00082].
3. A. Corma et al., *Transforming Nano Metal Nonselective Particulates into Chemoselective Catalysts for Hydrogenation of Substituted Nitrobenzenes*, ACS Catal. **5**(12), 7114-7121 (2015) [doi.org/10.1021/acscatal.5b01846].

Electron-polaron dichotomy of charge carriers in perovskite oxides

M. A. Husanu,^{a,b*} L. Vistoli,^c C. Verdi,^{d,e} A. Sander,^c V. Garcia,^c J. Rault,^f F. Bisti,^b L. L. Lev,^g T. Schmitt,^b F. Giustino,^{d,h,i} A. S. Mishchenko,^{j,k} M. Bibes,^c and V. N. Strocov^{b*}

^a Swiss Light Source, Paul Scherrer Institute, 5232, Villigen-PSI, Switzerland

^b National Institute of Materials Physics, Atomistilor 405A, 077125, Magurele, Romania

^c Unité Mixte de Physique, CNRS, Thales, Université Paris-Sud, Université Paris-Saclay, 91767, Palaiseau, France

^d Department of Materials, Univ. of Oxford, Parks Road, Oxford, OX1 3PH, UK

^f Synchrotron SOLEIL, L'Orme des Merisiers Saint-Aubin, BP 48, 91192, Gif-sur-Yvette, France

^g Moscow Institute of Physics and Technology, 9 Institutskiy lane, 141700, Dolgoprudny, Russia

^h Oden Institute for Computational Engineering and Sciences, Univ. of Texas at Austin, Austin, TX, 78712, USA

ⁱ Department of Physics, The University of Texas at Austin, Austin, TX, 78712, USA

^j RIKEN Center for Emergent Matter Science (CEMS), 2-1 Hirosawa, Wako, 351-0198, Saitama, Japan

^k National Research Center "Kurchatov Institute", 123182, Moscow, Russia

Many transition metal oxides (TMOs) are Mott insulators due to strong Coulomb repulsion between electrons, and exhibit metal-insulator transitions (MITs) whose mechanisms are not always fully understood. A promising strategy to develop new material functionality is to work with systems at the verge of a phase transition. For Mott insulators, this defines the field of Mottronics. This approach is especially suitable for the functionalization of giant conductivity variations across the metal-insulator transition, with the change driven by various mechanisms such as structural distortions, substrate-induced strain, thickness, and bias, as well as for the switching of the spin order between different magnetic ground states.

CaMnO₃ (CMO) belongs to a vast class of perovskite oxides, which are insulating due to strong electronic Coulomb repulsion. It relaxes into an orthorhombically distorted structure due to the strain induced by the different ionic radii of the Ca and Mn cations, consistently with its tolerance factor $t = (r_{\text{Ca}} + r_{\text{O}}) / 2(r_{\text{Mn}} + r_{\text{O}}) = 0.74$ in the range of orthorhombic distortions, while electron-spin coupling stabilizes a G-type antiferromagnetic order. Unlike in many perovskite oxides, minute doping of CaMnO₃ can induce a sharp transition to a metallic state. The critical electron concentration n_e for metallicity is in the low 10^{20} cm^{-3} range, which exceeds the values typical of classical semiconductors by two orders of magnitude but does not introduce any significant disorder or structural changes. Ce⁴⁺ doping at the Ca²⁺ site, by bringing two additional electrons per formula unit, pushes the Fermi level E_F into the conduction band. The consequent mixed Mn³⁺/Mn⁴⁺ valence state accounts for electronic properties and magnetic ground state driven by the interplay of electron itinerancy due to double exchange interaction with polaronic self-localization. This material is thus an ideal platform to explore band formation through the MIT. Here, by doping CMO with only 2 and 4% Ce (CCMO2 and CCMO4), we explore the nature of charge carriers emerging at the early stages of band filling inducing the transition from the insulating to a metallic state. For this purpose we use angle-resolved photoelectron spectroscopy (ARPES), which directly visualizes the electronic band structure and the one-electron spectral function $A(\mathbf{k}, \omega)$, reflecting many-body effects of electron coupling with other electrons and bosonic excitations. Our results show that the doping of CMO forms a system of dichotomic charge carriers, where three-dimensional (3D) light electrons, weakly coupled to the lattice, coexist with quasi-two-dimensional (q2D) heavy strongly coupled polarons. The latter form due to a boost of the electron-phonon interaction (EPI) on the verge of MIT where the occupied bandwidth stays comparable with the phonon energy. As in CCMO the energy scale of all elementary electronic and magnetic excitations is well separated from that of phonons, it gives us a unique opportunity to single out the EPI-specific effect.

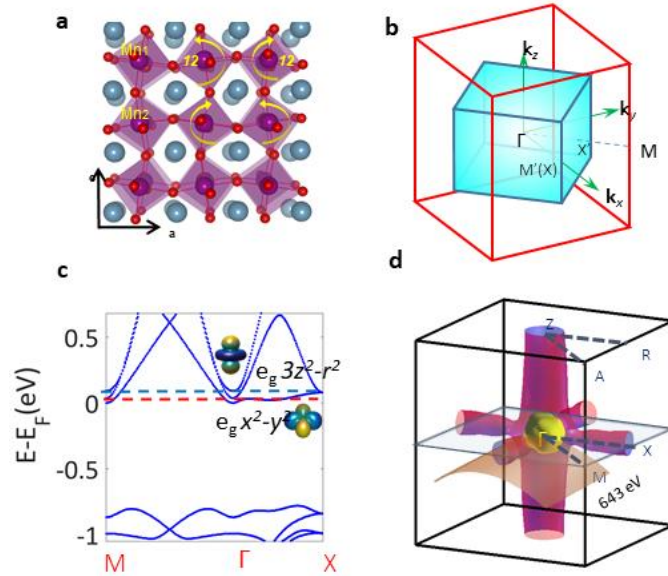


Fig. 1 **a** Density functional theory-relaxed orthorhombically distorted lattice of CaMnO_3 (CMO). **b** The Brillouin zone (BZ) of the distorted lattice inscribed into that of the undistorted cubic pseudo-cell. **c** Bandstructure and rigid shift of the Fermi energy E_F corresponding to 2% (red) and 4% doping (blue). **d** Theoretical Fermi surface (FS) unfolded to the cubic pseudo-cell BZ.

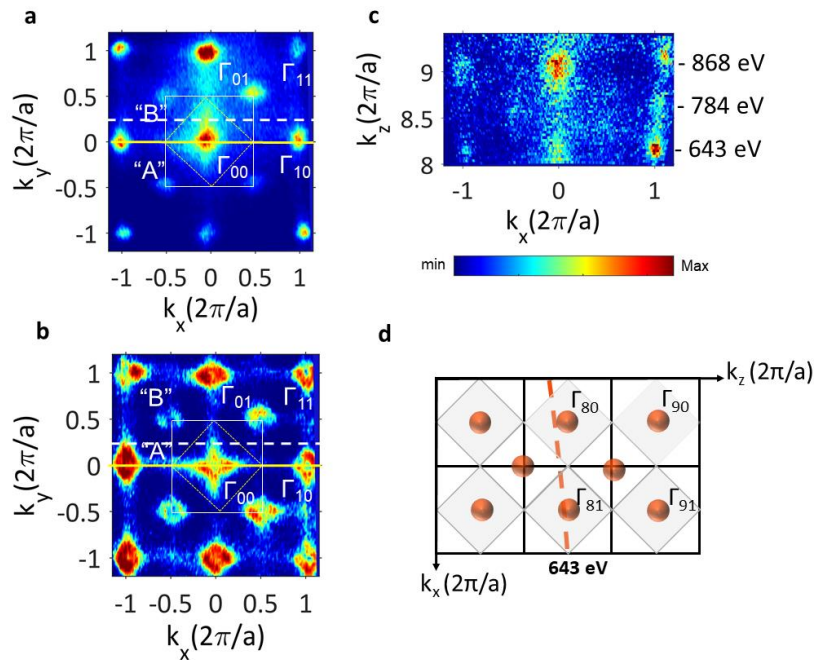


Fig. 2 **a, b** Fermi surface (FS) maps in the $\Gamma X M$ plane for the 2% Ce-doped sample—CCMO2 (**a**) and 4% Ce-doped—CCMO4 (**b**) measured with $h\nu$ at the Mn 2p resonance. The white square designates the cubic pseudo-cell surface Brillouin zone (BZ). The doping clearly increases the experimental Luttinger volume. **c** Out-of-plane FS map for CCMO2 in the $\Gamma Z R$ plane recorded under variation of $h\nu$. **d** Sketch of the 643 eV line cutting the $\Gamma 8$ point in the second BZ in k_{\parallel} and the trajectory of the 643 eV energy in the k -space

The relaxed orthorhombic structure of this material is shown in Fig. 1a together with the corresponding Brillouin zone (BZ) in comparison to that of the ideal cubic lattice in Fig. 1b, whereas Fig. 1c and d describe the mechanism of doping-induced MIT and the expected FS. Indeed, Fig. 2a-c displays the features collected in photoemission measurements predicted by the theoretical calculations.

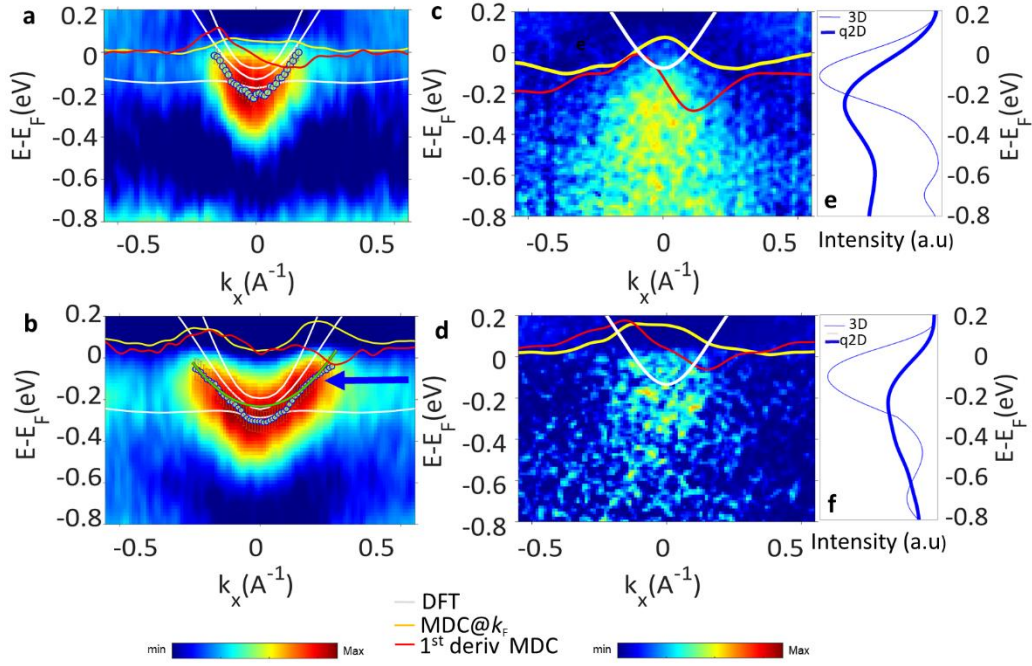


Fig. 3 a–d E(k) Band dispersions measured at the Mn 2*p* resonance for a, c CCMO2 and b, d CCMO4. E(k) of the 3D bands around the Γ -point (a, b) identifies light electron charge carriers. Blue arrow indicates the threshold energy of energy distribution curves (EDC) maxima deviating in CCMO4 from the parabolic dispersion. Angle resolved photoelectron spectroscopy (ARPES) images of the quasi-2D bands around $k_y = 0.5\pi/a$ (c, d) show massive humps extending down in binding energy (EB) which manifest heavy polaronic charge carriers. Also shown through (a–d) are the overlaid density functional theory (DFT)-theoretical bands and gradients of the energy-integrated ARPES intensity, identifying the Fermi wavevector k_F ; e, f Spectral function $A(k, \omega) \propto \text{EDC}$ at $k_x = k_F$ for the 3D bands (thin lines) and at $k_y = 0.5\pi/a$ for the q2D ones (thick lines) for CCMO2 (e) and CCMO4 (f). For the q2D bands, the whole $A(k, \omega)$ is dominated by the polaronic hump

Moreover, the band dispersions collected through the light (Fig. 3a,b) and heavy (Fig. 3c,d) electron bands reveal the gradual undressing of the electrons from their coupling with the phonons as the electron doping increases. This translates in increased carrier mobility on the one hand and on the other hand indicates that the insulating state of the oxide Mott insulators is inherently featured by strong electron-phonon interaction [1]. These findings open a new avenue of controlling the functionality of oxides by tuning their electron-phonon coupling strength using carrier concentration as a knob.

References

1. M. A. Husanu et al., “Electron-polaron dichotomy of charge carriers in perovskite oxides”, *Commun. Phys.* **3**, 62 (2020) 086001 (2006) [doi: [10.1038/s42005-020-0330-6](https://doi.org/10.1038/s42005-020-0330-6)].

***In situ* resistance hysteresis assessment correlated with surface science studies for graphene-like carbon layers deposited on atomically clean ferroelectric surfaces**

Nicoleta G. Apostol,^a Daniel Lizzit,^b George A. Lungu,^a Paolo Lacovig,^b Cristina F. Chirilă,^a Lucian Pintilie,^a Silvano Lizzit,^b and Cristian M. Teodorescu^{a,*}

^aNational Institute of Materials Physics, Atomiștilor 405A, 077125 Măgurele – Ilfov, Romania

^bElettra Sincrotrone Trieste, Strada Statale 14 – km 163,5, Area Science Park, 34149 Basovizza, Trieste, Italy

*e-mail teodorescu@infim.ro

Owing to its unique conduction properties, being assimilated with a zero bandgap semiconductor, and to the high charge carrier mobility, graphene is stipulated to be used in many novel semiconducting devices. One of these devices implies the association of graphene with ferroelectrics as gate materials (Fig. 1(a)), where the in-plane resistance of graphene exhibits maxima as soon as the polarization of the ferroelectric substrate is switched (Fig. 1(b)), together with a hysteretic behavior, with the compensation charge carriers needed at the ferroelectric surface [1–3] located into the graphene layer. Moreover, when the graphene exhibits an intrinsic doping, the switching occurs between two different resistance states (Figure 1(c)). This allows one to propose memory devices where the stored state in the orientation of the ferroelectric polarization is immediately read as the resistance state of the heterostructure. Owing to the high mobility of the charge carriers, this reading can be performed with minimal consumption and high frequency.

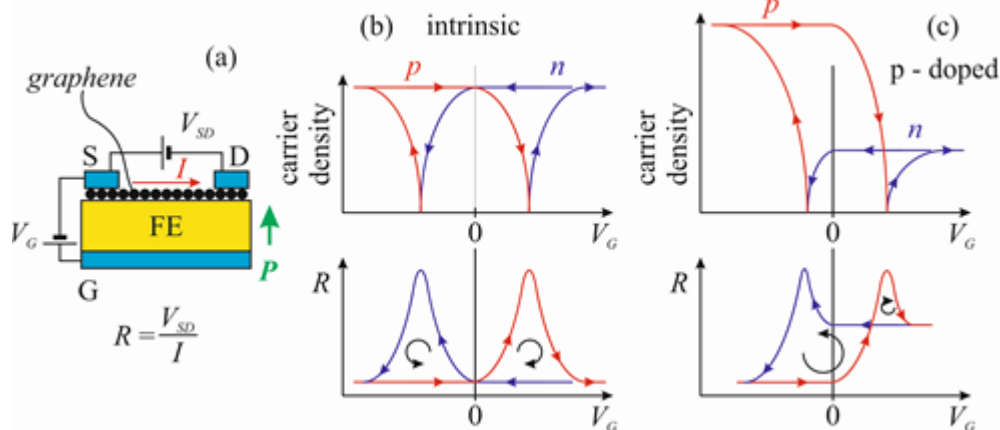


Fig. 1 (a) Scheme of a graphene-ferroelectric heterostructure, with the polarization circuit of the ferroelectric gate and the in-plane circuit for conduction through graphene. (b) The evolution of the resistance through the graphene layer vs. the gate voltage for intrinsic graphene. (c) The same evolution for an initially p-doped graphene layer.

However, experimentally in most cases the sense of the recorded hysteresis was opposite to the expected one from Fig. 1. This “anti-hysteresis” was attributed to yet unexplained conduction properties of adsorbates (contamination) located either on graphene or between graphene and the ferroelectric substrate [4]. Moreover, with temperature a switch from “hysteretic” to “anti-hysteretic” behavior was reported [5]. Therefore, the aim of this study was to perform *in situ* measurements of the resistance hysteresis in absence of any contamination by depositing carbon on atomically clean lead zirconate titanate films, then to pole *in situ* these films and to investigate the resistance hysteresis, together with synchrotron radiation based high resolution X-ray photoelectron spectroscopy (XPS) and angle dependent near-edge absorption fine structure (NEXAFS), which is a good fingerprint of the in-plane orientation of carbon sp² orbitals [6].

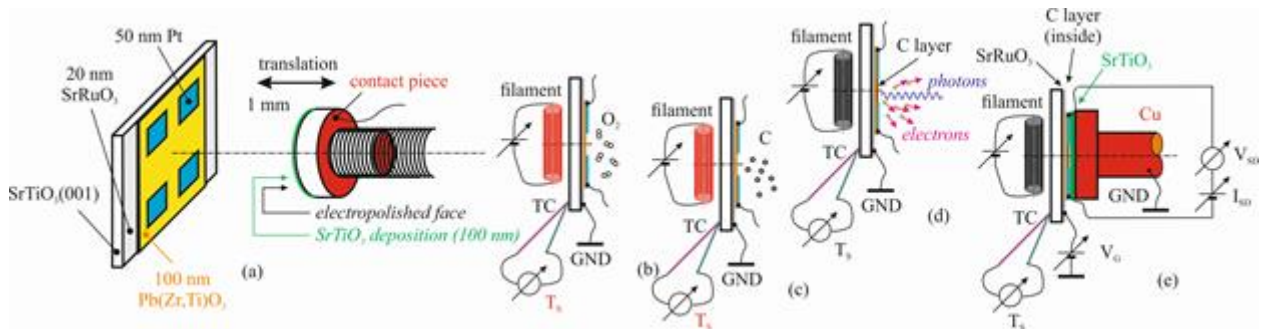


Fig. 2 Experimental setup: (a) the ferroelectric thin film with metal contacts and the poling piece; (b) the cleaning procedure; (c) carbon deposition; (d) X-ray photoelectron and X-ray absorption measurements; (e) poling procedure and electrical measurements [7]

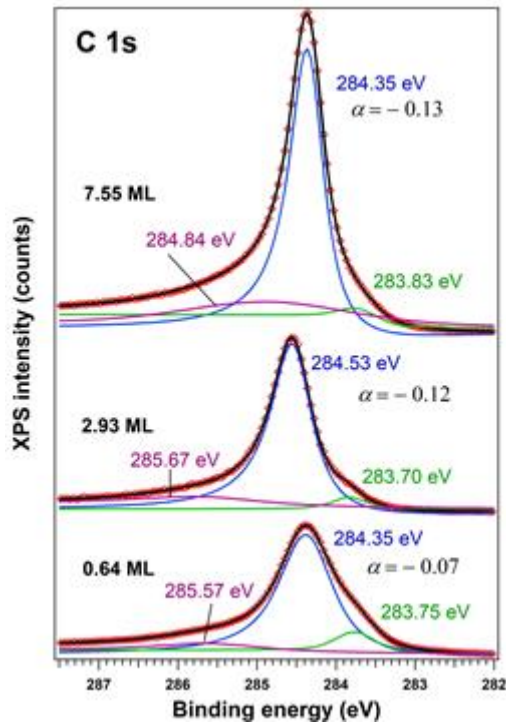


Fig. 3 C 1s photoelectron spectroscopy of graphene-like layers with several thicknesses [7]

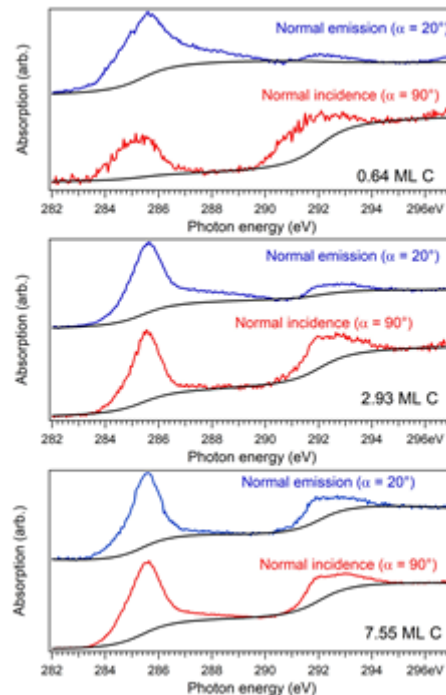


Fig. 4 Angle-dependent near-edge absorption spectra for three graphene-like layers, exhibiting a dichroism due to the in-plane orientation of sp^2 carbon orbitals [7]

The experimental setup is represented in Fig. 2. Substrates were cleaned by extended annealing in oxygen atmosphere (Fig. 2(b)) and carbon was deposited from an evaporator on heated substrates (Fig. 2(c)) [6,7]. This was followed by characterization with synchrotron radiation (Fig. 2(d)). C 1s XPS mainly revealed components attributed to graphene (Fig. 3), while NEXAFS yielded an increase proportion of in-plane sp^2 orbitals for thin graphene layers (Fig. 4). Scanning tunneling microscopy (STM) investigations evidenced areas with graphene-like layers (Fig. 5). These experiments were combined with *in situ* poling and in-plane measurement of the dependence of the resistance on the gate voltage (Fig. 2(e)) between a source (S) and a drain (D) platinum electrodes, with the results represented in Fig. 6. We unambiguously proved that ultrathin graphene layers exhibit “anti-hysteresis”, and, starting with 2 monolayers of graphene-like carbon, a “normal” hysteresis is obtained. The “anti-hysteresis” for thin graphene layers was explained by the competition between conduction through graphene and through a layer of accumulated charges in the ferroelectric substrate, since the graphene layers cannot provide sufficient charge for compensation [7].

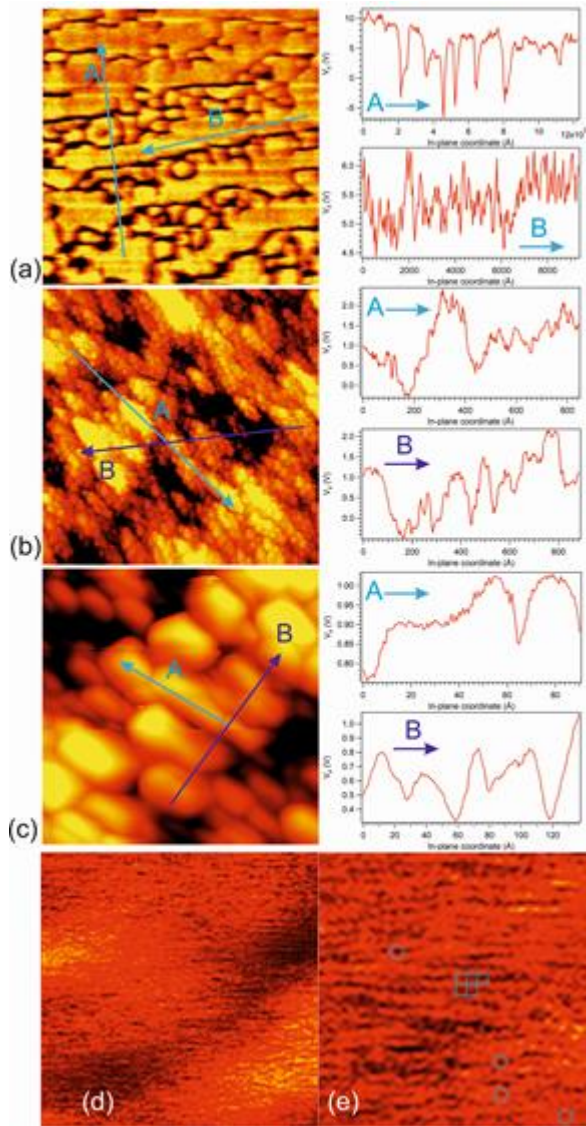


Fig. 5 Scanning tunneling microscopy (STM) investigations, at different scales. The curves at the right represent profiles along the lines from the images at the left [7].

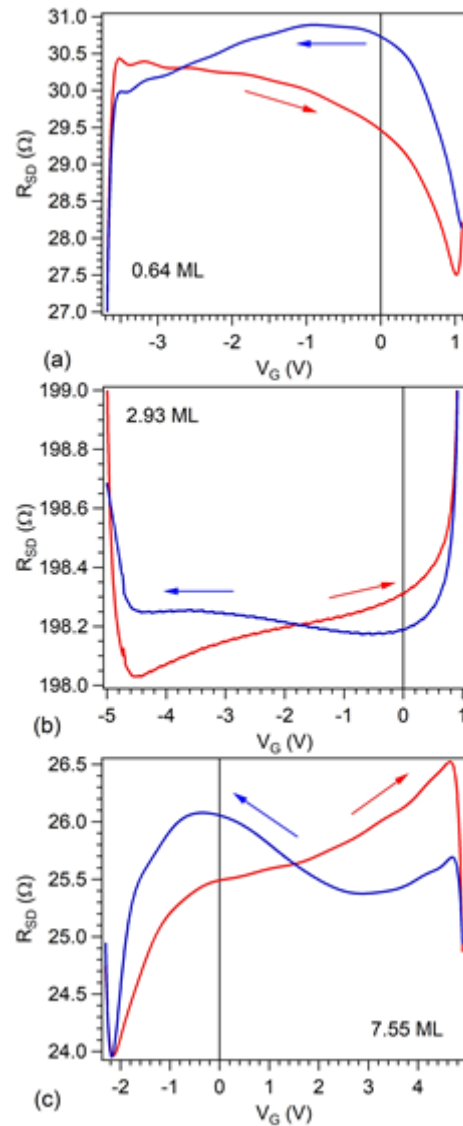


Fig. 6 Resistance variation between source and drain electrodes as function of the gate voltage [7].

References

1. L. Pintilie and M. Alexe, *Metal-ferroelectric-metal heterostructures with Schottky contacts. I. Influence of the ferroelectric properties*, J. Appl. Phys. **98**(12), 124103 (8 pp.) (2005) [doi: 10.1063/1.2148622].
2. L. C. Tănase et al., *Polarization orientation in lead zirconate titanate (001) thin films driven by the interface with the substrate*, Phys. Rev. Appl. **10**(3), 034020 (19 pp.) (2018) [doi: 10.1103/PhysRevApplied.10.034020].
3. C. M. Teodorescu, *Ferroelectricity in thin films driven by charges accumulated at interfaces*, Phys. Chem. Chem. Phys. **23**(7), 4085–4083 (2021) [doi: 10.1039/d0cp05617k].
4. X. Hong et al., *Unusual resistance hysteresis in n-layer graphene field effect transistors fabricated on ferroelectric Pb(Zr_{0.2}Ti_{0.8})O₃*, Appl. Phys. Lett. **97**(3), 033114 (3 pp.) (2010) [doi: 10.1063/1.3467450].
5. A. Rajapitamahuni et al., *Examining graphene field effect sensors for ferroelectric thin film studies*, Nano Lett. **13**(9), 4374–4379 (2013) [doi: 10.1021/nl402204t].
6. N. G. Apostol et al., *Non-interacting, sp² hybridized carbon layers on ferroelectric lead zirconate titanate*, RSC Adv. **6**(72), 67883–67887 (2016) [doi: 10.1039/c6ra12910b].
7. N. G. Apostol et al., *Resistance hysteresis in atomic layers of carbon synthesized on ferroelectric (001) lead zirconate titanate in ultrahigh vacuum*, RSC Adv. **10**(3), 1522–1534 (2020) [doi: 10.1039/c9ra09131a].

Polarization-dependent magnetism of the Ni/BaTiO₃ interface

A. E. Bocîrnea,^a D. G. Popescu,^{a*} C. Chirilă,^a R. M. Costescu,^a V. Kuncser,^a V. Stancu,^a L. Trupină,^a I. Pasuk,^a A. M. Vlaicu,^a and M. A. Huşanu^a

^aNational Institute of Materials Physics, Atomiştilor 405a, 077125 Măgurele-Ilfov, Romania

Systems combining different ferroic phases are an attractive realm for developing devices with enriched functionality at the interface between dissimilar materials [1]. We studied the ferroelectric/ferromagnetic interface in Ni/BaTiO₃(001) heterostructures and we emphasize the role between the polarization state of the ferroelectric and both the growth mode and the magnetism of the 5 nm thick Ni layers. We further refer to the samples as P1: Ni/3.5nm BaTiO₃/ 20 nm La_xSr_{1-x}MnO₃ / Nb–SrTiO₃ (x = 0.3) and P2: Ni/3.5nm BaTiO₃/ 20 nm La_xSr_{1-x}MnO₃ / 5 nm SrRuO₃ / Nb–SrTiO₃ (x = 0.3)

Ni was deposited *in situ* on a clean BaTiO₃ (BTO) surface, in two deposition steps: 0.5 nm and 4.5 nm, and we acquired XPS measurements on the clean surface and after each deposition step to study the interface phenomena. The surface morphology was characterized by means of atomic force microscopy (AFM), the magnetism was characterized using magnetic force microscopy (MFM) and magneto-optic Kerr effect (MOKE), and the results were explained with the use of Density Functional Theory (DFT). The crystallinity of the heterostructures was checked with X-ray Diffraction (XRD).

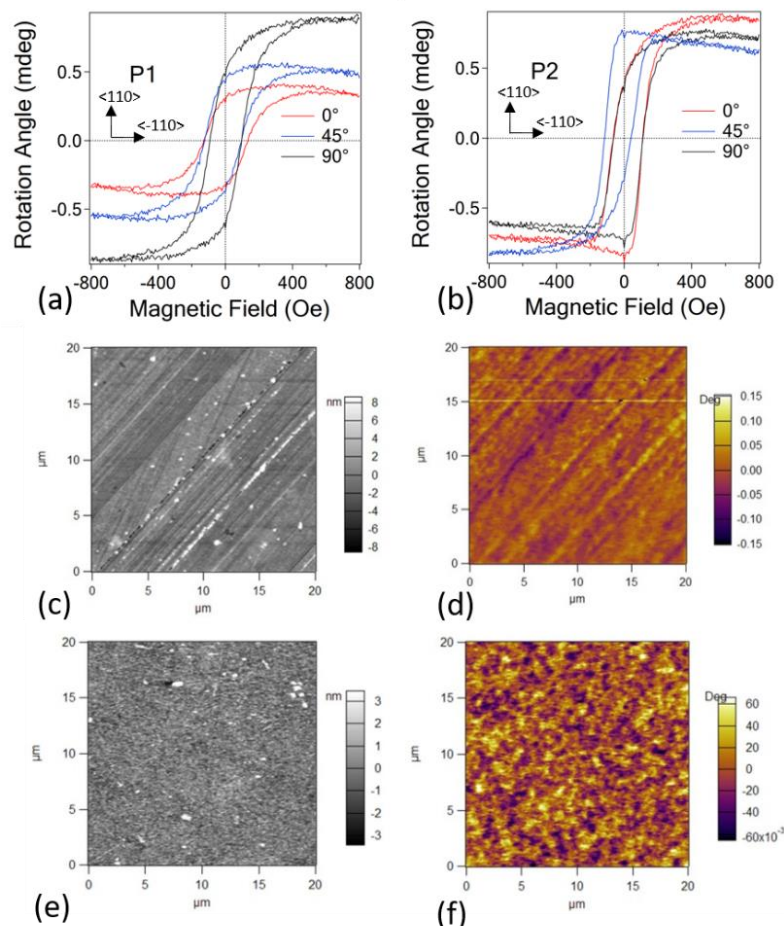


Fig. 1. The magnetic and morphological characterization of P1 and P2. The images a) and b) show MOKE hysteresis loops for P1 and P2 respectively; the black and white images c) and e) are AFM results for P1 and P2 respectively, and the d) and f) images represent the MFM magnetic contrast specific for the corresponding AFM images.

Fig. 1. shows the MOKE, AFM and MFM results for the two systems. When grown on a P+ polarized BTO, Ni shows uniform growth, with a terrace like surface, while the thin Ni film grown

on the P- polarized BTO has a granular surface. One can notice that the MFM images are identical with the morphological AFM images, represented in black and white. The lack of magnetic domains (contrast) on both Ni surfaces is translated by the in-plane orientation of the spins for both 5 nm nickel films. Additional characterization of the surface magnetism of the samples comes from MOKE. We can see that the sample P1 describes hysteresis loops that are symmetrical with respect to the axis origin, showing no magnetic textures. The variation of the Kerr angle as a function of the measurement angle is an optical effect due to the scattering of the radiation. The sample P2 is highly different, showing both the presence of an exchange bias, so the existence of an antiferromagnetic component opposite to the ferromagnetic one, and the presence of a magnetic easy axis, oriented at 45° with respect to the BTO $\langle 110 \rangle$ crystalline axis. We need to establish the provenience of the antiferromagnetic signal in the case of P2.

The growth modes of the thin Ni films are also different depending on the substrate. As we can see from Fig. 1 c) and d), the sample P1 presents terraces on the surface, while sample P2 (Fig. e) and f)) presents a granular surface. The information extracted from the morphology images is completed further by the results extracted from the XPS analysis (Fig 2.).

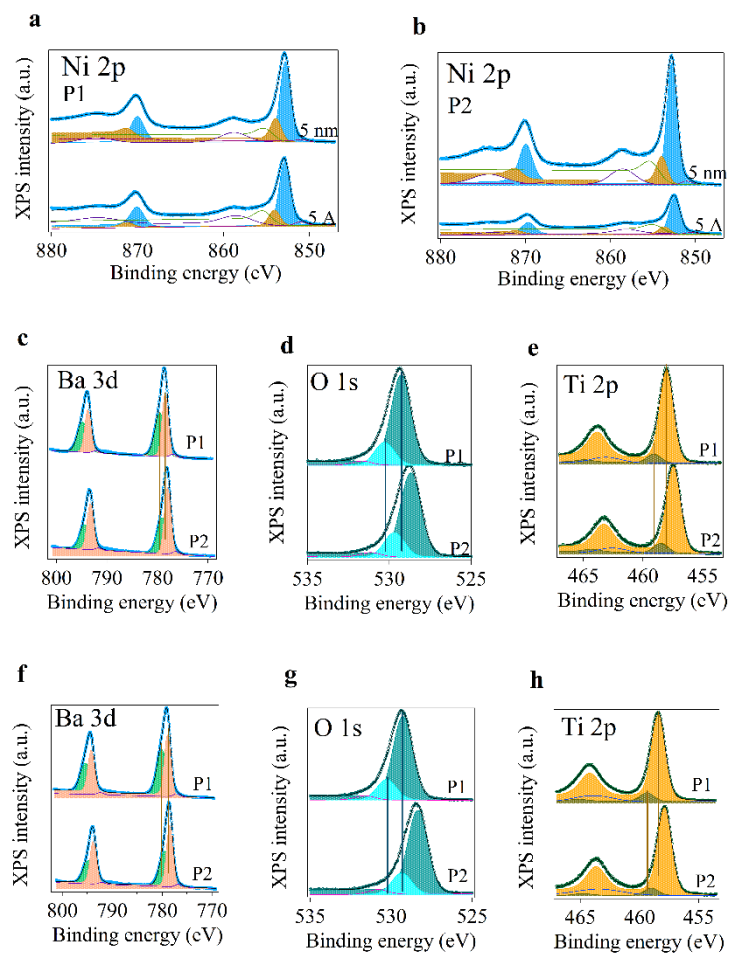


Fig. 2. XPS spectra of Ni 2p after each deposition step for samples a) P1 and b) P2; BTO core levels on the clean surface (c-e) and after 0.5 nm Ni deposited (f-h).

From the XPS spectra we can firstly see that the chemical structure of the two systems is the same and that the polarization states of the two samples are different. The BTO layer in the sample P1 is P+ polarized, with Ba 3d, Ti 2p and O 1s core levels shifted to higher binding energies, while the ferroelectric BTO layer in sample P2 is P- polarized for the core levels are all shifted to lower binding energies. From the integral amplitudes extracted from the fitting procedure, we extracted the Ba:Ti ratios in the 2 cases as 0.94 for P1 and 1.09 for P2 showing that the surfaces are Ti rich in the case of P1 and Ba rich in the case of P2. We can state that P1 presents a TiO_2 predominant termination and P2 presents a BaO predominant termination.

XRD showed that Ni films grew epitaxially on both supports, having a single (001) orientation, the same as the support. The Ni film is also highly crystalline and it has the ideal lattice constant of 3.519 Å [2]. The mismatch between the BTO lattice and fcc Ni was intermediated by the formation of an interface NiO layer that is thinner than the XRD detection limit. That contribution is nevertheless present in the XPS spectra for both samples (Fig. 2).

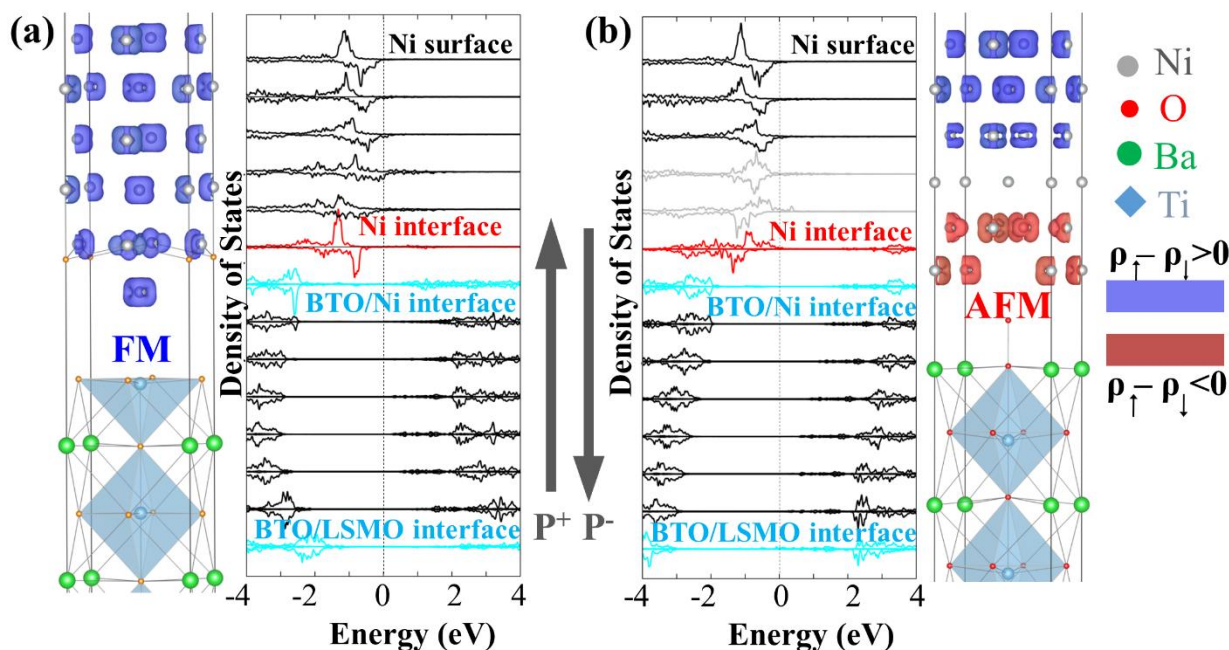


Fig. 3. Spin resolved DFT simulation for the interfaces between a) a P(+) polarized BTO that is TiO₂ terminated and b) a P(-) polarized BTO that is BaO terminated.

Spin resolved DFT calculations (Fig.2) determined that Ni spins have an antiferromagnetic orientation for the first 3 monolayers of Ni deposited on a P(-) polarized BTO with a BaO termination. This state is less favorable, and needs an energy that is 20 meV higher than in the case of Ni in P1. This information is answering the question regarding the origin of the exchange bias in the hysteresis loops as measured with MOKE.

In conclusion, we have studied the properties of Ni/BTO/LSMO(/SRO)/STO heterostructures and determined that the introduction of a thin SRO film in the perovskite multilayers changed both the polarization state of the 3.5 nm BTO films and the growth sequence of the top perovskite layers. The characteristics of the substrate determined both the growth mode and the magnetic character of the 5 nm Ni films, but in both cases the layers are highly crystalline and have an ideal structure. The creation of a full picture was possible with the use of a rich variety of experimental techniques and DFT simulations.

References

1. Y. Sun, Y. Ba, A. Chen, W. He, W. Wang, X. Zheng, L. Zou, Y. Zhang, Q. Yang, L. Yan, C. Feng, Q. Zhang, J. Cai, W. Wu, M. Liu, L. Gu, Z. Cheng, C.-W. Nan, Z. Qiu, Y. Wu, J. Li, and Y. Zhao, *ACS Appl. Mater. Interfaces* **9**, 10855 (2017).
2. A. E. Bocirnea, D. G. Popescu, C. Chirila, R. M. Costescu, V. Kuncser, V. Stancu, L. Trupina, I. Pasuk, A. M. Vlaicu, and M. A. Husanu *Phys. Rev. Materials* **4**, 034402 (2020)

Quantum dot exciton dephasing by Coulomb interaction: A fermionic analog of the independent boson model

I.V. Dinu,^{a,b} M. Țolea,^a and P. Gartner,^{b,*}

^aNational Institute of Materials Physics, Atomistilor 405A, Magurele 077125, Romania

^bCentre International de Formation et de Recherche Avancées en Physique - National Institute of Materials Physics, Atomistilor 407, Magurele 077125, Romania

Quantum dots (QD) in semiconductor heterostructures are sometimes regarded as artificial atoms, but one aspect in which they differ from real atoms is that they live in an invasive environment. QD carriers interact with phonons, and sometimes with free carriers in the wetting layer (WL). Such interactions play an important role in the QD optical properties, and especially in the dissipative behavior, like carrier population redistribution and polarization dephasing.

In this respect, the role of the phonons enjoyed a much larger attention in the literature, one reason being the availability of the independent boson model (IBM) [1], which is both simple and in certain circumstances exactly soluble by the polaronic unitary transform.

It is then legitimate to ask whether such a unitary transform exists for the interaction with the free carriers too. In this paper [2] we show that the answer is positive, if we frame the problem as above, i.e. if the interaction is diagonal in the QD states and the WL carriers do not mutually interact (independent fermions). We illustrate the situation in the case of an exciton whose charge distribution acts as a scattering center for the carriers in the continuum. It is known [3] that the free and the scattered continua are unitary equivalent, with the transform provided by the scattering matrix.

We illustrate the method by calculating the polarization decay and absorption line shape, with functions of bath temperature and carrier concentration. We also discuss in more detail the similarities and differences with respect to the IBM. As an example we consider an InAs/GaAs heterostructure, with a self-assembled QD on a WL with different widths. For QD we consider one s – state in each band ($\lambda = e, h$) and for the WL a continuum of plane waves, orthogonalized on the former. We denote these states as $|\varphi_i^\lambda\rangle$, where i stands for s -states in QD or \mathbf{k} for the WL ones. The QD is a two-level system. The Hamiltonian for the QD is denoted by $H_{QD} = \varepsilon_X X^\dagger X$, where ε_X is the exciton energy and $X^\dagger(X)$ is the raising (lowering) operator. The Hamiltonian for the WL is $H_{WL} = \sum_{\mathbf{k}} [\varepsilon_k^e e_k^\dagger e_k + \varepsilon_k^h h_k^\dagger h_k]$ and for the QD-WL interaction $H_V = X^\dagger X W$.

The form $W = \sum_{\lambda=e,h} \sum_{\mathbf{k},\mathbf{k}'} W_{\mathbf{k},\mathbf{k}'}^\lambda \lambda_{\mathbf{k}}^\dagger \lambda_{\mathbf{k}'}$ shows that the WL carriers are scattered by an external field produced by the exciton, with $W_{\mathbf{k},\mathbf{k}'}^\lambda = 2V_{s\mathbf{k},\mathbf{k}'s}^{\lambda,\lambda} - 2V_{s\mathbf{k},\mathbf{k}'s}^{\lambda',\lambda} - V_{s\mathbf{k},s\mathbf{k}'}^{\lambda,\lambda}$ ($\lambda, \lambda' = e, h$). The matrix elements of the Coulomb potential V_q are computed in the above-mentioned one-particle basis.

The first two terms from $W_{\mathbf{k},\mathbf{k}'}^\lambda$ describe direct, electrostatic interaction between WL carriers with the QD electron (e) and hole (h), respectively. The difference between repulsion and attraction is nonzero due to the different charge densities of these two. The third term represents the exchange contribution which is small because the matrix elements of the Coulomb potential become overlap integrals between orthogonal states.

Fig. 1 shows the time evolution of the real part of $\Phi(t)$ (Eq. 1) for two different temperatures. The exciton probability amplitude is $P(t) = \exp[\Phi(t)]$ and

$$Re[\Phi(t)] = - \sum_{\lambda,k,k'} |W_{k,k'}^\lambda|^2 (1 - f_k^\lambda) f_{k'}^\lambda \frac{1 - \cos(\varepsilon_{kk'}^\lambda t)}{(\varepsilon_{kk'}^\lambda)^2} \quad (1)$$

where f_k^λ is the Fermi function for WL carriers and $\varepsilon_{kk'}^\lambda = \varepsilon_k^\lambda - \varepsilon_{k'}^\lambda$.

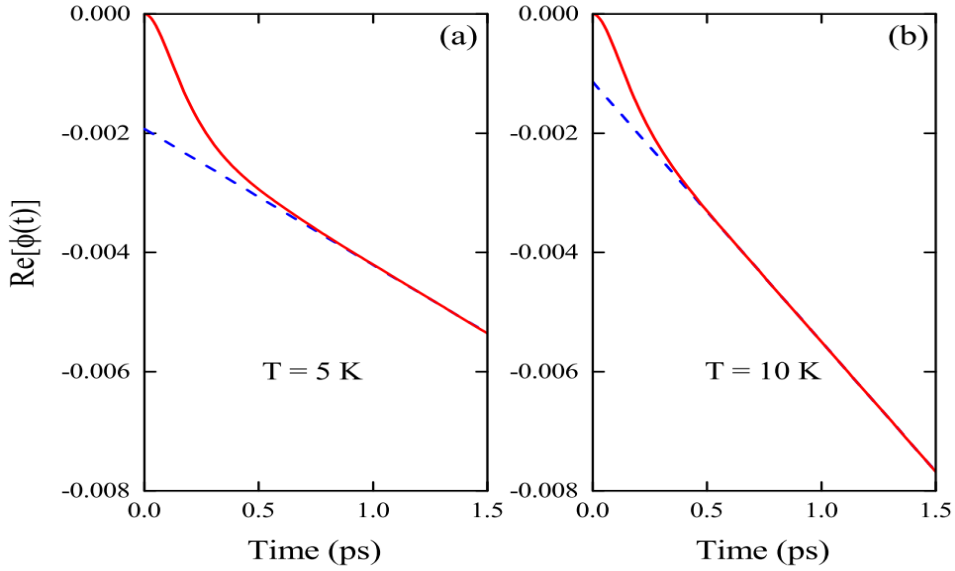


Fig. 1 Time evolution of the real part of Φ for two temperatures 5 K (a) and 10 K (b) for the same carrier concentration $n=10^{12} / \text{cm}^2$ (red line). In the asymptotic limit $t \rightarrow \infty$, the dephasing get to a linear decay whose rate increases with temperature (blue line).

In the small-time behavior the real part of Φ decays quadratically and in the long-time behavior becomes linear with a slope defined by the decay rate Γ (Eq. 2). Indeed, using the large t (time) asymptotics of $(1 - \cos xt)/x^2 \approx \pi \delta(x)t$, one finds an exponential attenuation $P(t) = \exp(-\Gamma t)$ of QD exciton with the decay rate given by

$$\Gamma = \pi \sum_{\lambda, k, k'} |W_{k, k'}^\lambda|^2 (1 - f_k^\lambda) f_{k'}^\lambda \delta(\varepsilon_{k k'}^\lambda). \quad (2)$$

Fig. 2 shows the increase of the dephasing rate with temperature and also with the carrier concentration. The range of $\hbar\Gamma$ is of the order of a few μeV which is comparable to the results for dephasing by phonons at low temperatures, obtained in both theoretical [4] and experimental [5] simulations.

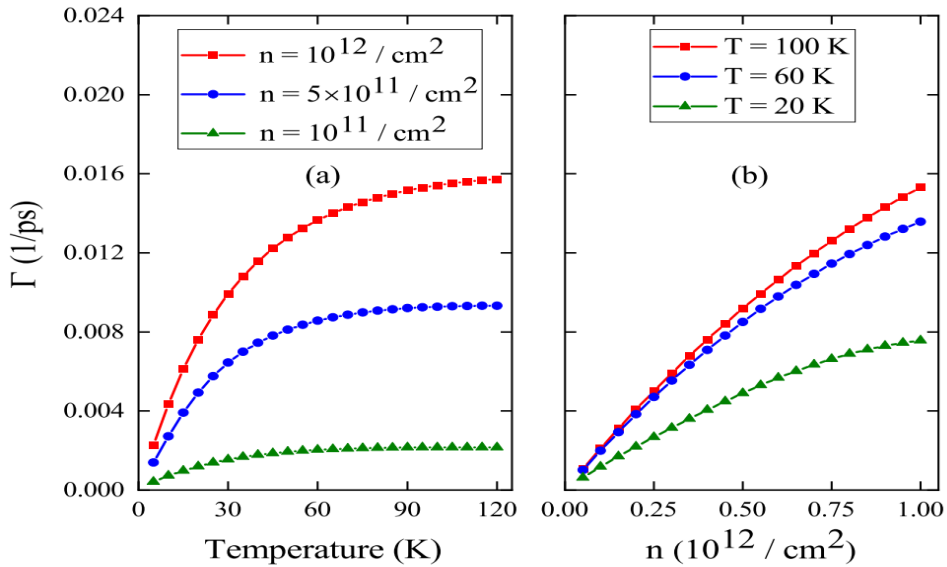


Fig. 2 Dephasing rates (a) as functions of temperature for different carrier concentrations and as (b) functions of carrier concentrations for different temperatures.

In Fig. 3, we present the dependence of dephasing for different geometric parameters (L & α). It is observed that Γ is not very sensitive to the WL width L , but is significantly influenced by the width α_λ of the QD s – states, which are taken as having Gaussian form:

$$\varphi_s^\lambda(r) = \frac{\alpha_\lambda}{\sqrt{\pi}} \exp(-\alpha_\lambda^2 r^2/2) \quad (3)$$

with r being the in-plane position. Such a behavior of large Γ (stronger dephasing) is due to more scattering processes when α is small (broader states).

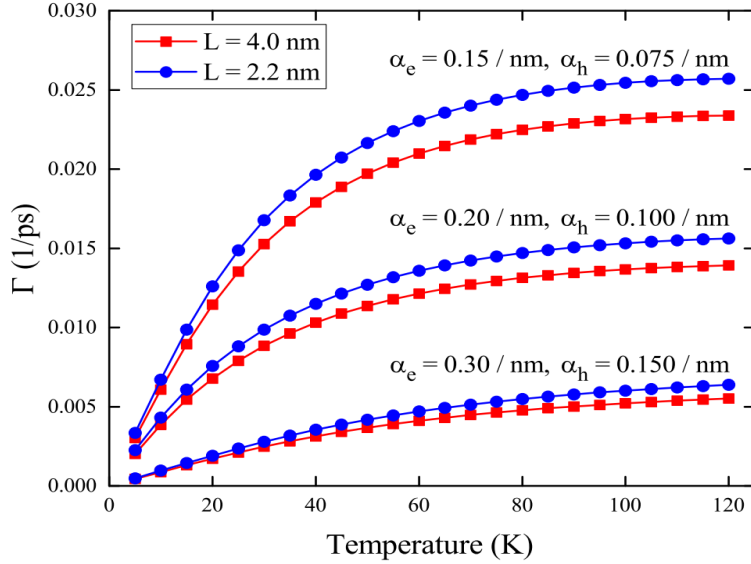


Fig. 3 Temperature dependence of the dephasing rate for different WL width L and wave-function extension parameters α . All curves are for $n=10^{12} / \text{cm}^2$.

In conclusion, it was shown that a fermionic analog of the IBM is possible for an interaction between a QD exciton and a fermionic bath. The dephasing process is controlled not only by temperature, as in the bosonic case, but also by the WL-carrier concentration. From numerical analysis we showed that at low temperatures and higher carrier concentrations, the dephasing times are comparable with those produced by the phonon interaction. Compared to IBM which is exact, our result is obtained through a diagrammatic series expansion, advantage of IBM which is lost when other interactions are present. The exciton decay rate is accentuated at higher temperature or higher carrier concentration and also when the charge distribution of QD states are broader.

References

1. G. D. Mahan, Many Particle Physics, 3rd ed. (Kluwer Academic/Plenum Publishers, New York, 2000).
2. I. V. Dinu, M. Țolea, and P. Gartner, Phys. Rev. B **101**, 085304 (2020) [[doi:10.1103/PhysRevB.101.085304](https://doi.org/10.1103/PhysRevB.101.085304)].
3. J. R. Taylor, Scattering Theory (Dover, New York, 2006).
4. T. Takagahara, Phys. Rev. B **60**, 2638 (1999) [[doi:10.1103/PhysRevB.60.2638](https://doi.org/10.1103/PhysRevB.60.2638)].
5. P. Borri, W. Langbein, S. Schneider, U. Woggon, R. L. Sellin, D. Ouyang, and D. Bimberg, Phys. Rev. Lett. **87**, 157401 (2001) [[doi:10.1103/PhysRevLett.87.157401](https://doi.org/10.1103/PhysRevLett.87.157401)].

Robust conductance zeroes in graphene quantum dots and other bipartite systems

M. Nita,^a M. Tolea,^a D.C. Marinescu^b

^aNational institute of Materials Physics , Bucharest-Magurele, Atomistilor 405A Romania, Magurele 77125

^bDepartment of Physics, Clemson University, Clemson, SC 29634

Interference effects in electronic conductance are quantum effects without correspondence in classical electronics. A particular case is the perfect cancellation of the conductance due to destructive quantum interference (DQI) which is robust to various perturbations and has been investigated previously in quantum dots or molecular systems [1-4]. Finding systems where such property occurs is both of fundamental and practical interest, as in designing on/off switches. The topic of conductance cancellation received renewed attention in connection to the transmission phase lapse of π occurring precisely at the conductance zeroes between the resonances of a quantum dot, arguably one of the longest standing puzzle in mesoscopic physics, whose elucidation spanned thirty years [5,6].

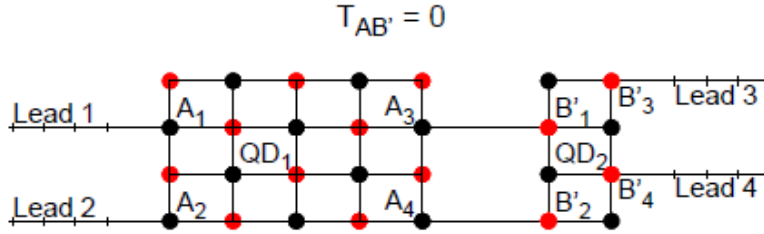


Fig. 1 A bipartite quantum conductor (the two sub-lattices are with red and black color, respectively) with incoming leads connected to “A” points and outgoing ones to “B” points. Our proof relies on decomposing the system in two sub-systems, and at the end $T_{AB'}$ conductances are calculated.

In this paper we demonstrate the presence of a robust zero transmission in graphene quantum dots (QD) and other specific molecules at half-filling (i.e. zero Fermi energy) starting from an analysis of quantum transport in bipartite lattices. Such systems, known to provide an appropriate description for graphene, are composed of two sublattices A and B with hopping only between A and B sites and no hopping in the same sub-lattice. In the Landauer formalism, where the conductance between two points G_{ij} is proportional to the transmittance T_{ij} , it was previously found that zeroes are obtained in graphene QDs when both leads are connected to the same sub-lattice, T_{AA} or T_{BB} [7,8], provided that the zero energy itself is not an eigenvalue of the system. Moreover, it was shown that this type of zeroes occurs with a π phase lapse of the transmission amplitude, a property characteristic to Fano zeroes. Here [9] we focus on the origin of the transmission zeroes and their characteristic properties in a setup that involves DQI when the transport leads are connected to both sublattices, T_{AB} (See Fig.1), a situation met, for instance, in graphene quantum dots with armchair edges.

The Hamiltonian that describes the system from Fig.1 can be written generically:

$$H^{\text{eff}} = H_1(A, B) + H_2(A', B') + V_{12}(A, B') + V_1(A) + V_2(B) \quad (1)$$

Where the first two terms describe the two quantum dots, the third describes the coupling between them and the last two the coupling to the leads. After some straightforward manipulations, the Green function between two sites, belonging to the first and the second QDs, respectively, reads:

$$G_{AB'}^{\text{eff}}(E) = G_{AA}V_1G_{AB'}^{\text{eff}} + G_{AA}V_{12}G_{B'B'}^{\text{eff}} \quad (2)$$

Which shows that the conductance cancellation between an A site from the first QD and a B site from a second dot follows from the cancellation of the G_{AA} Green functions between points from the same sub-lattice of a single dot, which was proven in [7,8].

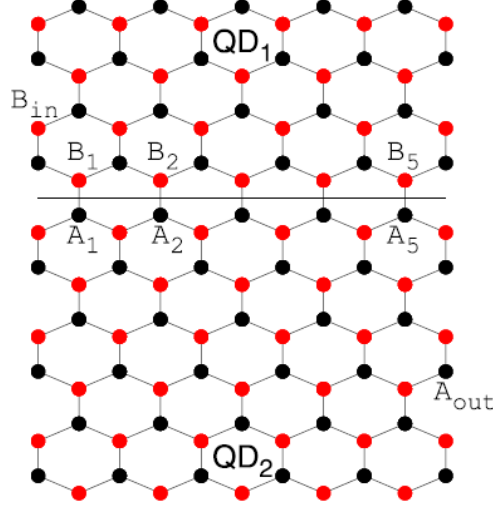


Fig. 2 A graphene sheet which can be formally regarded as two coupled QDs, so that the formalism developed for decompositions such as those in Fig.1 can be applied.

Next, we show how the general formalism described above applies to the graphene quantum dots. One general requirement for Green functions of type G_{AA} to vanish for bipartite systems at half-filling is that the system does not have an eigenenergy at that energy. In graphene quantum dots with armchair edges this is ensured by the analytical knowledge of zig-zag edge states [10]:

$$E_{zz\pm} = \pm \frac{\sinh(\partial j/2)}{\sinh \partial j(N_{ac}+1/2)} \quad (3)$$

Where N_{ac} is the number of hexagonal cells in the armchair direction ($N_{ac} = 5$ in Fig.2) and is determined from the characteristic equation: $\sinh(\partial j N_{ac}) = 2 \cos(\epsilon j/2) \sinh[\partial j(N_{ac} + 1/2)]$, with $\epsilon j = \pi j/(N_{zz} + 1)$, N_{zz} counting the zigzag points.

For the system depicted in Fig.2 the conductance and the transmittance phase evolution are plotted in Fig.3, for the case when the leads are coupled to opposite zigzag edges. Apart from the prediction of zero conductance, we also study its robustness and show that the zero survives to any single site perturbation. A minimum of two sites have to be perturbed to lift the zero conductance.

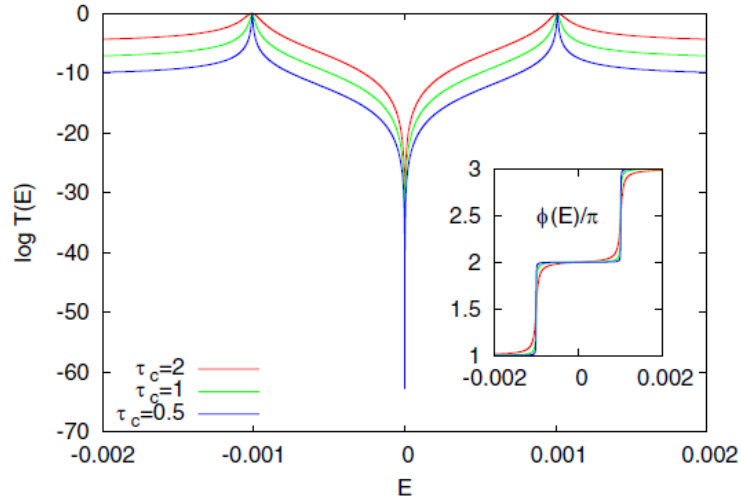


Fig. 2 Zero transmittance (for $E=0$) in the graphene QD depicted in Fig.2. For clarity, the conductance is plotted in logarithmic scale. The inset shows that in this case the transmittance phase does not exhibit a π lapse at the conductance cancellation point.

Our results can be used to predict the existence of DQIs and to understand their robustness in various physical systems –such as finite tight-binding lattices or molecules- that are composed from various building blocks with certain bipartite characteristics.

References

1. Y. Tsuji, E. Estrada, R. Movassagh, and R. Hoffmann, *Chem. Rev.*, **118**, 4887 (2018).
2. Colin J. Lambert and Shi-Xia Liu, *Chem. Eur. J.* **24**, 4193 (2018).
3. Timothy A. Su, Madhav Neupane, Michael L. Steigerwald, Latha Venkataraman and Colin Nuckolls *Nature Reviews Materials*, **1**, 16002 (2016).
4. Sriharsha V. Aradhya and Latha Venkataraman, *Nature Nanotechnology*, **8**, 399 (2013).
5. R. Schuster, E. Buks, M. Heiblum, D. Mahalu, V. Umansky, and H. Shtrikman, *Nature* **385**, 417 (1997).
6. H. Edlbauer, S. Takada, G. Roussely, M. Yamamoto, S. Tarucha, A. Ludwig, A.D. Wieck, T. Meunier, C. Bauerle, *Nature Comm.* **8**, 1710 (2017).
7. Tomofumi Tada and Kazunari Yoshizawa, *ChemPhysChem*, No.**12**, 1035 (2002).
8. M. Nita M. Tolea, and B. Ostahie, *Phys. Status Solidi RRL* **08**, 790 (2014).
9. M. Nita M. Tolea, D.C. Marinescu, *Phys.Rev.B* **101**, 235318 (2020).
10. L. Malysheva and A. Onipko, *Phys. Rev. Lett.* **100**, 186806 (2008).

Switching the electron-vibron coupling in hybrid quantum systems

R Dragomir,^a V. Moldoveanu,^a S. Stanciu,^a B. Tanatar^b

^aNational Institute of Materials Physics, Bucharest-Magurele, Atomistilor 405A Romania, Magurele 77125

^b Department of Physics, Bilkent University, Ankara, Turkey, Bilkent 06800

The quantum regime of nano-electromechanical systems (NEMS) allows one to scrutinize the subtle interaction between few-level open fermionic systems and quantized vibrational modes described by the so called “vibrons” [1]. Such hybrid systems are nowadays carefully designed [2] in order to achieve a precise control of the electron-vibron coupling. In a recent work [3] we investigated the vibron-assisted transport in the quantum turnstile regime [4]. The transport setting is sketched in Fig. 1. Source (L) and drain (R) electronic reservoirs described by chemical potentials μ_L , μ_R are connected to a quantum wire (QW). The contact regions are modulated by two switching signals and the turnstile operation assumes periodic out-of-phase oscillations of $\chi_{L,R}$. A nearby nanoresonator (NR) is described as a quantum harmonic oscillator of frequency ω , d being its displacement from the equilibrium position. We set the two chemical potentials such that electrons tunnel only on the spin-degenerate lowest energy level of the quantum wire.

The crucial ingredients of this hybrid device are the electron-vibron interaction H_{el-vb} and the corresponding vibron “dressed” states $|\varphi_{\nu,s}\rangle$ (see [3] for more details) :

$$H_{el-vb} = \lambda_0 \hat{N}(a + a^\dagger), \quad |\varphi_{\nu,s}\rangle = \sum_N A_{s,N}^{(\nu)} |\nu, N\rangle := |\nu\rangle \otimes |s_\nu\rangle \quad (1)$$

where \hat{N} is the electronic charge operator and a, a^\dagger are the annihilation and creation operators associated with the vibrational mode. Note that the “dressed” states are products of purely electronic configurations $|\nu\rangle$ and a linear superposition $|s_\nu\rangle$ of usual Fock states $|N\rangle$ of the 1D quantum harmonic oscillator. A simple intuitive picture of the vibron-assisted transport emerges by introducing the energy differences $\Delta_{N,N+1}(s, s')$ associated with sequential tunneling processes leading to transitions between electronic configurations with N and $(N + 1)$ electrons and vibrational component s, s' (see the right panel in Fig. 1). We denote by δ the difference between the average number of vibrons for the vibrational states $|s_\nu\rangle$ and $|s_{\nu'}\rangle$. The horizontal lines mark the chemical potentials for which one obtains various turnstile regimes.

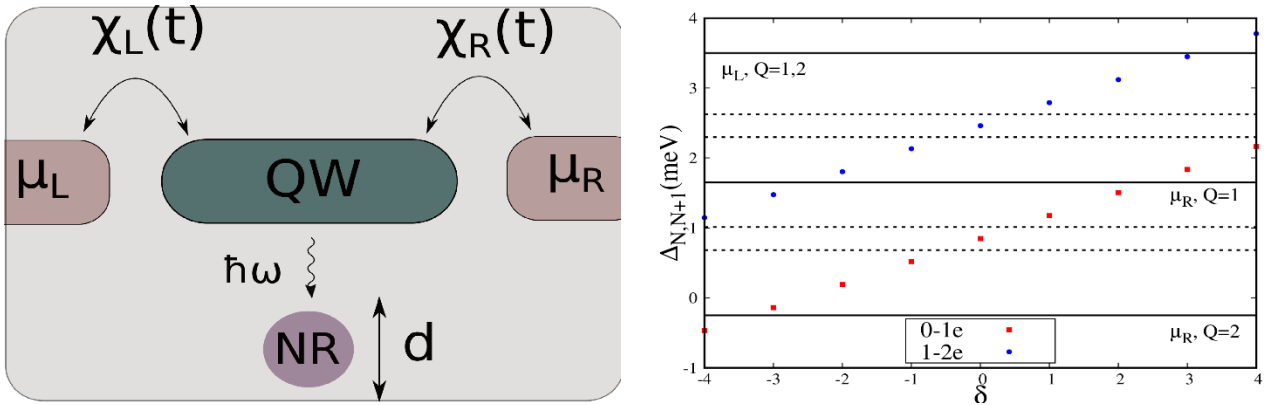


Fig. 1 (a) Sketch of a NEMS in the turnstile regime. (b) Energy gaps for vibron-assisted transitions (see the discussion in the text). The length and width of the nanowire are $L_x = 75$ nm and are $L_y = 75$ nm, $M = 2.5 \times 10^{-15}$ kg is the mass of the nanoresonator. The bias applied on the system is $eV = \mu_L - \mu_R$.

When writing down the various terms of the generalized master equation describing the open hybrid system one infers that tunneling from the left contact to the wire is allowed if the corresponding energy $\Delta_{N,N+1}(s, s') < \mu_L$. Similarly, electrons tunnel from the wire to the right contact if

$\Delta_{N,N+1}(s,s') > \mu_R$. For tunneling-in processes one has $\delta > 0$ if electrons have enough energy to tunnel *and* excite more vibrons. In contrast, for $\delta < 0$ the vibrations of the hybrid system are absorbed and allow tunneling of electrons with lower energies. The role of these transitions changes in the case of tunneling-out processes: the system is ‘heated’ for $\delta < 0$ and ‘cooled’ down if $\delta > 0$.

The transient currents in the two leads $J_{L,R}$, the charge occupation of the nanowire Q and the average vibron number N_V are calculated by solving the non-markovian master equation for the reduced density operator of the hybrid system. Also, we obtain the population of each vibron-dressed state such that each tunneling process can be discussed and analyzed in detail. The vibron energy is $\omega = 0.329$ meV which is in the range of the observed longitudinal stretching modes of carbon nanotubes. Also, $k_B T = 4.3$ μ eV and corresponds to a temperature of 50 mK.

The effects of the turnstile operations on the displacement d and average vibron number N_V are presented in Figs. 2a and 2b. For the two-particle, pumping the displacement of the single-mode nanoresonator is controlled by the signal χ_L applied on the left contact. More precisely, d increases quickly as the electrons enter the system, saturates once the charge occupation of the QW reaches the maximum value $Q = 2$ (not shown), and then drops to zero on the discharging half-periods. Note that the oscillations of the displacement match the period of the turnstile cycle $2t_p = 0.7$ ns. This behavior confirms that the electron-vibron coupling is indeed periodically switched on and off along a turnstile cycle. For $Q = 2$ turnstile operation the average vibron number reaches a 1st steady-state value on the first charging sequence but then drops to a lower yet nonvanishing value during the depletion cycle. (ii) By repeating the turnstile operation the same pattern is recovered as more vibrons are stored in the NEMS. We therefore conclude that along the depletion cycles the vibrons are stored in the system in spite of the fact that the electron-vibron coupling is ineffective since the electronic occupation vanishes (see Eq. 1).

In Fig. 3a we present the vibron dynamics for several values of the electron-vibron coupling strength λ_0 . This parameter can be tuned by changing either the equilibrium distance between the electronic system and the nanoresonator or the NR mass.

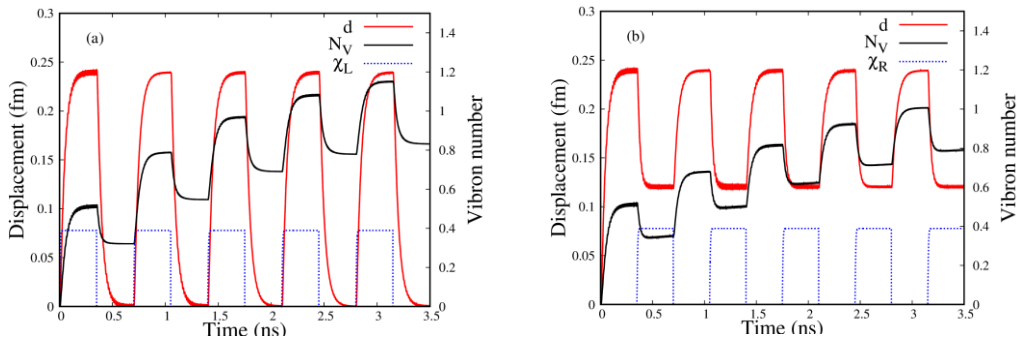


Fig. 2 The evolution of the vibron number N_V and of the displacement d in the : (a) two-particle turnstile $Q = 2$, for $\mu_L = 3.5$ meV, $\mu_R = -0.25$ meV and (b) single-particle turnstile $Q = 1$, for $\mu_L = 3.5$ meV, $\mu_R = 1.65$ meV. The dotted lines indicate the functions $\chi_{L,R}$ which simulate the periodic on and off switching of the two contacts.

The amplitude of the heating and cooling cycles decreases with λ_0 and the hybrid system approaches the quasistationary regime much faster at larger values of λ_0 . For example, a considerable difference is noticed between the first two cycles at strength $\lambda_0 = 0.162$ meV, the next cycles being rather similar. In Fig. 3b we collect the amplitudes associated to the first seven peaks of the transient current J_L and to the electron-vibron couplings considered in Fig. 3a. Let us stress that the peak evolution over few turnstile cycles can also be extracted from transport measurements and provides indirect insight on the vibron dynamics. In the weakly interacting case (i.e for $\lambda_0 = 0.028$ meV) the amplitudes of the peaks are nearly equal and one cannot discern the negligible effect of the electron-vibron coupling on the transport properties. In contrast, as λ_0 increases, the peaks display noticeable

differences. More precisely, their amplitude gradually decreases from one cycle to another until it reaches a quasi-stationary value (for strength $\lambda_0 = 0.096$ meV this value is roughly 5.5 nA). Note that the first peak of the charging current J_L is less sensitive with respect to changes of λ_0 because at such short times the vibrons are not yet activated. For the larger value strength $\lambda_0 = 0.162$ meV a steep reduction of the peak is noticed after two charging half-periods. A similar behavior is recovered for the output current J_R (not shown). By comparing Figs. 3a and 3b one infers that the attenuation of the peak amplitude is correlated to the emergence of the quasi-stationary regime for the heating/cooling sequences.

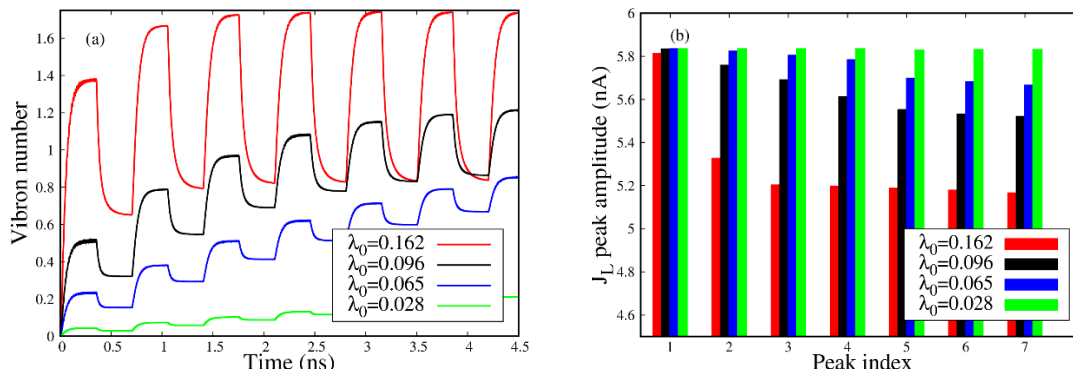


Fig. 3 The effect of the electron-vibron interaction λ_0 on the a) the average vibron number and b) on the peak amplitude of the current.

We also considered other shapes for the switching functions $\chi_{L,R}$ and we recovered similar effects of the turnstile regime on the nanoresonator, i.e., heating/cooling on the charging/ discharging half-periods. Although based on a rather simple model, our calculations provide the first theoretical study on the quantum turnstile regime for nano-electromechanical systems and predict sizable effects on the transient currents.

References

1. M. Poot and H. S. J. van der Zant, Phys. Rep. **511**, 273 (2012).
2. A. Benyamini, A. Hamo, S. V. Kusminskiy, F. von Oppen, and S. Ilani, Nat. Phys. **10**, 151 (2014).
3. R. Dragomir, V. Moldoveanu, S. Stanciu, B. Tanatar, Phys. Rev. **101**, 165409 (2020).
4. V. Moldoveanu, I. V. Dinu, B. Tanatar, C. P. Moca, New J. Phys. **17**, 083020 (2015).

New optical evidence concerning the cationic photopolymerization of the SU8 photoresist and its composites with carbon nanotubes

M. Baibarac,^a A. Radu,^a M. Cristea,^a R. Cercel^a, I. Smaranda^a

^a National Institute of Materials Physics, Optical Processes in Nanostructured Materials, Atomistilor 405A Street, Bucharest, Romania, R-077125

The effect of UV light on the cationic photopolymerization of SU8 negative photoresist was shown using PL studies. Carbon nanotubes-CNTs (i.e. single walled carbon nanotubes-SWNTs, double walled carbon nanotubes-DWNTs, multi walled carbon nanotubes-MWNTs and SWNTs functionalized with carboxyl groups- SWNTs-COOH) influence the effect of SU8 cationic photopolymerization. Under these conditions, the photopolymerization of SU8 was evidenced using photoluminescence (PL) studies as a complementary tool for Raman scattering and IR absorption spectroscopy [1].

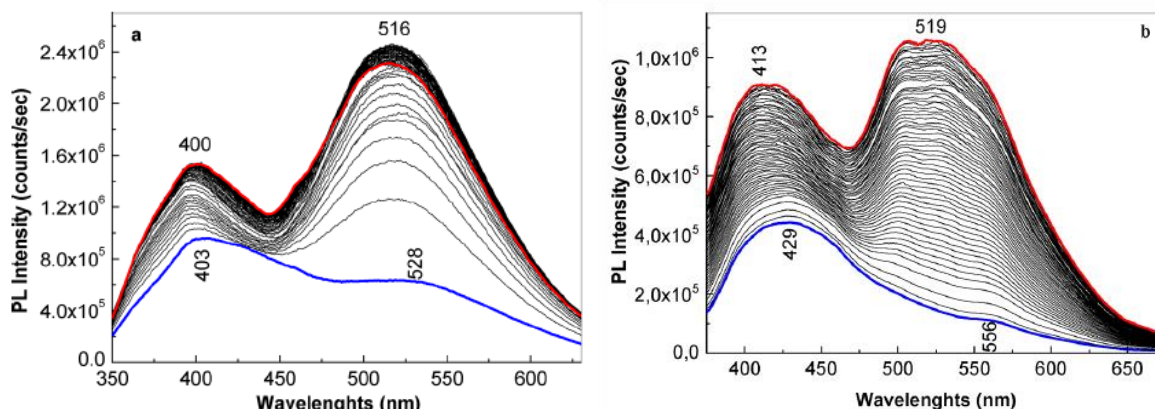


Fig. 1 The PL spectra of SU8 photoresist recorded at excitation wavelengths equal to 325 nm (a) and 350 nm (b). The blue and red curves correspond to the initial and final state of SU8 film, after the exposure to UVA light, time of 3h. The black curves correspond to the subsequent PL spectra of the first spectrum measured during the 3 h of exposure at the UVA light. [1]

According to Fig. 1, the PL spectra of the initial state of SU8 photoresist recorded at excitation wavelengths of 325 nm (Fig. 1a) and 350 nm (Fig. 1b) are characterized by two PL emission bands situated at approx. 403-429 nm and 528-556 nm, respectively. The UV irradiation for 3h led to the following modifications of the PL emission spectra: a) a down-shift of the PL band from 528-516 nm in the case of excitation wavelength equal to 325 nm similar to the case of the excitation wavelength of 350 nm, when a down-shift of PL emission bands from 429 and 556 nm to 413 and 519 nm, respectively occurs, b) the enhancement of the two PL bands situated at 400-403 nm and 528-518 nm with 37.64% and 72.58%, respectively when the used excitation wavelength was 325 nm. Similar behavior was observed in the case of the excitation wavelength of 350 nm, when an enhancement of PL bands situated at 429-413 nm and 556-519 nm of 51.34% and 86.9%, respectively, was observed. The increase of the PL emission bands presented above was explained based on the cationic photopolymerization reaction of the SU8.

The addition of 2 wt. % carbon nanotubes in SU8 photoresist matrix (15 wt. % solution concentration) led to important variations in PL spectra. Regardless of the CNTs type, i.e. SWNTs, DWNTs, or MWNTs, the presence of carbon nanotubes induced before the UV light exposure the decrease of relative intensities of PL band situated at approx. 400 nm. After UV light exposure of SU8/CNTs samples, the ratio between relative intensities of the two characteristic PL bands, i.e. $I_{413-399}/I_{506-520}$ ratio was equal to 1.736, 1.471, and 1.532, respectively. [1]

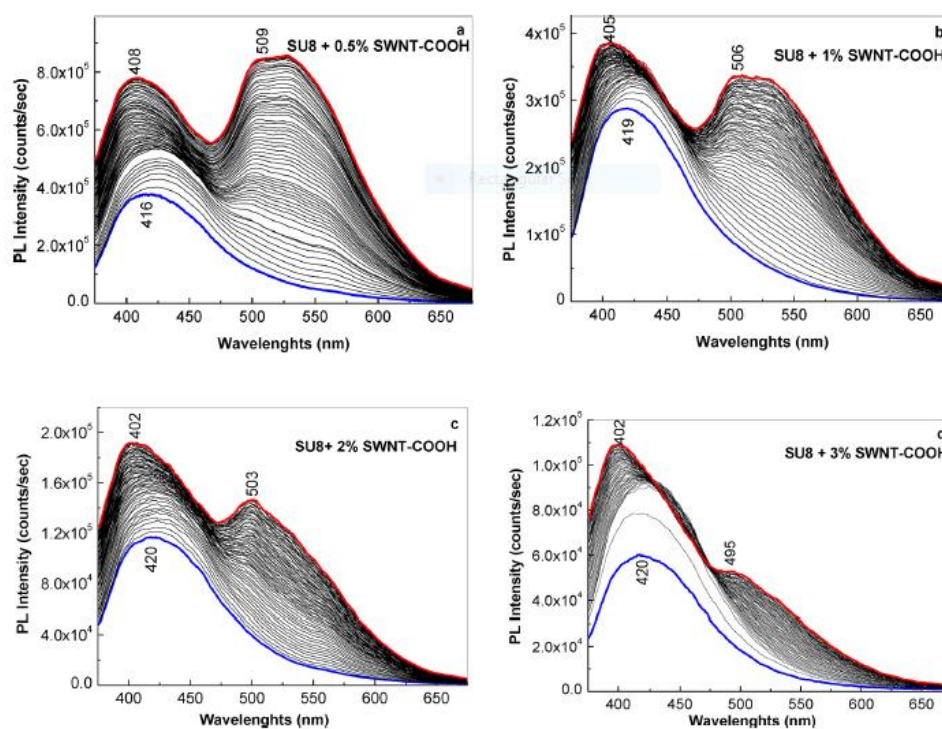


Fig. 2. The PL spectra of SU8/SWNTs-COOH composites with different SWNTs-COOH equal to 0.5 wt.% (a), 1 wt. % (b), 2 wt. % (c), and 3 wt. % (d). PL spectra were recorded at the excitation wavelength of 350 nm. The blue and red curves correspond to the initial and final state of the films' exposure to the UVA light, time of 3 h. The black curves correspond to the subsequent PL spectra of the first spectrum measured during the 3 h of exposure of the UVA light, each collected at 2 min. [1]

Fig. 2 illustrates the PL spectra of SU8/SWNTs-COOH with SU8 photoresist concentration of 30 wt. % and different SWNTs-COOH concentrations (0.5, 1, 2, and 3 wt. %) recorded at the excitation wavelength of 350 nm. Before UVA light exposure, the presence of SWNTs-COOH in the SU8 photoresist matrix induces a gradual decrease of the PL intensity of the SU8 band situated at approx. 400-413 nm (Fig. 1b). After UV light exposure for 3 h of SU8/SWNTs-COOH composites, the PL intensity of the emission band situated in the spectral domain 370-450 nm is higher than its counterpart from the PL spectra obtained before the UV light exposer, simultaneously with a gradual increase of the intensity of the PL band situated in the spectral range 500-650 nm. The variations from PL spectra of SU8/SWNTs-COOH composites indicated the presence of a mechanism of SU8 photoresist cationic polymerization. This mechanism was also demonstrated via Raman and IR studies. According to Raman studies, the increase of SWNTs-COOH concentration in SU8 photoresist matrix leads to: a) the presence of the Raman line situated at 167 cm^{-1} assigned to the radial breathing mode (RBM) of SWNTs-COOH [2]; b) a gradual down-shift of the Raman line from 1608 cm^{-1} to 1600 cm^{-1} and 1592 cm^{-1} , when SWNTs-COOH concentration was 0, 1 and 3 wt. % and c) the gradual decrease of the Raman lines relative intensity of the SU8 photoresist situated in the spectral ranges $600\text{-}1500$ and $2750\text{-}3100\text{ cm}^{-1}$. These results explained the chemical interactions between SWNTs-COOH and SU8 photoresist. A confirmation of these chemical interactions was proven using IR spectroscopy, results illustrated in Fig. 3. By the exposure to the UVA light of the three samples of SU8/SWNTs-COOH, one observes the following: i) a decrease in absorbance of the IR band peaked at 912 cm^{-1} ; ii) a down-shift of the IR bands from 831 and 1126 cm^{-1} (Fig. 3a) to 827 and 1111 cm^{-1} (Fig. 3b); iii) the IR band at 1772 cm^{-1} with the maximum shifted to 1732 and 1769 cm^{-1} , when the SWNTs-COOH concentration was increased. The increase in the absorbance of the IR band peaked at 1769 cm^{-1} indicates the presence of the functional groups of the ester type in the SU8/SWNTs-COOH composite molecular structure. The formation of the functional groups of the ester type takes place both in the photoinitiation stage in the TSHAS presence and in the termination stage of the growth of the macromolecular chain of SU8 due to the presence on the

SWNTs surface of the carboxylic groups. According to the reaction mechanism of the cationic photopolymerization process of the SU8 photoresist, proposed by Lima et al.,[3] the three stages are described by i) an initiation reaction, ii) a propagation reaction, and iii) a termination reaction. [1]

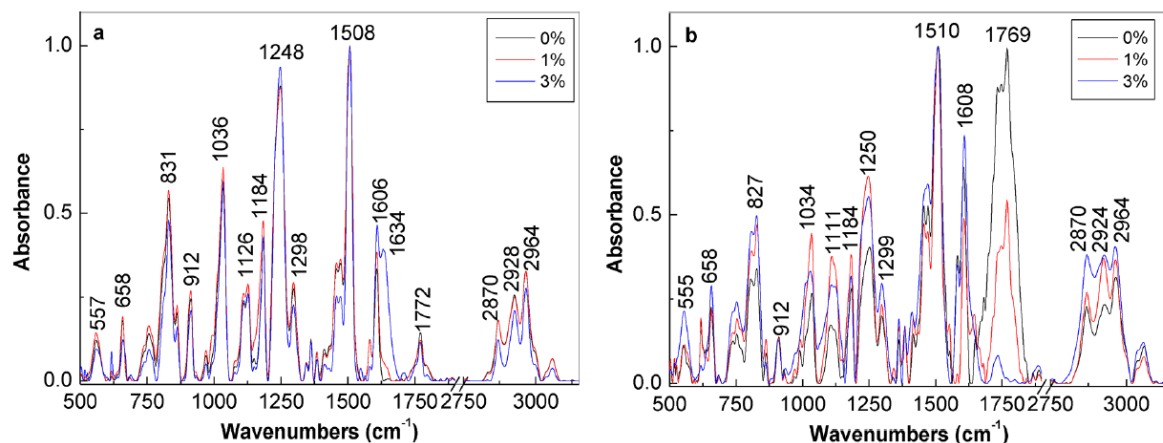


Fig. 3 IR spectra of the SU8 photoresist in the absence (black curve) and the presence of SWNTs-COOH, with the carbon nanotube concentration being equal to 1 wt. % (red curve) and 3 wt. % (blue curve). Figs. a and b correspond to the initial state and the state after exposure to UVA light for 3 h. [1]

PL anisotropy studies indicated that the alignment of the excitation and emission transition dipoles is nearly parallel to the wall of the CNTs. The angle between the SU8 photoresist adsorption and emission dipoles (θ_{PL}) was equal to 19° . The diminution of the θ_{PL} value in the case of SU8/CNTs composites was correlated with the molecular structure of the composite based on the SU8 photoresist and SWNTs-COOH. The covalent bonding of the macromolecular chains of SU8 onto the SWNTs-COOH surface via carboxylic groups induces the formation of new π - π stacking bonds between the phenyl rings of the SU8 photoresist and those of SWNTs-COOH. [1]

References

1. M. Baibarac et al., *UV Light Effect on Cationic Photopolymerization of the SU8 Photoresist and Its Composites with Carbon Nanotubes: New Evidence Shown by Photoluminescence Studies*, J. Phys. Chem. C. **124**, 7467-7476 (2020) [[doi:10.1021/acs.jpcc.9b11925](https://doi.org/10.1021/acs.jpcc.9b11925)]
2. M. Majidian et al., *SU8-Graphene: A New Photo-Patternable Conductive Polymer Composite*, Advanced Manufacturing Electronics and Microsystems: TechConnect Briefs, 79-82 (2016)
3. R. S. Lima et al., *Sacrificial Adhesive Bonding: a Powerful Method for Fabrication of Glass Microchips*, Sci. Rep. **5**, 13276 (2015) [[doi:10.1038/srep13276](https://doi.org/10.1038/srep13276)].

Optical properties of composites based on graphene sheets functionalized with macromolecular compounds

M. Baibarac,^a M. Stroe,^a M. Cristea,^a M. Daescu,^a M. Socol,^a E. Matei,^a A. Galatanu,^a L.C. Cotet,^{b,c} L.C. Pop,^b M. Baia,^{c,d} V. Danciu,^{b,c} I. Anghel,^e L. Baia,^{c,d} C. Bartha,^a C. Negrila,^a S.N. Fejer^f

^a National Institute of Materials Physics, Optical Processes in Nanostructured Materials, Atomistilor 405A Street, Bucharest, Romania, R-077125

^b Babes-Bolyai University, Faculty of Chemistry and Chemical Engineering, Department of Chemical Engineering, Arany Janos 11 Street, Cluj-Napoca, Romania, 400028

^c Babes-Bolyai University, Institute of Research-Development-Innovation in Applied Natural Sciences, Advanced Materials and Applied Technologies Laboratory, Fantanele 30 Street, Cluj-Napoca, Romania, 400294

^d Babes-Bolyai University, Faculty of Physics, M. Kogalniceanu 1 Street, Cluj-Napoca, Romania, 400048

^e "Alexandru Ioan Cuza" Police Academy, Fire Officers Faculty, Morarilor 3 Street, Bucharest, Romania, 022451

^f Pro-Vitam Ltd., Muncitorilor 16 Street, Sfantu Gheorghe, Romania, 520032

This study aims to illustrate the optical properties of composites based on graphene sheets functionalized with different macromolecular compounds such as: I) composites based on graphene oxide (GO) and polystyrene (PS) [1] and II) composites based on reduced graphene oxide (RGO) and 5-amino-1-naphthol (5A1N) [2].

I. Optical Properties of Composites Based on Graphene Oxide and Polystyrene (PS/GO)

The radical polymerization of styrene in the presence of benzoyl peroxide, pentane and GO induced the appearance of new ester groups in the PS macromolecular chains [1]. The adopted synthesis method for the expandable PS lead to spheres with diameters of between 300 nm and 3.5 μm (Fig. 1). Adding the GO sheets suspension in the mixture of the radical polymerization reaction of styrene induces the adsorption of the GO sheets onto the PS spheres' surface as shown in Figs. 1b-g. A wrapping of the PS spheres with the GO sheets is observed to occur in Figs. 1f, 1g. [1]

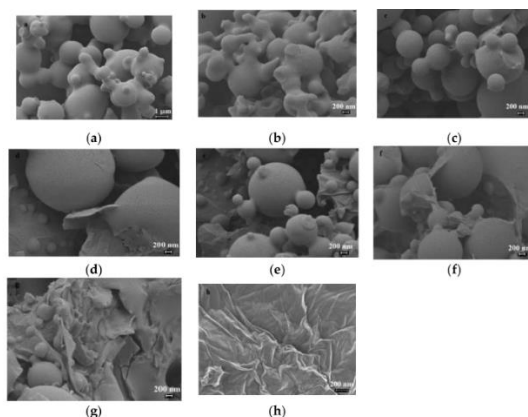


Fig. 1 Scanning electron microscopy pictures of the PS/GO composites with different GO concentrations: 0 wt.%. (a), 0.5 wt.% (b), 1 wt.% (c), 2 wt.% (d), 3 wt.% (e), 4 wt.% (f) and 5 wt.% (g). Fig. (h) shows the SEM picture of the GO sheets [1]

The vibrational properties of these compounds investigated by Raman scattering and IR spectroscopy confirmed that the morphological structures presented in Fig. 1 belong to the expandable PS and PS/GO composites. The main changes induced in the Raman spectra of PS by the GO presence are: i) the change of the value of the ratio between the intensities of the Raman lines peaked at 997 and 1598 cm^{-1} , from 3.22 to 2.38, 2.16 and 0.77, when the concentration of the GO sheets in the PS matrix increased from 0 to 1, 2 and 3 wt. %, respectively; ii) an up-shift of the D band from 1324 cm^{-1} to 1333, 1344, 1346, and 1351 cm^{-1} , when the GO sheets concentration varied from 1 wt.% to 2, 3, 4, and 5 wt.%, respectively. [1] These changes were accompanied by a gradual increase in the intensity of the Raman line at 1579 cm^{-1} vs. the Raman line at 1595 cm^{-1} ; iii) the

diminution of the ratio between the intensities of the Raman lines at 997 and 3050 cm^{-1} from 2.00 to 0.77 when the GO sheets concentration in the PS matrix was 0 and 5 wt. %, respectively. These changes indicated that as the GO sheets concentration is increasing, the generation of the PS oligomers takes place. IR spectroscopy studies of PS/GO composites, reported in Ref. [1], illustrated that with the increase of GO sheets concentration in the PS matrix, one observes a gradual increase in the absorbance of the IR band at 1743 cm^{-1} . This fact indicated that the $\text{C}_6\text{H}_5\text{COO}$ -bonding onto the GO sheets' surface is induced. The covalent functionalization of the GO sheets with PS induced significant changes in the PLE and PL spectra of the polymer. The PLE and PL spectra of the expandable PS are characterized by bands with maxima at 328 and 397 nm, respectively. One can notice a gradual decrease in the intensity of the PLE and PL spectra of the expandable PS when the GO sheets concentration in the PS/GO composite was increased from 0 wt.% to 5 wt.%. This PS PL quenching process originates in the new luminescent centers generated during the radical polymerization of styrene when a covalent functionalization of the GO sheets with PS took place. As observed in Fig. 2, significant changes were induced to new luminescent centers in the presence of UVA light. In comparison with PS (Fig. 2a) or its composites with the GO sheets having a concentration of between 0.5 and 4%, in the case of the PS/GO sample with a concentration of 5 wt.% GO (Fig. 2b), under the excitation wavelength of 327 nm, one observes a decrease in the PL spectrum intensity as the exposure time at UVA light increases to 3 h. This behavior originates in the appearance of defects on the PS macromolecular chain by the generation of new chemical bonds such as $-\text{CH}=\text{C}-(\text{C}_6\text{H}_5)-$. [1]

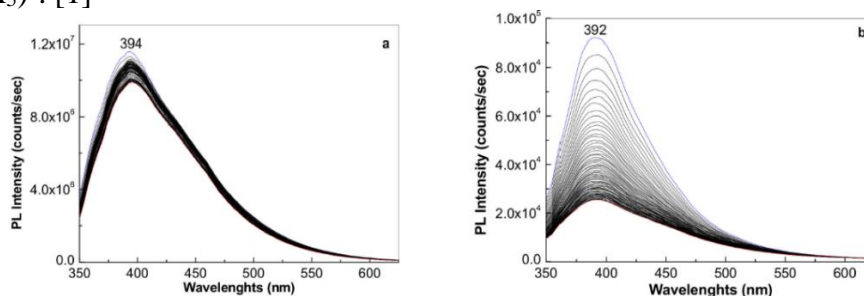


Fig. 2 PL spectra of PS (a) and the PS/GO composite with 5 wt. % GO sheets concentration (b) under UV light exposure for 3 h. The PL spectra of the two samples in the initial and final state correspond to the blue and red curves. Black curves correspond to intermediate PL spectra. [1]

II. Influence of RGO on the electropolymerization of 5A1N and the interaction of 1,4-phenylene diisothiocyanate (PDITC) with the P5A1N/RGO composites

The electrochemical polymerization of 5A1N in the presence of HClO_4 , $\text{H}_4\text{SiW}_{12}\text{O}_{40}$ and the RGO sheets by cyclic voltammetry led to new optical properties of P5A1N/RGO composites, revealed by Raman scattering and IR spectroscopy. Evidence for the generation of P5A1N onto the blank Au electrode and the Au electrode covered with the RGO sheets are shown by Raman scattering and IR spectroscopy (Figs. 3a, 3b, 3c). The Raman spectrum of P5A1N electrosynthesized onto the Au electrode covered with the RGO sheets highlights as the main difference in comparison to the P5A1N electrogenerated onto the blank Au electrode, a change in the value between the intensities of the Raman lines peaked at 1579 and 1620 cm^{-1} from 1.46 to 1.87. This fact can be explained as a consequence of the superposition of the P5A1N Raman lines with those of RGO in the spectral range 1550–1650 cm^{-1} [3,4]. Other vibrational changes in the case of P5A1N electrosynthesized onto the blank Au electrode and the Au electrode covered with the RGO sheets were reported by IR spectroscopy (Fig. 3b) highlights the main IR bands of the P5A1N synthesized in the presence of HClO_4 and $\text{H}_4\text{SiW}_{12}\text{O}_{40}$ on the Au electrode.

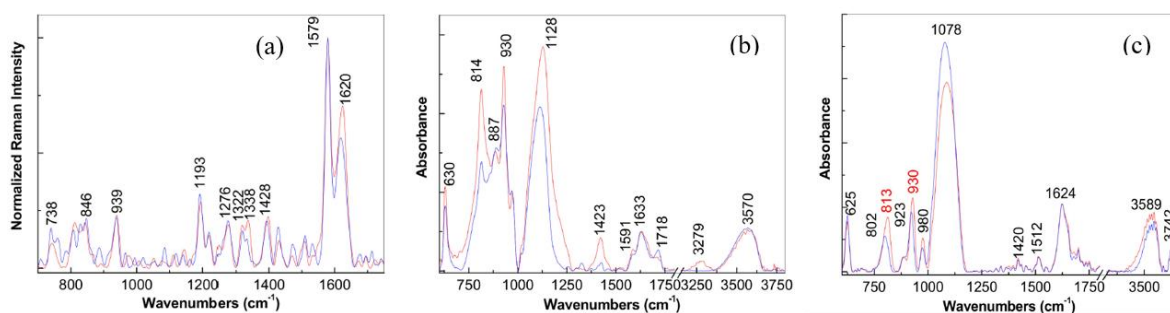


Fig. 3 (a) The Raman spectrum of P5A1N electro synthesized onto the blank Au electrode (blue curve) and the Au electrode covered with the RGO sheets (red curve); the IR spectra of P5A1N electrochemical synthesized onto the blank Au electrode (b) and the Au electrode covered with the RGO sheets (c) by recording 5 (blue curve) and 25 (red curve) cyclic voltammograms. [2]

The main differences in the case of the electro synthesis of P5A1N onto the Au electrode covered with the RGO sheets (Fig. 3c) in contrast with the Au electrode (Fig. 3b) are: i) a decrease in the absorbance of the IR bands situated in the spectral range $850\text{--}1000\text{ cm}^{-1}$ simultaneously with the appearance of the IR band with a maximum at 980 cm^{-1} which belongs to the vibrational mode W-O of the $\text{H}_4\text{SiW}_{12}\text{O}_{40}$ heteropolyanions; ii) a down-shift of the IR bands from 630 , 1128 and 1633 cm^{-1} to 625 , 1078 and 1624 cm^{-1} , accompanied by a change of the ratio between the absorbance of the IR bands at $813\text{--}930$ and $1000\text{--}1200\text{ cm}^{-1}$; and iii) an up-shift of the IR band from 3570 to 3589 cm^{-1} simultaneously with the appearance of a new IR band at 3742 cm^{-1} . The new IR band at 3742 cm^{-1} belongs to the stretching vibrational mode of the N-H bond in the R-NH-R functional groups [5]. The electrochemical polymerization reaction of 5A1N in the presence of HClO_4 and $\text{H}_4\text{SiW}_{12}\text{O}_{40}$ when as the working electrode is used an Au plate covered with the RGO layers leads to the RGO sheets covalently functionalized with P5A1N doped with the $\text{H}_4\text{SiW}_{12}\text{O}_{40}$ heteropolyanions. The interaction of 1,4-phenylene diisothiocyanate with the P5A1N/RGO composites was studied in Ref [2] using Raman scattering and IR spectroscopy. The adsorption of PDITC onto the RGO sheets covalently functionalized with P5A1N doped with the $\text{H}_4\text{SiW}_{12}\text{O}_{40}$ heteropolyanions involves a chemical reaction, which induces the appearance of the functional groups similar to the substituted thiourea.

References

1. M. Stroe et al., *Optical Properties of Composites Based on Graphene Oxide and Polystyrene*, *Molecules*, **25**(10), 2419 (2020) [[doi:10.3390/molecules25102419](https://doi.org/10.3390/molecules25102419)]
2. M. Baibarac et al., *Influence of Reduced Graphene Oxide on the Electropolymerization of 5-Amino-1-Naphthol and the Interaction of 1,4-Phenylene Diisothiocyanate with the Poly(5-Amino-1-naphthol)/Reduced Graphene Oxide Composite*, *Polymers*, **12**(6), 1299 (2020) [[doi:10.3390/polym12061299](https://doi.org/10.3390/polym12061299)]
3. I. Smaranda et al., *Electrochemical grafting of reduced graphene oxide with polydiphenylamine doped with heteropolyanions and its optical properties*, *J. Phys. Chem. C* **118**(44), 25704–25717 (2014) [[doi:10.1021/jp507324r](https://doi.org/10.1021/jp507324r)]
4. M. Baibarac et al. *Infrared dichroism studies and anisotropic photoluminescence properties of poly(para-phenylene vinylene) functionalized reduced graphene oxide*, *RSC Adv.*, **7**(12), 6931-6942 (2017) [[doi: 10.1039/C6RA26445J](https://doi.org/10.1039/C6RA26445J)]
5. R.M. Silverstein et al., “Spectrometric Identification of Organic Compounds”, 4th ed.; John Wiley and Sons: New York, NY, USA, 1981.

Photoluminescence studies concerning the photodegradation of drugs

M. Daescu^a, N. Toulbe^{a,b}, M. Baibarac^a, A. Mogos^c, A. Lőrinczi^a, C. Logofatu^d, A. Matea^a, C. Negrila^a, C. Serbschi^e, A.C. Ion^f

^a National Institute of Materials Physics, Optical Processes in Nanostructured Materials, Atomistilor 405A Street, Bucharest, Romania, R-077125

^b Interdisciplinary School of Doctoral Studies, University of Bucharest, M. Kogalniceanu Blvd. 36-46, Bucharest, Romania, 050107

^c S.C. Agilrom Scientific S.R.L. Grigore Cobalcescu 39 Street, Bucharest, Romania, 010193

^d National Institute of Materials Physics, Atomistilor 405A Street, Bucharest, Romania, R-077125

^e Bioelectronic SRL, Cercelus 54 Street, Ploiesti, Romania, 2000

^f Faculty of Applied Chemistry and Materials Science, University Politehnica of Bucharest, Gh. Polizu 1-7 Street, Bucharest, Romania, 011061

I. The Photodegradation of Melatonin (MEL) evidenced by the UV-VIS spectroscopy and photoluminescence (PL) studies

Fig. 1 shows the UV-VIS spectra of the aqueous solutions of: i) MEL 1 mg/3ml (MEL-1), ii) 2 ml MEL 0.7 mM interacted with 1ml NaOH 1.5 mM (MEL-2), and iii) 2 ml MEL 0.7 mM interacted with 1ml NaOH 3 mM (MEL-3), before and after the exposure to UV light for 5h. Before UV irradiation, the UV-VIS spectra of MEL alone interacted with NaOH and are characterized by two bands at 221 nm and 278 nm, respectively. Significant changes were observed when the three samples were exposed to UV light. In the case of the MEL-1 sample, as the exposure time to UV light increased to 5 h, one observes a shift in the absorption band from 278 nm to 269 nm, which occurs simultaneously with the emergence of a new band in the 300–350 nm spectral range, whose absorbance gradually increases. The isosbestic points at 308, 275, and 230 nm indicate the production of new chemical compounds in the MEL-1 solution. According to Figs. 1b, 1c, the MEL-2, and MEL-3 samples have a similar behavior as the exposure time to UV light increased to 5 h. This consists of the disappearance of the band at 278 nm, which occurs simultaneously with the appearance of the band localized in the 300–350 nm spectral range. In contrast to the MEL-1 spectral changes reported under exposure to UV light, a gradual up-shift of the band from 221 nm to 233 and 242 nm is highlighted in the case of the MEL-2 and MEL-3 samples, respectively, when the exposure time to UV light increases from 0 to 5 h. All these changes suggest the generation of new compounds in the MEL-2 and MEL-3 samples under UV light. [1]

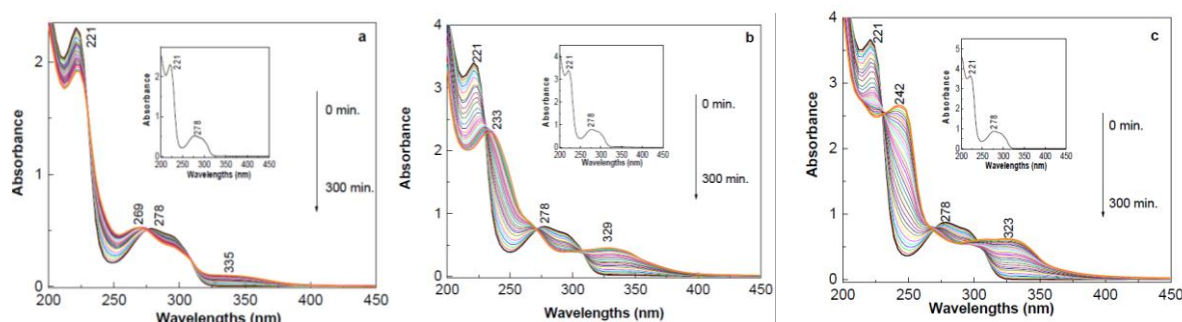


Fig. 1. UV-VIS spectra of the MEL-1 (a), MEL-2 (b), and MEL-3 (c) samples under exposure to ultraviolet (UV) light for up to 300 min. The UV-VIS spectra of the three samples before being exposed to UV light are shown in the inserts

The exposure to UV light for 131 min. induced in the PLE spectra of MEL samples, which have interacted to NaOH solutions of concentrations, equals to 0.06 M and 1.5 M (Figs. 2b, 2c), the following modifications: i) an increase of the PLE spectra intensity; ii) the broadening of the band localized in the 310-360 nm spectral range simultaneously with the increase in the band intensity at

323 nm; iii) as the UV light exposure time increases to 131 min, the appearance and a gradual increase of a new band peak at 252 nm was observed. [1]

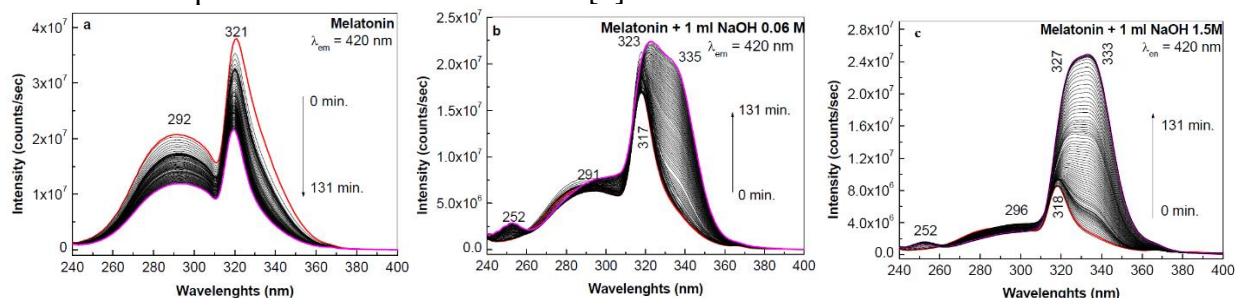


Fig. 2 The PLE spectra of MEL solution (a) and the mixtures of the MEL solution with the NaOH solutions with concentrations of 0.06 (b) and 1.5 M (c). The red curves indicate the PLE spectra of the samples before UV irradiation. The magenta curves show the PLE spectra of the samples after 131 min. of exposure to UV light [1]

According to Fig. 3, the PL spectra of MEL samples led to the following important features: i) in the presence of aqueous solutions of NaOH 0.06 and 1.5 M, the MEL emission band intensity peaked at 365 nm decreases; ii) the exposure to UV light for 131 min. of MEL samples induced a progressive decrease in the PL spectra intensity of MEL; iii) the increase of the half-width of the main emission band as a result of the intensity increase of a new emission band situated at 420 nm. The band peaked at 420 nm originates from the interaction between MEL and NaOH, when the formation of a larger amount of 5-methoxy tryptamine takes place. [1]

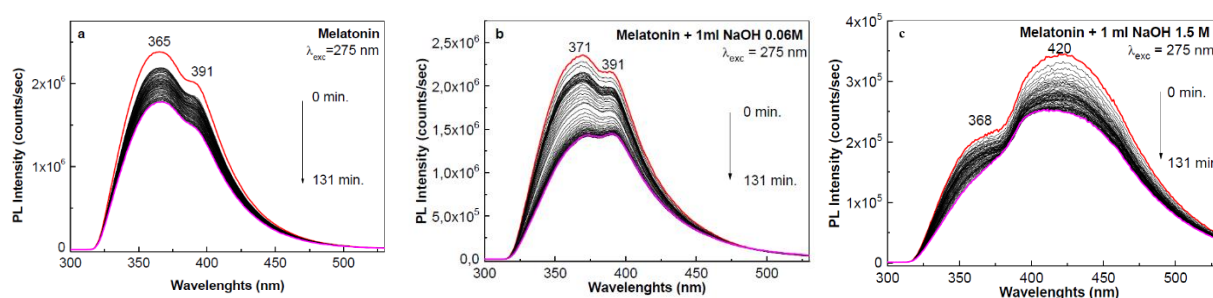


Fig. 3 PL spectra of the MEL solution (a) and the mixtures of the MEL with the NaOH solutions with concentrations of 0.06 (b) and 1.5 M (c). The red curves indicate the PLE spectra of the samples before UV irradiation. The magenta corresponds to the PL spectra of the samples after 131 min of exposure to UV light. [1]

II. The PL properties of acetaminophen and its photodegradation

The chemical interaction of acetaminophen (AC) with NaOH solutions induces a gradual enhancement of the PLE and PL spectra, when the time exposure of samples to UV light increases up to 140 min., because of the formation of p-aminophenol and sodium acetate. This behavior is not influenced by the excipients or other active compounds in pharmaceutical products. [2]

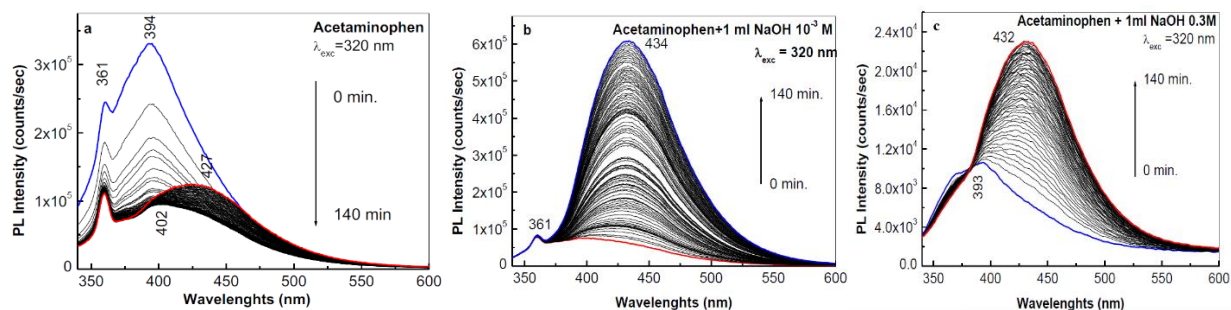
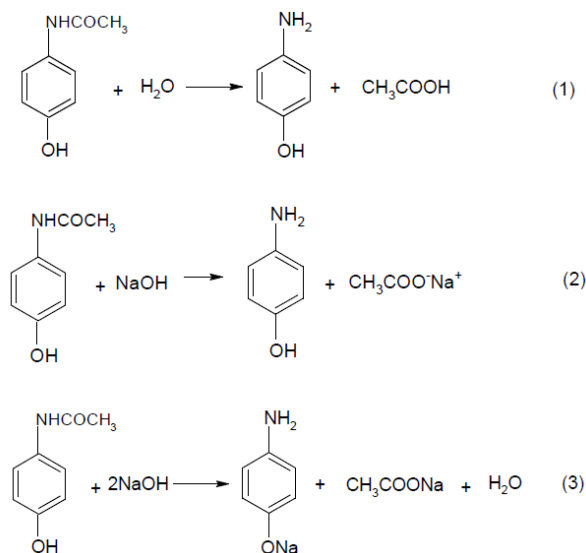


Fig. 4 The PLE spectra of the aqueous solution of AC 0.33 M before (a) and after the interaction with the aqueous solution of NaOH 10^{-3} (b) and 3×10^{-1} M (c). [2]

The PL spectrum of AC illustrates two emission bands peaked at 361 and 394 nm. The exposure of the AC aqueous solution to UV light, for 140 min., led to a shift of the maximum of emission band from 394 nm to 427 nm simultaneously with a decrease in the intensity of this band

(Fig. 4a). The interaction of the AC with NaOH solutions having concentrations 10^{-3} and 0.3 M induced a variation in the intensity of the PL spectrum because of the chemical interaction between AC and NaOH according to reaction (2) in Scheme 1. Scheme 1 illustrates that depending on the molar ratio between AC and NaOH (equations (2) and (3)), the reaction products correspond to sodium acetate and p-aminophenol or sodium p-aminophenoxide, respectively. Regardless of the concentration of the NaOH solution that interacted with the AC, after 140 min. exposure to UV light, it is noticed that the PL spectra shown in Figs. 4b, 4c have a maxima at 430–434 nm [2].



Scheme 1 The chemical reactions of AC with H₂O (equation (1)) and NaOH (equation (2)). The interaction of AC with an excess of NaOH is described by equation (3).

The generation of two compounds proposed in Scheme 1 was proved also using Raman scattering and IR spectroscopy. The main evidence shown in Raman spectra for the formation of p-aminophenol and sodium acetate consists of the presence of the line at 1608 cm^{-1} and the change of the ratio between the relative intensities of the Raman lines at 1649 and 2931 cm^{-1} in the favor of the last one. IR spectra indicated: i) a decrease of the amide group weight in AC as a consequence of the interaction with NaOH by the absence of the bands situated at 1329 , 1373 , and 3327 cm^{-1} ; ii) the decrease of the IR absorbance bands situated in the spectral ranges 1510 – 1700 and 3500 – 3600 cm^{-1} and iii) the presence of the IR band peaked at 1492 cm^{-1} attributed to the C=C stretching vibrational mode in aniline-derived compounds. The variation in the PLE and PL spectra of AC are found in the case of pharmaceutical compounds marked under the name of Paracetamol, Parasinus, and Pararerim. These PL studies indicated that the excipients do not influence the evolution of PLE and PL spectra under UV light exposure for 140 min. [2]

References

1. M. Daescu et al., *Photoluminescence as a Complementary Tool for UV-VIS Spectroscopy to Highlight the Photodegradation of Drugs: A Case Study on Melatonin*, *Molecules*, **25**(17), 3820 (2020) [[doi:10.3390/molecules25173820](https://doi.org/10.3390/molecules25173820)]
2. M. Daescu et al., *Photoluminescence as a Valuable Tool in the Optical Characterization of Acetaminophen and the Monitoring of Its Photodegradation Reactions*, *Molecules*, **25**(19), 4571 (2020) [[doi:10.3390/molecules25194571](https://doi.org/10.3390/molecules25194571)]

Electron Paramagnetic Resonance and Microstructural Insights into the Thermal Behavior of Simonkolleite Nanoplatelets

Arpad Mihai Rostas^a, Andrei Cristian Kuncser^a, Daniela Ghica^a, Alexandra Palici^a, Valentin Adrian Maraloiu^a and Ioana Dorina Vlaicu^a

^aNational Institute of Materials Physics, Bucharest-Magurele, Ilfov, 077125, ROMANIA

Introduction: Zinc oxide, ZnO, is one of the most studied materials of the last century mostly due to its plenty morpho-structural related properties which enable a wide range of applications in various fields ^[1-3]. There are numerous ways to control the morphology of zinc oxide particles, one of them is the thermal decomposition of the precursors used to obtain ZnO. Zinc hydroxide salts (ZHS) are promising precursors for zinc oxide particles with controlled size and morphology ^[4]. Among Layered Hydroxide Salts (LHS), zinc hydroxychloride (ZHC) and other Zn-LHS have been studied because of their interesting properties as catalyst support ^[5], drug carrier ^[6], UV and visible light absorption ^[7], filler for polymeric systems and super capacitors ^[8]. ZHS also proved to be excellent precursors for the preparation of ZnO with different morphological characteristics by calcination or pyrolysis treatments ^[9]. The thermal transformation of ZHC to ZnO is a controversial subject since the conversion mechanisms are not established. Several sequences of the thermal decomposition of ZHC to ZnO were observed and various mechanisms have been proposed but none of them is clearly representative. Even though most data do not agree on the same intermediate stages, the presence of ZnCl₂ and HCl as intermediate products is undoubtedly mentioned by most of the studies. Considering the importance of ZHC as a zinc oxide precursor, its thermal decomposition was investigated in order to understand and to control the final properties of zinc oxide for different applications. Following this idea, the thermal transformation process of ZHC towards ZnO was characterized at a structural level by Electron Paramagnetic Resonance (EPR) spectroscopy, X-Ray Diffraction (XRD) and Transmission and Scanning Electron Microscopy (TEM / SEM) techniques.

Results: ZHC characterization: The synthesis of ZHC (Zn₅(OH)₈Cl₂ H₂O) was carried out as presented above. The as-prepared material was first analyzed by powder XRD (Figure 1). The diffraction pattern showed a well crystallized Zn₅(OH)₈Cl₂ H₂O phase with rhombohedral structure, space group R-3m (JCPDS 77-2311). A barely detectable amount (about 1-2 %) of a minority phase with poor crystallinity was identified and indexed as ZnO (hexagonal structure, space group P63mc, JCPDS 89-1397). TEM (inset Figure 1) and SEM analysis (Figure 2) revealed very thin (approx 10 nm) small quasi-hexagonal platelets with mean diameter of about 300 nm nanoplatelets. EPR measurements (Figure 3 - RT) show a strong signal with a g-value of $g = 1.9596$, which we tentatively associate to the so-called shallow effective mass (EM) donor center, or briefly the shallow donor (SD) center ^[10].

Thermal treatment: ZHC was thermally treated for different periods of time at different temperatures. The sample was heated for 15 minutes at 150, 210, 240 and 300 °C respectively. have been recorded for each of the temperature steps.

The EPR signal at $g = 1:959$ increased significantly after the first heating cycle, reaching a maximum value at around 210 °C, followed by a certain decrease. A similar behavior of the SD signal was reported in the case of the thermal decomposition of Zn(OH)₂ towards ZnO ^[11]. At 240 °C a new but weak EPR signal with a g-value of 2.0033 was observed. The defects responsible for the new EPR signal, at a g-value of 2.0033, have been reported in the literature ^[12] and can be related to complex zinc defects in the ZnO nanocrystals.

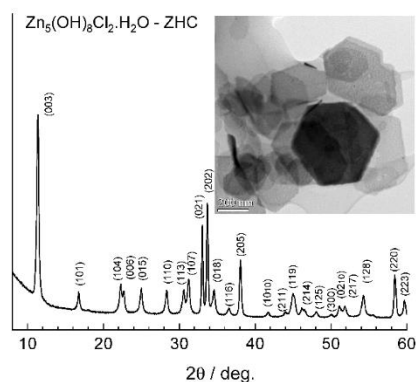


Fig. 1 Powder X-ray diffractogram and TEM image (inset) of the as prepared ZHC sample

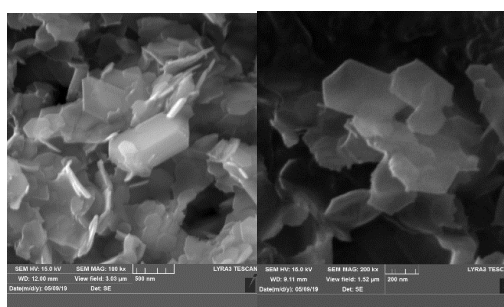


Fig. 2 SEM images of the as prepared sample at 100 kx (left) and 200 kx magnification (right)

Further, ZHC was annealed at 500 °C for different time periods and EPR measurements have been performed. The recorded EPR spectra show a fast increase of the signal associated to the complex Zn defects ($g = 2.0033$) and a decrease of the SD EPR signal ($g = 1.959$). The formation of well crystallized ZnO phase based on the partial decomposition of the ZHC phase can be concluded from the X-Ray diffraction diffractogram.

By a careful correlation with XRD spectroscopy, X-ray mapping and based on a priori knowledge on the chemical process in the studied system as already argued in the literature, the morphologies can be unambiguously associated to ZHC (Figure 3, zones A2 and A3) and ZnO phases (Figure 3, zone A1).

Thermal reaction kinetics: The EPR spectra were simulated and after separation of the two EPR signals with $g_{\text{Zn:ZnO}} = 2:0036$ and $g_{\text{SD}} = 1:959$, the second integral was calculated. The second integrals of the simulated EPR spectra were used to calculate, via spin counting the number of the paramagnetic species that were plotted as a function of the annealing time (Figure 4). In the first part of the kinetic $t < 200$ s the nanocrystals EPR signal starts growing, with a rate constant $k_1 = 0.54 \pm 0.11 \text{ min}^{-1}$. In this process the Zn related defects of the ZnO crystal structure multiply as the form of the particles increases. After an annealing time of 200 s the EPR signal decreases until it almost disappears with a rate constant $k_2 = 0.48 \pm 0.02 \text{ min}^{-1}$.

Conclusions: ZHC nanoplatelets were successfully synthesized by adopting a simple precipitation method. They were micro-structurally characterized by means of XRD, TEM and SEM showing a well crystallized phase with an average lateral plate size of 270 nm and the thickness of 10 nm. The thermal behavior of the ZHC nanoplatelets and their transformation into ZnO nanocrystals was concomitantly monitored by means of XRD, TEM, SEM and EPR. The experimental data were correlated and they are in agreement with the thermal analysis data reported in the literature. The monitoring of the evolution of the paramagnetic species versus the annealing processes show a direct relation between the size of the newly formed ZnO nanocrystals and the defects generated in the material, offering more information about the growth mechanism. To our knowledge, this is the first time that such a detailed study, on a nanometric scale, of the early stages of crystal growth has been carried out for the thermal transformation of the ZHC into zinc oxide.

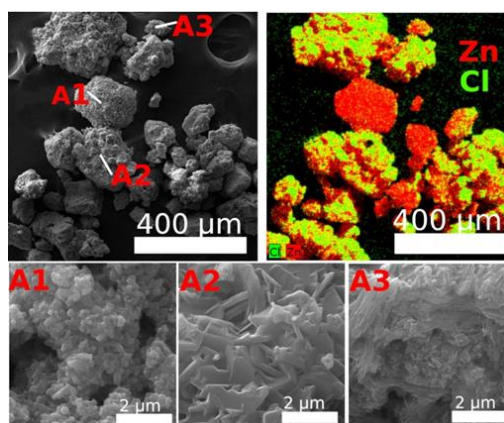


Fig. 3 EDX mapping of the ZHC sample annealed at 500 °C for 1 hour (A1-A3 zones correspond to the different morphologies observed in Figure 6)

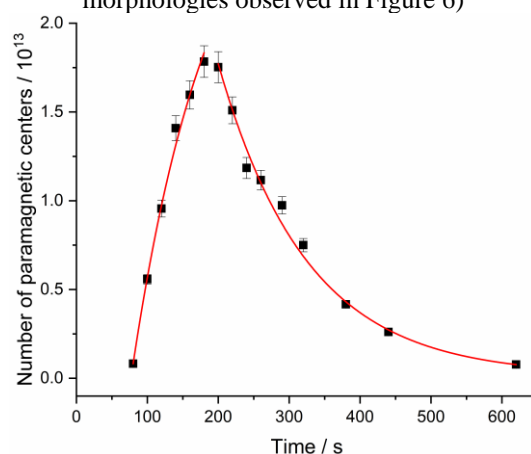


Fig. 4 Paramagnetic defects concentration vs. annealing time at 500 °C with $g_{\text{Zn:ZnO}} = 2.0036$

References

1. J. Wang, J. Yang, X. Li, B. Feng, B. Wei, D. Wang, H. Zhai and H. Song. *Effect of surfactant on the morphology of ZnO nanopowders and their application for photodegradation of rhodamine B*. Powder Technology, **286**:269–275, (2015).
2. S. Singh, K.C. Barick and D. Bahadur. *Inactivation of bacterial pathogens under magnetic hyperthermia using Fe₃O₄-ZnO nanocomposite*. Powder Technology, **269**:513–519, (2015).
3. T. Yang, S. Oliver, Y. Chen, C. Boyer and R. Chandrawati. *Tuning Crystallization and morphology of zinc oxide with polyvinylpyrrolidone: Formation mechanism and antimicrobial activity*. Journal of Colloid and Interface Science, **546**:43–52, (2019).
4. Y. Zhang, C. Liu, F. Gong, B. Jiu and F. Li. *Large scale synthesis of hexagonal simonkolleite nanosheets for ZnO gas sensors with enhanced performances*. Material Letters, **186**:7–11, (2017).
5. G. S. Machado, F. Wypych and S. Nakagaki. *Anionic iron(III) porphyrins immobilized on zinc hydroxide chloride as catalysts for heterogeneous oxidation reactions*. Applied Catalysis A: General, **413-414**:94–102, (2012).
6. R. Rojas and C. E. Giacomelli. *Effect of structure and bonding on the interfacial properties and the reactivity of layered double hydroxides and Zn hydroxide salts*. Colloids and Surfaces A: Physicochemical and Engineering Aspects, **419**:166–173, (2013).
7. A. C. T. Cursino, J. E. F. C. Gardolinski and F. Wypych. *Intercalation of anionic organic ultraviolet ray absorbers into layered zinc hydroxide nitrate*. Journal of Colloid and Interface Science, **347**(1):49–55, (2010).
8. S. Khamlich, A. Bello, M. Fabiane, B.D. Ngom and N. Manyala. *Hydrothermal synthesis of simonkolleite microplatelets on nickel foam-graphene for electrochemical supercapacitors*. Journal of Solid State Electrochemistry, **17**(11):2879–2886, (2013).
9. W. Zhang and K. Yanagisawa. *Hydrothermal synthesis of zinc hydroxide chloride sheets and their conversion to ZnO*. Chemistry of Materials, **19**:2329–2334, (2007)
10. W. E. Carlos, E. R. Glaser and D. C. Look. *Magnetic resonance studies of ZnO*. Physica B: Condensed Matter, **308**:976–979, (2001)
11. S.V. Nistor, D. Ghica, M. Stefan, I. Vlaicu, J. N. Barascu and C. Bartha. *Magnetic defects in crystalline Zn(OH)₂ and nanocrystalline ZnO resulting from its thermal decomposition*. Journal of Alloys and Compounds, **548**:222–227, (2013).
12. L. S. Vlasenko. *Magnetic resonance studies of intrinsic defects in ZnO: Oxygen vacancy*. Applied Magnetic Resonance, **39**(1-2):103–111, (2010).

On the atomic structure of the high-temperature precipitates in Ni-base superalloy VDM 780 Premium

Corneliu Ghica,^a Cecilia Solís,^b Johannes Munke,^b Andreas Stark,^c Bodo Gehrman,^d Martin Bergner,^e Joachim Rösler,^e Ralph Gilles^b

^aNational Institute of Materials Physics, 405A, Atomistilor Street, Magurele, Romania, 077125

^bTU München, Heinz Maier-Leibnitz Zentrum (MLZ), Lichtenbergstr. 1, Garching, Germany, 85748

^cHelmholtz-Zentrum Geesthacht, Institute of Materials Research, Geesthacht, Germany, 21502

^dVDM Metals International GmbH, Kleffstraße 23, Altena, Germany, 58762

^eTechnische Universität Braunschweig, Institut für Werkstoffe, Braunschweig, Germany, 38106

Among the Ni-base superalloys, Alloy 718 is the most widely used due to its excellent mechanical properties and processing characteristics as well as an increased resistance to degradation in corrosive or oxidizing environments, with a wide industrial applicability in manufacturing aircraft engines or gas turbines. However, Alloy 718 can only be used for applications up to 650 °C above which the alloy loses its strength and ductility due to the formation of δ -phase (Ni_3Nb based orthorhombic Pmmn structure) precipitates. A new superalloy has been developed, VDM 780 Premium, in an attempt to push the industrial applicability in a temperature range up to 750 °C [1]. VDM 780 Premium is based on the austenitic matrix (γ phase) strengthened by intermetallic Ni_3Al -like precipitates (γ' phase, fcc $L1_2$ structure). Other co-precipitates may be formed in function of the applied heat treatment, such as Ni_3Nb -based (δ phase, orthorhombic) or Ni_3Ti -based (η phase, hexagonal) precipitates, with a key role regarding the grain size evolution during processing as well as the mechanical properties at high temperature. The atomic structure of the high-temperature plate-like precipitates has been investigated in relation with the surrounding matrix lattice. Transmission electron microscopy (TEM) investigations using several techniques were performed on a Cs probe-corrected JEM ARM 200F microscope provided with a JEOL energy-dispersive X-ray spectroscopy (EDS) and a Gatan GIF Quantum SE EELS analytical units.

Fig. 1 shows the typical TEM image of an edge-on high-temperature precipitate at the border between several host lattice crystal grains in a sample of VDM 780 after a thermal treatment of up to 955 °C [2]. The diffraction pattern in Fig. 1c corresponds to the host lattice crystal grain in dark contrast surrounding the plate-shaped precipitate. The faint diffraction spots in the hhl positions, with h and l odd (red arrowhead in Fig. 1c) indicate a local modification of the structure factor caused by compositional variation. They appear consistently inside NbAl rich square-like precipitates evidenced by STEM-EDS mapping. Therefore, this diffraction pattern perfectly fits the $\mathbf{B}_{\gamma'} = [1-10]$ zone axis orientation of the γ' phase. The plate-shaped precipitate is structurally coherent with the host lattice, showing a well-defined crystallographic orientation with respect to it. The SAED pattern in Fig. 1d corresponds to a selected area including both the precipitate and the host lattice. The precipitate diffraction pattern can be indexed according to the orthorhombic structure of Ni_3Nb (δ phase) along the $\mathbf{B}_{\delta} = [100]$ zone axis (green arrowheads). The spots belonging to the adjacent lattice are indicated by red colored tilted arrowheads. The crystallographic relationship between the adjacent crystal grain and the analyzed plate-shaped precipitate is: $[100]\delta \parallel [1-10]\gamma'$, $(010)\delta \parallel (-1-11)\gamma'$. At a close inspection of the diffraction pattern in Fig. 1d, one can notice the presence of diffraction spots in fractional positions $\frac{1}{2}0kl$, with k odd (yellow arrowheads). As these spots cannot be explained by the orthorhombic δ phase, their origin has been explained by analyzing the corresponding HRTEM micrographs.

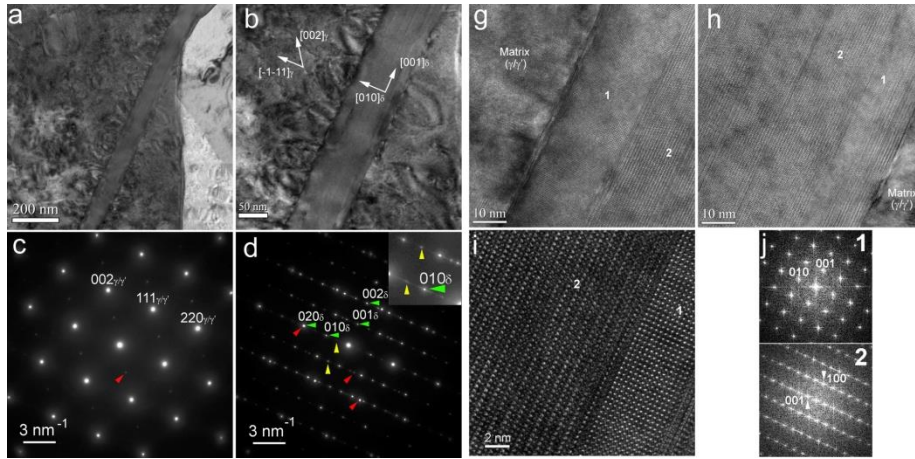


Fig. 1 (a) TEM image of an edge-on plate-shaped precipitate in sample VDM 780-b at the boundary between several host lattice crystal grains; (b) TEM image of the precipitate showing the presence of internal planar defects; (c) SAED pattern along $[1-10]$ the host lattice crystal grain in dark contrast surrounding the plate-shaped precipitate; (d) SAED pattern from a selected area enclosing the precipitate and the surrounding host lattice; red arrowheads indicate the γ' host lattice, yellow arrowheads point to η phase, green arrowheads indicate the δ phase; (g), (h) HRTEM image showing the band structure of the precipitate; (i) HRTEM image showing different atomic structures inside two adjacent bands; (j) FFT diagrams corresponding to the two adjacent bands 1 and 2.

Two different HRTEM patterns can be observed inside the precipitate, corresponding to the structural bands noted with 1 and 2 in Fig. 1g-i. The FFT patterns from areas selected inside the two structural bands are presented in Fig. 1j. The FFT pattern of area 1 was indexed according to the crystal structure of the orthorhombic δ phase. The FFT pattern of area 2 contains an additional set of spots located in the fractional positions $\frac{1}{2}0kl$ positions, k odd, when indexed according to the δ phase crystal structure. The explanation comes from the formation of a second crystalline phase corresponding to area 2 inside the plate-shaped precipitate, namely the hexagonal η phase specific to Ni_3Ti -based compositions. The FFT of area 2 in Fig. 1j was indexed according to the hexagonal structure of the η phase, resulting into the $\mathbf{B} = [010]\eta$ zone axis orientation of the η phase precipitate.

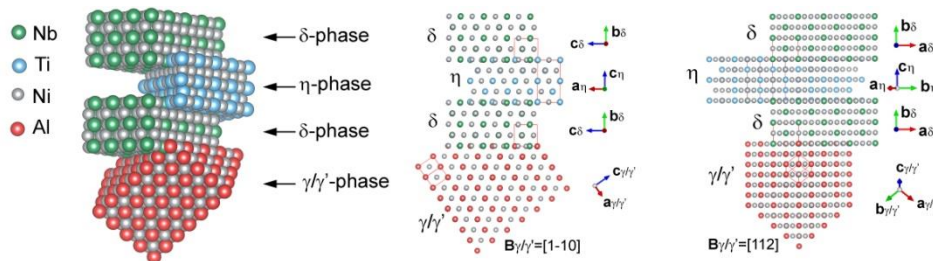


Fig. 2 Structural atomic model of the δ , η phases within the plate-like precipitate in relation with the $\{111\}$ plane of the γ'/γ phase according to the crystallographic relationship $[010]\eta \parallel [100]\delta \parallel [1-10]\gamma'$, $(001)\eta \parallel (010)\delta \parallel (-1-11)\gamma'$. 3D rendering and projections along the $[-110]$ and $[112]$ axes of the γ'/γ phase. VESTATM software has been used.

In **Fig. 2** we present a structural atomic model of the δ , η and γ' phases obeying the crystallographic orientation relationship deduced from the SAED and HRTEM analysis: $[010]\eta \parallel [100]\delta \parallel [1-10]\gamma'$, $(001)\eta \parallel (010)\delta \parallel (-1-11)\gamma'$ clearly illustrating the coherent crystallographic relationship between the δ/η plate-like precipitate and the $\{111\}\gamma'$ plane of the γ' phase. Geometrical Phase Analysis (GPA) was used to analyze the strain field around the δ - η interfaces within the plate-like precipitate (Fig. 3). The Bragg-filtered image in Fig. 3b shows the degree of lattice coherence across the interface, revealing the presence of dislocations at the interface with strain accumulation around the dislocations cores.

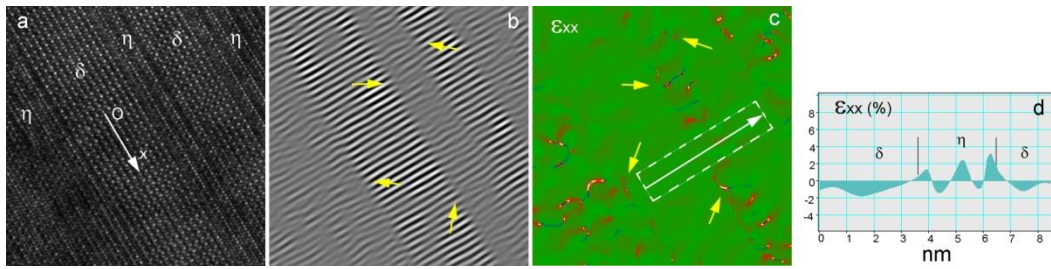


Fig. 3 Strain mapping within adjacent δ/η stripes using GPA: (a) HRTEM micrograph; (b) Fourier filtered image using the $(001)\delta/(100)\eta$ spots in the associated FFT diagram; (c) false color representation of the in-plane ϵ_{xx} strain map; (d) numerical plot of the ϵ_{xx} along the arrow indicated in (c).

The local elemental composition within and around the plate-shaped precipitate has been carried out in the STEM-EDS mode (Fig. 4). The bands exhibiting a brighter STEM-DF contrast correspond to the δ phase stripes identified by HRTEM. The brighter STEM-DF contrast is associated with the presence of a heavier chemical element (higher Z). On the elemental maps in Fig. 4 b-f, Ni shows a rather complementary distribution with respect to Co and Cr. The precipitate shows a relatively higher concentration of Nb, whereas its borders are slightly richer in Nb and Co, while poorer in Ni.

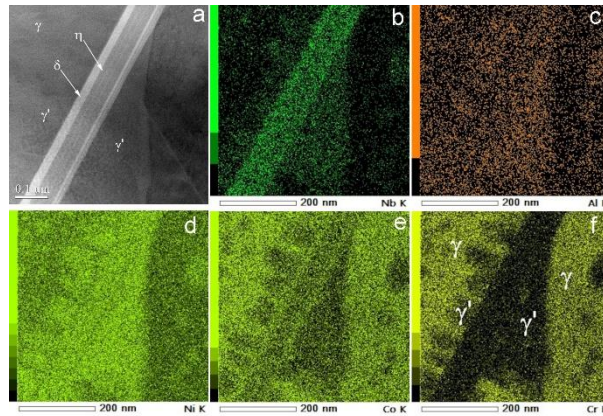


Fig. 4 (a) STEM-DF image of the plate-shaped precipitate in sample VDM 780-b showing Z-contrast variations associated to the band-like structural domains; (b)-(f) STEM-EDS elemental maps showing the relative spatial distribution of Nb, Al, Ni, Co and Cr.

References

1. T. Fedorova, J. Rösler, J. Klöwer, B. Gehrmann, *Development of a new 718-type Ni-Co superalloy family for high temperature application at 750 °C*, in MATEC Web Conf. **14**, 01003 (2014)
2. C. Ghica et al., *HRTEM analysis of the high-temperature phases of the newly developed high-temperature Ni-base superalloy VDM 780 Premium*, J. Alloys Compd. **814**, 152157 (2020)

Atomic resolution analytical TEM study of chemical ordering in BaLnCo₂O_{6-δ} double perovskites for electrochemical applications

Corneliu Ghica,^a Marian Cosmin Istrate,^a Sebastian Lech Wachowski,^b Iga Szpunar,^b Magnus Helgerud Sørby,^c Aleksandra Mielewczyk–Gryń,^b María Balaguer,^d Maria Gazda,^b Anette E. Gunnæs,^e José M Serra,^d Truls Norby,^f Ragnar Strandbakke^f

^aNational Institute of Materials Physics, 405A, Atomistilor Street, Magurele, Romania, 077125

^bGdańsk University of Technology, Faculty of Applied Physics and Mathematics, Gdańsk, Poland, 80-233

^cInstitute for Energy Technology, Department for Neutron Materials Characterization, Kjeller, Norway, NO-2027

^dUniversitat Politècnica de València, Instituto de Tecnología Química, Valencia, Spain, 46022

^eUniversity of Oslo, Department of Physics, Gaustadalléen 21, Oslo, Norway, NO-0349

^fUniversity of Oslo, Department of Chemistry, Gaustadalléen 21, Oslo, Norway, NO-0349

Double perovskites such as barium lanthanide cobaltite, BaLnCo₂O_{6-δ} (Ln = La, Pr, Nd, Sm, Gd, Tb or Dy) are intensively studied for applications as components in electrochemical and electrocatalytic devices. They may present several polymorphs out of which the cubic (SG Pm-3m) and A-site ordered tetragonal (SG P4/mmm) or orthorhombic (Pmmm) structures are the most frequent. The cubic symmetry involves the random distribution of Ba and Ln on the over the A-type crystallographic position according to the formula unit Ba_{0.5}Ln_{0.5}CoO₃, while the double perovskite structure consists in a layered structure caused by the Ba and Ln ion ordering on alternating A-type positions along the *c* axis, leading to a doubling of the corresponding cell parameter. This abstract illustrates the results obtained by transmission electron microscopy at atomic resolution throughout the CERIC application No 20187079 within an extended study involving Synchrotron Radiation Powder X-ray Diffraction (SR-PXD) and Neutron Powder Diffraction (NPD). The analytical TEM/STEM investigations have been performed on a Cs probe-corrected JEM ARM 200F instrument provided with EDS and EELS analytical units. The aim of the HRTEM study was to refine the atomic structure of the synthesized BaLnCo₂O_{6-δ} double perovskites and to reveal different structural ordering variants likely to occur such as Ba/Ln cation ordering or oxygen vacancy ordering.

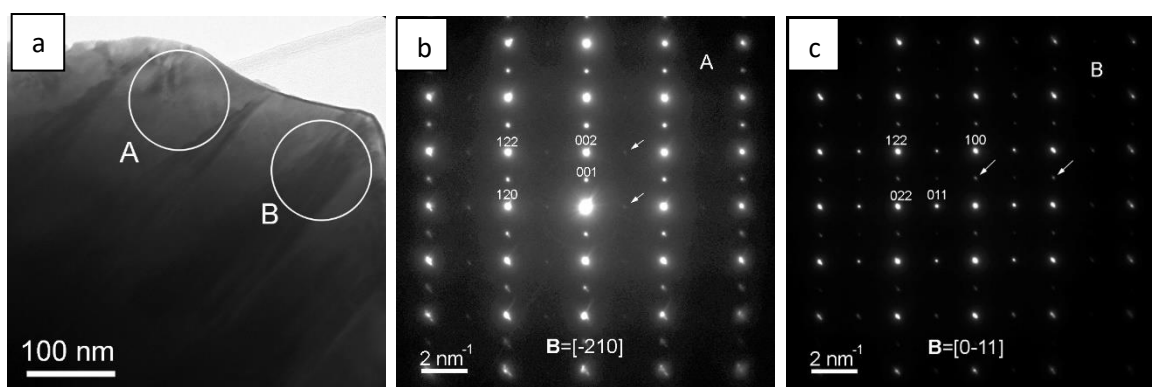


Fig. 1 (a) TEM image of a BaPrCo₂O_{6-δ} grain showing structural domains evidenced by alternating dark/bright diffraction contrast; (b) and (c) SAED patterns corresponding to the two contrast domains denoted A and B on the micrograph in (a).

The analyzed crystal grains from BaPrCo₂O_{6-δ} sample typically contain structural domains showing additional spots in halfway positions on the SAED patterns. The SAED patterns in Fig. 1 b and c, corresponding to the two contrast areas denoted with A and B on the micrograph in Fig. 1a, contain rows of diffraction spots of alternating strong/soft intensity, disposed vertically or horizontally. The two patterns can be indexed in agreement with the double-perovskite orthorhombic structure of BPCO (S. G. Pmmm) with *a*=0.386 nm, *b*=0.770 nm and *c*=0.750 nm lattice parameters. The presence of the soft *hkl* diffraction spots, *k* odd, in Fig. 1b indicates the doubling of the *b* lattice parameter with respect to the simple perovskite. Similarly, the presence of the soft *hkl* spots, with *k*

and l odds, in Fig. 1c indicates the doubling of the b and c lattice parameters. The two domains correspond to two different crystal orientations according to the $\mathbf{B}=[-210]$ and $\mathbf{B}=[0-11]$ zone axes, sharing the (122) family of planes. The crystallographic relation between the A and B domains is $[-210]_A \parallel [0-11]_B$, $(001)_A \parallel (100)_B$.

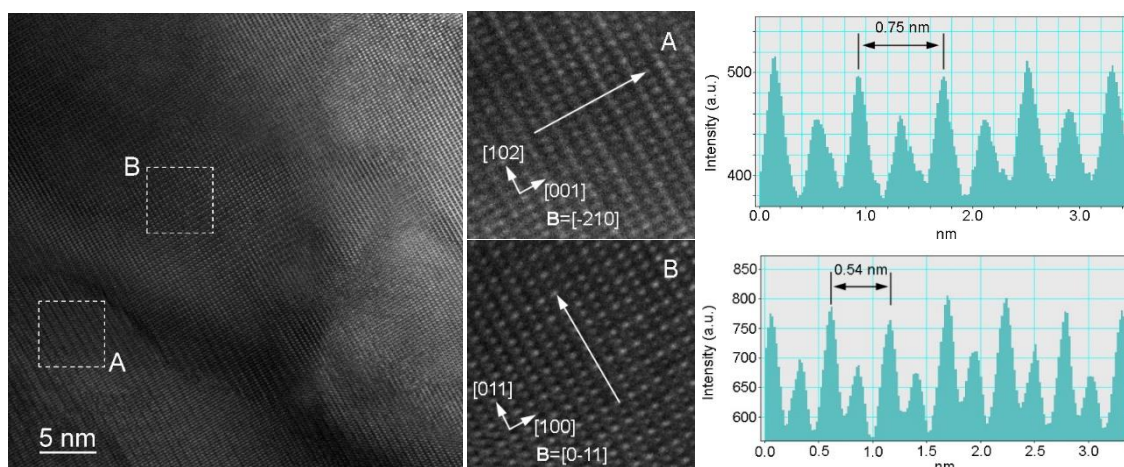


Fig. 2 HRTEM micrograph of two adjacent domains denoted A and B oriented along $\mathbf{B}=[-210]$ and $\mathbf{B}=[0-11]$ zone axes and associated line profiles along the indicated white arrows.

The HRTEM pattern of the two neighboring types of domains A and B shows intensity modulation along the [001] and [011] directions corresponding to a doubling of the interplanar distance to 0.75 nm and 0.54 nm, respectively (Fig. 2). The intensity modulation along [001] with a 0.75 nm period can be associated with the Ba/Pr cation ordering along the c -axis. However, cation ordering cannot explain the observed contrast variation along [011]. In order to correctly understand the intensity modulation on the HRTEM micrographs and to associate it with the atomic structure, we have simulated the HRTEM patterns along the two zone axes, $\mathbf{B}=[-210]$ and $\mathbf{B}=[0-11]$, using the Crystal Kit and Mac Tempas software kits for structure generation and HRTEM image simulation (Fig. 3). For the $\mathbf{B}=[-210]$ orientation, overlapping the structural model and the simulated image demonstrates that the intensity modulation associated to the lattice parameter doubling along [001] corresponds indeed to the Ba/Pr cationic ordering. Similarly, for the $\mathbf{B}=[0-11]$ orientation, overlapping the structural model and the simulated image demonstrates that the observed intensity modulation indicating the doubling of the lattice parameter along [011] is associated to the oxygen positions, pointing to a process of oxygen vacancies ordering.

With the aim of further proving the cation ordering, we have analyzed the samples in the STEM mode using the bottom-mounted Gatan Quantum EEL Spectrometer. The elemental mapping has been obtained using the spectrum imaging (SI) mode in which an EEL spectrum has been acquired in each pixel inside an area delimited by a green rectangle on the atomic resolution HAADF-STEM image. A typical example is presented in Fig. 4 for the $\text{BaLaCo}_2\text{O}_{6-\delta}$ sample.

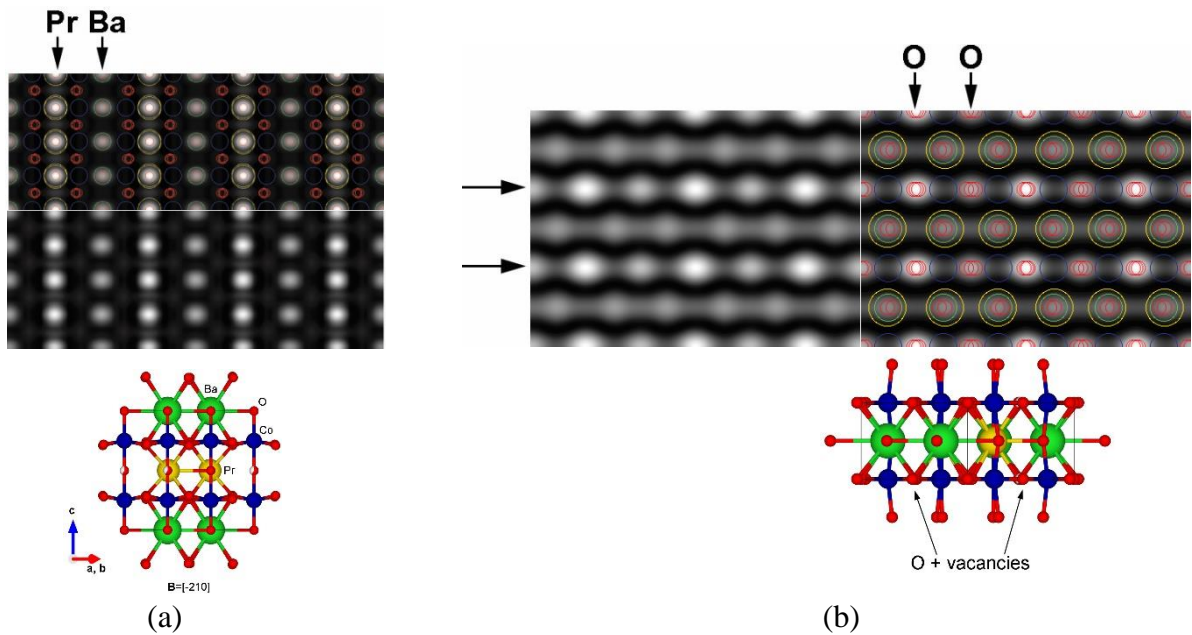


Fig. 3. (a) Simulated HRTEM pattern obtained for $t=40$ nm and $\Delta f=-10$ nm; the corresponding structural model is overlapped on the simulated pattern and displayed underneath (rotated 90°); (b) simulated HRTEM pattern obtained for $t=50$ nm and $\Delta f=-20$ nm; the corresponding structural model is overlapped and displayed underneath, pointing the oxygen vacancy ordering on alternating $\{011\}$ planes.

The atomic resolution elemental mapping of the identified atomic species clearly shows the interleaving Ba and La atomic planes due to Ba/La ordering, with the formation of the double perovskite cell with a lattice parameter $c=0.77$ nm, twice as long with respect to the perovskite structure. The rows and columns of Co are placed between the Ba and La rows.

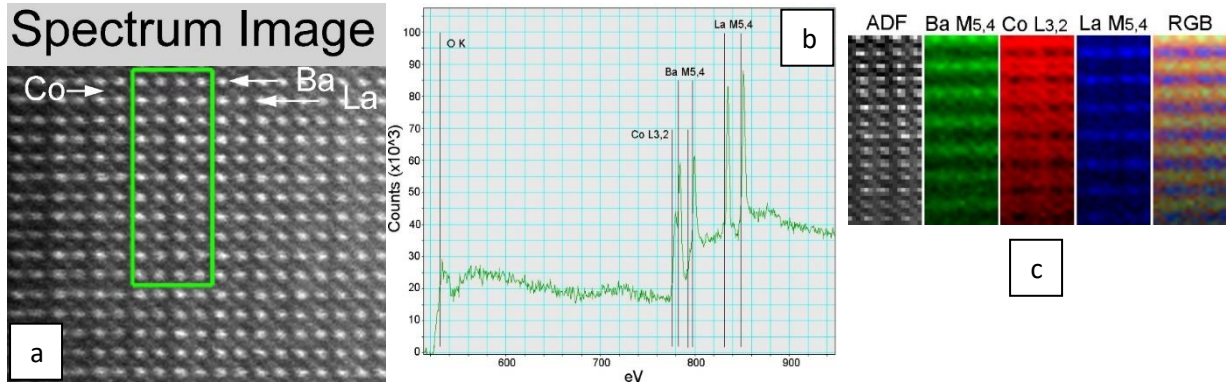


Fig. 4. (a) STEM-HAADF image of the atomic structure of the $BaLaCo_2O_{6-\delta}$ sample; (b) EEL spectrum extracted from the spectrum image showing the absorption edges of the identified elements; (c) atomic resolution elemental map obtained by EELS spectrum imaging inside the green rectangle.

References

1. S. L. Wachowski, I. Szpunar, M. H. Sørby, A. Mielewczyk-Gryn, M. Balaguer, C. Ghica, M. C. Istrate, M. Gazda, A. E. Gunnæs, J. M Serra, T. Norby, R. Strandbakke, *Structure and water uptake in $BaLnCo_2O_{6-\delta}$ ($Ln=La, Pr, Nd, Sm, Gd, Tb$ and Dy)*, *Acta Materialia* **199**, 297-310 (2020)

EPR insight into the magnetic interactions driving anisotropic growth of Si-doped hematite nanocrystals

Mariana Stefan,^a Daniela Ghica,^a Mattia Allieta,^b Klára Beranová,^{c,d} Marcello Marelli,^e Mauro Coduri,^{f,g} Giorgio Morello,^h Francesco Malara,^e Alberto Naldoniⁱ

^aNational Institute of Materials Physics, 077125 Magurele, Romania

^bUniversità degli Studi di Milano, Dipartimento di Chimica, 20131 Milano, Italy

^cFZU – Institute of Physics of the Czech Academy of Sciences, 18221, Prague, Czech Republic

^dElettra-Sincrotrone Trieste SCpA, 34149 Trieste, Italy

^eCNR-SCITEC Istituto di Scienze e Tecnologie Chimiche “G. Natta”, 20138 Milano, Italy

^fESRF- The European Synchrotron, 38000 Grenoble, France

^gUniversity of Pavia, Department of Chemistry, 27100 Pavia, Italy

^hInorganic Chemistry Laboratory, Department of Chemistry, University of Oxford, Oxford OX13QR, UK

ⁱRegional Centre of Advanced Technologies and Materials, Faculty of Science, Palacký University Olomouc, 771 46 Olomouc, Czech Republic

Hematite (α -Fe₂O₃) is a promising and Earth abundant material for solar fuel production, and Si-doping has been employed as a general strategy to improve its performance. However, an atomistic description that reconciles the modifications that Si-doping induces on the morphology, crystalline lattice, and electronic and magnetic properties of α -Fe₂O₃ has remained elusive.

This work is focused on the role of electron small polarons in driving the morphological transition from nearly rounded-shaped to nanowire nanocrystals in Si-doped α -Fe₂O₃ [1]. Electron small polaron formation is evidenced by the formation of Fe²⁺ and the increase of FeO₆ distortion at increasing Si content. Local analysis via pair distribution function (PDF) highlights an unreported crossover from small to large polarons, which affects the correlation length of the polaronic distortion from short to average scales. Ferromagnetic double exchange interactions between Fe²⁺/Fe³⁺ species are found to be the driving force of the crossover, constraining the chaining of chemical bonds along the [110] crystallographic direction. This promotes the increase in the reticular density of Fe atoms along the hematite basal plane only, which boosts the anisotropic growth of nanocrystals with more extended [110] facets. These results show that magnetic and electronic interactions drive preferential crystallographic growth in Si-doped α -Fe₂O₃, thus providing new insights for the nanoscale structural design of efficient solar fuel devices.

Recently, the role of morphology has been well evidenced in the performance of doped hematite (α -Fe₂O₃), which has triggered a great interest as a prototypical photoanode material for photoelectrochemical (PEC) water splitting [2-4]. In particular, the application of PEC water splitting on a large scale requires cheap, abundant, stable, and nontoxic materials. α -Fe₂O₃ fulfils all these requirements, but the low electrical conductivity, the short hole diffusion length, and the fast electron-hole recombination limit its PEC performance. *n*-type doping with aliovalent elements such as Si enhances the conductivity by orders of magnitude, while nanostructuring improves light-trapping and charge collection by modulating the nanoparticles (NPs) to a size comparable to that of hole diffusion. The accepted conduction mechanism in α -Fe₂O₃ involves the formation of the electron small polarons, which are induced by Fe²⁺ species that localize the carriers to specific lattice sites until the thermal energy can activate the electron hopping through Fe²⁺/Fe³⁺ couples. Because of the spin coupling pattern imposed by antiferromagnetism (AFM) parallel to the crystal *c*-axis, the additional electron can only be transferred to the Fe sites within the same basal layer giving rise to an anisotropic conductivity, which has been reported to be four times greater along the [001] direction. Hence, the conductivity of doped α -Fe₂O₃ is strongly influenced by the morphology and NPs preferentially grown along the [110] crystallographic direction has indeed shown an improved PEC activity. The mechanism of doping inducing morphological transitions has been recently discussed for Cu- and Al-doped α -Fe₂O₃.

In this work [1], the effect of Si doping on the long range and local order structure of α -Fe₂O₃ NPs with doping levels in the 0.22 – 50% range was explored using synchrotron powder diffraction and X-ray total scattering method based on PDF. High-resolution transmission electron microscopy

was used to determine the morphology of the α -Fe₂O₃ NPs. The presence of Fe²⁺- related electronic states in the Si-doped α -Fe₂O₃ was detected by synchrotron photoemission spectroscopies.

The exchange spin-spin interactions were investigated by electron spin resonance (ESR) spectroscopy at NIMP in the frame of a CERIC-ERIC project [5]. A summary of the ESR results is given in the following.

The ESR measurements were performed in the X-band (9.8 GHz) at room temperature using a Bruker ELEXSYS-E580 spectrometer equipped with a calibrated X-band Super High QE (SHQE) cylindrical cavity resonator (ER4123SHQE) (<http://cetRESav.infim.ro/>). The derivative dP/dH of the microwave power P absorbed by the sample was recorded as a function of the static magnetic field H . The deconvolution and lineshape simulation of the spectra were performed with the EasySpin v. 5.1.3 program [6].

The ESR spectra of the α -Fe₂O₃ nanostructures change from a broad two-line pattern for the undoped hematite to a Lorentzian shaped line L1 in the Si-doped samples (Fig. 1a). The evolution of the L1 peak-to-peak linewidth ΔH_{pp} with the Si-content in the samples is displayed in Fig. 1b. The ESR spectrum of the hematite is attributed to Fe³⁺ ions situated either in the same layer (A) or in adjacent layers (A and B), interacting through superexchange (SE), leading to AFM coupling (Fig. 1c).

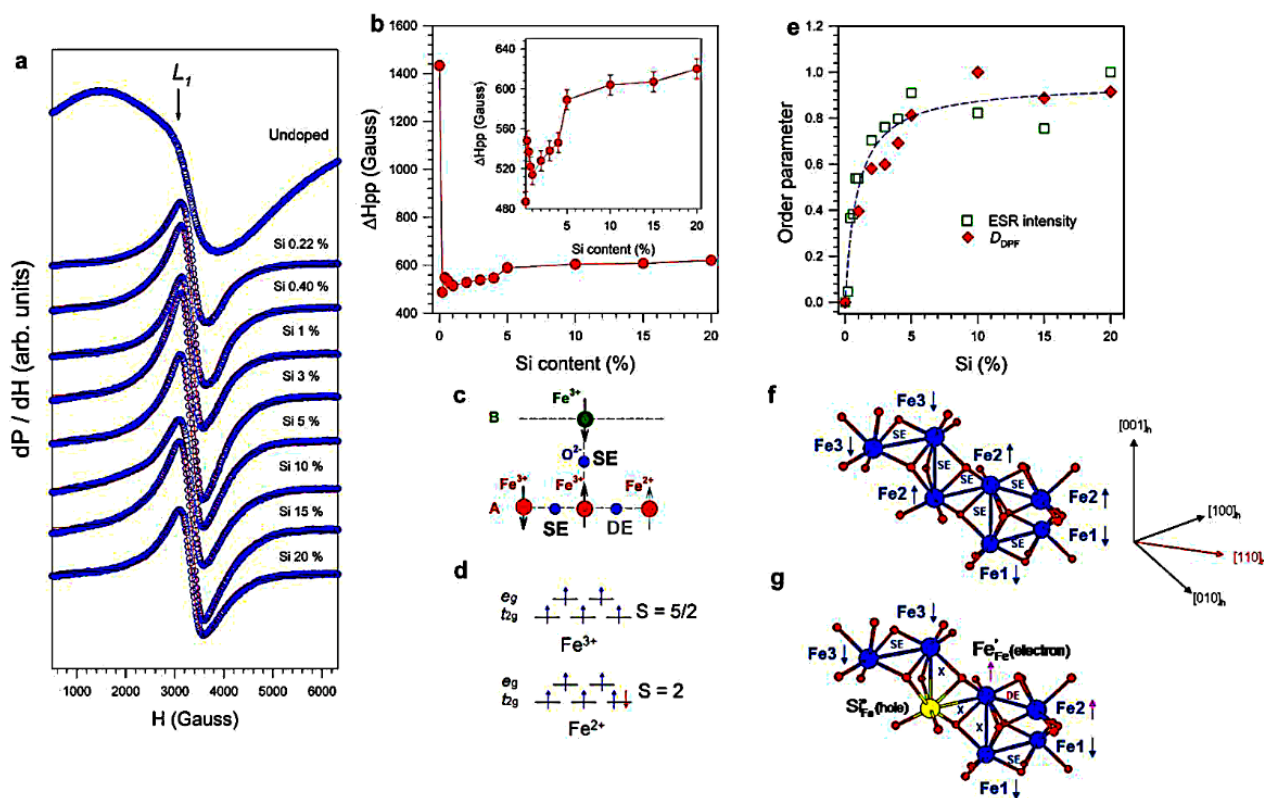


Fig. 1. (a) Experimental (dots) and calculated Lorentzian (solid line) ESR spectra for pure hematite and selected samples of Si-doped α -Fe₂O₃. (b) ESR linewidth (ΔH_{pp}) as a function of Si content. Inset: detailed view of the ΔH_{pp} variation for the 0.22–20% Si content. (c) Schematic representation of the superexchange (SE) between Fe³⁺ ions and the double exchange (DE) between Fe³⁺ and Fe²⁺ ions from the A and B layers. (d) Representation of the electronic structure of the Fe³⁺ and Fe²⁺ ions in FeO₆ involving DE of the t_{2g} electron. (e) Doping-dependency of the normalized degree of distortion of FeO₆ as obtained from PDF, D_{PDF} (diamonds) and normalized integrated ESR intensity (squares). (f, g) Cluster models for crystallite growth mechanism in undoped and Si-doped hematite, respectively. Labelling on Fe1, Fe2, and Fe3 refers to different layers stacked along the $[001]_h$ direction. Spin orientations are reported on each cation and magnetic interactions between atoms are indicated by SE, DE and x (null). Reprinted with permission from Cryst. Growth Des. 2020, 20, 7, 4719-4730. Copyright 2020 American Chemical Society.

If one of the Fe³⁺ ions in the A layer changes into Fe²⁺ as a result of the Si-doping, the mixed valence Fe³⁺/Fe²⁺ ions could interact through double exchange (DE), where the additional electron

introduced by doping (Fe^{2+}) can hop into empty t_{2g} orbitals on the second ion (Fe^{3+}), leading to ferromagnetic (FM) coupling (Fig. 1d). These two exchange mechanisms affect the ESR linewidth in opposite ways, SE inducing exchange narrowing and DE leading to exchange broadening. The final linewidth ΔH_{pp} depends on the relative strength of these two mechanisms.

The observed increase of ΔH_{pp} above 0.22% Si (Fig. 1b) is thus due to the DE exchange broadening mechanism, proving the increase of the Fe^{2+} species concentration with Si doping level. The drop of the ESR linewidth from the undoped to the 0.22% Si spectra can be qualitatively explained by motional narrowing as a result of the small polaron mobility.

As shown in Fig. 1e, the integrated ESR intensity and the degree of distortion of FeO_6 (D_{PDF}) extracted from PDF display similar variations with Si doping level, with a saturation above the solubility limit at $\sim 5\%$ Si. This result confirms that the distortion of FeO_6 could be related to the $\text{Fe}^{3+}\text{-O-Fe}^{2+}$ spin-spin DE via strong spin-lattice interactions that strengthen with increasing Si content.

Figs. 1f and **1g** display cluster models of undoped and Si-doped $\alpha\text{-Fe}_2\text{O}_3$, with the magnetic couplings of Fe_{Fe^x} within three different layers, i.e., Fe1, Fe2, Fe3. In the undoped $\alpha\text{-Fe}_2\text{O}_3$, at room temperature, the Fe ions are AFM coupled by SE interactions across the shared octahedral faces along the [001] direction, while in the ab plane there are two interpenetrating AFM sublattices assembled by spins with a canting angle of $< 0.1^\circ$, resulting in a weak FM interaction. The addition of one Si_{Fe} changes the magnetic interactions in the cluster, as reflected in the evolution of the ESR spectra. The induced $Fe_{Fe'}$ polaron interacts ferromagnetically with the first neighbors Fe_{Fe^x} via DE, whereas the addition of Si reduces the density of SE coupling because of the increase in non-magnetic Si-O-Fe interactions.

The lower dimensionality of the magnetic interactions, together with itinerant electrons that can be only transferred within the same layer, constrain the polarons to interact only along the [110] direction (Fig. 1g). With increasing Si-content, more $Fe_{Fe'}$ polarons are induced and start aggregating, forming large polarons, due to the strong collective interactions of the anisotropic DE paths along [110], driving anisotropic nanocrystal growth with preferential orientation.

Our findings provide atomistic insights into how structural, magnetic, and electronic properties affect the preferential nanocrystal growth in Si-doped $\alpha\text{-Fe}_2\text{O}_3$ where the charge transport is ruled by electron small polarons, thus offering a new framework for the nanoscale design of efficient solar fuel devices.

References

1. M. Allieta et al., *Electron Small Polaron and Magnetic Interactions Direct Anisotropic Growth of Silicon-Doped Hematite Nanocrystals*, Cryst. Growth Des. **20**(7), 4719–4730 (2020) [[doi:10.1021/acs.cgd.0c00496](https://doi.org/10.1021/acs.cgd.0c00496)].
2. A. Kay, I. Cesar and M. Grätzel, *New Benchmark for Water Photooxidation by Nanostructured $\alpha\text{-Fe}_2\text{O}_3$ Films*, J. Am. Chem. Soc. **128**, 15714–15721 (2006).
3. S. P. Schwaminger et al., *Formation of Iron Oxide Nanoparticles for the Photooxidation of Water: Alteration of Finite Size Effects from Ferrihydrite to Hematite*, Sci. Rep. **7**, 12609 (2017).
4. M. Allieta et al., *Shaped-controlled silicon-doped hematite nanostructures for enhanced PEC water splitting*, Catal. Today, **328**, 43–49 (2019).
5. CERIC_ERIC proposal number 20162015, *Enhancing the solubility of silicon in hematite nanostructures for solar water splitting: interplay among morphology, crystallographic, magnetic and electronic properties*.
6. S. Stoll and A. Schweiger, *EasySpin, a comprehensive software package for spectral simulation and analysis in EPR*, J. Magn. Reson. **178**(1), 42–55 (2006).

Second magnetization peak, rhombic-to-square Bragg vortex glass transition, and intersecting magnetic hysteresis curves in overdoped $\text{BaFe}_2(\text{As}_{1-x}\text{P}_x)_2$ single crystals

L. Miu,^a A. M. Ionescu,^a D. Miu,^b M. Burdusel,^a P. Badica,^a D. Batalu,^c and A. Crisan^a

^aNational Institute of Materials Physics, 077125 Magurele, Romania

^bNational Institute of Laser, Plasma, and Radiation Physics, 077125 Magurele, Romania

^cSC Fileo Buildup SRL, 060816 Bucharest, Romania

Vortex pinning enhancement at high external magnetic fields H in superconducting single crystals with randomly distributed vortex pinning centres is one of the most relevant aspects for the understanding of the vortex-phase diagram of superconductors. In the case of weakly pinned specimens, one has the so called peak effect, where the maximum in the magnetic field dependence of the critical current density J_c (proportional to the irreversible magnetic moment) is rather sharp and located close to the DC irreversibility line. When vortex pinning is stronger, the peak effect is substituted by a wide second magnetization peak (SMP) in increasing H , with the onset field H_{on} and the peak field H_p far below the irreversibility line, leading to fishtail-shaped DC magnetic hysteresis $m(H)$ curves. Among many SMP mechanisms and models, a pinning-induced disordering of the low- H quasi-ordered vortex solid (the Bragg vortex glass, BVG, stable against dislocation formation) has been considered to be at the origin of the SMP for various superconducting single crystals [1-2].

Significant progress for the understanding of the vortex phase diagram and the occurrence of the SMP has been made by considering the competition between the thermal energy, the pinning energy, and the elastic energy in the vortex system. In the low- T domain, the thermal energy can be neglected, and the simple energy balance relation leads to an onset field which is independent of temperature. This is also the result of an order-disorder transition. It has been shown [1] that the upward curvature of the $H_{\text{on}}(T)$ variation in the low- T range can be explained by considering the reduction of the effective pinning energy at low temperatures, where the probing current density is closer to J_c . This approach was suggested by the often observed time evolution of the SMP, with the characteristic fields decreasing at high relaxation levels. Since the SMP extends over a large magnetic field interval, it has been proposed that the pinning-induced BVG disordering is continuous [2], starting at H_{on} , where the energy for the plastic vortex deformation is smaller than the effective pinning energy, and finishing at H_p , where the vortex system is amorphous. The essential point is the proliferation of dislocations in the vortex system for H between H_{on} and H_p , where the pinning increase is caused by the efficient accommodation of vortices to the pinning centres in the presence of vortex dislocations. This idea is strongly supported by the repeatedly reported elastic vortex creep-plastic creep crossover across the SMP.

Alternatively, it has been argued that in (tetragonal) $\text{La}_{2-x}\text{Sr}_x\text{CuO}_4$ single crystals, with fourfold symmetric inter-vortex interactions, the SMP is the direct result of the characteristic, structural rhombic-to-square transition (RST) of the BVG, in which case the upward curvature in $H_{\text{on}}(T)$ at low T results directly. The 122-type iron pnictide single crystals in H parallel to the crystallographic c axis exhibit a well-developed SMP [3], and the above RST-related SMP model has been extended to these fourfold symmetric superconductors, as in the case of $\text{Ba}(\text{Fe}_{0.925}\text{Co}_{0.075})_2\text{As}_2$ and $\text{BaFe}_2(\text{As}_{0.68}\text{P}_{0.32})_2$. The anisotropic interaction with fourfold symmetry induces a rhombic rather than hexagonal vortex arrangement, which transforms into a square one when the vortex separation decreases. Thermal fluctuations assist in breaking the rhomb symmetry, lowering the transition field H_{RST} as the temperature increases.

It is well established that by increasing the P doping level beyond the optimal one (where T_c is maximum) the critical current density of P-Ba122 single crystals decreases. A quantitative analysis of the $J_c(T)$ dependence indicated that the characteristic pinning mechanisms [related to the spatial variation of T_c (δT_c pinning) and the fluctuations in the charge carrier mean free path] are enhanced for optimally doped and underdoped samples. The P-Ba122 specimen thoroughly investigated here is an overdoped single crystal, with the nominal $x \sim 0.33$, denoted below P-Ba122od, which has the critical temperature $T_c = 27.5$ K. To highlight the specific shape of the magnetic hysteresis curves of overdoped samples, an optimally doped single crystal (P-Ba122op, $x \sim 0.30$, $T_c = 29$ K), with stronger pinning, has been considered.

Fig. 1a (main panel) illustrates the $J_c(H)$ variation for P-Ba122od and P-Ba122op at $T = 10$ K, where J_c has been determined with the Bean model for rectangular specimens from the descending branches of the $m(H)$ curves plotted in the inset. By increasing doping from ~ 0.30 to ~ 0.33 , J_c for H around the SMP onset at $T = 10$ K decreases from $\sim 7 \times 10^4$ A/cm² to $\sim 10^4$ A/cm². The particular difference between the $m(H)$ curves of P-Ba122od and of the optimally doped specimen P-Ba122op is that in the former case, there is a wide magnetic field range of weak elastic (collective) pinning (in the BVG), followed by an increase of $|m|$ around $H = 60$ kOe on the ascending $m(H)$ branch (see the inset of Fig. 1a). We associate below the RST with this precipitous enhancement of the effective pinning in increasing H just above H_{on} .

The DC magnetic hysteresis curve of P-Ba122od at $T = 20$ K is plotted in Fig. 1b, where H_{on} and H_p of the SMP are indicated by arrows. One notes the development of an intriguing $m(H)$ “shoulder” (leading to “pear-like” shaped hysteresis curves). The $m(H)$ shoulder exhibits history effects. On the descending $m(H)$ branch, the vortex system seems to remain trapped in more strongly pinned high- H states (see the inset of Fig. 1a). For this reason, we considered the shoulder on the ascending $m(H)$ branch, and the transition field H_{RST} has been taken at the local minimum of dm/dH , as illustrated in Fig. 1b.

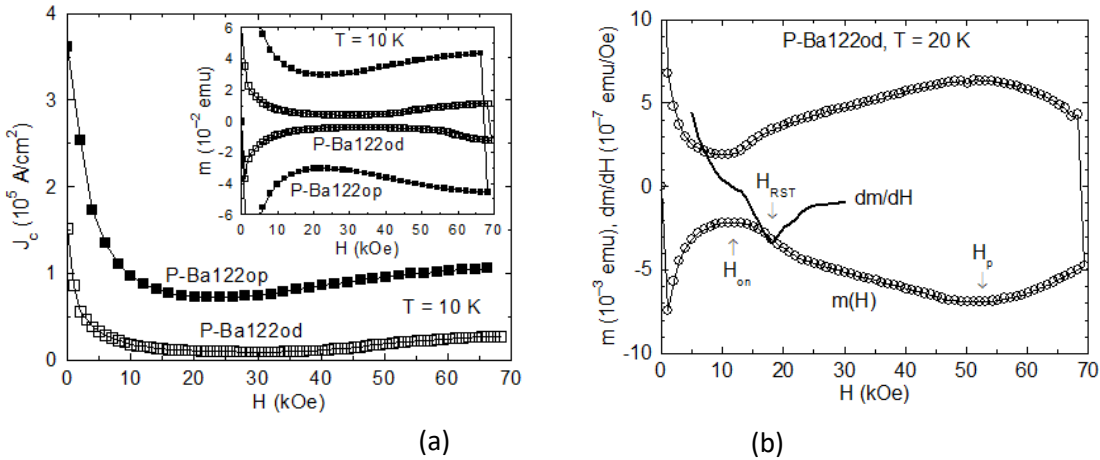


Fig. 1 (a) Field dependence of critical current density (main panel), and magnetic hysteresis curves (inset) of the two samples, and (b) the magnetic hysteresis curve $m(H)$ of P-Ba122od at $T = 20$ K, with the onset field H_{on} and the peak field H_p of the SMP indicated by arrows. We associate the structural rhomb-to-square vortex phase transition with the “step-like” enhancement of $|m|$ in increasing H , giving rise to an $m(H)$ shoulder. The structural transition field H_{ST} has been taken at the local minimum of dm/dH (represented by a continuous line).

It was found that the (elastic) RST does not generate the SMP, but the RST can influence the pinning-dependent SMP onset field when this is close to the intrinsic RST line, through the appearance of a shoulder on the magnetic hysteresis $m(H)$ curves. The temperature evolution of the $m(H)$ shoulder leads to the intersection of isothermal $m(H)$ curves (a rare phenomenon), and, consequently, to a peak in the temperature variation of the DC critical current density $J_c(T)$. However, this particular peak does not appear in the temperature variation of the screening current in AC magnetic measurements where the vortex system is dynamically ordered in the RST domain. This

emphasizes the essential role of vortex dislocations for an effective accommodation of the vortex system to the pinning landscape and the occurrence of the SMP [4,5].

We conclude that the observed DC $m(H)$ shoulder is the effect of a precipitous pinning-induced proliferation of dislocations when the BVG elastic squash modulus softens at the structural transition between a rhombic and a partially disordered square BVG. The pinning-induced vortex-system disordering continues above the RST domain (as indicated by the magnetization relaxation results), and represents the basic SMP mechanism for the fourfold symmetric superconductors, as well. The absence of a notable effect of the RST on the SMP in the case of optimally doped and underdoped P-Ba122 single crystals can easily be explained in terms of the pinning-induced disordering of the vortex system across the SMP. The stronger pinning exhibited by optimally doped and underdoped P-Ba122 single crystals shifts the onset field well below the structural transition field, and the RST cannot manifest in a significantly disordered vortex system.

The whole report is published as Second magnetization peak, rhombic-to-square Bragg vortex glass transition, and intersecting magnetic hysteresis curves in overdoped $\text{BaFe}_2(\text{As}_{1-x}\text{P}_x)_2$ single crystals, L. Miu, A. M. Ionescu, D. Miu, M. Burdusel, P. Badica, D. Batalu, and **A. Crisan**, SCIENTIFIC REPORTS, **10**, 17274 (2020), <https://doi.org/10.1038/s41598-020-74156-z>

FI-3.998; AIS-1.261; Q1

References

1. Miu, L., Ionescu A.M., Miu D., Petrisor T., Park A., Tamegai T., and Crisan A, Physica C **555**, 1 (2018) <https://doi.org/10.1016/j.physc.2018.10.002>.
2. Ionescu A.M., Miu D., Crisan A, Miu L., J. Supercond. Nov. Magn. **31**, 2329 (2018), <https://doi.org/10.1007/s10948-017-4487-5>.
3. Salem-Sugui S. jr., Mosqueira J., Alvarenga A.D., Sonora D., Crisan A., Ionescu A.M., Sundar S., Hu D., Li S-L, Luo H-Q, Supercond. Sci. Technol., **30**, 055003 (2017), <https://doi.org/10.1088/1361-6668/aa62f1>

Magnetic Phase Evolution in Novel FePt and FeMnPt Nanocomposite Magnets

Ovidiu Crisan,^a Petre Palade,^a Alina Daniela Crisan,^a Aurel Leca,^a Ioan Dan^b

^aNational Institute for Materials Physics, PO Box MG-7, 077125, Magurele, Romania

^bR&D Consulting and Services S.R.L., 023761 Bucharest, Romania

With the aim of demonstrating phase coexistence of two magnetic phases in an intermediate annealing regime and obtaining highly coercive FePt nanocomposite magnets, two alloys of slightly off-equiatomic composition of a binary Fe-Pt system were prepared by dynamic rotation switching and ball milling. The alloys, of composition Fe₅₃Pt₄₇ and Fe₅₅Pt₄₅, were subsequently annealed at 400 °C and 550 °C and structurally and magnetically characterized by means of X-ray diffraction, ⁵⁷Fe Mössbauer spectrometry and Superconducting Quantum Interference Device (SQUID) magnetometry measurements. Gradual disorder–order phase transformation and temperature-dependent evolution of the phase structure were monitored using X-ray diffraction of synchrotron radiation. It was shown that for annealing temperatures as low as 400 °C, a predominant, highly ordered L₁₀ phase is formed in both alloys, coexisting with a cubic L₁₂ soft magnetic FePt phase. The coexistence of the two phases is evidenced through all the investigating techniques that we employed. SQUID magnetometry hysteresis loops of samples annealed at 400 °C (Fig. 1) exhibit inflection points that witness the coexistence of the soft and hard magnetic phases and high values of coercivity and remanence are obtained. For the samples annealed at 500 °C, the hysteresis loops are continuous, without inflection points, witnessing complete exchange coupling of the hard and soft magnetic phases and further enhancement of the coercive field. Maximum energy products comparable with values of current permanent magnets are found for both samples for annealing temperatures as low as 500 °C. These findings demonstrate an interesting method to obtain rare earth-free permanent nanocomposite magnets with hard–soft exchange-coupled magnetic phases.

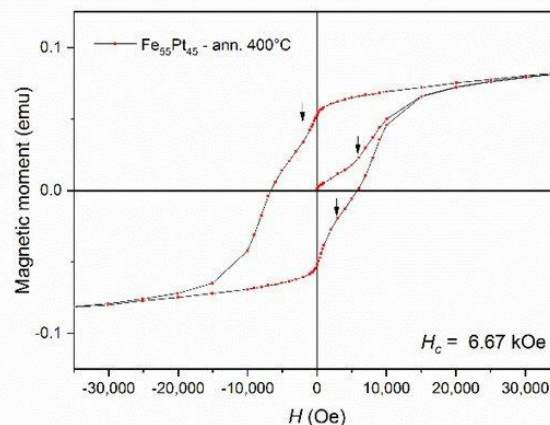


Fig. 1 SQUID magnetometry hysteresis loops of samples annealed at 400 °C.

On the other hand, ternary alloys derived from FePt show most promising magnetic properties as a novel class of rare earth free permanent magnets with high operating temperature. A granular alloy derived from binary FePt with low Pt content and the addition of Mn with the nominal composition Fe₅₇Mn₈Pt₃₅ has been synthesized in the shape of melt-spun ribbons and subsequently annealed at 600 °C and 700 °C for promoting the formation of single phase, L₁₀ tetragonal, hard magnetic phase [2]. Proton-induced X-ray emission spectroscopy PIXE has been utilized for checking the compositional effect of Mn addition.

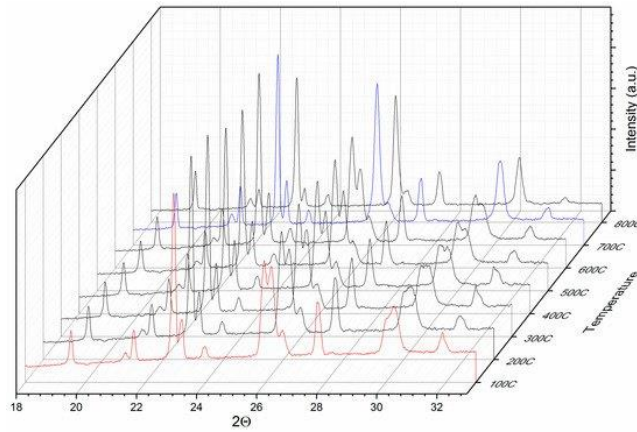


Fig. 2 Synchrotron X-ray diffraction of Fe-Mn-Pt recorded between 50 – 800°C.

Structural properties were analyzed using X-ray diffraction and diffractograms were analyzed using full profile Rietveld-type analysis with MAUD (Materials Analysis Using Diffraction) software. By using temperature-dependent synchrotron X-ray diffraction, the disorder–order phase transformation and the stability of the hard magnetic $L1_0$ phase were monitored over a large temperature range (50–800 °C) (Fig.2). It can be observed that the Bragg lines observed are consistent throughout the whole range of investigated temperatures and similar features are observed for all investigated temperatures. The observed Bragg lines are similar for all the investigated temperatures with a certain position shifting, due to the lattice parameters overall increase with temperature. Particular aspects are however to be noted, especially for the reflections situated at around 26° and 30°. During the disorder-order phase transformation, some of the Bragg lines of the cubic phase split due to tetragonal distortion. Upon occurrence of $L1_0$ phase, these Bragg lines split as for example (200) of the cubic phase into (200) and (002) of the tetragonal phase. The more obvious the splitting the more significant is the phase transformation and the more abundant is the formed $L1_0$ phase. It is worthwhile noticing that in the diffractograms recorded at 50°C and 100°C, there is an obvious splitting of the peaks at 26° and 30° in 2θ . This splitting disappears at 700°C. These results confirm that there is a large interval of structural stability of the $L1_0$ phase. Moreover, this stability was interpreted in terms of higher ordering of the $L1_0$ phase promoted by the Mn addition. It was moreover found that both crystal growth and unit cell expansion are inhibited, up to the highest temperature investigated (800 °C), proving thus that the Mn addition furthermore stabilizes the formed $L1_0$ structure.

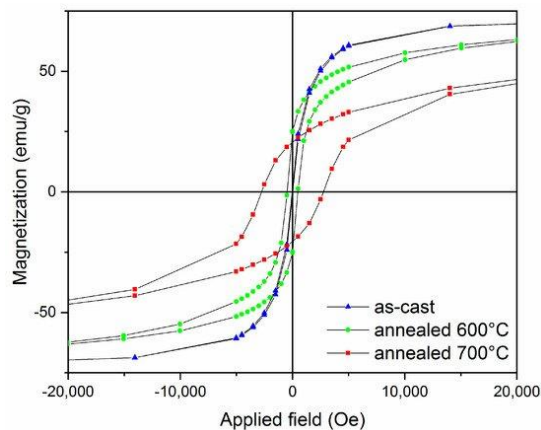


Fig. 3: Magnetic hysteresis loops of as-cast and annealed Fe-Mn-Pt sample.

Magnetic properties of samples submitted to static annealing at 600°C and 700°C have been measured with SQUID magnetometry (Fig.3). The hysteresis loop for as-cast sample show typical soft ferromagnetic behavior with approach to saturation at low applied fields and high saturation magnetization (70 emu/g) with virtually no coercivity (only 95 Oe coercive field). The sample annealed at 600°C shows similar soft magnetic features with slightly smaller saturation magnetization (around 67 emu/g) but increased coercivity (470 Oe). The increase of the coercive field is related to the presence of the hard magnetic L1₀ phase co-existing with the soft magnetic, cubic A1, which is the only phase present in the as-cast sample. The magnetic data are thus in agreement and confirms the structural data obtained on the as-cast and annealed sample. Co-existence of cubic and tetragonal phases in the alloy lead to modifications in the hysteresis loop of the annealed samples. An optimal coupling of these two phase would mean to observe a hysteresis loop exhibiting both features: high magnetization and high coercivity, ultimately leading to a maximum energy product (BH)_{max} superior to any of the constituent phases. The lack of inflection points shows that the two observed phases, hard and soft magnetic, are fully exchange coupled in the intermediate annealing regime (600°C). This may potentially lead to the creation of a Fe-Mn-Pt exchange coupled nanocomposite magnet where both soft and hard magnetic phase coexist and may yield good magnetic performances, comparable with existing permanent magnets. Strong increase of the coercivity is observed for the sample annealed at 700°C where the coercive field reaches 2.8 kOe and a saturation magnetization of about 49 emu/g. This is again consistent with the structural data where we have noticed that the disorder-order phase transformation has been completed, the cubic A1 phase is no more observed and hard magnetic L1₀ tetragonal phase is the only magnetic phase present in the sample. The findings confirm thus the features observed through structural data and point out the beneficial effect of Mn addition in view of stabilizing the L1₀ phase structure on a large temperature range, needed for technological applications in extreme operation conditions. It opens good perspectives for use as RE-free magnets, operating in extreme conditions.

References

1. O. Crisan, I. Dan, P. Palade, A.D. Crisan, A. Leca, A. Pantelica, *Magnetic Phase Coexistence and Hard-Soft Exchange Coupling in FePt Nanocomposite Magnets*, *Nanomaterials* **10**, 1618 (2020). <https://doi.org/10.3390/nano10081618>
2. A.D. Crisan, A. Leca, D. Pantelica, I. Dan, O. Crisan, *Mn-Induced Thermal Stability of L1₀ Phase in FePt Magnetic Nanoscale Ribbons*. *Nanomaterials* **10**, 1278 (2020) <https://doi.org/10.3390/nano10071278>

Unidirectional magnetic anisotropies in 0D and 1D nanostructures

S. G. Greculeasa,^a C. Locovei,^{a,d} A. Kuncser,^a P. Palade,^a G. Schinteie,^a A.-E. Stanciu,^a A. Leca,^a C.-F. Florica,^a A. Costas,^a I. Enculescu,^a V. Kuncser^{a*}, F. Dumitrache,^b I. Lungu,^b N. Filipoiu,^c S. Antohe,^c V.-A. Antohe^c

^aNational Institute of Materials Physics, 405A Atomistilor, Magurele, Romania, 077125.

^bNational Institute for Laser, Plasma and Radiation Physics, Laser Department, 409 Atomistilor, Magurele, Romania, 077125.

^cFaculty of Physics, R&D Center for Materials and Electronic & Optoelectronic Devices (MDEO), University of Bucharest, Atomistilor Street 405, 077125 Magurele, Romania

The magnetic specificities of nanoarchitectures can be tuned by introducing interfacial interactions. Particularly, the bisystems consisting of a ferromagnet (F) interfaced with an antiferromagnetic (AF) component are of high technological importance in spin-valve devices based on either Giant Magneto-Resistance or Tunneling Magneto-Resistance effects). The main magnetic phenomenon specific to these F/AF systems is the unidirectional anisotropy, either by the specific exchange bias field (positive or negative), or by the increased coercive fields of the F interfacially-coupled to the AF, relative to a simple free F. An interesting AF/F system is represented by dense arrays of vertically-aligned nickel nanotubes (NTs) with internal ultra-thin NiO concentric layers with cylindrical F/AF interfaces (see fig. 1) [1]. The samples (S1 to S4) were modified by varying the cathodic reduction potential between -0.95 V and -1.10 V (versus SCE), in order to obtain Ni NTs with slightly different wall thicknesses (6-11 nm \pm 1).

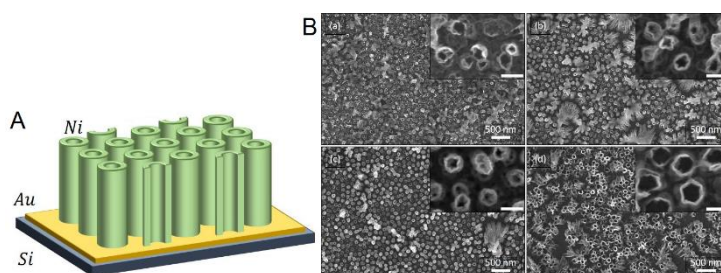


Fig 1. A. Schematic representation of Ni NTs perpendicularly-aligned to the Au/Si substrate. B. Top-view SEM micrographs of the samples: (a) S1, (b) S2, (c) S3, and (d) S4.

The thickness of the NT walls and of the thin AF NiO layer strongly influences the magnetic behavior of the dense array of exchange-coupled Ni/NiO NTs. As evidenced in fig. 2, the coercive field (H_C) values increase with wall thickness and are slightly higher in parallel geometry. The exchange bias field (H_{ex}) values usually increase with wall thickness (except for $t=9$ nm in parallel geometry) and are slightly higher in parallel geometry. The H_C values are almost one order of magnitude larger at 10 K as compared to 300 K and in addition, they closely respect the variation of the exchange bias field along the analyzed samples in both measuring geometries, thus definitely proving their direct connection to the unidirectional anisotropy induced at lower temperatures.

Such dense arrays of pinned F NTs may potentially withstand individual magnetic addressability, by carefully further tuning their magnetic properties in terms of changing the magnetic packing fraction either by adjusting the template porosity, or ultimately by controlling the degree of NTs oxidation. The entire fabrication protocol assures full compatibility with the standard Si processing and is quite amiable to further optimizations, opening an outstanding pathway towards large-scale integrability and manufacturing of a new generation of magnetic devices relying on large dense arrays of vertically-standing quasi-1D nanostructures with easily tuneable magnetic features.

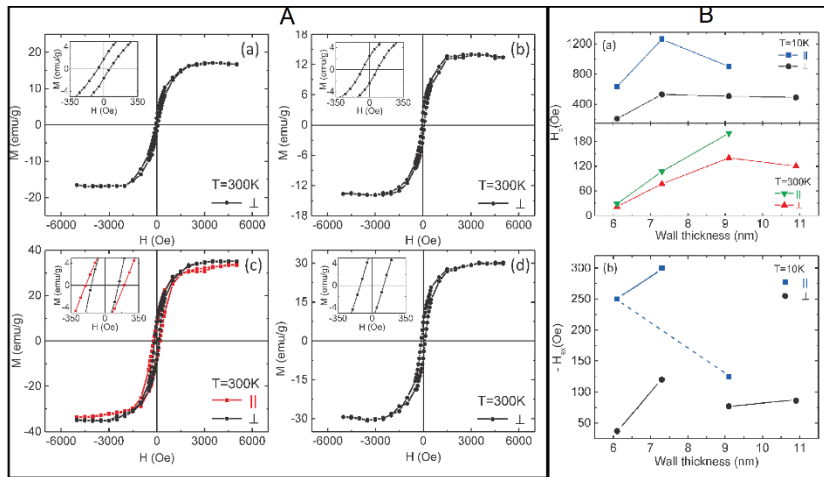


Fig 2. A Hysteresis loops of samples S1 (a), S2 (b), S3 (c) and S4 (d), recorded at 300 K with the magnetic field applied perpendicular and parallel to the NTs axis. B (a) H_c determined at 300 K and 10 K in parallel and perpendicular geometry and (b) H_{ex} of the analyzed samples at 10 K.

Another important AF/F material is a 0-D core-shell-type Fe-oxide based nanoparticle system. Along with the synthesis procedure, the annealing treatments offer a valuable tool to optimize Fe and Fe oxide based NPs with respect to specific applications. The effects of the annealing treatments in hydrogen atmosphere on the structural and magnetic properties of Fe-based NPs prepared by laser pyrolysis were investigated [2]. The pristine sample (A) and the samples annealed in hydrogen atmosphere at 200 °C (A200C) and 300 °C (A300C) were considered.

From Rietveld refinements it was deduced that sample A contains NPs with specific structure in-between of very distorted magnetite and maghemite, with small crystallite size of 5.6 nm and high r.m.s. microstrain of 0.006%. Sample A200C contains NPs of better formed magnetite, with crystallite size of 10.3 nm and lower microstrain (0.003%). The lattice constant of the sample A200C (0.8406 nm) is roughly similar with one of sample A (0.8391 nm). The complete conversion of magnetite into metallic iron with bcc structure has been obtained in sample A300C, with considerably increased crystallite size up to 57.8 nm, whereas the microstrain diminished by few times relative to the sample A200C.

The magnetic hysteresis curves, negative exchange bias field (H_E) values are evidenced at low temperatures (Fig. 3c), suggesting the presence of interactions between antiferromagnetic or spin disordered oxides and ferrimagnetic oxide phases, most probably in a core-shell-like configuration. As expected, the exchange bias interaction is stronger after cooling the sample in the presence of a magnetic field (Fig. 3d). H_E is cancelled out at a temperature of 50 K, also known as the blocking temperature of exchange bias (T_{EB}). Hence, samples A and A200 are representative cases of nanoparticulate systems with $T_{EB} < T_B$.

The annealing treatment performed at 200 °C in hydrogen atmosphere induces a partial reduction of Fe, giving rise to nanoparticles with an average size of about 10 nm and with a core-shell structure consisting of a very well formed magnetite core (about 6.5 nm size) and a magnetically disordered shell.

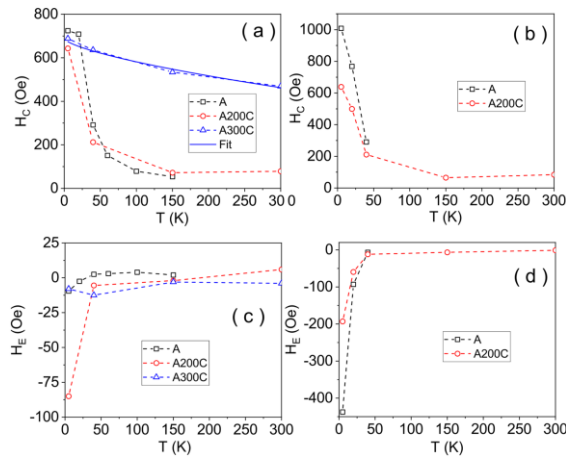


Fig 3. Temperature dependence of coercive field before (a) and after (b) in-field cooling procedure. Temperature dependence of exchange bias field before (c) and after (d) in-field cooling procedure.

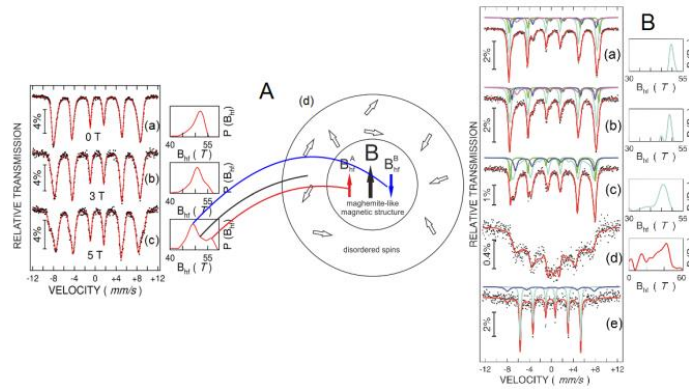


Fig 4. A. Mössbauer spectra of the as-prepared sample A, collected at 3 K without applied magnetic field (up), under 3 T applied magnetic field (middle) and under 5 T applied magnetic field (down). A graphical representation of the spin structure specific to a magnetic NP with more ordered spins in the core and more disordered spins in the shell (d). B. Mössbauer spectra of samples: A200C, collected at 5 K (a), 80 K (b), 160 K (c), room temperature (d); A300C, collected at 6 K (e).

Annealing treatments at 300 °C in hydrogen atmosphere succeeded at inducing the formation of a α -Fe-like phase with the metallic nanoparticles (tens of nm in size) remaining stable with oxidation. In agreement with these changes in phase composition, as well as due to the increase in particle size and crystallinity improvement, T_B , H_C , M_S and M_R values increase significantly after annealing at 300 °C.

Acknowledgements: This research was funded at NIMP through the grants: PN-III-P1-1.1-TE-2019-0868 (TE115/2020), PN-III-P1-1.1-PD-2019-1141 (PD 163/2020), 7PCCF/2018, 47PCCDI/2018 and POC P_37_697 REBMAT (28/01.09.2016), the Core Program PN19-03.

References

1. C. Locovei, *et al*, *Unidirectional Magnetic Anisotropy in Dense Vertically-Standing Arrays of Passivated Nickel Nanotubes*, *Nanomater.* **10**, 2444 (2020) [doi:10.3390/nano10122444].
2. S. G. Greculeasa, *et al*, *Tuning structural and magnetic properties of Fe oxide nanoparticles by specific hydrogenation treatments*, *Sci. Rep.* **10**, 17174 (2020) [doi:10.1038/s41598-020-74188-5].

Towards applications

Removal and Oxidation of As (III) from Water Using Iron Oxide Coated CTAB as Adsorbent

Daniela Predoi,^{a,*} Simona Liliana Iconaru,^a Mihai Valentin Predoi,^b Mikael Motelica-Heino^c

^a National Institute of Materials Physics, Atomistilor Street, No. 405A, Magurele, Ilfov, Romania, 077125

^b University Politehnica of Bucharest, Department of Mechanics, 313 Splaiul Independentei, Sector 6, Bucharest, Romania, 060042

^c ISTO, UMR 7327 CNRS Université d'Orléans, 1A rue de la Férollerie, Orleans, France, 45071

In the last decades due to rapid technological development, heavily industrialized countries are severely affected due to the continuous and rapid expansion of contaminated areas worldwide. An increased interest in the development of novel materials for environmental applications has been given to nanoscale materials due to their specific properties caused by the increase of the surface due to the decrease of the volume/surface ratio. Previous studies have reported that different iron oxide species such as Fe_3O_4 , $\alpha\text{-Fe}_2\text{O}_3$, and $\gamma\text{-Fe}_2\text{O}_3$ that interact with As had the ability to remove both As (III) and As (V) from water [1]. Iron oxide nanoparticles with a highly specific surface area have been investigated as low-cost adsorbents with a high adsorption capacity for metal ions, which could also be conveniently recovered by magnetic separation after the decontamination process [1]. Iron oxides such as magnetite and maghemite coated with cetyltrimethylammonium bromide (CTAB) are very promising materials for wastewater treatment because iron oxide can be easily separated from solutions using the magnetic separation procedure. Iron oxide (IO) coated CTAB was synthesized by an adapted co-precipitation method. According to the literature, in this study, we present for the first time the results concerning the removal and oxidation of As (III) from water using iron oxide coated CTAB as an adsorbent. Ultrasound studies have shown a behavior similar to that of double distilled water for depolluted water. Moreover, cell viability tests were performed on the IO-CTAB biocomposite used in the removal of arsenic, but also on contaminated and decontaminated waters [1].

The CTAB coated iron oxide (IO-CTAB) nanoparticles were synthesized by coprecipitation by a modified method [1]. The crystal structure and phase purity of the synthesized IO-CTAB composite were examined by XRD analysis and the results are presented in Figure 1a [1]. The XRD pattern of IO-CTAB was indexed and resembled to a cubic phase Fd-3m of Fe_3O_4 with lattice constant $a = 8.40 \text{ \AA}$. The average crystal size of IO-CTAB evaluated using the Scherrer equation was $17.26 \pm 3 \text{ nm}$. No obvious XRD peaks corresponding to other phases were found in the XRD model of the analyzed sample, which shows a good purity of the IO-CTAB prepared sample. The shape and morphology of IO-CTAB was examined by TEM and SEM analysis. The TEM image (Figure 1b) showed that the sample was composed of nanoparticles with spherical shapes. The observed IO-CTAB nanoparticles had sizes between 10 and 25 nm. The histogram of particle size distribution from the TEM image is presented in Figure 1c [1]. The mean particle size was $19.86 \pm 1.7 \text{ nm}$, which is in accordance with the result derived from the XRD analysis. The SEM image of IO-CTAB showed that the particles were agglomerated with nanometric dimensions and spherical shape (Figure 1d) [1]. Furthermore, the effect of the initial concentration of As (III) of the solution on the efficiency of IO-CTAB nanoparticles in the removal of arsenic ions from aqueous solutions at pH 5 was investigated using solutions with different concentrations of As (III) in the range of 0–100 mg/L. Figure 2a presents the effect of the initial concentration of As (III) on the removal of arsenic ions from aqueous solutions by IO-CTAB nanoparticles. It can be seen that the arsenic removal efficiency depends on the initial concentration of As (III) [1].

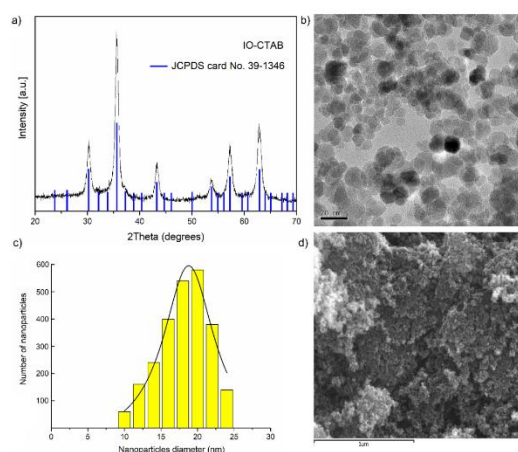


Fig 1. XRD patterns of the prepared IO-CTAB nanoparticles (a); TEM image of IO-CTAB nanoparticles (b); Size distribution histogram of the synthesized IO-CTAB nanoparticles (c); SEM image of IO-CTAB nanoparticles (d) [1].

For an arsenic concentration smaller than 5 mg/L, the removal efficiency of arsenic ions from the contaminated solution of IO-CTAB nanoparticles was between 88% and 90%, thus demonstrating that the adsorbent material (IO-CTAB nanoparticles) had a strong affinity for As (III) ions [1]. For arsenic concentrations in the range of 10 mg/L to 100 mg/L, it could be seen that the removal efficiency of As (III) ions was approximately 93%. Figure 2b presents the experimental data and the theoretical Langmuir model when the IO-CTAB nanoparticles were used for the adsorption of As (III) ions from aqueous solutions. The graphical representations of the As (III) adsorbed ions on the mass unit by IO-CTAB nanoparticles (q_e), depending on the concentration of As(III) remaining in solution (C_e) are shown in Figure 2b [1]. Furthermore, the graphical representation of the C_e/Q_e function of C_e was also obtained and is depicted in Figure 2c [1]. The results of the studies showed that at ambient temperature, the R^2 coefficient calculated from the Langmuir isotherm was equal to 0.996 for IO-CTAB. Figure 2d shows the graphical representations of the $(\ln Q_e)$ function of $(\ln C_e)$ for the As (III) ion adsorption experiments on IO-CTAB nanoparticles [1]. The k_f , Freundlich constant is an indicator of the adsorption capacity of the materials used as the adsorbent, while $1/n$ is a function of the power adsorption from the process [1-2]. The values obtained for n from the linearized form of the Freundlich equation for the As (III) ions adsorption experiments on IO-CTAB nanoparticles were greater than 1, leading to a value of $1/n$ smaller than 1, which corresponds to a normal adsorption process [1]. Ultrasound measurements provide information about the interaction with the suspension of solid nanoparticles in the liquid. The results of the cell viability test of HeLa cultures incubated with solutions contaminated with arsenic ions at different concentrations (As10, As50, and As100) and with decontaminated solutions using IO-CTAB nanoparticles (IO-CTAB:As10, IO-CTAB:As50, and IO-CTAB:As100) are presented in Figure 3 [1]. Moreover, it has been observed that the survival rates of HeLa cells significantly decreased with the increase in the arsenic ions concentration. Moreover, the results showed that the toxicity of contaminated solutions can be correlated with the concentration of arsenic ions, showing that cell viability decreased with the increase of the concentration of arsenic ions in contaminated solutions [1]. The results emphasize that the decontaminated solutions had no effect or a small toxic effect on the cell viability of the HeLa culture after 24 h of incubation. The MTT test showed that for the decontaminated solutions, the cell viability of the HeLa culture was above 90%, which highlighted that the IO-CTAB nanoparticles were efficient in removing the As (III) ions from the aqueous solutions.

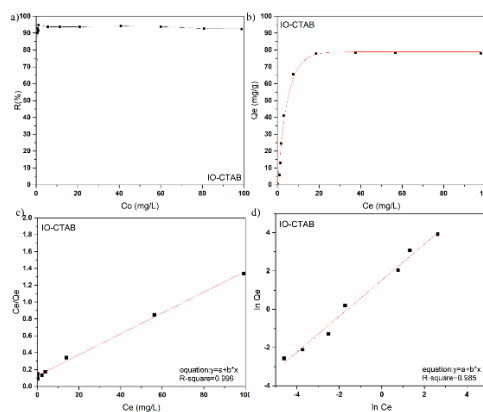


Fig 2. The effect of the initial concentration of As (III) of the solution on the removal (%) of As (III) from contaminated aqueous solutions using IO-CTAB nanoparticles (a); graphic representation of the amount of material adsorbed at equilibrium (b); Langmuir linearized fits (c); Freundlich linearized fits (d) [1].

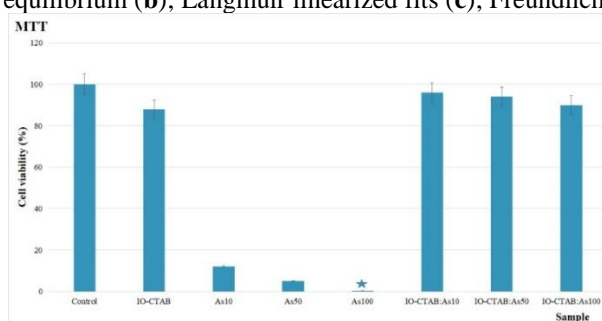


Fig 3. Cell viability of HeLa cells incubated with water in the presence of IO-CTAB nanoparticles, As (III) contaminated solutions, and decontaminated using IO-CTAB nanoparticles. HeLa cell culture was used as the control [1].

The results of the MTT assay showed that IO-CTAB presented no toxicity on HeLa cells after 24 h. This research demonstrated, for the first time, the effectiveness of IO-CTAB as an adsorbent for the removal and oxidation of As (III) from contaminated water. The results also suggest that IO-CTAB nanoparticles could be suitable candidates for the development of new technologies for water treatment purposes [1].

Acknowledgments: We thank Alina Mihaela Prodan from Carol Davila University of Medicine and Pharmacy for assistance with the biological assays. This work was supported by a grant of the Romanian Ministry of Research and Innovation, project number PN-III-P1-1.2-PCCDI-2017-0134, Contract No. 23PCCDI/2018, Component Project No. 2 “Development and evaluation of the toxicological effects of nanoparticles used in environmental applications, Core Program PN19-030101 (contract 21N/2019), and Scientific Research Contract Nr.1/4.06.2020.

References

1. D. Predoi et al., *Removal and Oxidation of As(III) from Water Using Iron Oxide Coated CTAB as Adsorbent*, *Polymers*. **12**(8), 1687 (2020) [doi: 10.3390/polym12081687].
2. E. Voudrias et al., *Sorption description isotherms of dyes from aqueous solutions and waste waters with different sorbent materials*, *Global Nest. Int. J.* **4**(1), 75–83 (2002).

Photodetecting behavior of individual CuO-ZnO core-shell nanowires with p-n radial heterojunction

Andreea Costas,^a Nicoleta Preda,^a Camelia Florica,^a Andrei Kuncser,^a Ionut Enculescu^a

^aNational Institute of Materials Physics, 405A Atomistilor Street, Magurele, Ilfov, Romania, 077125

Nowadays, nanoscale optoelectronic devices based on heterostructure nanowires are emerging as a novel class of devices with enhanced performances and new functionalities. Recently, radial core-shell nanowires based on CuO and ZnO, arranged in a type II band alignment, are extremely interesting, their internal structure augmenting the charge carrier separation efficiency, fundamental in photodetector based devices.

The present work proposes a simple path to obtain p-n junction CuO-ZnO core-shell nanowire arrays using thermal oxidation in air and radio frequency magnetron sputtering. Further, the nanowires were successfully integrated as individual photodetecting elements in devices employing lithographic techniques. Moreover, the properties of the prepared CuO nanowire arrays and CuO-ZnO core-shell nanowire arrays were thoroughly analyzed. Thus, Fig. 1 presents the TEM investigations of a single CuO nanowire and of a single CuO-ZnO core-shell nanowire, evidencing a diameter of 50 nm for CuO and of 80 nm for the CuO-ZnO core-shell nanowires. Furthermore, the p-n heterostructure of the CuO-ZnO core-shell nanowires was proved by EDX elemental mappings of a single CuO-ZnO core-shell nanowire.

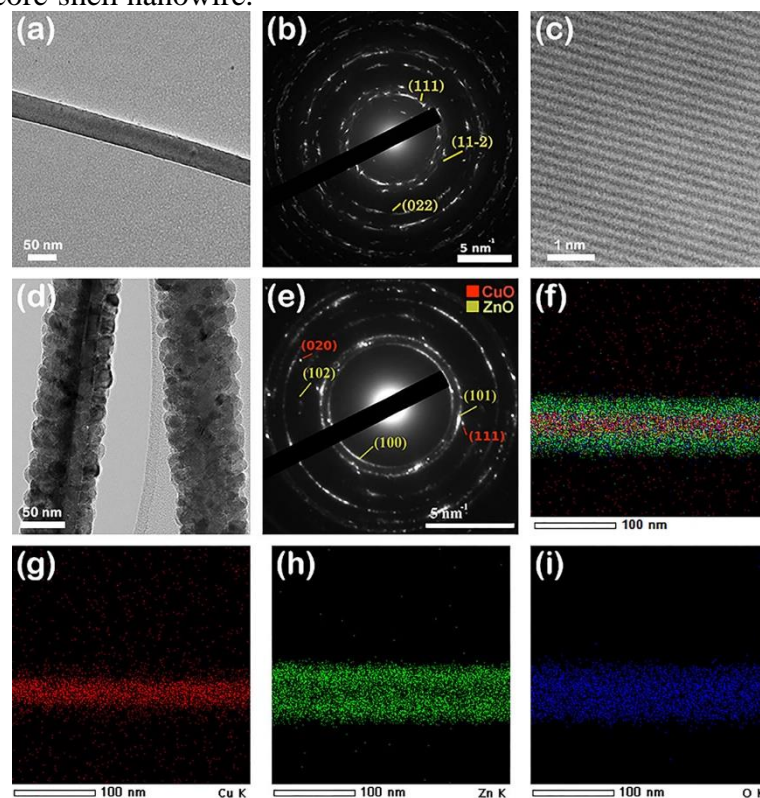


Fig. 1 (a) TEM image, (b) SAED pattern and (c) HRTEM image of a single CuO nanowire; (d) TEM image and (e) SAED pattern of a single CuO-ZnO core-shell nanowire, (f) – (i) EDX elemental mapping of a single CuO-ZnO core-shell nanowire and of its Cu, Zn and O as individual elements.

The FESEM images (Fig. 2 (a), (b)) revealed a typical cylindrical shape and a high aspect ratio for both type of nanowire arrays. Additionally, an average diameter of about 50 nm for the CuO nanowires and of 80 nm for the CuO-ZnO core-shell nanowires can be noticed, being in agreement with the TEM measurements. The XRD patterns of the nanowire arrays (Fig. 2 (c), (d)) confirm the monoclinic phase for the CuO nanowires (core) and the hexagonal wurtzite phase for the ZnO shell.

Also, using Kubelka-Munk representation, the band gap value for the both type of nanowire arrays was estimated at $\sim 1.5 \pm 0.1$ eV (Fig. 2 (e), (f)).

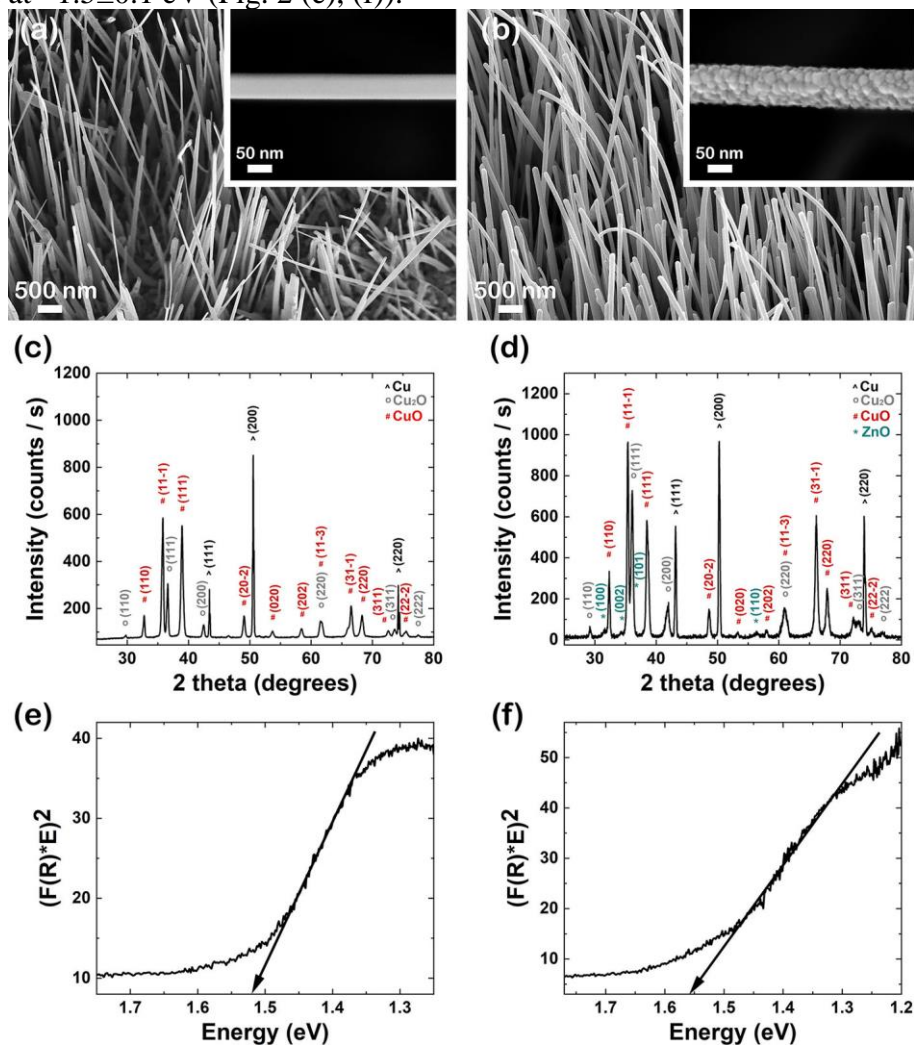


Fig. 2 FESEM images of the obtained array of nanowires: (a) CuO and (b) CuO-ZnO core-shell; (c), (d) XRD patterns and (e), (f) Kubelka-Munk function representations for (c), (e) CuO nanowires and (d), (f) CuO-ZnO core-shell nanowires.

Fig. 3 (a) and (b) evidence the FESEM images of a single CuO nanowire contacted by FIBID (focused ion beam induced deposition) and of a single CuO-ZnO core-shell nanowire contacted by EBL (electron beam lithography) and FIBID. Furthermore, the current-voltage characteristics (Fig. 3 (c), (d)) of the contacted single nanowires exhibit an Ohmic contact for the single CuO nanowire and a rectifying behavior coming from the p-n radial heterojunction formed between CuO and ZnO in the single CuO-ZnO core-shell nanowire.

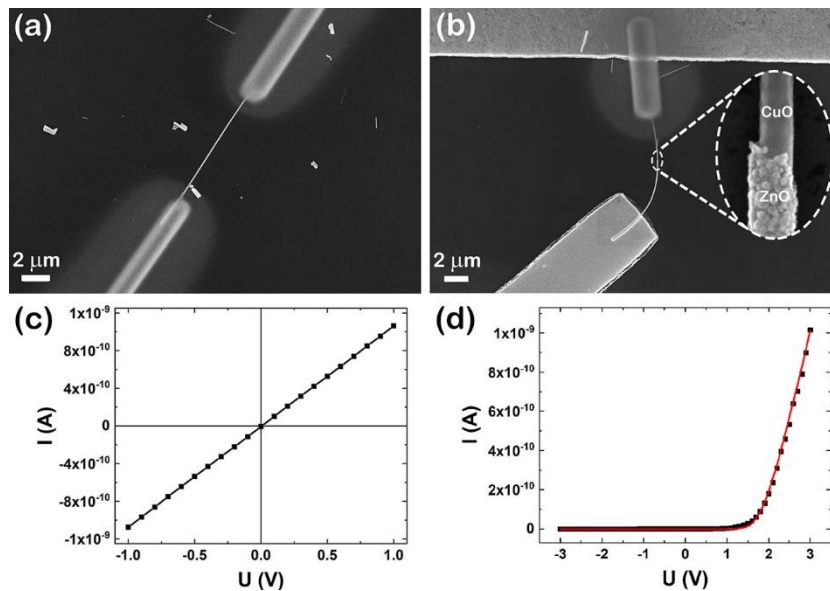


Fig. 3 (a) FESEM image and (c) current-voltage characteristic of a single CuO nanowire contacted by FIBID, (b) FESEM image and (d) current-voltage characteristic (and theoretical fitting) of a single CuO-ZnO core-shell nanowire contacted by EBL and FIBID.

Fig. 4 (a) reveals the current-voltage characteristic of a single CuO-ZnO core-shell nanowire under dark (black) and under illumination at 635 nm (red), 520 nm (turquoise) and 405 nm (magenta) wavelengths, evidencing an increase in the photocurrent for the 520 nm and 405 nm wavelengths. Moreover, the current-time characteristic of the contacted CuO-ZnO core-shell nanowire at 405 nm shows a rise and decay time of 35 s and a photocurrent gain of 4.01 nA, demonstrating a photodetector behavior for the CuO-ZnO core-shell nanowires.

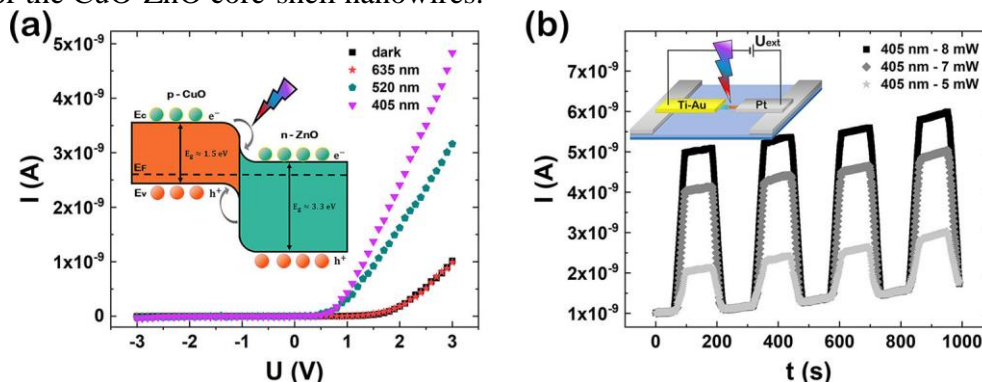


Fig. 4 (a) Current-voltage characteristic of a single CuO-ZnO core-shell nanowire under dark (black) and under illumination at 635 nm (red), 520 nm (turquoise) and 405 nm (magenta) wavelengths and (b) current-time characteristic at 405 nm (at different applied power) for a single CuO-ZnO core-shell nanowire based p-n diode. Inset: schematic representations of: (a) band diagram of the CuO-ZnO heterojunction and (b) of a single CuO-ZnO core-shell nanowire contacted by EBL and FIBID under illumination.

The results proved that these core-shell nanowires having a type II band alignment formed at the CuO-ZnO interface lead to an enhancement of the photodetector performances, promoting them as the new building blocks for the next generation of photodetector devices.

References

1. A. Costas et al., *Photodetecting properties of single CuO-ZnO core-shell nanowires with p-n radial heterojunction*, *Sci. Rep.* **10**, 18690 (2020) [[doi:10.1038/s41598-020-74963-4](https://doi.org/10.1038/s41598-020-74963-4)].

Ionophore-Nafion™ modified gold-coated electrospun polymeric fibers electrodes for determination of electrolytes

Anca Aldea,^{a,b} Elena Matei,^a Ricardo J.B. Leote,^{a,c} Ileana Rau,^b Ionut Enculescu,^a Victor C. Diculescu^{a,*}

^aNational Institute of Materials Physics, Atomistilor 405A, 077125 Magurele, Romania

^bFaculty of Applied Chemistry and Material Science, Politehnica University of Bucharest, Gheorghe Polizu 1-7, 011061 Bucharest, Romania

^cFaculty of Physics, University of Bucharest, Atomistilor 405, 077125 Magurele, Romania

The present research describes a new sensor for detection of electrolytes based on ionophores immobilized within a Nafion™ matrix at the surface of electrodes obtained from gold-coated electrospun polymeric fibers. The sensor surface was characterized by scanning electron microscopy coupled with energy-dispersive X-ray spectroscopy, cyclic voltammetry and electrochemical impedance spectroscopy in order to understand surface morphology and elemental distribution, as well as the electrochemical properties of the ionophores. In order to prove the concept of ionophore-based sensors [1,2] for the analysis of some electrolytes, Ca²⁺, NH₄⁺, Cl⁻ and H⁺ ionophores were immobilized in a Nafion™ matrix at the surface of these flexible electrodes and tested in different media including artificial sweat [3] for the determination of the target ions by potentiometry.

The Au/PMMA/PET electrodes [4] were obtained from poly (methyl methacrylate) submicrometer fibers prepared by electrospinning, coated with a gold layer by magnetron sputtering and then transferred on polyethylene terephthalate (PET). SEM-EDX analysis presented in **Fig 1A** showed a uniform fibers distribution over the entire surface, the fibrous structure of the polymers being maintained with an average diameter of 0.5 μm. The fibers are uniformly coated with gold, which presented a granular structure with granule size of approximately 20 nm.

After the deposition of the mixed Ca²⁺ ionophore- Nafion™ film on the surface of the Au/PMMA/PET electrode, compositional maps by EDX analysis were recorded, **Fig 1B**. The image showed that specific elements of Nafion™ such as sulphur and fluorine are mostly oriented along the fibers direction. At the same time, a specific element of Ca²⁺ ionophore is nitrogen and the EDX map showed a similar orientation, uniformly coating the entire fiber.

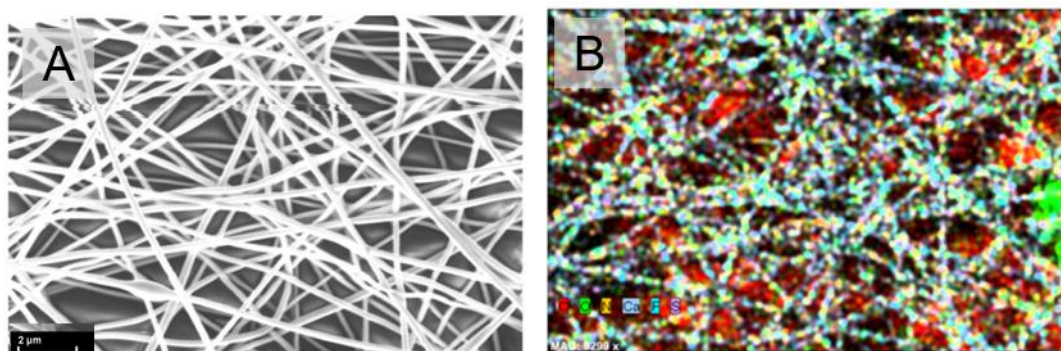


Fig 1. Elemental maps by EDX imaging on the Ca²⁺ ionophore immobilized in Nafion™ matrix at Au/PMMA/PET sensor for: **A)** selected area, **B)** the composed image (fluorine, sulphur and nitrogen). Adapted from ref. [4].

The Ca²⁺ ionophore immobilized in the Nafion™ matrix at the surface of Au/Ti/SiO₂/Si was investigated by cyclic voltammetry in 0.1 M KCl in the absence and presence of Ca²⁺ ions, **Fig 2A**. The voltamogram with the Au/Ti/SiO₂/Si electrode showed the redox peaks specific to gold and the formation of an oxo/hydroxide layer at high positive potential values ($E_{pa} > +0.90$ V) on the anodic component of the voltamogram, and its reduction ($E_{pc} \sim +0.50$ V) on the cathodic-scan. The coating of the electrode surface with Ca²⁺ ionophore imposed a diffusional barrier and, therefore, the redox processes are no longer observed in a pure KCl solution. However, upon addition of Ca²⁺ ions to the electrolyte solution, the redox process specific to gold appeared at their specific potential values

although with lower currents and new evident anodic and cathodic processes related to Ca^{2+} ion diffusion through the specific ionophore occurred at $E_{\text{pa}} \sim +1.20$ V and $E_{\text{pc}} \sim +0.10$ V. This experiment showed that the Ca^{2+} ionophore immobilized in the Nafion™ matrix allows the specific diffusion of the Ca^{2+} target ions at the electrode/solution interface while imposing a barrier to non-specific cations and anions.

Electrochemical impedance spectroscopy was used to investigate the physical and interfacial properties of the Ca^{2+} ionophore immobilized in the Nafion™ matrix at the surface of Au/Ti/SiO₂/Si electrode. Spectra were recorded at open circuit potential values in 0.1 M KCl in the absence and in the presence of different concentrations of Ca^{2+} ion, in the frequency range from 0.1 Hz to 100 kHz. The charge-transfer resistance decreased with increasing Ca^{2+} concentration in agreement with the CV measurements and the admittance plot in **Fig 2B**, which showed the increase of conductivity with solution concentration.

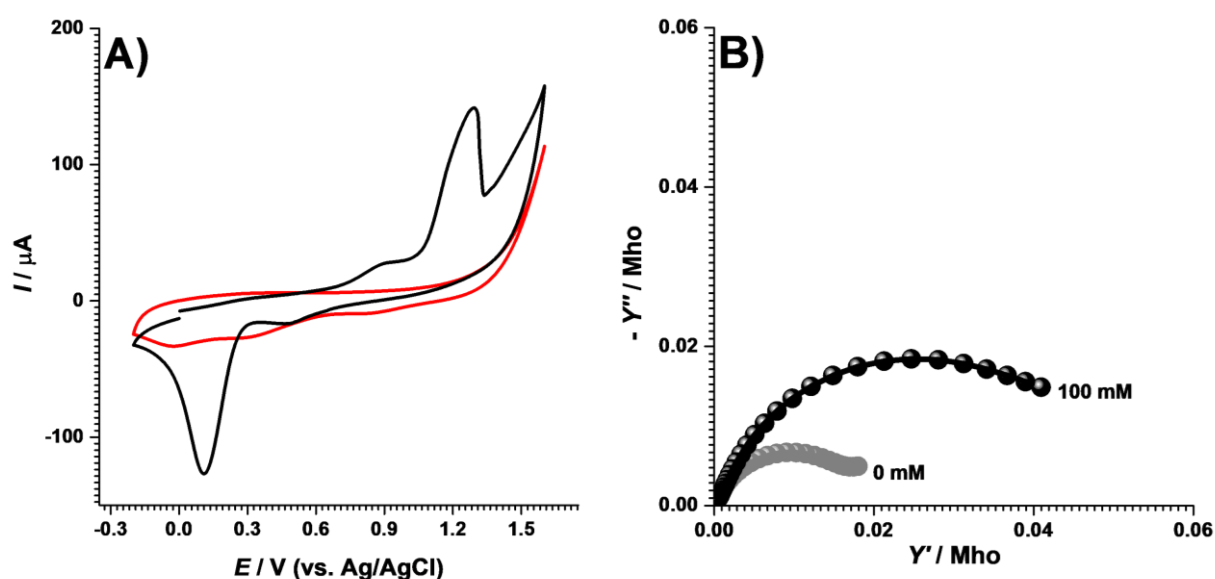


Fig 2. **A)** CVs recorded in 0.1 M KCl, before (red curve) and after (black curve) the addition of 100 mM Ca^{2+} and **B)** EIS (correspondent admittance plot) at OCP in 0.1 M KCl (gray) and in the presence of 100 mM (black) Ca^{2+} recorded at the Au/Ti/SiO₂/Si electrode with the Ca^{2+} ionophore immobilized in Nafion™ matrix. Adapted from ref. [4].

The typical response of the Ca^{2+} sensor obtain on the Au/PMMA/PET electrodes was recorded in artificial sweat (A.S.) and is shown in **Fig. 3A**. The time course of the sensor potential shift was investigated upon changing the Ca^{2+} solution concentration from 1.0×10^{-7} M to 1.0×10^{-3} M. The open circuit potential value increased with increasing Ca^{2+} concentration. The limit of detection calculated was $\text{LOD} = 1.4 \times 10^{-8}$ M. The storage stability of the sensor was also investigated and the response decreased to 80% of the initial value after three days. It has to be taken into account that the sensor fabrication is fast, involves cheap materials and can be considered as a disposable device, being suitable for only one measurement.

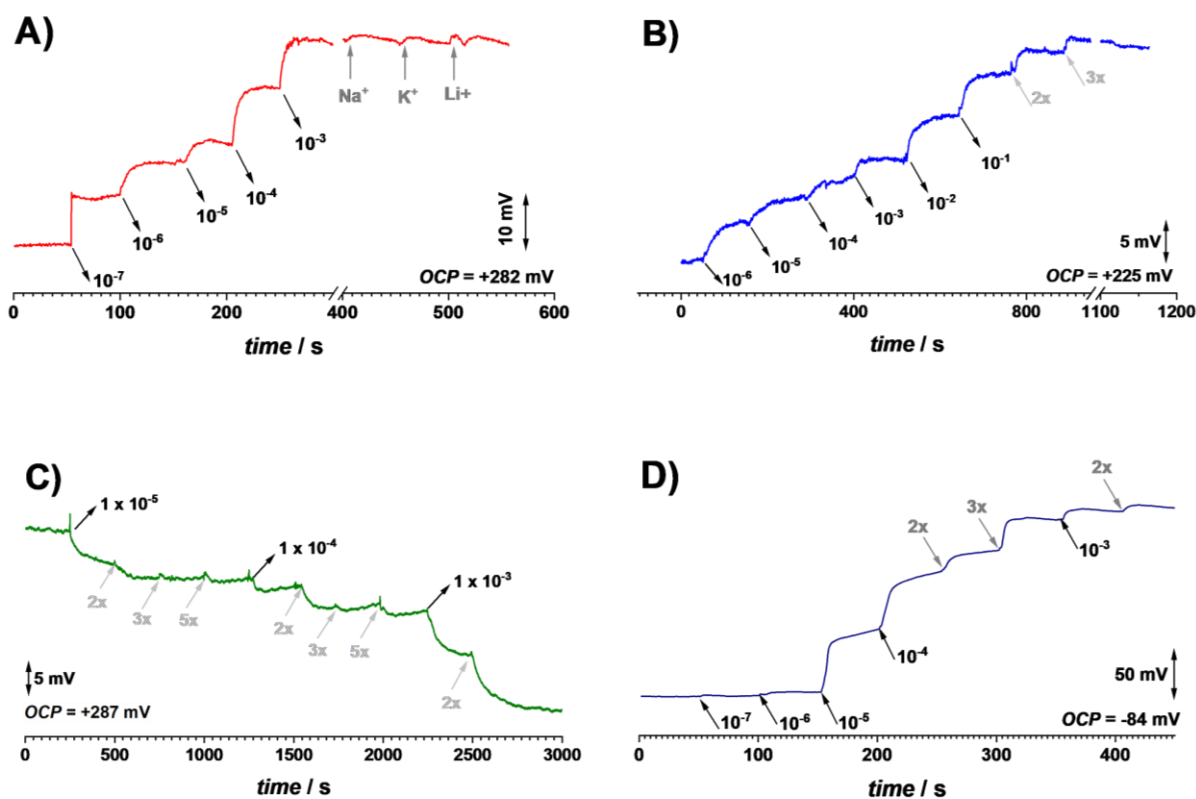


Fig 3. Potentiometric measurements in artificial sweat recorded at the sensors with: **A)** Ca^{2+} , **B)** NH_4^+ , **C)** Cl^- and **D)** H^+ ionophores immobilized in NafionTM matrix at the surface of Au/PMMA/PET electrode after successive injections of different concentrations of target ions and interfering ions. Adapted from ref. [4].

Following the example and the procedures described above, ionophores specific to NH_4^+ , Cl^- and H^+ were immobilized in a NafionTM matrix at the surface of the flexible Au/PMMA/PET electrodes, and the determination of the target ions was performed in artificial sweat. The potentiometric curves are presented in **Fig. 3B-D** and the corresponding detection limits calculated for each ionophore were $\text{LOD}_{\text{NH}_4^+} = 1.1 \times 10^{-7} \text{ M}$, $\text{LOD}_{\text{Cl}^-} = 5.4 \times 10^{-6} \text{ M}$ and $\text{LOD}_{\text{H}^+} = 7.6 \times 10^{-7} \text{ M}$.

In all cases a Nernstian behavior can be observed, in which the potential value increase with concentration for cations, while decreasing for anions. However, in most cases, the sensor sensitivities were below the theoretical values, with the exception of H^+ ionophore, which presented a sensitivity of +55 mV per pH unit.

References

1. M. Parrilla, M. Cuartero, G.A. Crespo, *Wearable potentiometric ion sensors*, *TrAC - Trends Anal. Chem.*, **110**, 303, (2019) [doi:[10.1016/j.trac.2018.11.024](https://doi.org/10.1016/j.trac.2018.11.024)]
2. M. Chung, G. Fortunato, N. Radacsi, *Wearable flexible sweat sensors for healthcare monitoring: a review*, *J. R. Soc. Interface.*, **16**, Article 20190217, (2019) [doi:[10.1098/rsif.2019.0217](https://doi.org/10.1098/rsif.2019.0217)]
3. V.C. Diculescu, M. Beregoi, A. Evangelidis, R.F. Negrea, N.G. Apostol, I. Enculescu, *Palladium/palladium oxide coated electrospun fibers for wearable sweat pH-sensors*, *Sci. Rep.*, **9**, 8902 (2019), [doi:[10.1038/s41598-019-45399-2](https://doi.org/10.1038/s41598-019-45399-2)]
4. A. Aldea, E. Matei, R. J.B. Leote, I. Rau, I. Enculescu, V. C. Diculescu, *Ionophore- NafionTM modified gold-coated electrospun polymeric fibers electrodes for determination of electrolytes*, *Elect. Acta* **363**, 137239, (2020) [doi:[10.1016/j.electacta.2020.137239](https://doi.org/10.1016/j.electacta.2020.137239)]

Electrospun conductive gold covered polycaprolactone fibers as electrochemical sensors for O₂ monitoring in cell culture media

Ariana Serban,^a Alexandru Evanghelidis,^a Melania Onea,^a Victor Diculescu,^a Ionut Enculescu,^a Madalina M Barsan^{a*}

^aNational Institute of Materials Physics, Atomistilor Str. 405A, 077125, Magurele, Romania

Flexible meshes of submicronic diameter polymer fibers fabricated by electrospinning have gained interest and applicability in the medical area, due to the slow biodegradation and biocompatible characteristics¹. Among them, electrospun polycaprolactone (PCL) fibers have many medical applications²⁻⁴, being able to mimic the natural extra cellular morphology (ECM) and thus promote optimal cell growth. Monitoring O₂ levels in 3D tissue constructs is crucial for many tissue engineering applications since the delivery of sufficient O₂ supply is the key for the survival of cells within the scaffold⁵. We propose a fiber mesh made of electrospun PCL fibers covered with Au as an electrochemical sensing platform for O₂ detection⁶.

The sensor fabrication involved two steps: i) the fabrication of PCL polymer fibers by electrospinning a 16% PCL solution in 4:1 w/V chloroform:DMF, at 1.5 mL/h under 15 kV applied potential on the spinneret and ii) the coverage of PCL fiber mats with Au by magnetron sputtering with a 200 nm metallic layer (Au/PCL).

Fig. 1 displays SEM images of PCL electrospun fibers, with similar diameters, of $\approx 1 \mu\text{m}$ and aligned preferentially on one direction in the same plane.

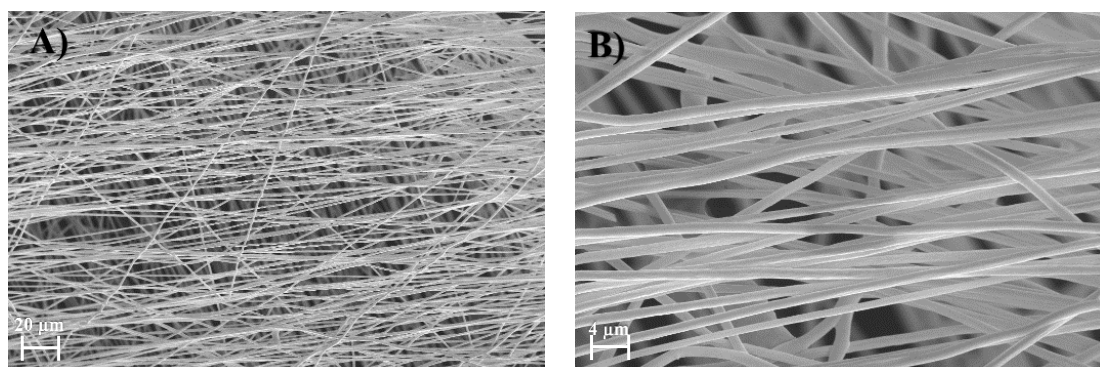


Fig. 1. SEM images at PCL electrospun fibers.

The Au bulk and Au/PCL electrodes were evaluated electrochemically in O₂ saturated phosphate buffer saline (NaPB) solution and showed similar cyclic voltammetric profiles, with significant higher currents recorded at Au/PCL due to its higher surface area. Therefore, the peak current associated with the O₂ reduction is higher by a factor of 2 for the Au/PCL compared to the Au bulk electrode. The scan rate study (Fig. 2A) revealed a diffusion controlled process of O₂ reduction, with a calculated diffusion coefficient (D_{O_2}) value at 25 °C of $4.6 \times 10^{-5} \text{ cm}^2 \text{ s}^{-1}$. The voltammetric profile of Au/PCL was also evaluated in cellular media with the reduction process of dissolved O₂ being similar to that observed in 0.1 M NaPB pH 7.0. The diffusion coefficient $D_{\text{O}_2} = 2.9 \times 10^{-5} \text{ cm}^2 \text{ s}^{-1}$ was lower than in NaPB, but higher compared with pure water⁷.

Cyclic voltammograms recorded at Au/PCL in O₂ (1.3 mM), air (0.25 mM) and N₂ (0.0 mM) saturated solutions (Fig. 2B) showed a decrease of the O₂ reduction peak with the decrease in dissolved O₂ concentration following the equation $j_{\text{pc}} \text{ (mA cm}^{-2}\text{)} = 0.17 + 1.37 \times [\text{O}_2] \text{ (mM)}$, $R^2 = 0.9996$.

Electrochemical impedance spectroscopy spectra recorded at Au/PCL in O₂, air and N₂ saturated NaPB are shown as complex plane plots in **Fig. 2C**. Spectra were fitted using an equivalent circuit presented as insert of Fig. 2C, and consisted in R_s in series with a Warburg impedance W , and a RCPE combination, representing the diffusional process and charge transfer process of O₂ at the Au/PCL, respectively. The results obtained after fitting the experimental data showed that both W

and R increased upon O_2 removal from the solution, as they are correlated to the diffusional process and charge transfer process of O_2 at the Au/PCL, respectively, in agreement with data obtained at a chemisensor for dissolved O_2 detection⁸.

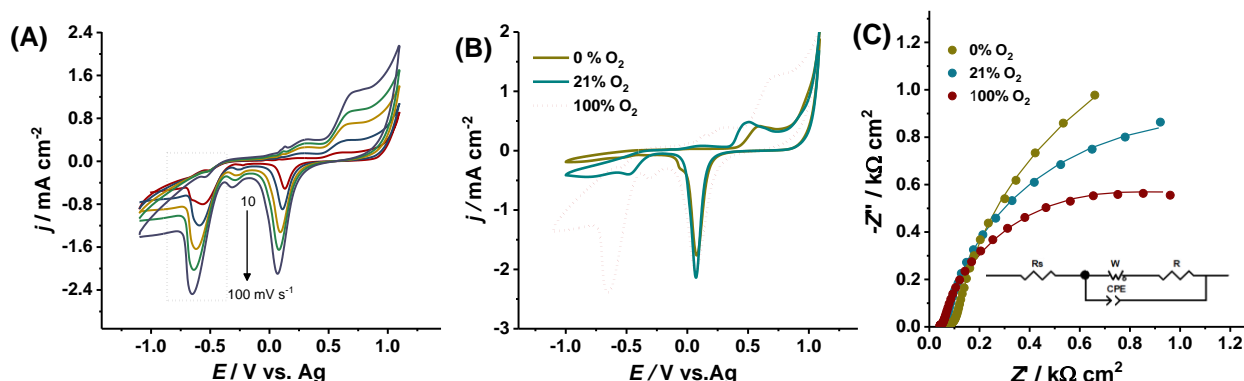


Fig. 2. A) CV-s recorded at Au/PCL in 0.1 M NaPB pH 7.0 at different scan rates; B) CV-s (100 mV s⁻¹) and C) Complex plane impedance plots (10 mV amplitude, frequency range 65 kHz-1 Hz) at Au/PCL in O_2 , air and N_2 saturated solutions-inset is the equivalent circuit used to fit the spectra.

Linear sweep voltammetry (LSV) was recorded in O_2 saturated NaPB (**Fig. 3A**) and in cellular media (**Fig. 3B**) upon successive additions of Na_2SO_3 , showing a gradual decrease of the cathodic peak corresponding to the O_2 reduction, upon consumption of O_2 by Na_2SO_3 . The sensor had two linear domains in both NaPB and cellular media, being of 1.3-0.9 and 0.9-0.5 mM, with sensitivity values of 2.04 and 0.38 mA cm⁻² mM⁻¹, respectively in NaPB (inset **Fig. 3A**).

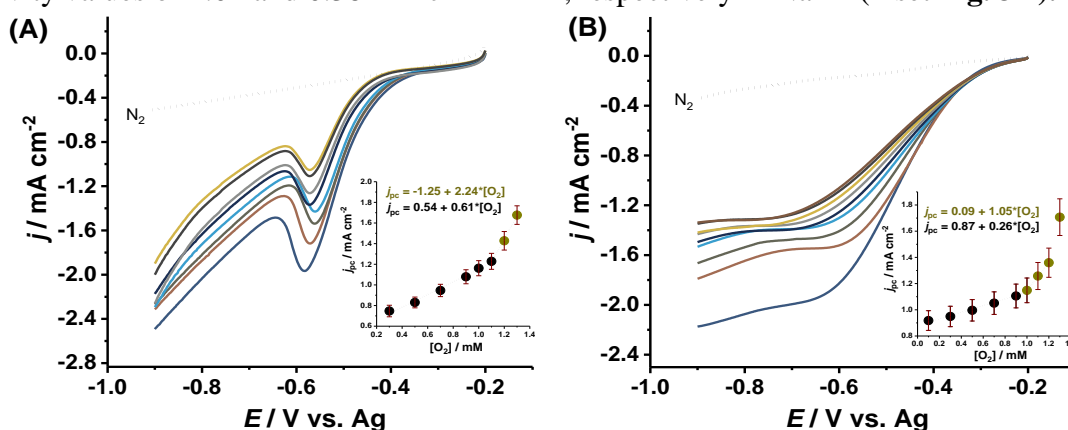


Fig. 3. Linear sweep voltammograms recorded at Au/PCL in A) 0.1 M NaPB pH 7.0 and B) cellular media upon successive additions of Na_2SO_3 in O_2 saturated solutions ($v = 100$ mV s⁻¹).

In cellular media, the sensitivity value of the linear range 1.1-0.9 mM was lower, of 1.02 mA cm⁻² mM⁻¹, while the one for the second linear domain, 0.58 mA cm⁻² mM⁻¹, was higher than that obtained in NaPB (inset **Fig. 3B**). RSD values, corresponding to sensor sensitivity, calculated for 3 different sensors were $\approx 7\%$, indicating a good reproducibility of the sensor fabrication. RSD for three different measurements at the same sensor in the same day was lower than 4%, with a good repeatability of the present analytical method.

O_2 levels in solution were also monitored by EIS, by recording an EIS spectra upon successive additions of Na_2SO_3 in O_2 saturated solution of cellular media, as shown in **Fig. 4A**.

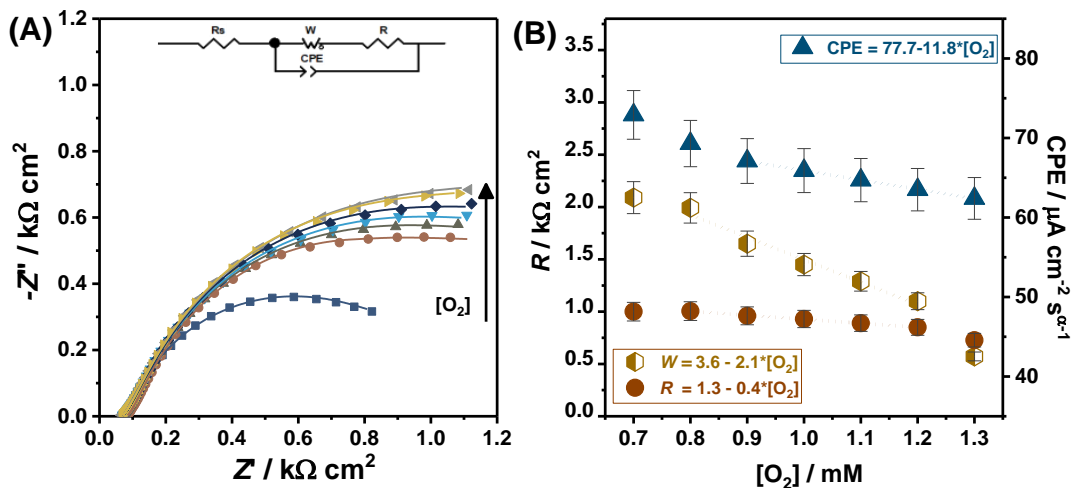


Fig. 4. A) Complex plane impedance plots recorded Au/PCL fibers in 0.1 M NaPB pH 7.0 upon successive additions of Na_2SO_3 in O_2 saturated solution-inset is the equivalent circuit; B) Linear correlation between R , W and CPE values with O_2 concentration.

Spectra were similar to those recorded in NaPB. Sulfite additions lead to changes in the impedance profile only in the middle and low frequency range. Both diffusional resistance (W) and charge transfer resistance (R) values displayed a linear dependency with the amount of O_2 , following the equations: $3.6 - 2.1[\text{O}_2]$, $\text{RSD} = 7.3\%$, $n=3$ and $1.3 - 0.4[\text{O}_2]$, $\text{RSD} = 8.9\%$, $n=3$, respectively (**Fig. 4B**). The values of CPE also decreased linearly by lowering the O_2 concentration ($CPE = 77.7 - 11.8[\text{O}_2]$, $\text{RSD} = 4.2\%$, $n=3$).

The electrochemical measurements revealed the possibility to use the Au/PCL as O_2 sensor in cellular media, promising for their applicability in cellular culture.

References

1. S. Agarwal, J. H. Wendorff and A. Greiner, *Polymer (Guildf)*, 2008, **49**, 5603–5621.
2. M. J. Mochane, T. S. Motsoeneng, E. R. Sadiku, T. C. Mokheba and J. S. Sefadi, *Appl. Sci.*, 2019, **9**, 1–17.
3. J. L. Lowery, N. Datta and G. C. Rutledge, *Biomaterials*, 2010, **31**, 491–504.
4. C. Del Gaudio, A. Bianco, M. Folin, S. Baiguera and M. Grigioni, *J. Biomed. Mater. Res. - Part A*, 2009, **89**, 1028–1039.
5. B. Weyand, M. Nöhre, E. Schmäzlin, M. Stolz, M. Israelowitz, C. Gille, H. P. Von Schroeder, K. Reimers and P. M. Vogt, *Biores. Open Access*, 2015, **4**, 266–277.
6. A. Serban, A. Evanghelidis, M. Onea, V. Diculescu, I. Enculescu and M. M. Barsan, *Electrochem. commun.*, 2020, **111**, 106662.
7. W. Xing, M. Yin, Q. Lv, Y. Hu, C. Liu and J. Zhang, in *Rotating Electrode Methods and Oxygen Reduction Electrocatalysts*, Elsevier B.V., 2014, pp. 1–31.
8. A. Olean-Oliveira and M. F. S. Teixeira, *Sensors Actuators, B Chem.*, 2018, **271**, 353–357.

The use of degenerated TiO₂ semiconductors modified with Ni and Zn in the photocatalytic water splitting reaction

Florentina Neațu,^a Laura E. Abramiuc,^a Mihaela M. Trandafir,^a Raluca F. Negrea,^a Mihaela Florea,^a Cristian M. Teodorescu,^a Ștefan Neațu^{a,*}

^aNational Institute of Materials Physics, 405A Atomistilor Street, Magurele, Romania, 077125

Once with the introduction of the concept of pairing different semiconductors for the water splitting reaction,¹ sustained efforts have been made to develop active photocatalysts for this process. In this direction, different TiO₂-based oxide heterostructures, such as n-type/n-type (e.g. ZnO/TiO₂) or p-type/n-type (e.g., Cu₂O/TiO₂ or NiO/TiO₂) metal oxides, have been designed.² In the second case, during this pairing process, the semiconductors are interfaced by a p-n junction, where the energy bands are bent to reach a new balance between diffusion and migration.³ In this way, a space-charge region is formed and the potential integrated in this region allows an efficient separation of mobile charge carriers, a process which improves the activity of paired semiconductors. Although, for the construction of highly flexible photocatalysts for the separation of photogenerated electron-holes pairs, most studies involve pairing two semiconductors, then preparing and optimizing three-component structures, in which one component acts as an electrocatalyst, should create excellent opportunities for further improvement. Moreover, the concept of “ternary catalysis” has recently been attributed as one to control the effect of three discrete catalysts, each contributing significantly to the reaction result.⁴

In this regard, it seems interesting to explore the photocatalytic activity of composites comprising different p- and n-type metal oxides. In this line of research, this study aims to explore the photocatalytic properties of a ternary system containing some of the most widely used oxide semiconductors (TiO₂ and ZnO) and an exceptional electrocatalyst, such as Ni, whose use could reduce the production costs of the entire composite while performing the water splitting reaction at high conversions.⁵ Thus, in this synthesized report we present only the photocatalytic performance of a new Ni-Zn/TiO₂ ternary composite system for the photocatalytic water splitting reaction. The experimental data derived from the characterization of these materials are presented in detail in a recent ChemCatChem paper (see ref. 5). This report also demonstrates not only the ability of these ternary composites to efficiently split the water, but also provides information in surface science by demonstrating the alignment of ZnO/TiO₂/Ni bands to local heterointerfaces and the formation of degenerate TiO₂ semiconductor, in this case.

Starting from these premises, our group designed and prepared a NiO-ZnO/TiO₂ photocatalytic system capable of splitting water under irradiation with UV light and producing up to 17 mmol H₂ per gram of material per hour, a photocatalytic efficiency of almost 1000 times higher than the one obtained with the help of the most famous photocatalyst, TiO₂ Evonik P25. Given these results, the next step was to optimize the ratio between the components of the photocatalytic system consisting of Ni/NiO, ZnO and TiO₂ Evonik P25. To this end, two directions of research were considered: a) optimizing the ratio between the components of the photocatalytic system so that the yield of the photocatalytic water splitting reaction is as high as possible and at a total cost as low as possible; b) complex structural, morphological and functional characterization of the obtained photocatalysts.

Thus, the synthetic approach adopted in this study, the precipitation-deposition method, allows such optimization to be performed at low costs. To be in line with our research direction, before performing the reaction under UV light irradiation, the optical, structural, morphological and surface properties of the prepared samples were thoroughly investigated using several characterization techniques.

The photocatalytic performances of the samples prepared in the water decomposition reaction are presented in Table 1. The experiments were performed both in the absence and in the presence of

an electron donor (a hole collector), such as sodium thiosulfate or methanol. As can be seen, in the absence of any electron donor, the samples show photocatalytic activity for the overall decomposition reaction of water under irradiation with UV light, generating H₂ and O₂ in almost stoichiometric amounts. The two-component composite systems (Ni-Zn/TiO₂ (1:0) and Ni-Zn/TiO₂ (0:1)) show, under the same reaction conditions, higher photocatalytic activities than those of the pure components.

Table 1. H₂ generation rate on Ni-Zn/TiO₂ photocatalysts under UV light irradiation^[a] and the apparent quantum yield (AQY) calculus.

Photocatalyst	Amount of H ₂ and O ₂ formed ($\mu\text{mol g}^{-1} \text{h}^{-1}$)			AQY(%) ^[c]
	Without sacrificial agent	Na ₂ S ₂ O ₃	Methanol	
TiO ₂ Evonik P25	4 (1) ^[b]	9	18	0.025
1 wt.% Pt/TiO ₂	148 (72)	460	10250	14.46
NiO	2 (0)	5	9	0.013
ZnO	2 (0)	7	12	0.017
Ni-Zn/TiO ₂ (1:0)	16 (6)	94	7250	10.22
Ni-Zn/TiO ₂ (1:1)	106 (46)	314	580	0.82
Ni-Zn/TiO ₂ (3:1)	110 (54)	350	608	0.85
Ni-Zn/TiO ₂ (6:1)	112 (54)	456	5120	7.22
Ni-Zn/TiO ₂ (9:1)	130 (62)	560	17100	24.13
Ni-Zn/TiO ₂ (0:1)	24 (10)	115	256	0.36

^[a]Reaction conditions: 25 mg photocatalyst dispersed in 25 mL solution (deionized water, 1% by weight Na₂S₂O₃ in distilled water or a mixture of deionized water and methanol in a volume ratio of 4:1); irradiation with a MAX-303 illuminator (Asahi Spectra) equipped with UV mode (250–385 nm); 6 hours of irradiation. ^[b]The numbers in parentheses correspond to the amount of O₂ formed during the overall photocatalytic water splitting reaction. ^[c] AQY = 2 × number of moles of H₂ formed × Avogadro's number × 100 / number of incident photons. The following parameters were used to calculate the number of incident photons (1.28×10^{22}): wavelength: 365 nm (XHQA365 high transmission band-pass filter), light intensity: 0.073 W/cm², irradiated area: 4.41 cm².

This behavior could be related to the presence of a Schottky barrier (Ni-Zn/TiO₂ (1:0)) and/or the formation of an n-n homojunction (Ni-Zn/TiO₂ (0:1)), which improves the separation of mobile carriers created in conditions of irradiation with UV light. From the series of ternary composites, it was proven that Ni-Zn/TiO₂ (9:1) is the most active photocatalyst for this reaction (130 μmoles of H₂ and 62 μmoles of O₂ per g of material per hour, respectively). The temporal evolution of the overall water splitting reaction on the Ni-Zn/TiO₂ photocatalyst (9:1) under the same reaction conditions is shown in Fig. 1a, the results obtained highlighting the stability of this photocatalyst.

The addition of Na₂S₂O₃ or methanol as a sacrificial agent allows us to study the process of water reduction (with H₂ generation) by stopping the process of oxygen formation (the water oxidation). When the photocatalytic decomposition reaction of water was performed under such conditions, the rate of hydrogen generation increases and again the most active photocatalyst was found to be the Ni-Zn/TiO₂ material (9:1), which could reach an apparent quantum yield (AQY) of about 24% (see Table 1).

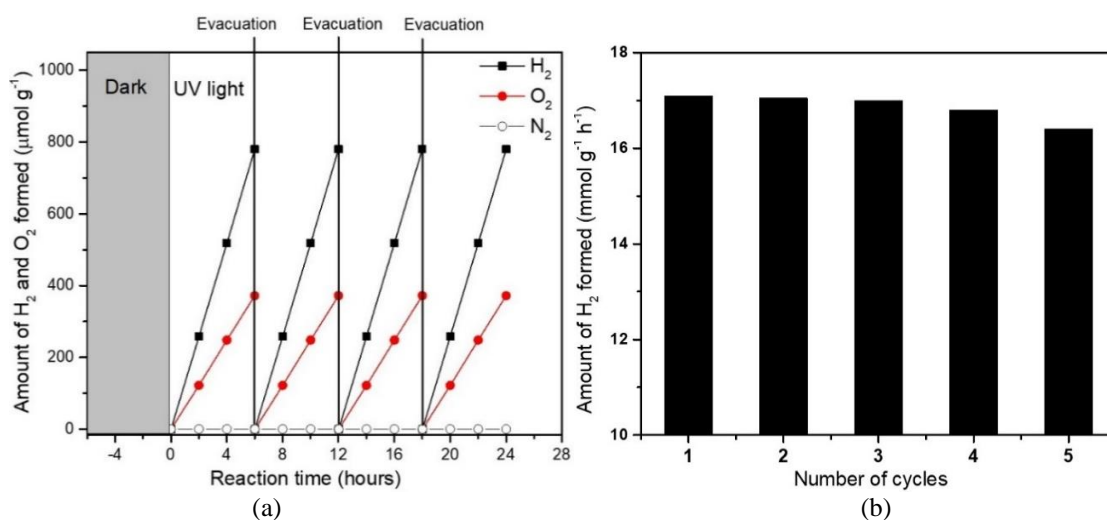


Fig. 1. (a) The temporal evolution of the overall water splitting reaction and (b) cyclic tests for H₂ generation by water decomposition reaction on Ni-Zn/TiO₂ photocatalyst (9:1).

To obtain more information on the stability of the Ni-Zn/TiO₂ material (9:1), cyclic tests were performed for the generation of H₂ by the water decomposition reaction in the presence of methanol as a sacrificial agent (see Fig. 1b).

Given these findings, we could speculate that the optimization between the appropriate amount of electrocatalyst on the surface of a photocatalyst and the number of heterojunctions present inside an oxide heterostructure based on a highly active semiconductor, such as TiO₂ Evonik P25, can intensify the process of hydrogen generation. From this point of view, the current study achieves this goal, but perhaps the highest level of optimization has not yet been reached, and future studies will address these issues.

In conclusion, we showed that active Ni-Zn/TiO₂ materials for the water splitting reaction can be prepared using a simple and low cost synthesis method. A series of Ni-Zn/TiO₂ ternary composites with different Ni:Zn ratios were synthesized by the deposition-precipitation method. Examination of the alignment of the energy band of the best Ni-Zn/TiO₂ photocatalyst by X-ray photoelectron spectroscopy reveals that TiO₂ becomes a degenerate semiconductor, which accumulates electrons and under UV irradiation transfers these electrons to Ni nanoparticles, while the gaps are directed to ZnO. The results open new opportunities in the preparation of very active materials for hydrogen generation based on the optimization of three-component structures.

References

1. A. J. Bard, *Photoelectrochemistry and heterogeneous photocatalysis at semiconductors*, J. Photochem. **10**, 59-75 (1979) [doi:10.1016/0047-2670(79)80037-4].
2. Md. T. Uddin et al., *Band alignment investigations of heterostructure NiO/TiO₂ nanomaterials used as efficient heterojunction earth-abundant metal oxide photocatalysts for hydrogen production*, Phys. Chem. Chem. Phys. **19**, 19279-19288 (2017) [doi:10.1039/C7CP01300K].
3. G. Liu et al., *Charge transport in two-photon semiconducting structures for solar fuels*, ChemSusChem **9**, 2878-2904 (2016) [doi:10.1002/cssc.201600773].
4. S. P. Sancheti et al., *Ternary catalysis: A stepping stone toward multicatalysis*, ACS Catal. **10**, 3462-3489 (2020) [doi:10.1021/acscatal.9b04000].
5. F. Neatu et al., *Degenerated TiO₂ semiconductor modified with Ni and Zn as efficient photocatalysts for the water splitting reaction*, ChemCatChem **12**, 4642-4651 (2020) [doi:10.1002/cctc.202000691].

Synergetic effect of Ni species and undoped SnO₂ manuscript in oxygen evolution reaction

Ștefan Neațu,^a Florentina Neațu,^a Victor C. Diculescu,^a Mihaela M. Trandafir,^a Nicoleta Petrea,^b Simona Somacescu,^c Frank Krumeich,^d Julian T. C. Wennmacher,^{d,e} Amy J. Knorpp,^d Jeroen A. van Bokhoven,^{d,e} Mihaela Florea^{a*}

^aNational Institute of Materials Physics, 405A Atomistilor Street, Magurele, Romania, 077125

^bScientific Research Centre for CBRN Defence and Ecology, 225 Oltenitei Road, Bucharest, Romania, 041309

^c“Ilie Murgulescu” Institute of Physical Chemistry, Romanian Academy, Spl. Independentei 202, Bucharest, Romania, 060021

^dETH Zurich, Institute for Chemical and Bioengineering, Zurich, Switzerland, 8093

^ePaul Scherrer Institute, Viligen, Switzerland, 5232

Alkaline water electrolysis represents an alternative to the actual unfriendly energy conversion and storage systems.¹ This process involves two electrode systems, with oxygen evolution reaction (OER) or oxidation of chemical fuels taking place at anode.² Commercial RuO₂ and IrO₂ are one of the most active OER electrocatalysts.³ However they present low operating overpotential values, therefore a higher attention is directed to find solutions for materials with a correct cost/performance ratio as alternative. Ni-based electrodes are such promising materials which show good electroactivity in OER.⁴ However, these materials need to be adjusted in order to increase the accessibility to active sites, by improving the surface area and the electrons/ions transport at the electrode-electrolyte interface. In this study we emphasize the synthesis bimodal mesoporous SnO₂ support on which was deposited Ni (NiSn), which are very active for OER applications.

Hydrothermal route was used for the synthesis of bimodal mesoporous SnO₂, while the uniform dispersion of Ni onto the support was realized by deposition-precipitation method. Several compositions were considered for this study and the prepared materials contain different Ni loading (1 and 5 wt. %) that were treated at different temperatures (80, 200 and 600 °C). The successful preparation of the materials was confirmed by different characterization methods, such as powder X-ray diffraction (XRD), Raman spectroscopy, scanning electron microscopy (SEM), textural analyses, temperature programmed reduction analysis (H₂-TPR) or X-ray photoelectron spectroscopy (XPS).

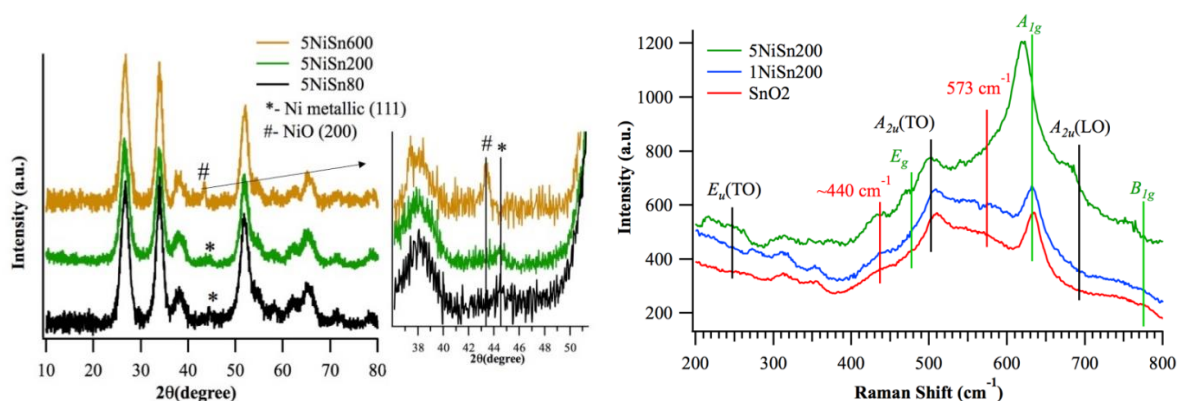


Fig. 1 Powder X-ray diffraction patterns for supported and unsupported SnO₂ based materials (left) and Raman shift for SnO₂ (red), 1 NiSn200 (blue) and 5NiSn200 (green) samples (right).⁵

The textural measurement revealed that pure SnO₂ have a mesoporous structure and high surface area of 134 m² g⁻¹, and the Ni deposition only slightly decrease the surface area (123–128 m² g⁻¹), when sample was treated at 80 and 200 °C. The increase of temperature to 600 °C, leads to Ni species agglomeration and a decrease of surface area with 20–30%. Due to the low amounts of Ni loadings (<5 wt. %), no structural changes were observed in XRD analysis. However, for 5% Ni loading, the presence of NiO and Ni was evidenced in different ratio depending on the thermal

treatment. A higher temperature resulted in a higher amount of oxide, while a lower temperature shown a higher amount of Ni metallic (see Fig. 1). Corroborated with the TPR-H₂ and XPS analyses, the presence of Ni³⁺ was excluded, only Ni²⁺ and Ni⁰ being observed.

The special behavior of these materials is related to the OH⁻ and defects presence at the surface, which were highlighted by Raman spectroscopy and XPS analyses. The material with the highest electroactivity presents an increased number of OH⁻ groups onto the surface and activated modes *A_{1g}*, *B_{1g}*, and *A_{2u}(TO)* in Raman, that normally should be silent. This activation of IR modes was correlated with lattice disorder, surface defects, and oxygen vacancies, most probably produced during synthesis of material. Also observed in Raman, was the appearance of a new shoulder at 440–450 cm⁻¹ associated with intrinsic oxygen vacancies (see Fig. 1). The materials prepared were deposited on electrodes by two methods, immersion and drop casting, and their activity was tested in OER. Between all the materials prepared, the highest currents were revealed for the samples with the higher amount of Ni loading: 5%Ni/SnO₂ treated at 200 °C (5NiSn200) and 600 °C (5NiSn600) (see Fig. 2a). Besides the higher amount of Ni, such behaviour can be due to the presence NiO/Ni(OH)₂ species as evidenced by XPS and XRD, which are essential for the OER process. The OER activity can also be due to the higher conductivity observed, induced by oxygen vacancies. The oxygen vacancies are expected to decrease with thermal treatment at 600 °C, expectation confirmed by the lower electroactivity obtained for the 5NiSn600 sample in comparison with 5NiSn200⁵.

Table 1. Values of equivalent circuit elements obtained by fitting the spectra recorded for different NiSn samples at different potential values in 0.1 M NaOH; equivalent circuit in Fig. 2d.

Material	E (V)	<i>R_s</i> (Ω cm ²)	CPE		<i>R_{ct}</i> (Ω cm ²)	<i>W_s</i>		
			<i>C</i> (F cm ²)	<i>n</i>		<i>R_{diff}</i> (Ω cm ²)	<i>τ</i> (ms)	<i>α</i>
1NiSn200	-0.17 ^[a]	1.02	1.4 × 10 ⁻⁴	0.91	5.5 × 10 ⁴	904	0.877	0.41
5NiSn200	-0.22 ^[a]	1.02	2.5 × 10 ⁻⁴	0.89	2.1 × 10 ⁴	136	0.132	0.32
	+ 0.70	1.4	4.8 × 10 ⁻⁴	0.89	3.2	1.0	0.002	0.50

[a] OCP values

Interfacial properties of the samples were probed by electrochemical impedance spectroscopy in 0.1 M NaOH (Fig. 2d and Table 1). From the spectra fitting resulted a finite diffusional process inside NiO-Ni(OH)₂ layer, depending especially on the film porosity. Moreover, in Table 1 it can be observed that these samples behave as systems with high charge transfer resistances. The *R_{ct}* values decrease with the increase of conductivity when Ni loading enlarged into the SnO₂ matrix. Such diffusional process can be related to the reported high surface area of SnO₂. Additionally, the preparation method used for 5NiSn200 maintains the textural properties of the support and this could be an advantage. Ni species are well dispersed onto the support in the sample 5NiSn200 as evidenced by SEM and TEM.

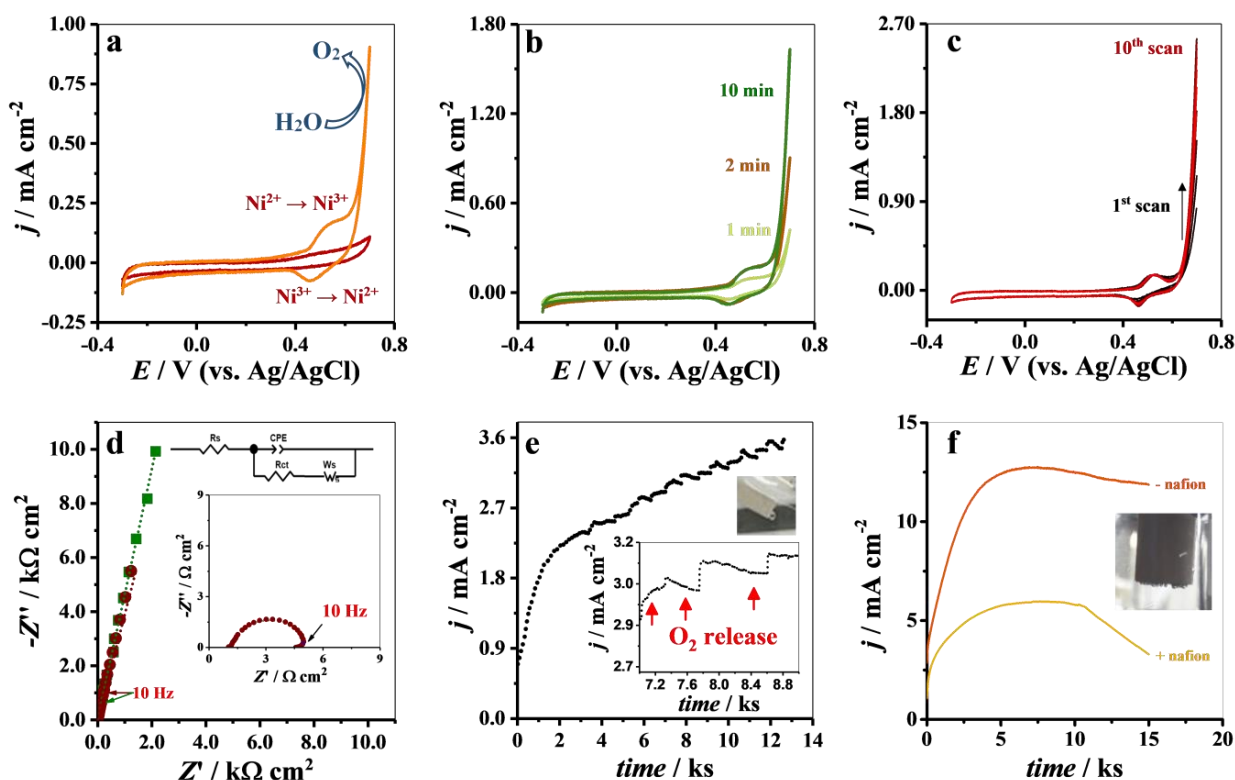


Fig. 2 Cyclic voltammograms in 0.1M NaOH of: **a.** 1NiSn200 (—) and 5NiSn200 (—), first scan at $v = 50 \text{ mVs}^{-1}$ after adsorption during 3 min; **b.** 5NiSn200, first scan at $v = 50 \text{ mVs}^{-1}$ after different adsorption time intervals; **c.** 5NiSn200, consecutive scans at $v = 50 \text{ mVs}^{-1}$ after adsorption during 3 min; **d.** impedance spectra at OCP and at $E = +0.70 \text{ V}$ vs. Ag/AgCl (inset) of 1NiSn200 (■) and 5NiSn200 (●), after adsorption during 3 min; **e.** **f.**: chronoamperogram at $E = +0.70 \text{ V}$ vs. Ag/AgCl in 0.1 M NaOH recorded at 5NiSn200 **e.** after adsorption during 3 min and **f.** drop casted at the GCE surface in 0.1 M or 1.0 M NaOH, with and without a Nafion protective membrane. The insets show current variation upon O_2 bubble release from the electrode surface and the photograph presents the O_2 bubble formation at the surface of the GCE.⁵

In conclusion, the best material for OER (5NiSn200) displays a turnover frequency value of 1.14 s^{-1} and a mass activity of 374 A g^{-1} , which are remarkable results compared to literature data. The synergistic behavior of Ni species and bimodal mesoporous SnO_2 increase the electronic properties and the electrocatalytic activity OER. The features that contribute to this behaviour are high surface area, high number of defects, and high amounts of OH^- species on the surface.

References

1. J. Suntivich et al., *Design principles for oxygen-reduction activity on perovskite oxide catalysts for fuel cells and metal-air batteries*, Nat. Chem. **3**(8), 647–647 (2011) [doi:10.1038/nchem.1093].
2. N. Suen et al., *Electrocatalysis for the oxygen evolution reaction: recent development and future perspectives*, Chem. Soc. Rev. **46**(2), 337–365 (2017) [doi:10.1039/c6cs00328a].
3. Q. Yin et al. *Fast Soluble Carbon-Free Molecular Water Oxidation Catalyst Based on Abundant Metals*, Science **328**(5976), 342–345 (2010) [doi:10.1126/science.1185372].
4. R. Subbaraman et al., *Trends in activity for the water electrolyser reactions on 3dM(Ni,Co,Fe,Mn) hydr(oxy)oxide catalysts*, Nat. Mater. **11**(6), 550–557 (2012) [doi:10.1038/nmat3313].
5. S. Neatu et al., *Undoped SnO_2 as a Support for Ni Species to Boost Oxygen Generation through Alkaline Water Electrolysis*, ACS Appl. Mater. Interfaces **12**(16), 18407–18420 (2020) [doi:10.1021/acsami.9b19541].

The cytotoxicity of ZnO–CdS composites and of AgZnONPs biocomposites on human fibroblast cells

I. Zgura,^{a,*} N. Preda,^a M. Enculescu,^a L. Diamandescu,^a C. Negrila,^a C. Istrate,^a R. Negrea,^a L. Nedelcu,^a M. Bacalum,^b C. Ungureanu,^c M. E. Barbinta-Patrascu^d

^aNational Institute of Materials Physics, Atomistilor 405A, Magurele, Romania, 077125

^bDepartment of Life and Environmental Physics, Horia Hulubei National Institute for Physics and Nuclear Engineering (IFIN-HH), Bucharest, Magurele, Romania, 077125

^cFaculty of Applied Chemistry and Materials Science, University “Politehnica” of Bucharest, 1-7, Polizu Street, Bucharest, Romania, 011061

^d Faculty of Physics, University of Bucharest, 405 Atomistilor Street, PO Box MG-11, Bucharest, Magurele, Romania, 077125

The cytotoxicity on human fibroblast BJ cells of ZnO-CdS-based composites and AgZnO nanoparticles (NPs) biocomposites was investigated. The study presents the results obtained on samples synthesized by the classical chemical method but also by green methods. Such researches are important because the human skin is the first organ which comes into contact with the semiconductor nanostructures. However, to our knowledge, up to now there is no report on the effect of ZnO–CdS composites and on the “green” synthesis of AgZnONPs composites using aqueous vegetal extracts of *Caryophyllus aromaticus L.* flower buds and *Citrus reticulata L.* peels, and their effects on human fibroblast cells.

In the first part of the study, the results obtained on ZnO-CdS composite and pristine ZnO and CdS powders that were synthesized by a simple chemical precipitation method, are presented. ZnO, CdS, and ZnO–CdS powders were synthesized in water, at room temperature, according to the procedure described in [1]. Depending on the CdS concentration (5, 10, 15, 20, and 25 mM), the ZnO–CdS composite powders were labeled as follows: ZnO–CdS5, ZnO–CdS10, ZnO–CdS15, ZnO–CdS20, and ZnO–CdS25 [2]. The morphological and biological properties of the prepared powders were evaluated. The scanning electron microscopy (SEM) images of ZnO–CdS composite powders (Figure 1) reveal flower-like structures, with sizes depending on the CdS amount added during the chemical synthesis. In the following their biological properties are given, such as cytotoxicity of ZnO, CdS and ZnO - CdS compounds (Figure 1 center). The cytotoxicity was tested against BJ cells for concentrations between 0.03 and 0.25 mg/mL; The obtained results are: ZnO and CdS in pristine form do not affect the viability of human fibroblast cells in the range of tested concentrations; for the ZnO–CdS5 composite, the viability of the cells decreases with the increase of the composite concentration, the viability decreasing to ~10% for the highest tested concentration. From the viability curve of this sample, the concentration that reduced the viability of the cells by half (IC₅₀) value was evaluated as being 57 µg/mL. The ZnO–CdS10 composite affects even more the viability of the cells having an IC₅₀ of 50 µg/mL. The other composites, containing larger CdS amounts, were toxic even at the lowest tested concentrations, having IC₅₀ of 17 µg/mL (ZnO–CdS15), 8.7 µg/mL (ZnO–CdS20), and 3 µg/mL (ZnO–CdS25) [2]. Although, the toxicity of ZnO–CdS composites increases with the CdS amount, taking into account the cytotoxic data, the ZnO–CdS5 and ZnO–CdS10 composites can be safely used, at concentrations less than 0.05 mg/mL. In addition, another important result is that the ZnO–CdS composites present biocidal activity against *Escherichia coli*, and by combining the both components into composites, the presence of ZnO improves the CdS water solubility, allowing a considerable better cellular uptake of the ZnO–CdS into the *E. coli* cells.

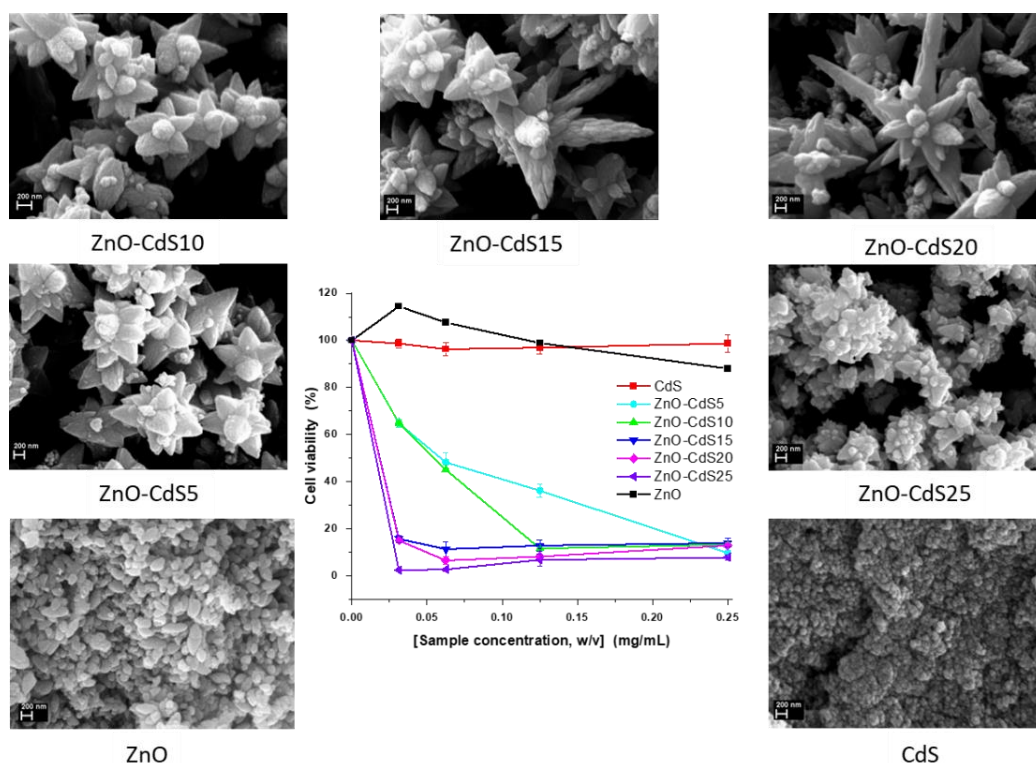


Fig. 1 SEM images of pristine ZnO, CdS and ZnO - CdS compounds. In -center- the cytotoxic effect of ZnO, CdS, and ZnO–CdS powders on BJ cells evaluated using MTT assay. Each value represents the mean \pm SD (standard deviation) of three experiments.

In the second part of the study, the results obtained on metallic and semiconductor nanoparticles (AgNPs, ZnONPs and AgZnONPs) that were phyto-synthesized using aqueous plant extracts from: *Caryophyllus aromaticus L.* (cloves-CUI) and *Citrus reticulata L.* (mandarin-MAND) are presented [3]. The investigated samples are noted as follows: AgZnO-CUI; AgZnO-MAND, ZnO-CUI, ZnO-MAND.

Synthesis of AgZnO composites involves the following stages:

- $\text{AgNO}_3 + \text{phyto-molecules (proteins, sugars and phenolic compounds)} \rightarrow \text{Ag}^0$
- $\text{Ag}^0 \rightarrow \text{AgNPs}$ through the process of capturing Ag^0 by the extract biomolecules
- $\text{Zn(NO}_3)_2 + 2\text{NaOH} \rightarrow \text{Zn(OH)}_2 \downarrow + 2\text{NaNO}_3$
- $\text{phyto-AgNPs} + \text{Zn(OH)}_2 \xrightarrow{100^\circ\text{C}} \text{phyto-AgZnONPs} + \text{H}_2\text{O}$

The “green” synthesis of ZnO-CUI and ZnO-MAND involves the following steps:

- $\text{Zn(NO}_3)_2 + 2\text{NaOH} + \text{plant extract} \rightarrow \text{Zn(OH)}_2 \downarrow + 2\text{NaNO}_3 + \text{plant extract}$
- $\text{plant extract} + \text{Zn(OH)}_2 \xrightarrow{100^\circ\text{C}} \text{ZnONPs (capped with phyto-molecules)} + \text{H}_2\text{O}$

The structure and morphology were investigated by scanning transmission electron microscopy-high angle annular dark field (HAADF-STEM) imaging and energy-dispersive x-ray (EDX) line analysis spectroscopy measurements (Figure 3), and reveal star-like structures in the case of the AgZnO-CUI sample decorated with AgNPs, while in the case of the AgZnO-MAND sample, spherical particles of ZnO decorated with AgNPs were obtained. For pure ZnO-CUI and ZnO-MAND samples, TEM images highlight the ZnO particles in spherical form. The obtained compounds showed biocompatibility (on BJ cells of human fibroblasts). The biocompatibility of the samples was tested against BJ cells for concentrations between 0.012 and 1 mg/mL.

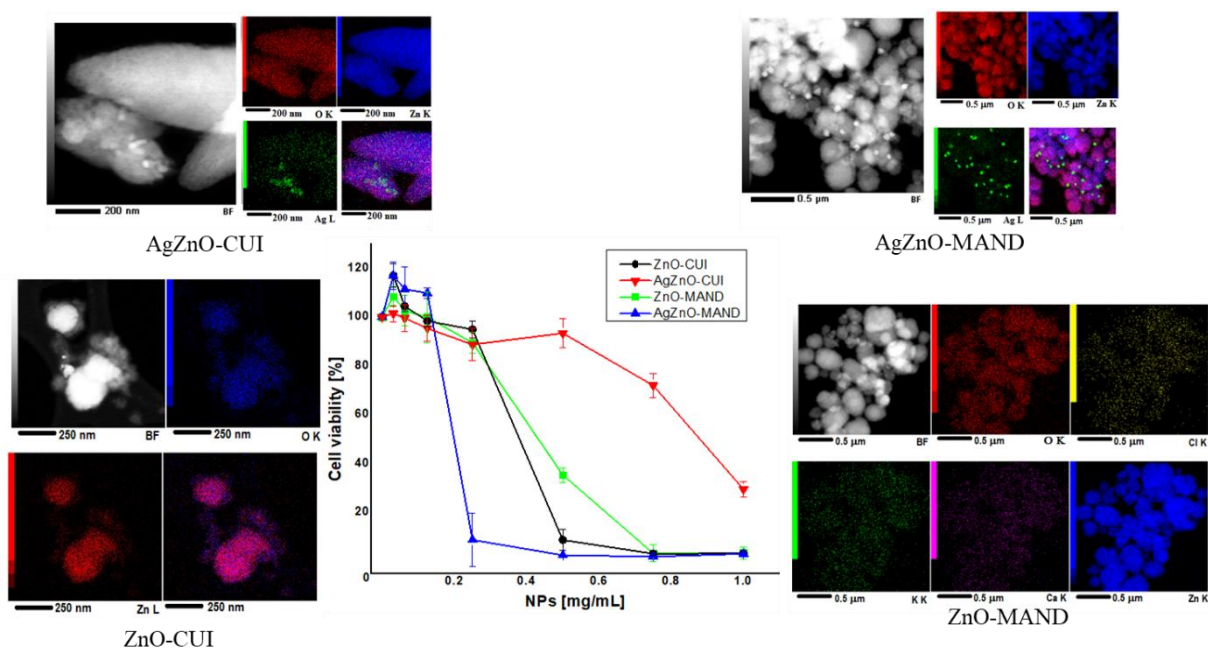


Fig. 3 HAADF-STEM image at low magnification and elementary maps obtained by EDS mapping corresponding to the HAADF-STEM image, for AgZnO-CUI (Ag L-green, Zn K-blue and O K-red), ZnO-CUI (Zn K-red and O K-blue), AgZnO-MAND (Ag L-green, Zn K-blue and O K-red), ZnO-MAND (O K-red, Cl K-yellow, K K-green, Ca K-purple and Zn K-blue). In center: the cytotoxic effect of the samples on viability of BJ cells evaluated at 24h using MTT assay. Each value represents the mean \pm SD of three experiments.

The results are presented in Figure 3. ZnO-MAND and ZnO-CUI samples showed a similar behavior against BJ cells, decreasing cells viability in dose dependent manner with increasing concentrations of the NPs (figure 3 center). Their IC₅₀ values are 0.43 mg/mL for ZnO-MAND and 0.35 mg/mL for ZnO-CUI. AgZnO-MAND proved to be more toxic than ZnO-MAND, reducing the cell viability at ~ 10% for concentrations higher than 0.2 mg/mL. The IC₅₀ value of AgZnO-MAND is 0.22 mg/mL, two times smaller compared to IC₅₀ of ZnO-MAND. The most efficient NPs were AgZnO-CUI. For them, cell viability becomes affected at concentrations higher than 0.6 mg/mL and it decreases at ~30% for the highest concentration tested. When calculated, IC₅₀ was 0.9 mg/mL, almost 3 times higher than the one of ZnO-CUI. Based on these results we can say that from the four obtained NPs, AgZnO-CUI is less toxic for eukaryotic cells. In addition, another important result is that the presence of silver in composite materials has improved the bactericidal action of these nanomaterials against the most common nosocomial pathogen, *Staphylococcus aureus*.

References

1. I. Zgura et al., *Wet chemical synthesis of ZnO–CdS composites and their photocatalytic activity*, Mater. Res. Bull. **99**, 174–181 (2018) [[doi:10.1016/j.materresbull.2017.11.013](https://doi.org/10.1016/j.materresbull.2017.11.013)]
2. I. Zgura et al., *Cytotoxicity, Antioxidant, Antibacterial, and Photocatalytic Activities of ZnO–CdS Powders*, Materials **13**(1), 182 (2020) [[doi:10.3390/ma13010182](https://doi.org/10.3390/ma13010182)]
3. I. Zgura et al., *Performant composite materials based on oxide semiconductors and metallic nanoparticles generated from cloves and mandarin peel extracts*, Nanomaterials, **10**(11), 2146 (2020) [[doi:10.3390/nano10112146](https://doi.org/10.3390/nano10112146)]

Organic heterostructures with hybrid and nanostructured active layer

A. Stanculescu^a, M. Socol^a, O. Rasoga^a, C. Breazu^a, N. Preda^a, A. Costas^a, B. Borca^a, A. M. Solonaru^b, M. Grigoras^b, G. Socol^c, G. Popescu-Pelin^c, A. Mihailescu^c, F. Stanculescu^d, M. Girtan^e

^aNational Institute of Materials Physics, Atomistilor 405A, Magurele, Romania, 077125

^b“P. Poni” Institute of Macromolecular Chemistry, Iasi, Romania

^cNational Institute for Laser, Plasma and Radiation Physics, Magurele, Romania

^dUniversity of Bucharest, Faculty of Physics, Magurele, Romania

^eUniversity of Angers, Lab. LPHIA Angers, France

The synthesis of new organic semiconductors and development of new device configurations represent ways to surpass the limitations related to low mobility of the charge carriers, reduced diffusion length of the exciton and limited interfacial contact area between the donor and acceptor for obtaining organic devices with improved performances.

An alternative for increasing the efficiency of charge carrier collection could be represented by the nanostructuring of the interfaces between the electrode(s) and active layer which can improve both the optical and electrical properties of the heterostructures. The nanostructures can increase the radiation absorption by light trapping, enhance the number of excitons and the number of the charge carriers generated by determining an increase in the current passing through the heterostructure. Therefore it reduced both the transit time between the active layer and electrode and the recombination of the charge carriers in the layer.

On the other hand, fast and long-range charge carrier separation could be obtained by an increased contact area between donor and acceptor which is characteristic for the mixed active layer named “bulk heterojunction” (BHJ). Different small molecule, oligomers and polymers have been tested as donor, while the most studied acceptors are based on fullerene whose main drawbacks are coming from their reduced solubility affecting the homogeneity of the active layer at the nanometer scale. This problem can be surpassed by using non-fullerene acceptors, for example from the family of perylene diimide derivatives.

The studies of the organic heterostructures with nano-patterned electrode and mixed layer based on star-shaped arylenevinylene compound, 4,4',4''-tris[(4'-diphenylamino) styryl] triphenylamine)-IT77 as donor and non-fullerene, N,N'-bis-(1-dodecyl)perylene-3,4,9,10 tetracarboxylic diimide)-AMC14 as acceptor have revealed that the nano-patterning of the ITO electrode was preserved independently of donor:acceptor weight ratio (1:2, 1:3 and 1:4) in the mixt layer deposited by Matrix Assisted Pulsed Laser Evaporation (MAPLE).

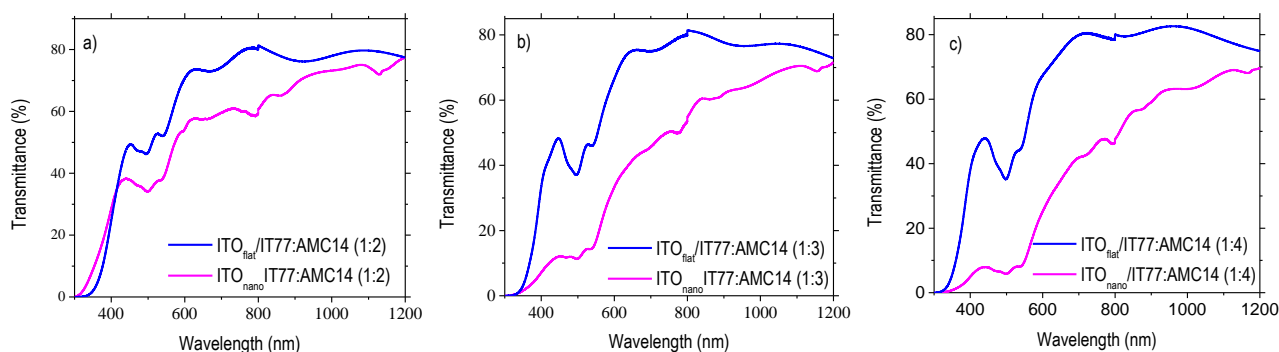


Fig.1. UV-Vis transmission spectra of the organic heterostructures realized on ITO nano-patterned: (a)-IT77:AMC14 (1:2); (b)-IT77:AMC14 (1:3); (c)-IT77:AMC14 (1:4) [1].

The nanostructured transparent conductor electrode (ITO_{nano}) has affected both the UV-Vis transmission and photoluminescence of the mixed layer through the multiple reflections inside the

cavities and at interfaces and particularities of the molecular arrangement [1]. The dips in the NIR transmission spectra of mixed layers deposited on ITO_{nano} can be associated with the plasmonic effect in ITO (Fig. 1) [1]. Even if the patterning was preserved independent of composition (Fig. 2), the roughness slightly increased with increasing the acceptor amount from RMS=46 nm for IT77:AMC14 (1:2) (Fig. 2a) to RMS=52 nm IT77:AMC14 (1:4) (Fig. 2c) [1].

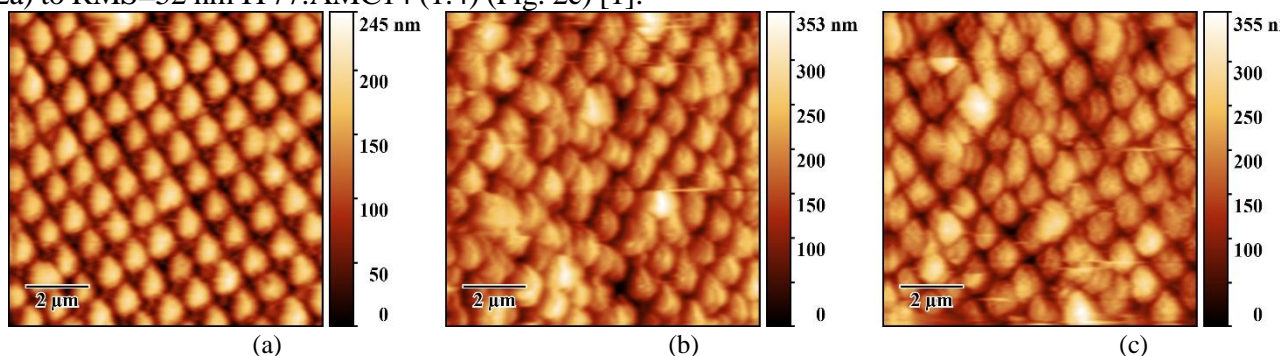


Fig.2. AFM 2D images of organic mixed layer on ITO nano-patterned: (a)-IT77:AMC14 (1:2); (b)-IT77:AMC14 (1:3); (c)-IT77:AMC14 (1:4) [1].

Independently of the mixed layer composition, the I-V characteristics drawn at room temperature in the dark revealed an ohmic contact behavior (Fig. 3). The increase in acceptor content has an opposite effect on the current of the same heterostructure realized on flat and nanostructure ITO electrode [1].

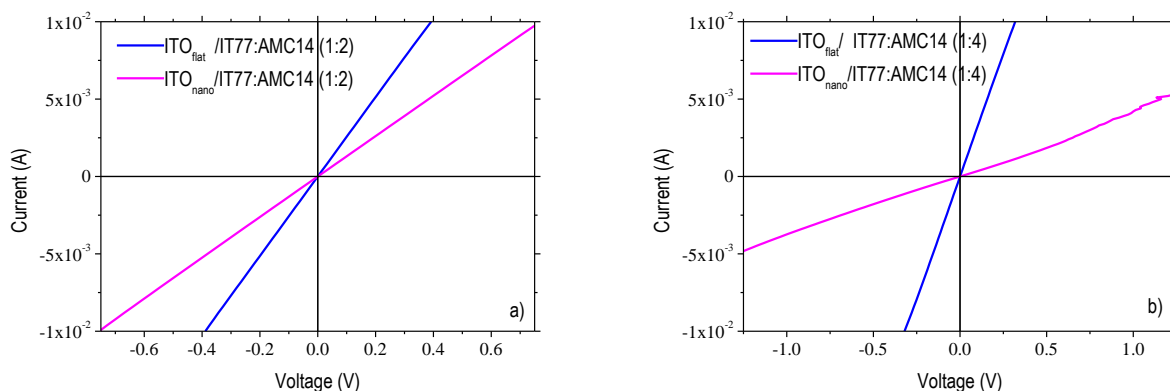


Fig. 3 Comparative I-V characteristics of the heterostructures with ITO_{flat} and ITO_{nano}-patterned: (a)-IT77:AMC14 (1:2); (b)-IT77:AMC14 (1:4) [1].

New insight in the MAPLE deposition of hybrid organic [zinc phthalocyanine (ZnPc)]-inorganic [ZnO] nanoparticles films have been provided, emphasizing the potential of this fabrication approach for the development of the structures with applications in the photovoltaic field. The transmittance and photoluminescence (PL) spectra recorded on hybrid films disclose the optical signature of both organic (ZnPc) and inorganic (ZnO) components (Fig. 4a,b) [2].

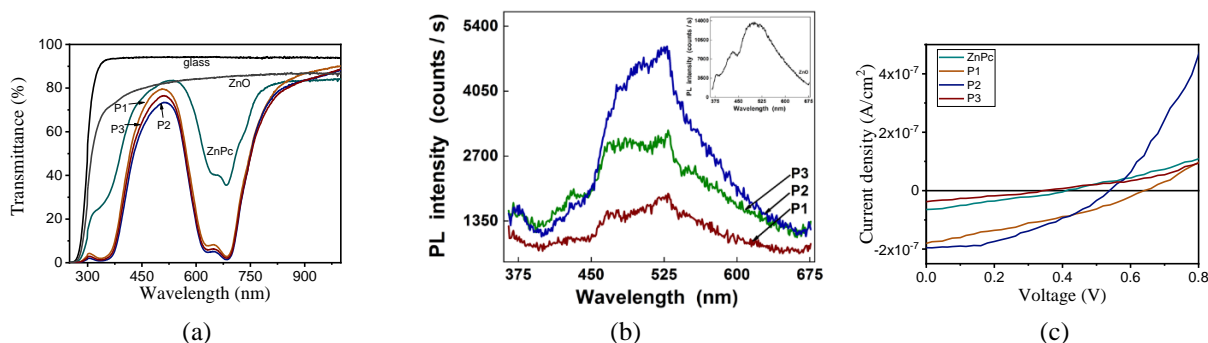


Fig. 4 UV-Vis transmission (a) and PL (b) spectra of ZnPc:ZnO thin films [2]. J-V characteristics of MAPLE ZnPc and hybrid d films (c) [2]. The ratio ZnPc:ZnO was: P1 (1:0.15); P2 (1:0.35); P3 (1:0.55).

The I-V characteristics carried out under illumination of these thin films emphasized the importance of the quantity of the inorganic component on the performance parameters of the structures prepared with the hybrid films and recommend them for potential applications in the photovoltaic cells area (Fig. 4c) [2]. The low mobility of the organic semiconductors and their inefficient charge transport can be overcome by adding inorganic semiconductors in order to obtain hybrid structures.

The investigations of MAPLE deposited hybrid nanocomposite thin films based on cobalt phthalocyanine (CoPc), C60 fullerene and ZnO nanoparticles with different CoPc:C60:ZnO ratio [P0 (1:1:0); P1 (1:1:0.25); P2 (1:1:0.75); P3 (1:1:1)] emphasized that the CoPc signature is dominant in the UV-Vis spectra (Fig. 5a,b), while the ZnO signature prevails in their photoluminescence spectra (Fig. 5c,d) [3]. The study has also revealed that the surface roughness of the hybrid nanocomposite layers is sensitive to the inorganic nanoparticles content (Fig. 6a,b) [3].

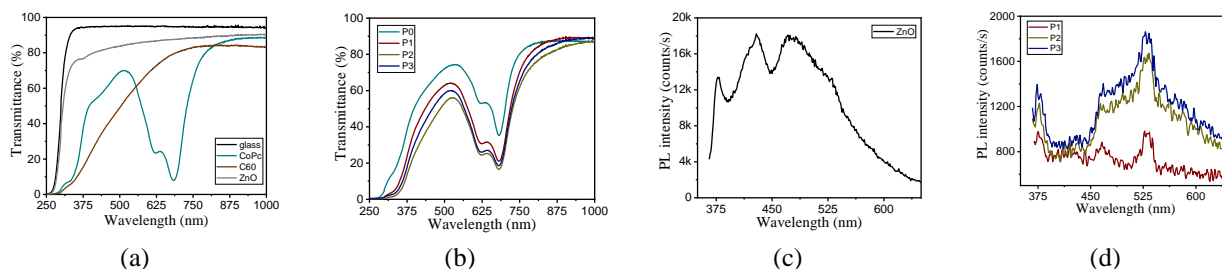


Fig.5: UV-Vis (a,b) and PL (c,d) spectra of MAPLE CoPc:C60:ZnO films [3].

The I-V characteristics of these thin films carried out under illumination emphasized the importance of the quantity of the inorganic component on the performance parameters of the structures prepared with the hybrid films and recommend them for potential applications in the photovoltaic cells area (Fig. 6c) [2].

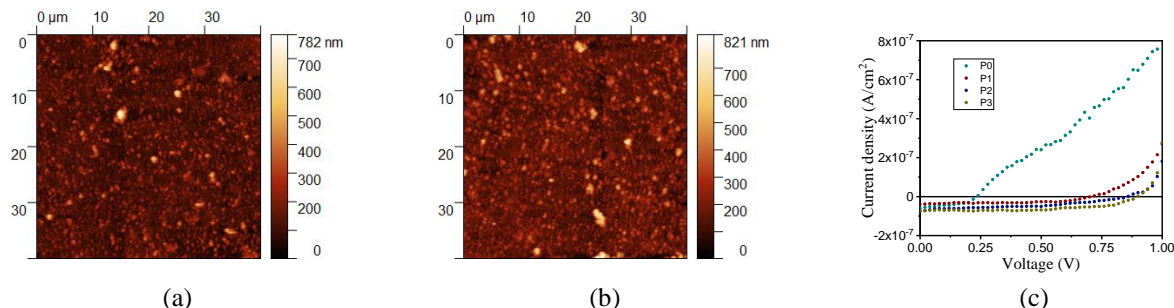


Fig.6: AFM images of organic-inorganic hybrid films [3] (a)-P2; (b)-P3. J-V characteristic of the structures based on MAPLE hybrid layer [3].

A more efficient charge transfer between the organic and inorganic components has been obtained through the addition of an appropriate amount of ZnO nanoparticles in the CoPc:C60 mixture (Fig.6c) [3].

References

1. A. Stanculescu, C. Breazu, M. Socol, O. Rasoga, N. Preda, G. Petre, A. M. Solonaru, M. Grigoras, F. Stanculescu, G. Socol, G. Popescu-Pelin, M. Girtan, *Effect of ITO electrode patterning on the properties of organic heterostructures based on non-fullerene acceptor prepared by MAPLE*, Appl. Surf. Sci. **509**, 145351 (2020) [<https://doi.org/10.1016/j.apsusc.2020.145351>].
2. M. Socol, N. Preda, A. Costas, C. Breazu, A. Stanculescu, O. Rasoga, G. Popescu-Pelin, A. Mihailescu, G. Socol, *Hybrid organic-inorganic thin films based on zinc phthalocyanine and zinc oxide deposited by MAPLE*, Appl. Surf. Sci. **503**, 144317 (2020) [<https://doi.org/10.1016/j.apsusc.2019.144317>].
3. M. Socol, N. Preda, A. Costas, B. Borca, G. Popescu-Pelin, A. Mihailescu, G. Socol, A. Stanculescu, *Thin Films Based on Cobalt Phthalocyanine:C60 Fullerene:ZnO Hybrid Nanocomposite Obtained by Laser Evaporation*, Nanomaterials **10**, 468 (2020) [<https://doi.org/10.3390/nano10030468>].

Low temperature CO sensing under infield conditions with In doped Pd/SnO₂

A. Stanoiu,^a C. Ghica,^a S. Somacescu,^b A. C. Kuncser,^a A. M. Vlaicu,^a I. F. Mercioniu,^a O. G. Florea,^a C. E. Simion^{a*}

^aNational Institute of Materials Physics, Atomistilor 405A, Magurele, Romania, 077125

^b“Ilie Murgulescu” Institute of Physical Chemistry, Romanian Academy, Spl. Independentei 202, Bucharest, Romania, 060021

The present study describes the sensing properties of 1 and 10 mol.% In doped 2 mol.% Pd-SnO₂. Advantages like: low operating temperature, reduced moisture interferences and high selective sensitivity to CO detection were highlighted. The associated sensing mechanism is proposed, based on phenomenological investigations, which provide valuable details about surface reactions. The as-prepared powder samples consist in nanometric crystallites [1] with a size in the range of 5-10 nm. A notable grain size variation appears between the samples with a low content of In, namely the sample Pd1InSn where the average grain size is around 10 nm, and the sample with a higher concentration of In (sample Pd10InSn) where the average grain size is around 5 nm (Figure 1). The TEM measurements confirm the inhibition of the grain growth with the addition of In.

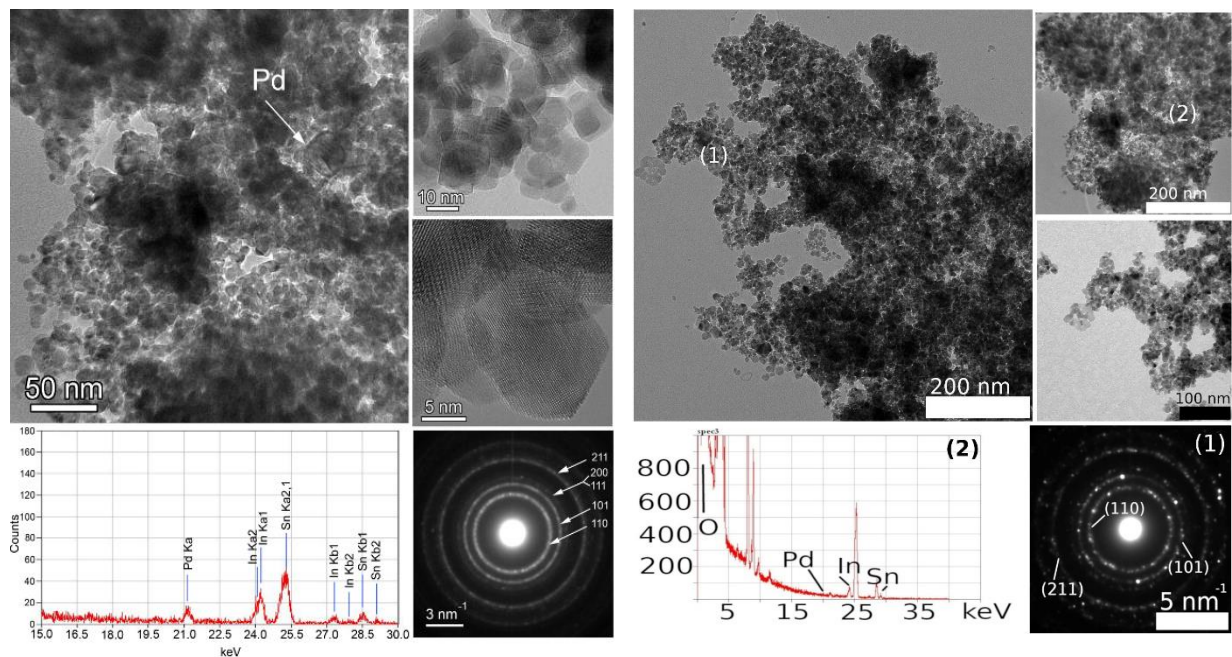


Fig. 1 Typical TEM image, SAED pattern and EDS spectrum of In:SnO₂ nanoparticles decorated with Pd from the sample Pd1InSn (left) and Pd10InSn (right).

Figures 2a-d display the deconvoluted Pd3d and O1s spectra for the Pd1InSn and Pd 10InSn. Pd 3d shows a wide spectrum, that accommodates three doublets (3d5/2, 3/2) under the envelope.

The photoelectron lines have been fitted by using the Voigt functions and the constraints were applied on the relative intensities of the doublet transitions as well as on the spin-orbit parameters. Three different chemical species such as Pd⁰, Pd²⁺ and Pd⁴⁺ were featured on the sensors' surface. In both samples, Pd is present on the surface mainly as Pd²⁺ due to the thermal treatment in air at 600 °C.

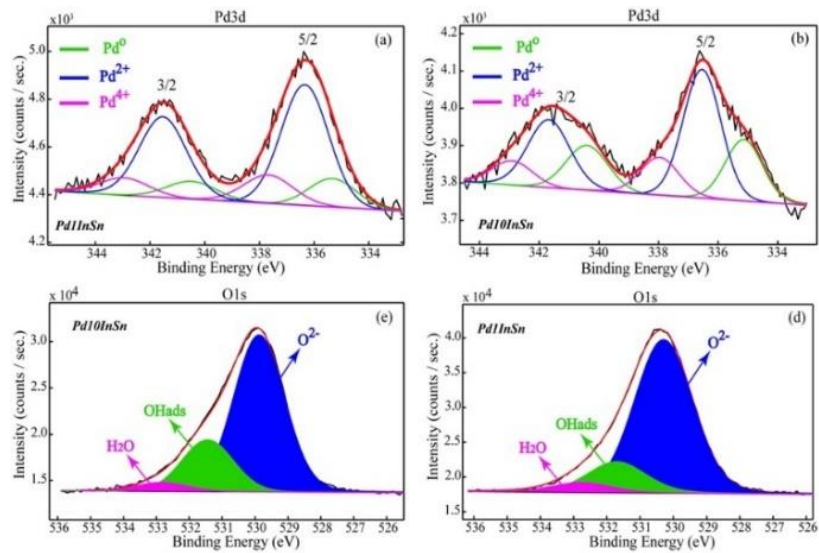


Fig. 2 Pd3d (a, b) and O1s (c, d) high resolution deconvoluted spectra for the samples Pd1InSn, and Pd10InSn.

The sensors have been exposed to different concentrations of carbon monoxide (CO) in dry and humid background (0, 10, 30, 50, 70% RH). The changes of the electrical resistance changes were acquired and represented in figure 3.

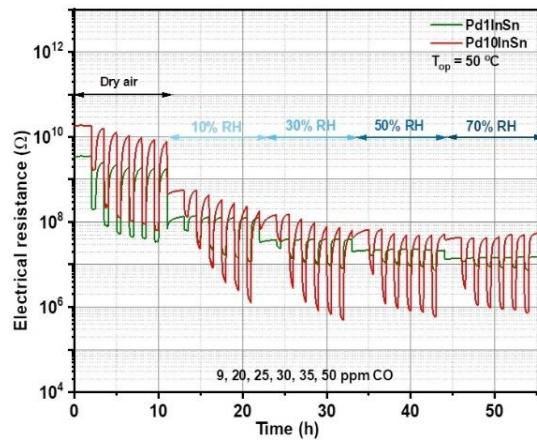


Fig. 3 Electrical resistance behavior towards CO exposure under different RH background conditions.

Aiming to explain the improved sensitivity of Pd10InSn to CO detection and to develop the possible gas sensing mechanism, additional phenomenological investigations have been involved [2, 3]. By simultaneous measurements of electrical resistance and work function changes one can evaluate electronic affinity changes according to the equation below:

$$\Delta\chi = \Delta\phi - e\Delta V_s \quad (1)$$

where: $\Delta\chi$ represents the electron affinity changes; $\Delta\phi$ is the change in work function; $e\Delta V_s$ is the surface potential change due to surface intergranular barriers.

In figure 4 are presented all the energetic potential changes of the Pd10InSn sensor towards CO exposure at 50 °C operating temperature under 50% RH background.

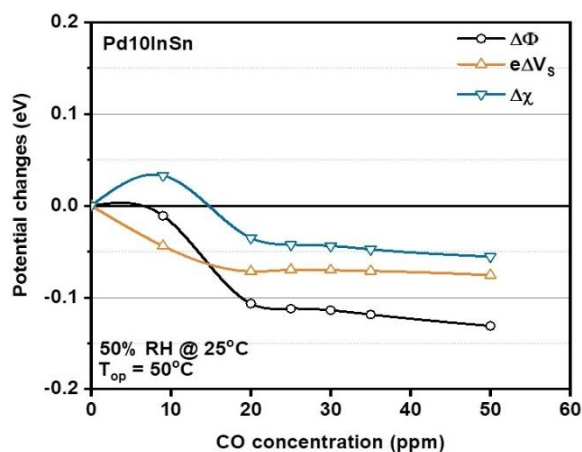


Fig. 4 Potential changes with respect to the CO concentration

Phenomenological investigations suggest the gas sensing mechanisms that involve surface oxygen, hydroxyl groups and low/high CO concentrations. In order to complete the gas sensing properties, Pd10InSn has been tested to different gases, according to the EU exposure limits, respectively: 2500 ppm CH₄, 50 ppm NH₃, 7 ppm SO₂, 50 ppm CO, 3 ppm NO₂ and to the mixture of 50 ppm CO and 3 ppm NO₂ (Figure 5). A comparison with Pd/SnO₂ highlights the effect of In doping over the CO selectivity at low operating temperature, for in-field conditions.

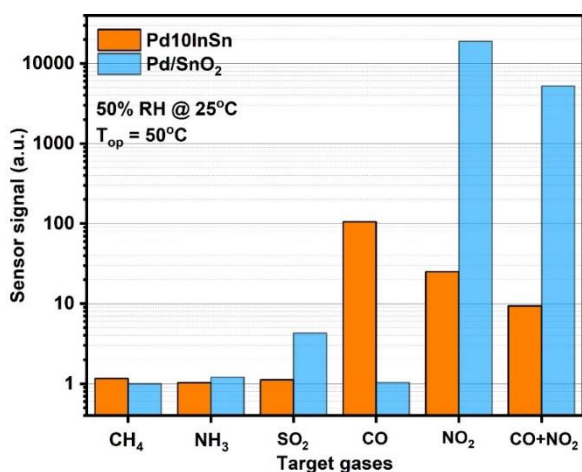


Fig. 5 CO selective sensitivity of Pd10InSn as comparison with Pd/SnO₂

References

1. A. Stanoiu et al., *Low temperature CO sensing under in-field conditions with In doped Pd/SnO₂*, *Sensors & Actuators B-Chemical* **308**, 127717 (2020) [<https://doi.org/10.1016/j.snb.2020.127717>].
2. N. Barsan et al., *Conduction Model of Metal Oxide Gas Sensors*, *Journal of Electroceramics* **7**, 143-167 (2001) [<https://doi.org/10.1023/A:1014405811371>].
3. N. Barsan et al., *Understanding the fundamental principles of metal oxide based gas sensors; the example of CO sensing with SnO₂ sensors in the presence of humidity*, *Journal of Physics: Condensed Matter* **15**, R813–R839 (2003) [<https://doi.org/10.1088/0953-8984/15/20/201>].

GeSn-based structures by magnetron sputtering deposition for short-wave infrared photonics

Adrian Slav,^a Ioana Dascalescu,^a Catalin Palade,^a Aana-Maria Lepadatu,^a Elena Matei,^a Nicolae C. Zoita,^b Sorina Iftimie,^c Florin Comanescu,^d Hermine Stroescu,^e Mariuca Gartner,^e Sorina Lazanu,^a Dan Buca,^f Valentin .S. Teodorescu,^a Magdalena L. Ciurea,^a Mariana Braic,^b Toma Stoica^{a,*}

^aNational Institute of Materials Physics, Magurele 077125, Romania;

^bNational Institute for Research and Development in Optoelectronics, Magurele 077125, Romania;

^cFaculty of Physics, University of Bucharest, Magurele 077125, Romania;

^dNational Institute for Research and Development in Microtechnologies, 077190 Voluntari, Romania;

^eInstitute of Physical Chemistry of the Romanian Academy, Bucharest 060021, Romania;

^fPeter Grünberg Institut 9 (PGI 9) and JARA, Forschungszentrum Jülich, Jülich 52425, Germany.

GeSn alloys have been intensively studied within the last decades offering a realistic alternative to the III–V and chalcogenide compounds that dominate the actual IR and mid-IR photonic market, being the only IV-group direct band gap and CMOS-compatible ecofriendly semiconductor. The transition from Ge indirect bandgap to direct bandgap is obtained in GeSn by increasing the Sn concentration above 6–8%, as earlier theoretically predicted. The increase of Sn concentration does not only increase the directness, but also results in narrowing the bandgap, making GeSn a material for light emitting and detection in the 1.5–3 μm wavelength range, also called short-wave infrared (SWIR). In spite of low miscibility of Ge and Sn (<1%), metastable crystalline GeSn with high Sn content and high crystalline quality were obtained by CVD. However, low-cost and efficient deposition methods, such as the versatile magnetron sputtering (MS) method, are also of high interest. We have reported SWIR detection in optimized GeSn nanocrystals (NCs) embedded in SiO_2 by MS deposition and rapid thermal annealing (RTA).¹ SWIR detection was further improved by two new MS methods of obtaining crystalline GeSn layers as published in Ref. 2 and 3 and presented below: i) GeSn NCs obtained by annealing of GeSn/ SiO_2 multilayer films; ii) GeSn obtained by sputtering epitaxy and its heterostructure with embedded GeSn NCs.^{2,3}

MS-deposited GeSn/ SiO_2 multilayer films.² The random process of NC formation in amorphous monolayers of $(\text{Ge}_{1-x}\text{Sn}_x)_y(\text{SiO}_2)_{1-y}$ alloys obtained by co-sputtering of Ge, Sn and SiO_2 has a consequence in the spreading of the NC sizes and Sn concentration values and in separation distances between neighboring NCs.¹ The control of these parameters is very important for obtaining high photosensitivity of the layers. Thus, a large distance between NCs results in a better passivation of the NCs surfaces, but has a negative consequence by electrical isolation between NCs. The size of the GeSn NCs and their passivation isolation is controlled in GeSn/ SiO_2 multilayer films deposited by MS, by the design of the thicknesses of the GeSn and SiO_2 layers.

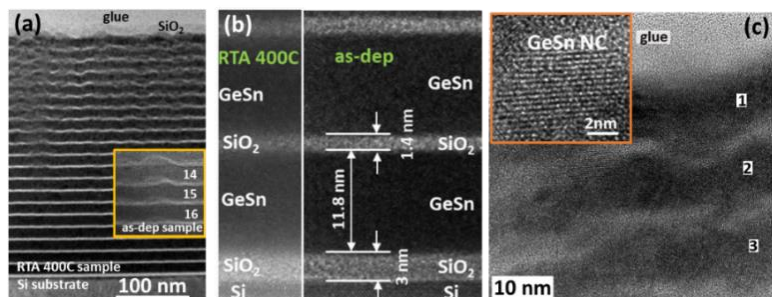


Fig. 1 (a) Low resolution TEM image of the GeSn/ SiO_2 multilayer by RF-MS deposition at 200 $^{\circ}\text{C}$, after RTA at 400 $^{\circ}\text{C}$; (b) HRTEM images of RTA and as-dep layers at Si substrate interface; (c) GeSn NCs in top layers.²

TEM cross-section image of a multilayer film $20\times(\text{Ge}_{1-x}\text{Sn}_x/\text{SiO}_2)/\text{Si}$ obtained by 20 times successive deposition of GeSn and SiO_2 layers on Si substrate at 200 $^{\circ}\text{C}$ is shown in Figure 1a. The morphology of the multilayer structure was preserved after RTA, with GeSn layer thickness of ~ 12

nm and SiO₂ spacers of ~1.5 nm, as shown by the comparison in Figure 1b between the 400 °C RTA and as-deposited (as-dep) samples. The GeSn/SiO₂ bilayer becomes more undulated toward the surface of the film (Figure 1a), that has the origin in a self-formation by deposition on heated substrates (200 °C) of GeSn domes vertically correlated with each other. The undulation is cumulative on vertical, but the thickness of the domes and the NC size remain close to the designed value of ~9 nm, as exemplified in Figure 1c and inset. The GeSn (111) interplanar distance can be accurately measured as 0.3335 ± 0.001 nm, which corresponds to the Sn concentration of 15.3% in GeSn NCs in good agreement to the value of 14.9 % evaluated from XRD analysis of the GeSn (111) diffraction peak. The diffractogram acquired from multilayer film annealed by RTA at 400 °C is compared with those of RTA 450 °C and as-dep samples in Figure 2a of Ref. [2]. The as-dep multilayer sample deposited at 200 °C shows broad maxima specific to the amorphous phase, while the peaks specific to GeSn NCs are clearly revealed for annealed samples. The RTA 450 °C sample additionally shows at 2θ in the range 30-33 degree a broad peak corresponding to metallic β-Sn. This is an evidence that at such annealing temperature Sn segregation from GeSn NCs takes place, decreasing the Sn concentration in NCs from 14.9% at 400 °C to 11.1% at 450 °C. The simulation of the XRD reflectivity measurement on multilayer sample (Figure 2b in Ref. [2]) corresponds to very similar thickness values for the component layers as those obtained by HRTEM analyses, and additionally gives information about the layer density and statistic fluctuations from mean values. The information about the periodic multilayer structure obtained from HRTEM and XRD was used for the simulation of spectral ellipsometry data obtaining the absorption coefficient dispersion (Figure 4c in Ref. [2]). The Tauc representation shows a reduction of the direct bandgap of GeSn multilayer in respect to Ge-bulk to about 0.4 eV in good agreement to the extended SWIR photosensitivity.

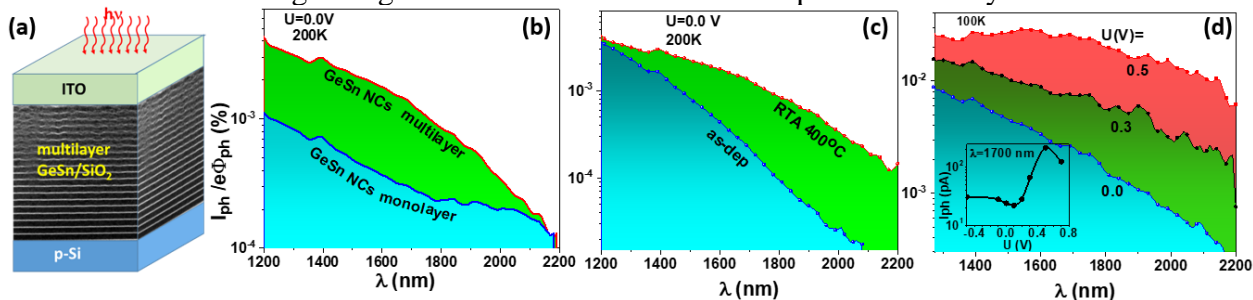


Fig. 2 (a)- schematic sandwich multilayer/Si heterostructure; (b) and (c) spectral photovoltaic current efficiency of the multilayer sample in comparison to the monolayer of embedded GeSn NCs and as-dep multilayers, respectively; (d) increase of the photosensitivity by applied reverse bias of 0.3 and 0.5V (inset - voltage dependence for $\lambda = 1.7 \mu\text{m}$).²

The photosensitivity of the film was investigated by measuring the spectral photocurrent efficiency of a heterojunction of GeSn/SiO₂ multilayer and Si substrate (Figure 2a). The photovoltaic (zero bias) current of the RTA 400 °C multilayer sample is clearly enhanced in respect to embedded GeSn NCs thick monolayer (Figure 2b) and to the as-dep amorphous multilayer (Figure 2c). The spectral photosensitivity is essentially increased and extended to longer than 2.2 μm wavelength for applied reverse voltage of 0.5V (Figure 2d and inset).

MS-epitaxy of GeSn layer and its heterojunction with embedded GeSn NCs.³ In order to avoid the grain boundary recombination in polycrystalline films, we have obtained by MS GeSn NCs embedded in oxide, in which the NC surface is passivated by the oxide matrix, as shown above.^{1,2} Another possibility is to grow GeSn by MS-epitaxy obtaining monocrystalline layers of high crystalline quality with reduced structural defects and improved photosensitivity. We have obtained GeSn films epitaxially grown on Ge virtual substrate (epitaxial Ge relaxed buffer on Si substrate) using high power impulse MS (HiPI-MS) (reported for the first time in Ref. [3]), as well as by the conventional RF-MS for comparison. The co-sputtering deposition of Ge and Sn was performed on heated substrates (200 °C) after in-situ removal of the native Ge oxide. Higher crystalline quality of epitaxial GeSn is obtained by HiPI-MS in comparison to the conventional RF-MS method as revealed by HRTEM and XRD reciprocal space mapping. In Figure 3, one can see by XRD mapping and rocking curves, a clear improvement of the epitaxial crystalline quality for sample epi#2 obtained by HiPI-MS (Figure 3b) in respect to the epi#1 RF-MS sample (Figure 3a), for both samples similar

growth parameters (substrate temperature and growth rate) being adjusted. The TEM analyses have also shown a columnar epitaxial growth and many structural defects and defectuos inter-columnar regions in epi#1 with almost 100% strain relaxation as can be deduced from the equality between $a_{||}$ and a_{\perp} lattice constants in Figure 3d. Instead, the epi#2 is an epitaxial completely strained layer, with $a_{||}$ equal to that of the Ge-buffer lattice constant.

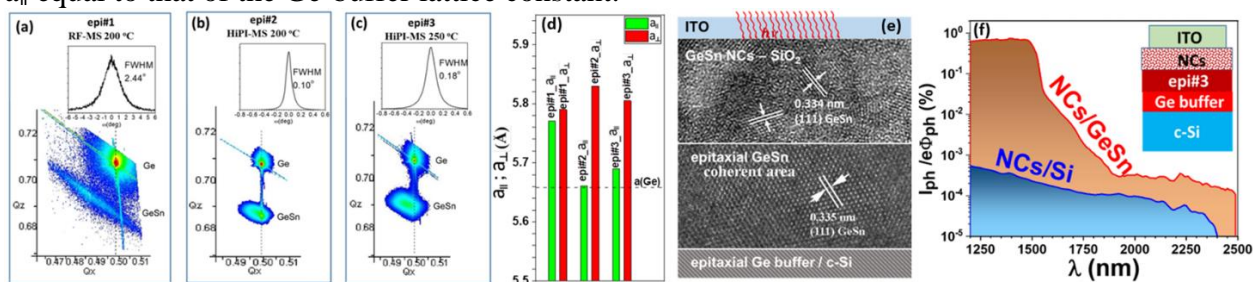


Fig. 3 (a–c) XRD reciprocal space mapping of Ge and GeSn(224) reflection. Insets correspond to GeSn(004) rocking curves. (d) XRD values of $a_{||}$ and a_{\perp} lattice constants; (e) schematic of the NCs/epi#3 heterostructure using HTEM images; (f) photoresponse efficiency of NCs/epi#3 heterostructure compared to embedded NCs on Si.

Using same growth parameters as for HiPI-MS epi#2, but increasing substrate temperature from 200 °C to 250 °C, samples epi#3 of good quality and slightly relaxed were obtained (Figure 3c). The strain relaxation is desired for increasing the directness of the bandgap and extending of the SWIR detection wavelength limit. We have obtained a p-n heterostructure by growing an epitaxial p-GeSn layer of type epi#3 followed by the deposition on top of a n-GeSn embedded NCs monolayer, as schematic shown using HRTEM images in Figure 3d. With this ensemble,³ the SWIR photoresponse is improved in intensity and SWIR extension (Figure 3e) as compared to the heterostructure of the n-GeSn embedded NCs monolayer directly deposited on p-Si substrate (Figure 3f).

References

1. A. Slav, C. Palade, C. Logofatu, I. Dascalescu, A. M. Lepadatu, I. Stavarache, S. Iftimie, S. Antohe, S. Lazanu, V. S. Teodorescu, D. Buca, M. L. Ciurea, M. Braic, and T. Stoica, *GeSn Nanocrystals in GeSnSiO₂ by Magnetron Sputtering for Short-Wave Infrared Detection*, ACS Appl. Nano Mater. **2**, 3626–3635 (2019) [doi:10.1021/acsanm.9b00571].
2. A. Slav, I. Dascalescu, A.M. Lepadatu, C. Palade, N.C. Zoita, H. Stroescu, S. Iftimie, S. Lazanu, M. Gartner, D. Buca, V.S. Teodorescu, M.L. Ciurea, M. Braic, and T. Stoica, *GeSn/SiO₂ Multilayers by Magnetron Sputtering Deposition for Short-Wave Infrared Photonics*, ACS Appl. Mater. Interfaces **12**, 56161–56171 (2020) [doi:10.1021/acsami.0c15887].
3. I. Dascalescu, N.C. Zoita, A. Slav, E. Matei, S. Iftimie, F. Comanescu, A.M. Lepadatu, C. Palade, S. Lazanu, D. Buca, V.S. Teodorescu, M.L. Ciurea, M. Braic, and T. Stoica, *Epitaxial GeSn Obtained by High Power Impulse Magnetron Sputtering and the Heterojunction with Embedded GeSn Nanocrystals for Shortwave Infrared Detection*, ACS Appl. Mater. Interfaces **12**, 56161–56171 (2020) [doi: 10.1021/acsami.0c15887]

SiGe nanocrystals-based photosensors with high sensitivity from visible to short-wave infrared for detection of slippery road conditions

I. Stavarache,^{a,*} C. Palade,^a C. Logofatu,^a V.S. Teodorescu,^a T. Stoica,^a M.L. Ciurea^{a,b,*}, M.T. Sultan,^c A. Manolescu,^c H.G. Svavarsson^c

^a National Institute of Materials Physics, 405A Atomistilor Street, PO Box MG-7, Magurele 077125, Ilfov, Romania

^b Academy of Romanian Scientists, 54 Splaiul Independentei, 050094 Bucuresti, Romania

^c School of Science and Engineering, Reykjavik University, IS-101, Reykjavik, Iceland

Due to tunable electrical and optical properties, SiGe nanoparticles (NPS) in oxides are the most appropriate candidate for various application with short-wave infrared (SWIR) detection requirements. These films are photosensitive as photogenerated holes (in SiGe NPS) are trapped on SiGe related states. We prepared *Al/GeSi-NCs:SiO₂ active layer/SiO₂/n-Si* structures with different SiGe concentrations in SiO₂(Si:Ge:SiO₂ compositions of 25:25:50 vol.% denoted S1 and 5:45:50 vol.% denoted S2). The GeSiSiO₂ layers were co-deposited by magnetron sputtering using three targets of Ge, Si and SiO₂, under DC and RF regimes. The deposition was made on n-type Si wafers chemically cleaned and then covered by 50 nm SiO₂ grown by dry oxidation in a rapid thermal processor (RTP) for electrical isolation of the GeSi-NCs:SiO₂ active layer from Si substrate. The as-deposited films have about 320 nm thickness. The samples were RTA annealed under flowing N₂ gas at temperatures of 700, 800 and 1000 °C. Top Al contacts in planar geometry were deposited.

The films are studied by x-ray Photoelectron Spectroscopy (XPS), Cross Section TEM (XTEM) and measurements of current density-voltage (*J-V*) and photocurrent spectra.

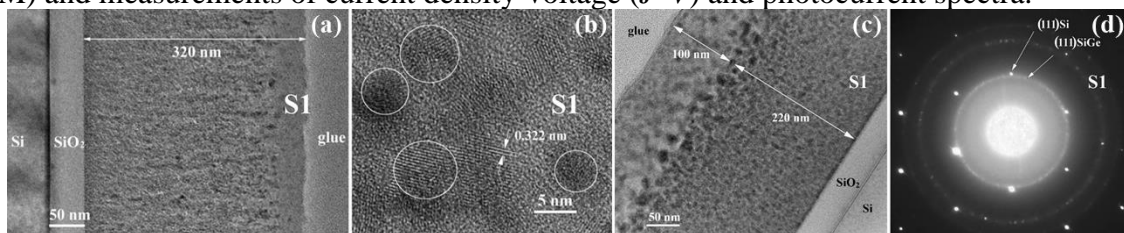


Fig. 1 Morphology of S1 film annealed by RTA for 15 min: (a) 700 °C_low magnification XTEM image; (b) 700 °C_high resolution image of SiGe nanospheres; (c) 800 °C_low magnification XTEM image, (d) 800 °C_SAED pattern of the film and Si substrate, showing the (111) Si spots and (111) ring spots of the SiGe NCs.

Fig.1a shows the TEM image of the S1 film cross section after RTA at 700 °C for 15 min. Small SiGe-NCs are present in the film, but the 40 nm top part of the film is free of NCs. The SiGe NCs have sizes between 5 and 8 nm (see Fig. 1b), and a quite uniform distribution in the SiO₂ amorphous matrix. **Fig. 1c** shows a XTEM image and Fig. 1d selected area electron diffraction (SAED) pattern of S1 sample with 800 °C RTA for 15 min. The morphology is similar to that of 700 °C RTA film, but the top part zone without SiGe NCs is expanded to 100 nm (**Fig. 1c**). At the interface between this zone (free of NCs) and the rest of the film, the SiGe NCs are bigger (from 10 to 15 nm) compared to 5–8 nm NCs from the rest of the film.

Fig. 2a shows the XTEM morphology of the high Ge content film (S2) annealed at 800 °C for 10 min. At the top of the film, one can see an amorphous layer (zone I) that is quite rich in Ge (21.3%) as it results from the EDX spectrum in **Fig. 2c**, followed in depth by a layer (zone II) with low Ge content of 10.5% (**Fig. 2d**) expanded over about 50 nm, containing only few SiGe NCs.

In the lowest part of the film (zone III) there is a uniform distribution (Ge content in film 30%

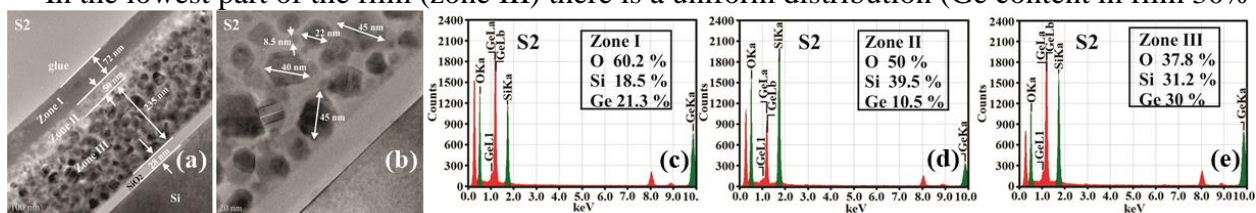


Fig. 2 Morphology of S2 film 800 °C RTA for 10 min: (a) XTEM image showing three zones with different morphology; (b) HRTEM image of zone III at the interface with the substrate, showing the SiGe NCs embedded in the SiO₂ matrix. The big SiGe NCs (over 30 nm) are faceted and contain nanotwins and stacking faults defects.

- **Fig. 4e**) of well crystallized SiGe NCs with sizes between 15 to 50 nm. The NCs bigger than 30 nm are faceted and contain lattice defects like stacking faults and nanotwins (see **Fig. 2b**).

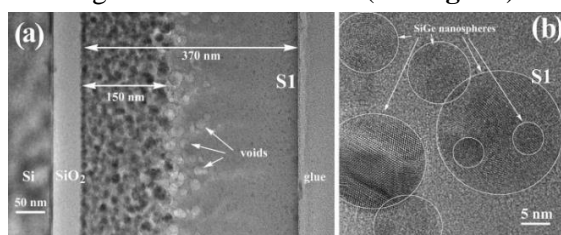


Fig. 3 S1 film annealed at 1000 °C for 15 min: (a) XTEM image; voids are observed in the middle part of film; (b) high resolution detail of SiGe crystalline nanospheres.

Fig. 3 shows a XTEM and HRTEM images taken on S1 film with 1000 °C RTA. In this case the SiGe NCs with sizes ranging between 5 and 25 nm are formed (**Fig. 3b**). The amorphous top part of the film, free of SiGe NCs, is now larger to about 200 nm. One can observe a quite high density of nanovoids (10 – 20 nm size) in the bottom part of the amorphous layer, at the interface with the region containing SiGe NCs. These nanovoids are formed by GeO gas accumulation.

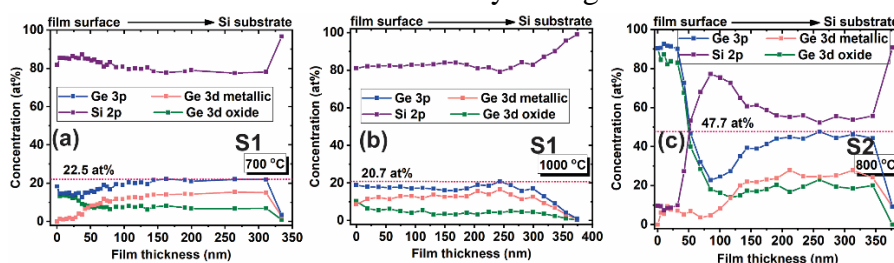


Fig. 4 XPS depth profiles of S1 films with 700 °C RTA for 15 min (a), 1000 °C RTA for 15 min (b) and S2 films with 800 °C RTA for 10 min (c). The curves of atomic compositions in function of depth are given for total Ge, total Si, $Ge_{metallic}$ and Ge_{oxide} .

In **Fig. 4** are shown the XPS results, i.e. atomic compositions of total Ge and Si, and also of metallic and oxidized Ge in the depth of S1 films with (a) 700 °C and (b) 1000 °C, and of S2 films with (c) 800 °C. In the 700 °C annealed S1 film, almost all Ge at the film surface is oxidized, down to ~50 nm and then in depth- the concentration of metallic Ge becomes higher than that of oxidized Ge and remains constant on the whole film thickness (Fig. 4a). In the sample S1 annealed at 1000 °C (Fig. 4b) the concentration curves have similar behavior with those in 700 °C RTA samples but Ge concentration is smaller due to the Ge loss. In sample S2 with high Ge content (**Fig. 4c**), Ge is almost completely oxidized at the film surface, and then in depth Ge is metallic but the concentration strongly decreases down to about 75 nm by Ge loss. For all samples, at depth bigger than 330 nm Ge signal disappears and the Si substrate is evidenced (Si2p peak at 99.7 eV).

Fig. 5 presents photocurrent spectra taken on 800 °C S2 samples. The curves were normalized to the incident light intensity and their maxima. Each figure contains as inset the corresponding spectral responsivity. The samples S2 photosensitivity spectra measured at RT

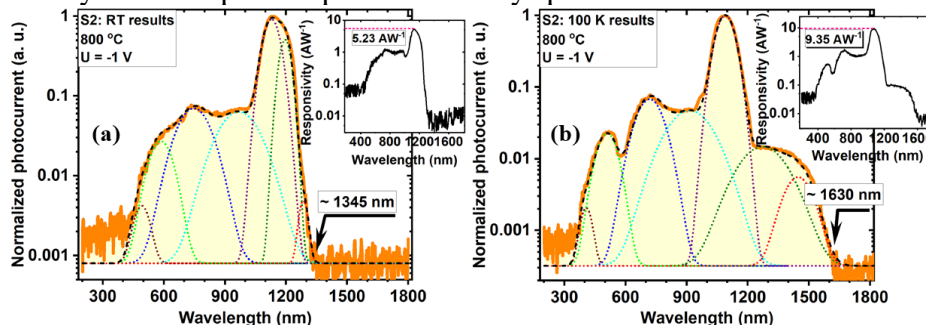


Fig. 5 Normalized photocurrent spectra taken on S2 samples annealed at 800 °C for 10 min and biased at -1 V: (a) measured at room temperature (RT) and (b) at 100 K. The frequency of modulated light was 80 Hz. Each graphic contains as inset the corresponding spectral responsivity.

between 400 nm and 1345 nm and expands to 1630 nm at 100 K. This is explained as follows: (i) the maximum positioned at 1100 nm (from deconvolution) is given by the contribution of Si substrate by surface photovoltage and gating effect; (ii) the photocurrent peak at wavelengths longer than 1100 nm is due to the contribution of GeSi NCs, according to the film morphology; (iii) the main maximum positioned between 710–750 nm is given by the contribution of defects present inside the film that are located at the interface of GeSi NCs/SiO₂ matrix.

Based on these findings we developed a sensor application for slippery road conditions, in the frame of MEra-Net project PhotoNanoP that was awarded as “Success Story”.

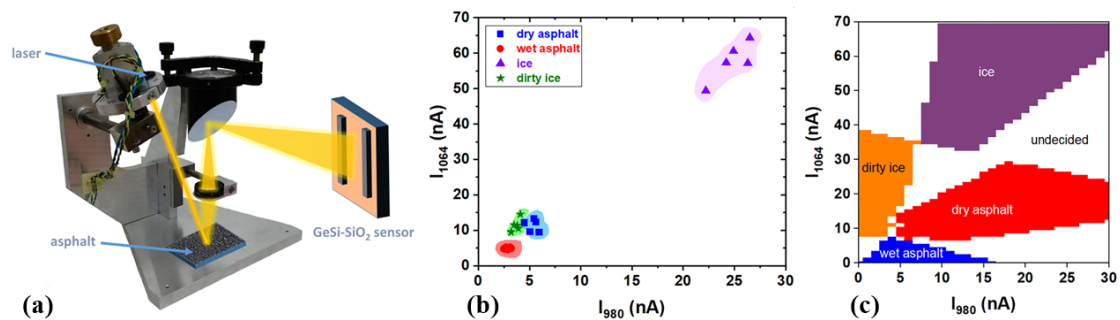


Fig. 6 (a) The working principle, (b) Experimental results obtained by multiple measurements of the photocurrent for the two laser diode illumination in the case of dry, wet, icy asphalt and dirty ice (frozen monolith of mixed asphalt powder, dust and water) and (c) KNN algorithm applied to array data.

The working principle of the proposed optical sensor setup is based on different specular/diffuse reflections of the dry, wet and icy asphalt at different illumination wavelengths that is sketched in **Fig. 6a**. The photocurrent I_{1064} , generated by the $\lambda = 1064$ nm wavelength illumination, is plotted as a function of the photocurrent I_{980} , generated by the $\lambda = 980$ nm illumination. So, a complete determination represents one point in the I_{1064} – I_{980} plot. The experimental results in **Fig. 6b** were obtained by multiple measurements (in different zones of the asphalt) of the photocurrent for the two laser illumination for each case of dry, wet, icy asphalt and dirty ice (a mixture of asphalt powder, dust and water, frozen together). We applied the KNN algorithm to our experimental data by generating an array of 30–70 points in the 0–30 nA and 0–70 nA ranges and classified them in **Fig 6c**. For database analysis by discrimination algorithms, the Python 3.7 programming language was used.

References

1. I. Stavarache et al., *SiGe nanocrystals in SiO₂ with high photosensitivity from visible to short-wave infrared*, Sci. Rep. **10**:3252 (2020) [<https://doi.org/10.1038/s41598-020-60000-x>]
2. C. Palade et al., *GeSi nanocrystals photo-sensors for optical detection of slippery road conditions combining two classification algorithms*, Sensors **20**, 6395 (2020) [[doi:10.3390/s20216395](https://doi.org/10.3390/s20216395)].

SiGe-TiO₂ films and multilayers based on SiGe nanocrystals in TiO₂ with extended SWIR photosensitivity

C. Palade,^a A.M. Lepadatu,^a A. Slav,^a O. Cojocaru,^a V.A. Maraloiu,^a V.S. Teodorescu,^a T. Stoica,^a M.L. Ciurea,^{a,*} S. Iftimie,^b F. Comanescu,^c A. Dinescu,^c M.T. Sultan,^d A. Manolescu,^d H.G. Svavarsson,^d J.T. Gudmundsson^{e,f}

^aNational Institute of Materials Physics, 405A Atomistilor Street, 077125 Magurele, Romania

^bUniversity of Bucharest, Faculty of Physics, 405 Atomistilor Street, 077125 Magurele, Romania

^cNational Institute for Research and Development in Microtechnologies, 126A Erou Iancu Nicolae Street, 077190 Voluntari, Romania

^dReykjavik University, School of Science and Engineering, IS-101 Reykjavik, Iceland

^eKTH Royal Institute of Technology, School of Electrical Engineering and Computer Science, Department of Space and Plasma Physics, SE-100 44 Stockholm, Sweden

^fUniversity of Iceland, Science Institute, Dunhaga 3, IS-107 Reykjavik, Iceland

The research dealt with the study of SiGe nanocrystals (NCs) in TiO₂ in two structures, i.e. single SiGe-TiO₂ films and TiO₂/6x(SiGe/TiO₂)/p-Si multilayers (Fig. 1) obtained by magnetron sputtering (MS) deposition followed by rapid thermal annealing (RTA). The stabilization of alloy SiGe NCs against fast Ge diffusion was aimed in order to ensure short-wave infrared (SWIR)-extended spectral photocurrent due to photocarrier generation in Ge-rich SiGe NCs. The SiGe NCs stabilization was achieved by the formation of SiO₂ thin layers with protective role against Ge diffusion through Si oxidation at the SiGe NCs surface in single films and at SiGe/TiO₂ interface in multilayers. This enabled the obtaining of SWIR sensitivity up to 1.7 μm for films and 1.6 μm for multilayers (Fig. 1), recommending these materials for group IV photonics [1].

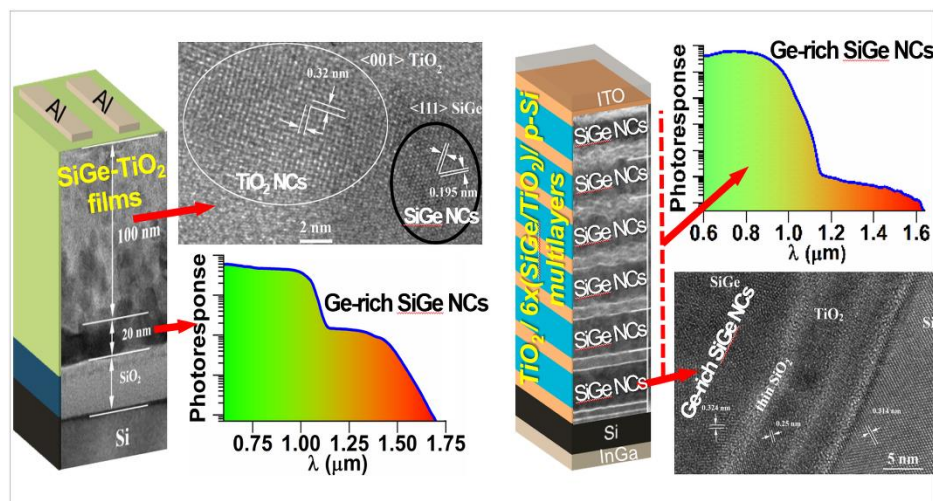


Fig. 1 Summary of the main findings: structure, morphology (by XTEM, HRTEM) and VIS-SWIR photosensitivity of single SiGe-TiO₂ films (left) and TiO₂/6x(SiGe/TiO₂)/p-Si multilayers (right). The schematics of samples with electrodes for photoelectrical characterization are also illustrated.

The structures, i.e. single film of SiGe-TiO₂ alloy and multilayer of TiO₂/6x(SiGe/TiO₂)/p-Si were obtained by using MS of Si (in dc), Ge (dc) and TiO₂ (rf) for layers deposition, followed by RTA. Single films (~120 nm thick) have designed volume concentrations of 50:50 for Si:Ge and 75:25 for (SiGe):TiO₂ and were deposited on thermally oxidized p-Si wafers (maintained at RT during MS). SiGe NCs and TiO₂ NCs formation was achieved by RTA at 800 °C for 10 min.

Multilayers were designed as 6-times repeated layers stacks of 5 nm Ge / 21 nm SiGe (50:50) / 5 nm Ge / 10 nm TiO₂ with a final 10 nm cap TiO₂ layer. The deposition was made on Si substrates heated at 250 °C for helping the SiGe nanocrystallization process (hindered by the TiO₂ spacers). RTA was performed in two steps, first one at 800 °C for 5 min for nucleation followed by a second

one at 600 °C for 20 min for further SiGe NCs growth. Also, Ge and SiGe in the Ge/SiGe/Ge sequences are mixed by RTA and the Ge/SiGe/Ge stack transforms into a Ge-rich SiGe layer.

Structure, morphology and composition were studied by HRTEM, XRD and Raman spectroscopy for elucidating the RTA-induced nanocrystallization process and for explaining the SWIR sensitivity (spectral photocurrent) in both RTA annealed structures. Photoelectrical characterization of single films was made on samples with coplanar Al electrodes, while for multilayers, top-down measurements were performed by using top ITO and bottom InGa electrodes.

In RTA single films, two regions with different morphologies are formed, i.e. a dense Ge-rich bottom one (20 nm thin) with big Ge-rich SiGe NCs (50 – 100 nm length) – Fig.2,c, and another one (100 nm thick) with low Ge content that has a complex structure, especially in the middle film by showing a columnar NCs arrangement of SiGe NCs and TiO₂ NCs (5 – 20 nm size) separated from each other by SiO₂-rich amorphous matrix – Fig. 2a,b. The stabilization of embedded SiGe NCs is induced by Si oxidation (by Si chemical reaction with surrounding TiO₂ matrix) at the NCs surface producing a SiO₂ barrier for Ge diffusion outside the SiGe NCs. The Ge content in the SiGe NCs from the bottom region is 77% ± 8%, while in the SiGe NCs from the rest of film is 37.5% ± 12.5%.

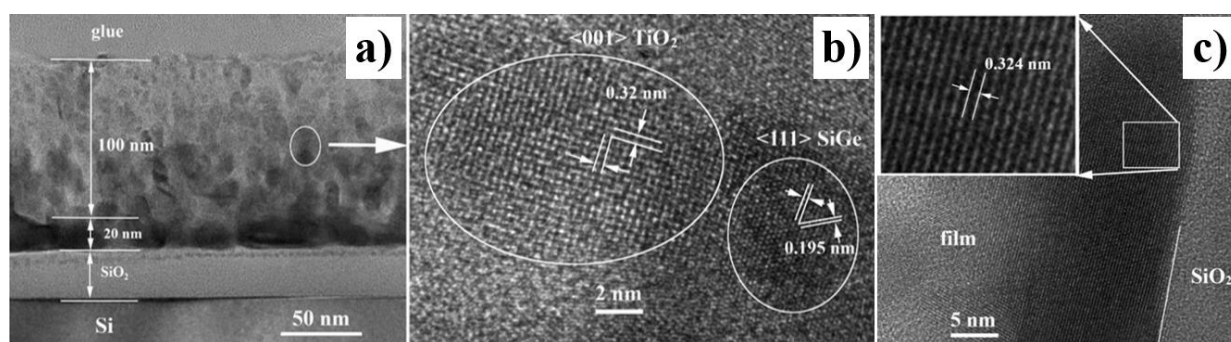


Fig. 2 SiGe NCs-based single SiGe-TiO₂ films: a) low magnification XTEM image; b) HRTEM detail from the middle of film; c) HRTEM image of the bottom part of film.

In RTA multilayers, the resulted Ge-rich SiGe layers formed of SiGe NCs are bordered by protective rich-SiO₂ thin films at interfaces with TiO₂ layers (Fig. 3). The SiO₂ thin layers have a protective role against Ge diffusion and are formed through Si oxidation at SiGe/TiO₂ interface.

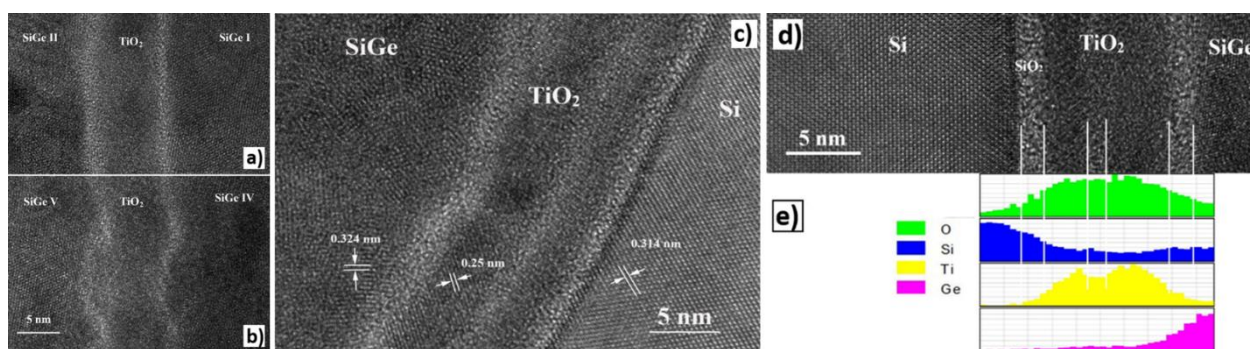


Fig. 3 SiGe NCs-based multilayers: HRTEM images of crystallized TiO₂ layer at (a) bottom and (b) near free surface of multilayer. (c) HRTEM image near the interface with Si substrate. (d) HRTEM image and (e) line scan EDX show the separation (after crystallization) in two parts of as-deposited bottom TiO₂ layer at the interface with Si substrate.

SiGe NCs have average size of 8 nm at the top of multilayer and 6 nm at the bottom. A stress field in the SiGe lattice is developed, being highly visible at the bottom of multilayer (Fig. 3a, b show that TiO₂/SiGe layers interfaces are quite flat and well defined by SiO₂ thin layers in the bottom part, while they are sinuous and non-precise in the top part of multilayer). The stress field is related to the partial crystallization of amorphous TiO₂ layers into dense rutile and the space resulted from contraction is filled with low density SiO₂ (Fig. 3c–e). The stress field compensates the local anisotropy of crystallization process in the bottom part, while at the sample surface, SiGe NCs growth is not constrained by the stress field.

In single films, enhanced SWIR photocurrent up to 1700 nm mainly due to the big Ge-rich SiGe NCs formed at the film bottom is obtained (**Fig. 4a1**). The photocurrent shows a super-linear voltage dependence due to field-effect electrostatic doping (**Fig. 4a2**).

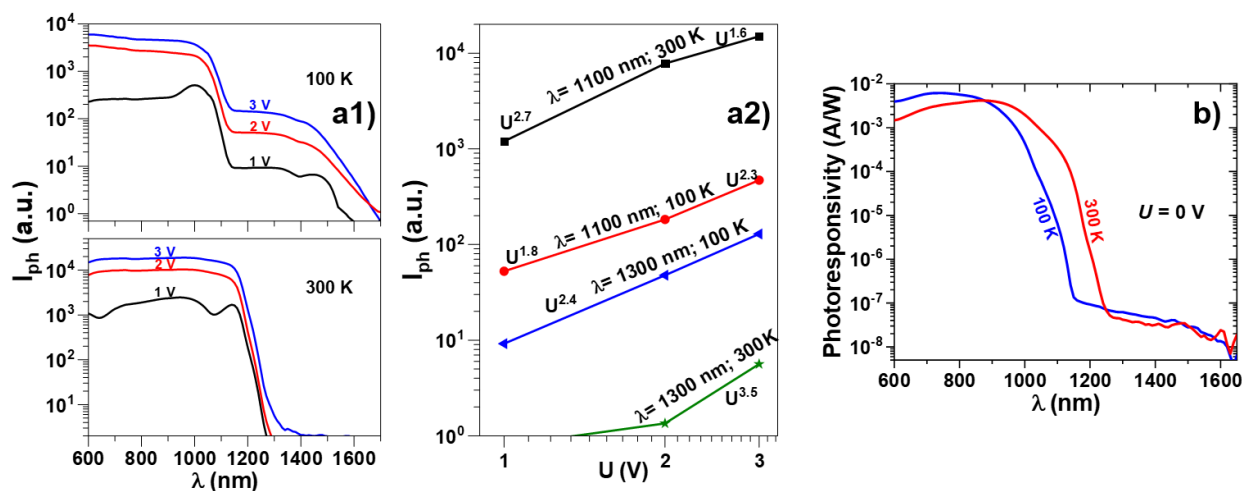


Fig. 4 Photocurrent results: single films – a1) $I_{ph} - \lambda$ spectra ($T = 300$ and 100 K, $U = 1, 2$ and 3 V), a2) $\log I_{ph} - \log V$ dependences ($\lambda = 1100$ and 1300 nm); multilayers – b) $I_{ph} - \lambda$ curves measured in photovoltaic regime ($T = 300$ and 100 K, $U = 0$ V). Illumination was done with monochromatic light modulated at 120 Hz.

SWIR sensitivity for multilayers up to 1600 nm is obtained in the spectral photocurrent measured in photovoltaic regime at 300 and 100 K, being due to the light absorption in Ge-rich SiGe NCs. In collaboration with Icelandic partners (in M-Era.NET PhotoNanoP), the formation of SiGe NCs by MS deposition only, without annealing was also demonstrated [2]. For this, $\text{TiO}_2/\text{SiGe}/\text{TiO}_2/\text{SiO}_2$ on Si structures were fabricated using a combination of dc MS for Si sputtering and high impulse power MS (HiPIMS) for Ge and TiO_2 sputtering. An increase of 1 – 2 orders magnitude in spectral intensity (600 – 1200 nm range) was achieved for these as-deposited structures in comparison to annealed structures that were deposited by conventional dc MS.

The obtained results recommend these materials for group IV photonics, with them also being ecologic and cost-effective.

References

1. A.M. Lepadatu, C. Palade, A. Slav, O. Cojocaru, V.A. Maraloiu, S. Iftimie, F. Comanescu, A. Dinescu, V.S. Teodorescu, T. Stoica, M.L. Ciurea, *Influence of SiGe nanocrystallization on short-wave infrared sensitivity of SiGe-TiO₂ films and multilayers*, J. Phys. Chem. C **124**(45), 25043-25053 (2020) [[doi:10.1021/acs.jpcc.0c06290](https://doi.org/10.1021/acs.jpcc.0c06290)].
2. M.T. Sultan, J.T. Gudmundsson, A. Manolescu, V.S. Teodorescu, M.L. Ciurea, H.G. Svavarsson, *Obtaining SiGe nanocrystallites between crystalline TiO₂ layers by HiPIMS without annealing*, Appl. Surf. Sci. **511**, 145552 (2020) [[doi:10.1016/j.apsusc.2020.145552](https://doi.org/10.1016/j.apsusc.2020.145552)].

Advanced local investigations and manipulations of nanostructures using Scanning Tunneling Microscopy

Bogdana Borca^a

^aNational Institute of Materials Physics, Atomistilor 405A, 077125, Magurele, Ilfov, Romania

Scanning Tunneling Microscopy and Spectroscopy (STM/STS) is one of the most powerful techniques that allow the investigation at an atomic scale of structural, electronic and spin-related phenomena on a variety of different emerging materials. Moreover, the technique permits to manipulate such properties, with nanometer and sub-nanometer precision, using acting stimuli in the tunneling junction as the electric field, charge carrier injection or mechanical forces. Thus, milestone analyses are realised on systems of individual atoms and molecules, biomolecules, surfaces and subsurfaces defects, 2D materials, artificial structures.

Here, I briefly present two individual research studies realised in close international collaborations exploiting STM techniques operated in ultra-high vacuum conditions and at cryogenic temperatures. One of them, developed in Ref. [1], is based on a well-established cooperation with the group of Prof. Klaus Kern, Nanoscale Science Department, Max-Planck Institute for Solid State Research, Stuttgart, Germany and included collaborations with scientists from different international research institutions.

The study reported in Ref. [1] and summarized here relies on STM for implementing two experimental approaches of control and analysis of properties of single organic molecules. Firstly, STM is used to induce a chemical reaction by means of the applied electric field at the apex of a STM tip. Using the electric field as a stimulus in chemical reactions is of actual scientific interest due to its catalytic activity and to the possibility to significantly improve reactions' efficiency. In our case, the reaction serves to strongly bind an organic molecule to a metallic electrode by a locally induced direct desulfurization in single tetraceno thiophene (TCT) molecules supported on the

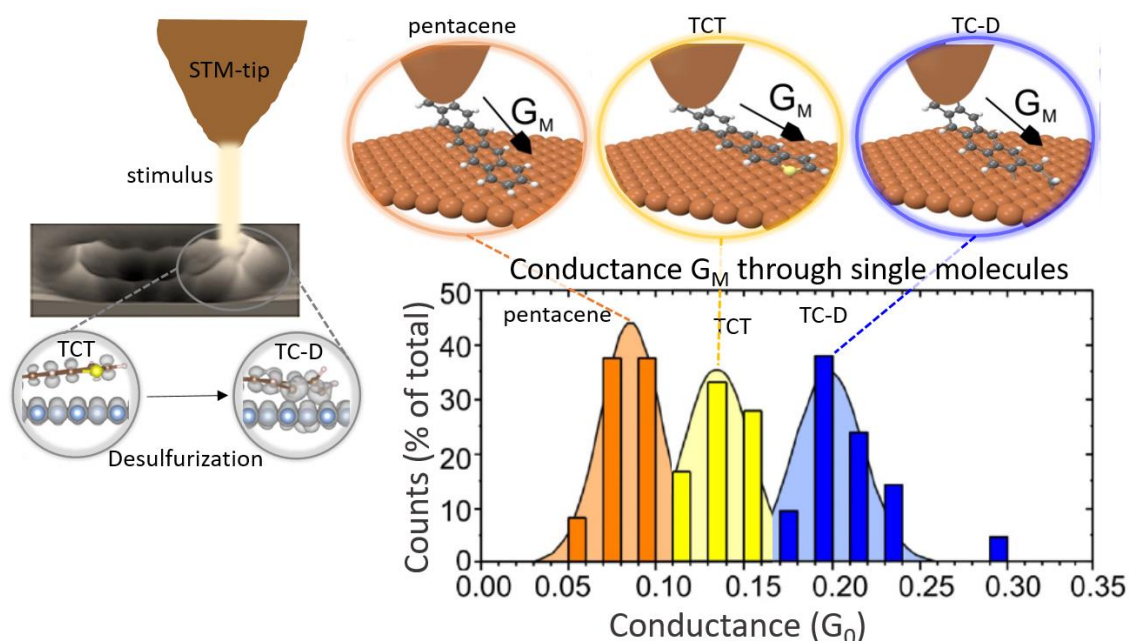


Fig. 1 -Left side: Schematic representation of a direct desulfurization reaction, induced locally by STM. Right side: Conductance measurements through single molecules of pentacene, TCT and TC-D joined in the STM junction between the tip and the surface (sketched in the top row). A significant increase of the conductance is observed for TC-D in comparison with TCT and pentacene molecules.

monocrystalline closed packed copper surface. The product molecule corresponds to a stable derivative TC-D that is anchored through covalent bonds to the metallic surface (Fig. 1). The study of the reaction mechanism was based on a previous collaboration and was published in Ref. [2]. This result is relevant in the field of molecular electronics, where for the integration of single molecules in electronic circuits, one important requirement is the formation of mechanically strong and electronically low-resistance contacts between the organic molecules and the metallic electrodes [3]. Thus, to verify if this requirement is completely fulfilled, STM is used further to realise conductance measurements through the individual TC-D and for comparison through TCT and pentacene molecules. The procedure consists in initially imaging the molecules on the surface. Next, the functional-free acene end-moiety of an individual molecule of each type is contacted, with sub-molecular precision, to the tip apex and the conductance is measured through the molecule, placed in between the STM tip and the surface (Fig.1). The conductance through the molecular systems (G_M) is expressed in units of the conductance quantum $G_0=2e^2/h=77.5$ mS. The obtained conductance values for each molecular type are summarized in the histogram in Fig. 1. Our investigations reveal a significant increase of the conductance of TC-D, that is more than 45% higher compared with TCT and 130% compared to pentacene molecules. Our density functional theory (DFT) calculations shown, for TC-D molecules, that an augmented overlap of the wave functions results in a significant increase of the density of states close to the Fermi level, especially at the reacted side of the thiophene unit. This, strongly enhances electronically and mechanically the anchoring of the molecule to the substrate and increases the conductance, result that is important for further generations of single-molecule electronic devices.

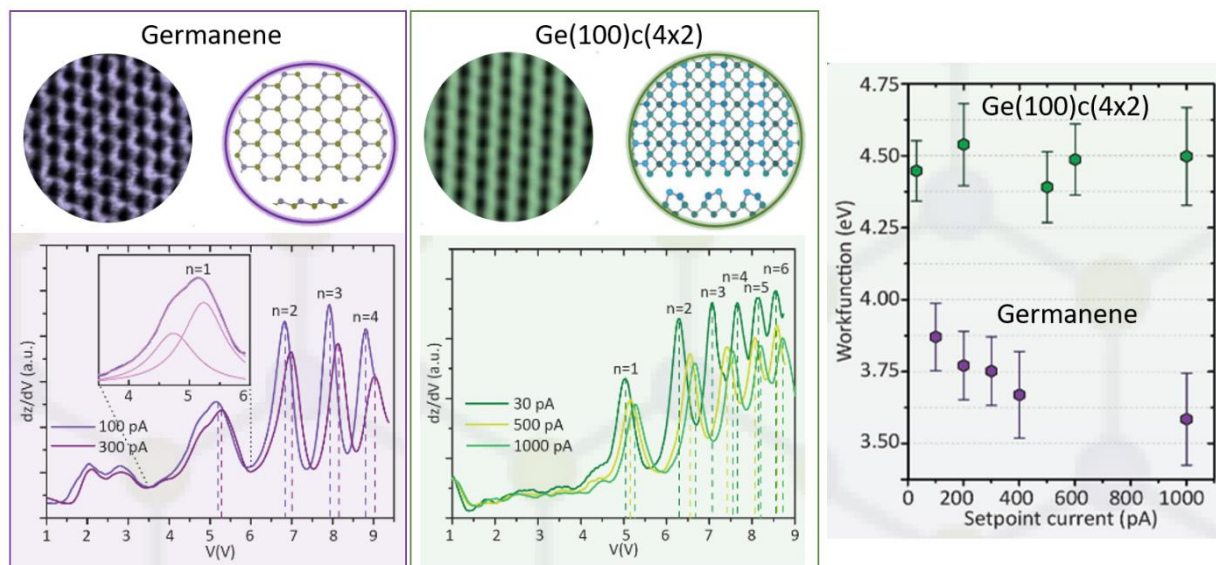


Fig. 2 - Top row: Atomic resolution - STM images on germanene and Ge(100)c(4x2) and the schematic representation of the corresponding structures. Bottom row: STM IPS dI/dV traces at different setpoint current on germanene and Ge(100)c(4x2). Germanene has the first peak $n=1$ with two contributions denoted $n=1^-$ and $n=1^+$, associated to the surface mirror-symmetric states with opposite parity. This feature suggests that the interaction between the germanene and the substrate is weak. Right column: work function of germanene and Ge(100)c(4x2), obtained from the IPS analysis. The work function of germanene is about 0.75 eV lower in energy than the work function of Ge(001).

The investigation developed in Ref. [4] is realised in collaboration with the group of Prof. Harold J.W. Zandvliet, Physics of Interfaces and Nanomaterials, MESA+ Institute for Nanotechnology, University of Twente, Enschede, The Netherlands. Two dimensional (2D) systems are nowadays among the most studied fields in materials sciences, due to their remarkable properties

and to the possibilities of their integration in further technological applications, especially regarding electronic devices. With the success of graphene – the single layer thick carbon in a honeycomb lattice, the research topics are focused on synthesizing and gaining control on the properties of new 2D materials. In this regard, important factors are the preparation methods, the structural quality, the interaction with the substrate and the electronic properties like the band-gap, the work function.

Our study is directed on a 2D-Xene: the germanene, which is the single layer buckled germanium analogue of graphene. We use STM and STS for the investigation of structural and electronic properties of germanene grown on a Ge₂Pt alloy in comparison with a pristine Ge(100)c(4x2) surface (Fig. 2). STM and the z(V)-(dz/dV) spectroscopic measurements are utilised to analyse the image potential states (IPS) resonances of the two surfaces. 2D-IPS are unoccupied electronic states that are confined on top of a surface in a potentially well defined by the surface projected bulk bandgap and the potential barrier produced by the interaction of an electron close to the surface with its image charge. These electronic states offer important information especially regarding the charge injection and the charge dynamics on surfaces, the effect of the electric field on the charge dynamics, variations of the work function and other electronic effects. In STM, IPS are trapped in the potential well between the tip and the surface. In z(V) measurements, the tip-surface distance is recorded while varying the bias voltage. When the bias voltage coincides with one of the IPS states, the z-piezo retracts in order to maintain a constant tunnel current and marks a step in the z(V) curves. In the derivative dz/dV traces, the IPS resonances appear as consecutive peaks at energies above the work function. By increasing the set point current and thus the electric field in the STM junction, a shift of the IPS peaks to higher energies occurs (Fig. 2). Our STM investigations of the IPS acquired at different setpoint current reveal, in agreement with our DFT calculations, that the work function of germanene is about 3.75 eV, a value lower than the 4.5 eV obtained for Ge(001)c(4x2) surface. Moreover, a detailed analysis of the IPS resonances shows that germanene has the first peak n=1 with two contributions denoted n = 1⁻ and n = 1⁺, associated to the surface mirror-symmetric states with opposite parity. This observation together with the spectroscopic features at energies below the n=1 IPS peak provide strong evidence that the germanene layer is weakly interacting and decoupled from the Ge₂Pt substrate.

References

- [1] T. Michnowicz⁺, B. Borca⁺,* R. Pétuya⁺, V. Schendel, M. Pristl, I. Pentegov, U. Kraft, H. Klauk, P. Wahl, P. Mutombo, P. Jelínek, A. Arnau, U. Schlickum,* K. Kern, *Controlling single molecule conductance by a locally induced chemical reaction on individual thiophene units*, *Angew. Chem. Int. Ed.* **59**, 6207-6215 (2020) <https://doi.org/10.1002/anie.201915200>
- [2] B. Borca⁺, T. Michnowicz⁺, R. Pétuya⁺, M. Pristl, V. Schendel, I. Pentegov, U. Kraft, H. Klauk, P. Wahl, R. Gutzler, A. Arnau, U. Schlickum,* K. Kern, *Electric-field-driven direct desulfurization reaction*. *ACS Nano* **11**, 4703 (2017) <https://doi.org/10.1021/acsnano.7b00612>
- [3] T. A. Su, M. Neupane, M. L. Steigerwald, L. Venkataraman, C. Nuckolls, *Chemical principles of single-molecule electronics*, *Nat Rev Mater* **1**, 16002 (2016). <https://doi.org/10.1038/natrevmats.2016.2>
- [4] B. Borca,* C. Castenmiller, M. Tsvetanova, K. Sothwes, A.N. Rudenko, H.J.W. Zandvliet*, *Image potential states of germanene*, *2D Mater.* **7**, 035021 (2020) <https://doi.org/10.1088/2053-1583/ab96cf>

Novel boron carbide based composites with special mechanical properties

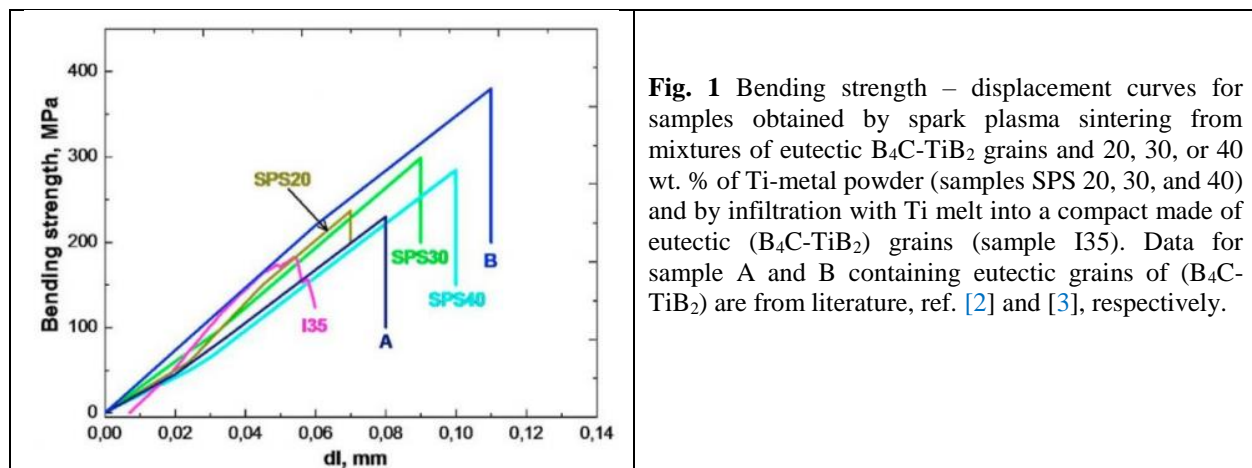
Andrei C. Kuncser,^a and Petre Badica^{a*}

^aNational Institute of Materials Physics, 077125 Magurele, Ilfov, Romania

In collaboration with National Institute for Materials Science, Tohoku University, National Technical University of Ukraine, and Otto von Guericke University Magdeburg

*badica2003@yahoo.com

Eutectic particles of B_4C - TiB_2 were reinforced with Ti by spark plasma sintering (SPS) or infiltration [1]. The SPSed samples with 20, 30 and 40 wt. % Ti consisted of ceramic phases, and had a bicontinuous macrostructure formed by the Ti-rich region and the eutectic particles region, while the infiltrated sample was a complex composite comprised of a 3D Ti-rich continuous network, composite in nature, that contained Ti-metal and in which are embedded isolated ceramic (eutectic) particles. The SPSed samples (Fig. 1, samples SPS 20, 30 and 40) are brittle with the maximum bending strength of 300 MPa for the 30 wt. % Ti, higher than for a reference sample produced by SPS from directionally solidified eutectic particles. A higher amount of added Ti results in a higher displacement in the bending test suggesting a higher fracture toughness. Simultaneous strengthening and toughening of the composite was realized. The infiltrated sample was ductile (Fig. 1, sample I35), while its bending strength (220 MPa) was comparable to the values measured for the brittle as-introduced reference sample and the sample with 20 wt. % Ti, both produced by SPS. In the SPSed and infiltrated samples at the interface between the Ti-rich region and B_4C - TiB_2 eutectic particles, a local ‘pull-out’ intergranular fracturing mechanism mainly involving Ti-B 1D-grains was observed. This local micromechanism together with a ‘pull out’ macromechanism of the eutectic grains from the Ti-rich component are considered important for the bridging/anchoring behavior responsible for the strengthening and toughening processes in our novel hierarchical composites.



Grain boundaries, twins, and defects are considered to influence the thermomechanical properties of ceramic materials. In covalent ceramic, such as the monolithic B_4C , the curves of bending strength with temperature present different shapes (Fig. 2) – descending, increasing, constant, or complex. At present time, theoretical models fail to fit them over the entire temperature range. To overcome these issues, we fabricated a novel high-density boron carbide and evaluated its high-temperature bending strength [2]. Raw materials were boron powders and carbon nanotubes functionalized with Pt nanoparticles. The as-obtained ceramic is composed of boron carbide grains and a fine grain-boundary metal Pt framework (Fig. 3). The material shows a decreased strength, which is due to a non-linear increase in the volume expansion coefficient of the B_4C . Remarkable is the recovery in strength above 1000 °C that is due to the presence of twins, their growth and

rearrangement. For example, twins with an unusual mismatch angle of $\sim 66^\circ$ were observed in the sample after bending at high temperatures (1000–1600 °C). Modifications in the twins' width under temperature and mechanical load were also revealed. We consider twins rearrangements are the pieces of evidence for a novel 'micro' mechanism of high-temperature stress accommodation for the boron carbide bulks.

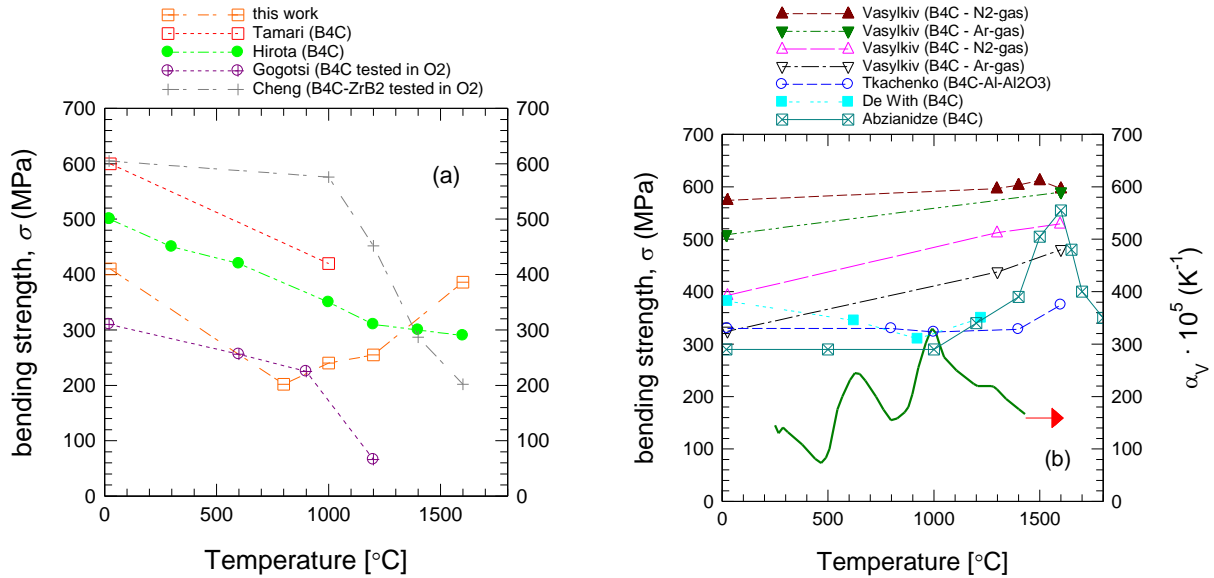


Fig. 2 Curves of bending strength with temperature from literature [5-13] showing a pronounced descending region (a) and curves showing a constant or increasing tendency (b). In (a) our data are presented, while in (b) is also shown the curve of the volume coefficient of the thermal expansion α_v of B₄C [14].

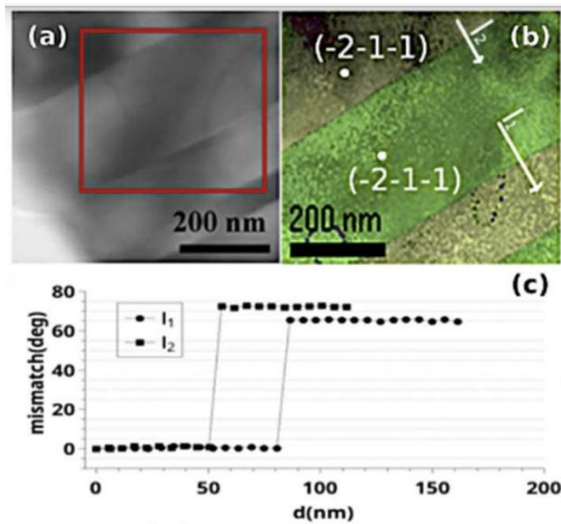


Fig. 3 The B₄C-Pt sample after bending test at 1000 °C: (a)- TEM image on a boron carbide grain with presumed twins; (b)- orientation map identifying and demonstrating the presence of twins; (c)- mismatch angle along the white line showing typical twins with a mismatch angle of 73 ° (I₁) and twins with atypical angle of 66 °.

References

1. I. Solodkyi, I. Bogomol, V. Bolbut, P. Loboda, A. Kuncser, O. Vasylykiv, P. Badica, *Hierarchical composites of B_4C - TiB_2 eutectic particles reinforced with Ti*, Ceram. Int. **46** 28138-28144 (2020) [doi.org/10.1016/j.ceramint.2020.07.312].
2. I. Bogomol, S. Grasso, T. Nishimura, Y. Sakka, P. Loboda, O. Vasylykiv, *Hard polycrystalline eutectic composite prepared by spark plasma sintering*, Ceram. Int. **38** 3947-3953 (2012) [[doi:10.1016/j.ceramint.2012.01.048](https://doi.org/10.1016/j.ceramint.2012.01.048)].
3. I. Bogomol, H. Borodianska, T. Zhao, T. Nishimura, Y. Sakka, P. Loboda, O. Vasylykiv, *A dense and tough (B_4C - TiB_2)- B_4C 'composite within a composite' produced by spark plasma sintering*, Scr. Mater. **71** 17-20 (2014) [[doi:10.1016/j.scriptamat.2013.09.022](https://doi.org/10.1016/j.scriptamat.2013.09.022)].
4. O. Vasylykiv, D. Demirskyi, H. Borodianska, A. Kuncser, P. Badica, *High-temperature strength of boron carbide with Pt grain-boundary framework in situ synthesized during spark plasma sintering*, Ceram. Int. **46** 9136-9144 (2020) [doi.org/10.1016/j.ceramint.2019.12.163].
5. O. Vasylykiv, D. Demirskyi, H. Borodianska, Y. Sakka and P. Badica, *High temperature flexural strength in monolithic boron carbide ceramic obtained from two different raw powders by Spark Plasma Sintering*, J. Ceram. Soc. Japan **124** 587-592 (2016) [doi.org/10.2109/jcersj2.15289].
6. O. Vasylykiv, D. Demirskyi, P. Badica, T. Nishimura, A.I.Y. Tok, Y. Sakka, H. Borodianska, *Room and high temperature flexural failure of spark plasma sintered boron carbide*, Ceram. Int. **42** 7001-7013 (2016) [doi.org/10.1016/j.ceramint.2016.01.088].
7. G. De With, *High temperature fracture of boron carbide: experiments and simple theoretical models*, J. Mater. Sci. **19** 457-466 (1984) [<https://link.springer.com/article/10.1007/BF00553569>].
8. Yu.G. Tkachenko, D.Z. Yurchenko, V.K. Sul'zhenko, G.S. Oleinik, V.M. Vereshchaka, *Temperature effect on bending strength of hot-pressed boron carbide materials*, Powder Metall. Metall. Ceram. **46** 60-68 (2007) [<https://link.springer.com/article/10.1007%2Fs11106-007-0041-5>].
9. N. Tamari, H. Kobayashi, T. Tanaka, I. Kondoh, S. Kose, *Mechanical properties of B_4C -SiC whisker composite ceramics*, J. Ceram. Soc. Jpn. **98** 1159-1163 (1990) [doi.org/10.1016/j.ceramint.2019.12.222].
10. K. Hirota, Y. Nakayama, M. Kato, S. Nakane, T. Nishimura, *The study on carbon nanofiber (CNF)- dispersed B_4C composites*, Int. J. Appl. Ceram. Technol. **6** 607-616 (2009) [doi.org/10.1111/j.1744-7402.2008.02323.x].
11. G.A. Gogotsi, Ya.L. Groushevsky, O.B. Dashevskaya, Yu.G. Gogotsi, V.A. Lavrenko, *Complex investigation of hot-pressed boron carbide*, J. Less Common Met. **117** 225-230 (1986) [[doi.org/10.1016/0022-5088\(86\)90037-8](https://doi.org/10.1016/0022-5088(86)90037-8)].
12. X.M. Cheng, R.J. He, Z.I. Qua, A.G. Ai, D.N. Fang, *High-temperature flexural strength of B_4C - ZrB_2 ceramic at 1000-1600 °C in air*, Ceram. Int. **41** 14574-14578 (2015) [doi.org/10.1016/j.ceramint.2015.07.174].
13. T.G. Abzianidze, A.M. Eristavi, S.O. Shalamberidze, *Strength and creep in boron carbide (B_4C) and aluminum dodecaboride (α - AlB_{12})*, J. Solid State Chem. **154** 191-193 (2000) [doi.org/10.1006/jssc.2000.8834].
14. G.V. Tsagareishvili, T.G. Nakashidze, J.Sh. Jobava, G.P. Lomidze, D.E. Khulelidze, D.Sh. Tsagareishvili, O.A. Tsagareishvili, *Thermal expansion of boron and boron carbide*, J. Less Common Met. **117** 159-161 (1986) [[doi.org/10.1016/0022-5088\(86\)90025-1](https://doi.org/10.1016/0022-5088(86)90025-1)].

Bulk MgB₂ for superconducting magnet and shielding applications

Mihai A. Grigorescu,^a Mihail Burdusel,^a Iuliana Pasuk,^a Gheorghe V. Aldica,^a Petre Badica^{a*}

^aNational Institute of Materials Physics, Magnetism and Superconductivity Lab., Atomistilor street 405A, 077125 Magurele, Ilfov, Romania

In collaboration with University Politehnica of Bucharest, Lorraine University, Saarland University, Shibaura Institute of Technology

*badica2003@yahoo.com

MgB₂ powder was mixed with Ge₂C₆H₁₀O₇ and bulk discs (20 mm diameter and 4.3 mm thickness) were prepared by Spark Plasma Sintering [1]. Six samples fabricated under similar conditions were magnetically characterized in order to determine the scattering of the superconducting properties and reproducibility. The main source of the scattering of the properties is the decomposition of the additive. The critical temperature at the midpoint of the transition, T_c, only shows a relatively small variation between 37.4 and 38 K, and the irreversibility field at a low temperature of 5 K takes values between 8 and 10 T. The pinning force and pinning force related parameters do not correlate with the carbon substituting for boron in MgB₂ and suggest a synergetic influence of the microstructural details and carbon. Overall, despite the superconducting properties scattering, the samples are of high quality.

The discs were stacked together in a column and measured (in collaboration with Lorraine University, Saarland University, Shibaura Institute of Technology) for trapped magnetic field at the center and on the surface. Trapped magnetic field B at the center (B^c_{tr}) and on the surface (B^s_{tr}) of the compound magnet made of 6 discs is presented in Fig. 1. The curves are without flux jumps when measured at 12, 20 and 30 K for the decrease rate of the DC applied magnetic field for excitation in the + 5 to - 5 T range of 0.01, 0.02, 0.1 and 0.5 T/min, respectively.

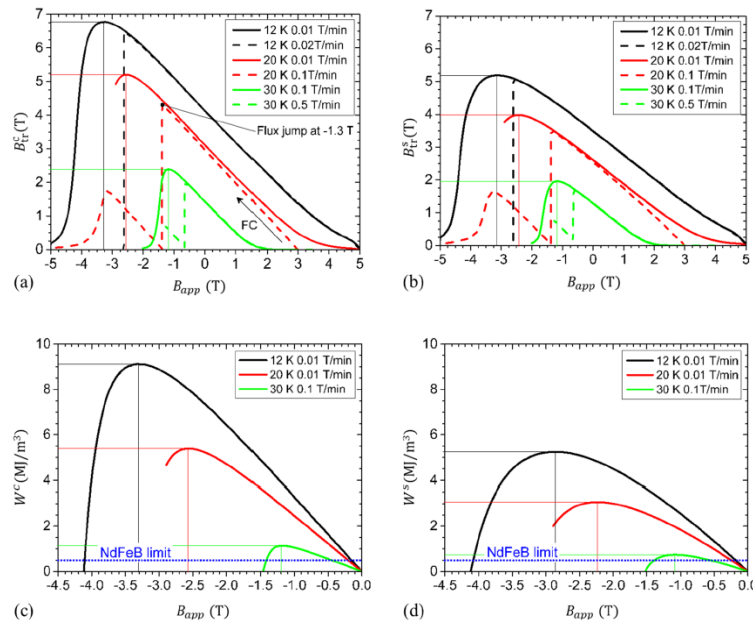


Fig. 1 Trapped magnetic field at the center (a) and on the surface (b) of the magnet composed of six MgB₂ superconducting discs. The local density of magnetic energy at the center (c) and on the surface (d) is compared with the magnetic energy of a NdFeB conventional magnet.

The trapped magnetic fields at the center and on the surface were 6.78 and 5.19 T at 12 K, 5.20 and 3.98 T at 20 K, and 2.39 and 1.96 T at 30 K. Relevant for applications are the values of the trapped field and the density of magnetic energy measured on the surface of the compound magnet (Fig. 1).

Results enable further studies and the use of small MgB₂ superconducting samples in large and complex-shape compound magnets and other applications. Furthermore, it demonstrates the feasibility of compound magnets made of small and reproducible MgB₂ discs.

The MgB₂ bulks can be also useful for fabrication of magnetic shields. A pure MgB₂ commercial powder was mixed with hexagonal BN. The mixture was loaded into a graphite die with 20 mm inner diameter and processed by spark plasma sintering. A cup-shaped shield (Fig. 2) [2] was fabricated by mechanical machining of the as-sintered MgB₂-hBN cylinder (25 mm height and 20 mm diameter). At first, it was partially bored by using drill bits and then it was refined in the final cup-shape by means of a lathe machine. Addition of hBN ensures full machinability of MgB₂ that is otherwise a hard and brittle ceramic-like compound.



Fig. 2 MgB₂ cup fabricated by spark plasma sintering, drilling and final refining on a lathe machine. Geometrical parameters: outer radius, $R_o = 10.15$ mm, inner radius, $R_i = 7.0$ mm, external height, $h_e = 22.5$ mm, internal depth,

$d_i = 18.3$ mm.

Shielding properties of the cup-shaped shield were investigated (in collaboration with University of Turin and Polytechnic University of Turin) in both axial- and transverse-field geometries as a function of temperature, applied magnetic field and Hall probe position along the sample's axis. Despite a height/external-radius aspect ratio of only 2.2, in the axial-field configuration, inside the cup and 1 mm away from its closed extremity, shielding factors, SFs exceed 10^4 at $T = 20$ K up to $\mu_0 H_{\text{appl}} = 1.8$ T. Moreover, in the same temperature and field region, SFs $> 10^2$ still persisted in the whole inner half of the cup. In addition, the range of external fields where such efficient shielding occurred is much larger than that expected on the basis of the modelling approach and related parameters reported in literature. This result proves the high influence of the quality of the raw MgB₂ powder on shield performance. Further improvements in the shielding performance are expected by further enhancing the critical current density or by superimposing additional superconducting or ferromagnetic layers. On the other hand, an increase of J_c could favor flux-jump occurrence, limiting the practical applications of MgB₂ shields. Thus, minimizing this phenomenon, without compromising J_c values and shielding performance, is the next challenging goal in this research field.

As already introduced in the previous paragraphs, the MgB₂ bulk superconductors are expected to be utilized as rare-earth-free and lightweight trapped field magnets. Bulk samples of MgB₂ - pristine and added with graphene - were fabricated by spark plasma sintering. The flux jumps frequently happen during the magnetizing processes, and heavily degrade the field-trapping performances. We have investigated the effect of additive to the MgB₂ bulk samples and observed various flux jumps during the *pulsed field magnetizing processes* (PFM). Experiments were carried out (in collaboration with Shibaura Institute of Technology) at 14 K which was obtained by the 2-stage GM cryocooler [3]. The flux motions were classified into three categories: “no flux flow”, “fast flux flow”, and “flux jump” regions. Conditions for occurrence of these regimes were investigated. We observed some drastic flux jumps in the pristine bulk MgB₂ sample and clarified the effect of graphene addition on the flux jumps. The experimental results showed a possible expansion of the region without flux jumps, and suggested the improvement of field trapping capability. The authors

defined the parameters, which estimate the flux-penetrating and -trapping properties as *the field penetration ratio* BP/BA and *field trapping ratio* BT/BP , respectively. The value of BP/BA reflects the shielding effects of the bulk sample in its flux-invasion stage, and BT/BP depends on the heat generation and its transfer. The focus is on the flux-trapping property BT/BP and the occurrence of flux jumps. The curve (a) in **Fig. 3** shows the trapped field BT for the pristine sample. The flux begins to invade into the center point of the sample surface at applied field $BA = 0.6$ T, and gradually increases with increasing applied field to the maximum value of 0.51 T at 1.3 T. The flux jumps often occur in the pristine sample when the applied field exceeded 1.3 T so that the trapped field drastically decreases to ~ 0.1 T, as shown by arrows. The curve (b) in **Fig. 3** for graphene added MgB_2 sample shows a field of invasion that starts at 0.5 T, almost similar to the value for pristine sample. However, there is no substantial increase of the trapped field BT for increasing applied field. The field trapping in the graphene doped sample is approximately constant and suppressed comparative to the pristine sample to less than 0.2 T till 2.0 T of applied field. This implies that the J_c value might have been lowered by graphene addition. Nevertheless, noteworthy is that no flux jumps occurred in this sample. The graphene added sample is also fully machinable by chipping.

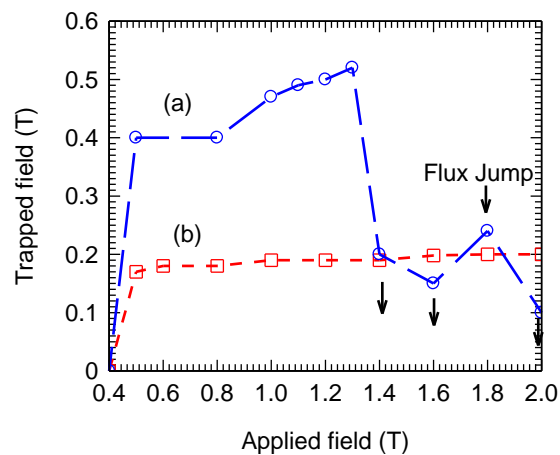


Fig. 3 Trapped fields of the pristine sample (a) and graphene doped MgB_2 spark plasma sintered samples after PFM operations.

References

1. P. Badica et al., *Reproducibility of small $Ge_2C_6H_{10}O_7$ -added MgB_2 bulks fabricated by ex situ Spark Plasma Sintering used in compound bulk magnets with a trapped magnetic field above 5 T*, *Sci. Rep.* **10**, 10538 (2020) [doi.org/10.1038/s41598-020-67463-y]
2. L. Gozzelino et al., *High magnetic shielding properties of an MgB_2 cup obtained by machining a spark plasma sintered bulk cylinder*, *Supercond. Sci. Technol.* **33**, 044018 (2020) [doi.org/10.1088/1361-6668/ab7846]
3. K. Yokoyama et al., *Investigation of flux jumps during pulsed field magnetization in graphene-added MgB_2 bulks*, *J. Phys.: Conf. Ser. (EUCAS 2019)* **1559**, 012080 (2020) [[doi:10.1088/1742-6596/1559/1/012080](https://doi.org/10.1088/1742-6596/1559/1/012080)].

Optimization of Fe oxide based nanoparticles for bio-medical and catalytic applications

P. Palade,^a C. Comanescu,^a A. Kuncser,^a N. Iacob,^a V. Kuncser,^a D. Berger,^b C. Matei,^b L. M. Cursaru,^c R. M. Piticescu,^c D. V. Dragut,^c I. A. Tudor,^c F. Stoiciu,^c I. Podolean,^d S. M. Coman,^d V. I. Parvulescu^d

^aNational Institute of Materials Physics, 405A Atomistilor, Magurele, Romania, 077125.

^bPolytechnic University of Bucharest, Faculty of Applied Chemistry and Materials Science 1–7 Polizu St, Bucharest, Romania, 011061.

^cNational R&D Institute for Non-Ferrous and Rare Metals, INCDMNR-IMNR, 102 Biruintei blvd, Pantelimon, Ilfov, Romania, 077145.

^dDepartment of Organic Chemistry, Biochemistry and Catalysis, Faculty of Chemistry, University of Bucharest, Bdul Regina Elisabeta 4-12, Bucharest, Romania, 030016.

Fe-oxide-based magnetic nanoparticles (NPs) are remarkable materials for applications in medicine (contrast agents for magnetic resonance imaging, carriers for controlled drug delivery and immunoassays, and in magnetic hyperthermia), biology (recyclable anti-polluting agents) and in catalysis. Their unique physical, chemical, thermal and mechanical properties can be optimized for specific applications.

In mesoporous systems, the pH proved to be the key factor for controlling not only NP size, but also the phase purity and the porosity properties of the mesostructures [1], thus influencing their magnetic properties. In the present work, a cheap, facile, and environmentally friendly surfactant-assisted hydrothermal method to prepare mesoporous CoFe_2O_4 structures with high BET surface area and significant magnetization at saturation at ambient temperature is shown. The pH values were: 7.3 (sample CFO73), 8.3 (CFO83) and 9.3 (CFO93). The crystallite sizes were in the range 7–10 nm, therefore the NPs are a magnetic single domain with Stoner–Wohlfarth-like behavior. The evolution of coercive field (H_C) vs. temperature for non-interacting NPs is well described by the Kneller formula (H_{C0} is the coercive field extrapolated to 0 K): $H_C = H_{C0} [1 - (T/T_B)^{1/2}]$ (eq. 1).

From eq. (1), the blocking temperatures (T_B) of 233 K for CFO73, 273 K for CFO83, and 248 K for CFO93 were obtained. Moreover, the NPs form the walls of a nanoporous foam with open and closed pores and a model of non-interacting NPs is not completely true. On the other hand, the barrier energy separating the two involved possible magnetic states which describes the ZFC curves depends on the applied magnetic field. In this case, it is possible to obtain a field-dependent maximum of the ZFC curve, which can provide the values of $T_B(H)$ as shown in fig. 1 (left) for CFO73. T_B decreases with the increase in the applied magnetic field. For non-interacting NPs: $T_B(H) = T_B(0) * (1 - H/H_K)^{\alpha}$ (eq. 2), where $T_B(H)$ is measured in the field H whereas $T_B(0)$ is measured in negligible magnetic field. H_K is the anisotropy magnetic field.

The value $H_K = 2 K/M_S$ for the switching magnetic field is the same for NPs with uniaxial magnetic anisotropy and for NPs with cubic anisotropy when the magnetization is orientated on the (100) direction which is the case of cobalt ferrite. The coefficient from eq. (2) should be $\alpha = 2$ for low magnetic fields and $\alpha = 2/3$ for high magnetic fields. Taking into account that for a random distribution of easy magnetic axis of NPs with cubic anisotropy $H_{C0} = 0.64 K/M_S$ and using the M_S values obtained by the approach to saturation law at the lowest measurement temperature (10 K), it is clearly shown that the experimental points (T_B, H) obey eq. (2) and provides $T_B = 340(7)$ K as extrapolated at an applied field $H = 0$ Oe (see fig.1 right).

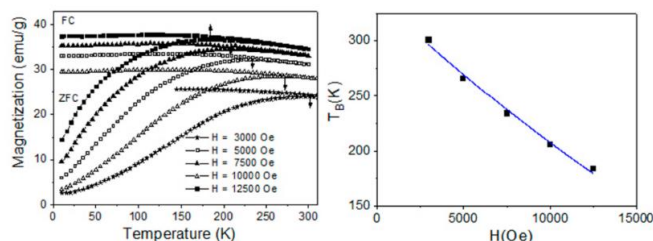


Fig. 1. ZFC-FC curves at various fields (left) and T_B dependence on applied magnetic field (right) for CFO73. [1]

Having magnetic fluid hyperthermia applications in medicine in mind, the key role in the conversion of electromagnetic energy to the thermal one via the superparamagnetic relaxation mechanism is played by the magnetic anisotropy of NPs, easily controlled via the shape anisotropy component. Therefore, superparamagnetic Fe_3O_4 ellipsoidal NPs with dominant shape anisotropy dispersed in different media, and having different sizes and aspect ratios were evaluated in frame of the Rosensweig model. It has been proven in [2] that the dissipated power can be maximized for a given set of biological compatible radiofrequency field parameters (frequency and field amplitude at the sample space) only for specific pairs of particle sizes and aspect ratios. For instance, it has been shown that ellipsoidal magnetite nanoparticles with 10 nm equatorial size and aspect ratio of 2 are optimal for a maximum transferred power under radiofrequency excitations of 250 kHz and field amplitude of 20 kA/m, if high viscosity dispersion media are used. The methodology for deriving the optimal shape (geometrical) parameters of a specific type of NPs in conditions of using available radiofrequency excitations, or vice versa, for deriving the optimal radiofrequency working parameters in the case of ferrofluids with specific nanoparticles (type and geometry) is described and discussed in detail in [2].

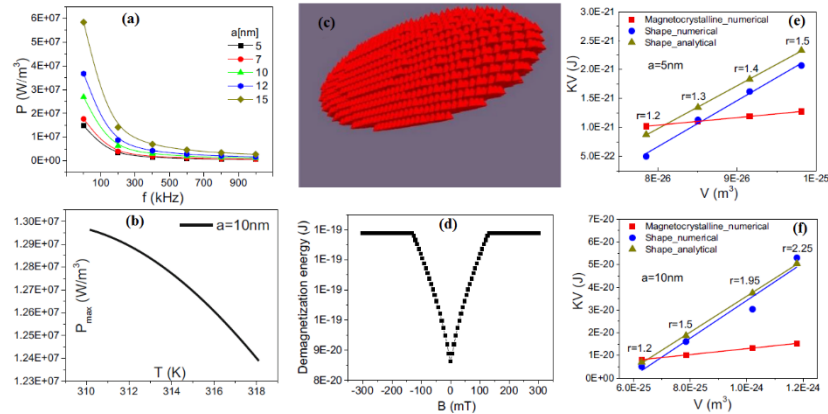


Fig. 2 Evolution of P_{\max} vs the frequency of the AC magnetic field for a in the range [5 nm, 15 nm] (a). Evolution of the dissipated power in the MFH temperature range. MNPs dispersed in high viscosity media and with optimal geometrical parameters ($a = 10$ nm, $r = 2$) were considered (b). Discretization of an ellipsoidal NP of magnetite ($a = 10$ nm, $r = 2$) in unit cells for micromagnetic calculations (c) and calculated demagnetization energy profile of the same NP (d). Shape anisotropy energy in function of the magnetic volume in the case of single domain ellipsoidal NPs with $a = 5$ nm (e) and $a = 10$ nm (f), calculated both analytically and numerically. The magnetocrystalline anisotropy energy is also plotted. [2]

Another parameter adjusting the magnetic behavior of the hydro-thermally prepared NPs for bio-medical applications is pressure. For the first time, the effect of high pressure (up to 1000 bar) on the formation and phase transformations of iron oxides in aqueous environments under hydrothermal conditions was performed in [3]. As evidenced by X-ray diffraction and Mössbauer spectroscopy, pressure and annealing parameters influence phase formation. At lower pressure, < 100 bar, iron oxide is predominantly formed as hematite, while, at pressures > 100 bar, the major crystalline phase is goethite and, consequently, magnetic parameters are also affected. The room temperature coercivity considerably increases with pressure from 190 Oe for sample NV4-TT ($p=20$ bar) to 450 Oe for sample NV7-TT ($p=1000$ bar). The H_C values at 10 K are even more different: 450 Oe for NV4-TT and 1 kOe for NV7-TT.

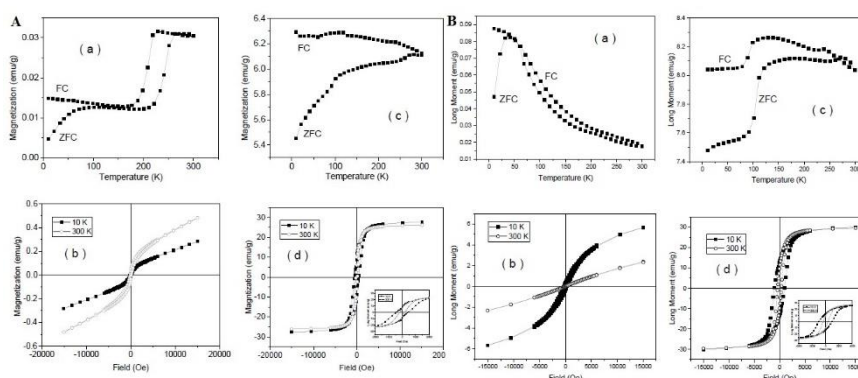


Fig. 3.A. ZFC-FC curves collected in 80 Oe DC applied field (a) and hysteresis loops (b) for sample NV4 ($p=20$ bar), similar ZFC-FC curve (c) and hysteresis loops (d) for sample NV4-TT (annealed at 680°C). B. ZFC-FC curves collected in 80 Oe DC applied field (a) and hysteresis loops (b) for sample NV7 ($p=1000$ bar), similar ZFC-FC curve (c) and hysteresis loops (d) for NV7-TT (annealed at 680°C).

An interesting application for Fe-based nanoparticles is the magnetic separation of catalysts for the valorification of biomass. Promising results were obtained for Fe@Y composites (carbon-coated magnetic iron nanoparticles incorporated in zeolite Y) to catalyze the hydrolysis of the marine sulfated polysaccharide ulvan with high conversion rates [4]. All Fe@Y composites were recycled 10 times with no change in their catalytic performance after recovery via a simple magnetic separation and washing with water.

Acknowledgements: This work was supported by the Romanian Ministry of Research and Innovation, through the following projects at NIMP: PN-III-P1-1.2-PCCDI-2017-0871, P4-ID-PCCF-2016-0688, PN-III-P4-ID-PCE-2016-0146, PN-III-P1-1.2-PCCDI-2017-0541, Core Program (PN19-030101, PN18-110201/2018), 12 PFE/2018.

References

1. P. Palade, *et al*, *Mesoporous Cobalt Ferrite Nanosystems Obtained by Surfactant-Assisted Hydrothermal Method: Tuning Morpho-structural and Magnetic Properties via pH-Variation*, *Nanomaterials* **10**, 476 (2020) [<https://doi.org/10.3390/nano10030476>].
2. N. Iacob, *et al*, *Optimization of magnetic fluid hyperthermia with respect to nanoparticle shape-related parameters: case of magnetite ellipsoidal nanoparticles*, *J Nanopart Res* **22**, 138 (2020) [<https://doi.org/10.1007/s11051-020-04842-6>].
3. L. M. Cursaru, *et al*, *The Influence of Synthesis Parameters on Structural and Magnetic Properties of Iron Oxide Nanomaterials*, *Nanomaterials* **10**, 85 (2020) [[doi:10.3390/nano10010085](https://doi.org/10.3390/nano10010085)].
4. Jan Prech, *et al*, *Magnetic Fe@Y Composites as Efficient Recoverable Catalysts for the Valorization of the Recalcitrant Marine Sulfated Polysaccharide Ulvan*, *ACS Sustainable Chem. Eng.* **8**, 319–328 (2020) [[DOI: 10.1021/acssuschemeng.9b05406](https://doi.org/10.1021/acssuschemeng.9b05406)].

Temperature dependence and defect related structure, photoluminescence, (ferro)magnetism and ammonia sensitivity of undoped nanocrystalline ZnO

V. Mihalache,^a M. Secu,^a C. Negrila,^a V. Bercu,^b I. Mercioniu,^a A. Leca^a

^aNational Institute of Materials Physics, Department of Magnetism and Superconductivity, Atomistilor 405A, Magurele, Romania, 077125

^bUniversity of Bucharest, Faculty of Physics, Atomistilor 405, Magurele, Romania, 077125

Undoped ZnO nanostructures (p400, p470, p600 and p970) with different intrinsic and extended defect states were produced by rapid decomposition of zinc-propionate and annealing at 400 °C–970 °C. The correlation between the structure/morphology, type of native defects (photoluminescence (PL), EPR) and ferromagnetism (Table 1, Figs. 1-5) was investigated, together with ammonia adsorption capacity (Fig. 6) [1]. It was also demonstrated that the obtained results can find applications in (gas) sensing, photonic/optoelectronic and spintronic devices.

Crystallite size increases while the unit cell volume, *c*-axis constant, microstrain and saturation (M_s) magnetization relax with increasing temperature (Table 1).

Table 1 The parameters evaluated from Rietveld fitting of the XRD patterns, the Zn/O ratio determined from EDX (with SEM), the saturation moment, M_s , at room temperature and the EPR parameters for the ZnO samples.

Sample	XRD results						Zn/O	M_s (10^{-3} emu g ⁻¹)	EPR parameters				
	<i>a</i> (Å)	<i>c</i> (Å)	Micro strain (%)	V_c (Å ³)	Crystallite size (nm)	<i>c/a</i>			Low-field g-factor		High-field g-factor		I_{g1}/I_{g2}
									g_1	ΔB (G)	g_2	ΔB (G)	
p400	3.2495	5.2111	0.440	47.6548	14.8	1.6037	1.08	7.0	2.0065	4.5	1.9632	9.0	4.2
p470	3.2493	5.2061	0.269	47.6026	27.2	1.6022	1.04	12.6	2.0065	3.4	1.9632	6.3	6.8
p600	3.2493	5.2047	0.224	47.5873	32.4	1.6018	0.96	7.8	2.0065	4.2	1.9632	4.5	0.2
p800	3.2495	5.2032	0.093	47.5807	103.3	1.6012	0.92	3.6	2.0065	5.4	1.9632	10.7	0.25
p970	3.2501	5.2014	0.07	47.5824	227.7	1.6004	0.96	2.3	2.1510	25.0			
p400 after PPMS								22.0					

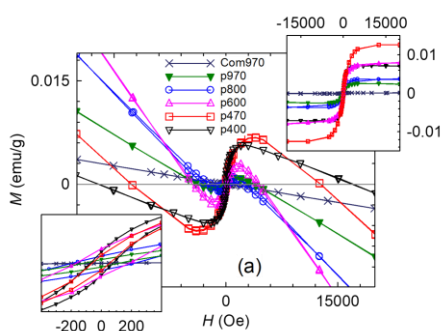


Fig. 1 M vs. H curves registered at 300 K for all ZnO samples. Upper inset: M vs. H curves after subtracting the diamagnetic signal. Lower inset: M vs. H curves at the origin.

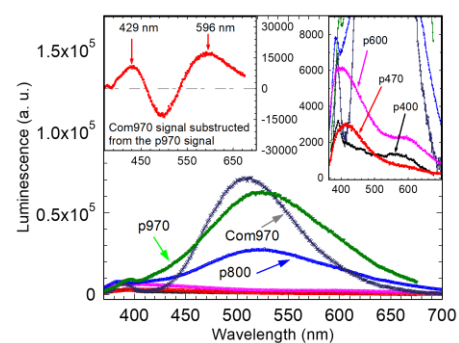


Fig. 2 RT luminescence spectra excited at 295 nm for the ZnO powders. Right inset: a magnified view. Left inset: the curve resulting from the subtraction of the Com970 (a commercial powder annealed at 970 °C) signal from the p970 signal

Morphology varies from aggregated nanoparticles to frameworks of well-welded crystals forming grain boundaries (GBs), interfaces, dislocations and other structural defects (Fig. 3, Fig. 4).

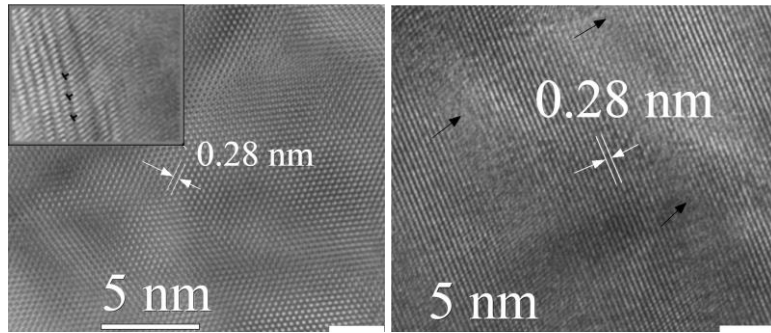
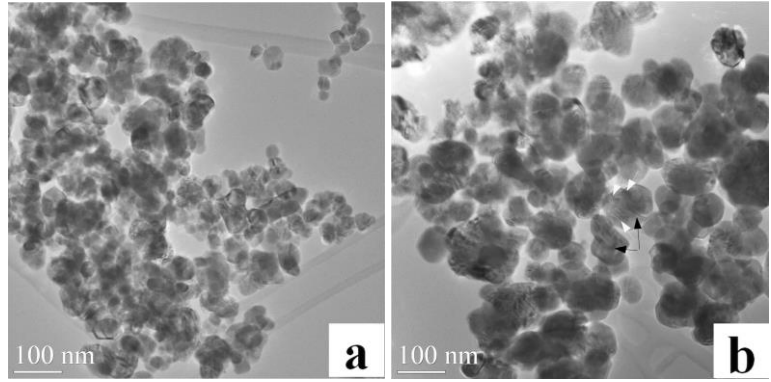
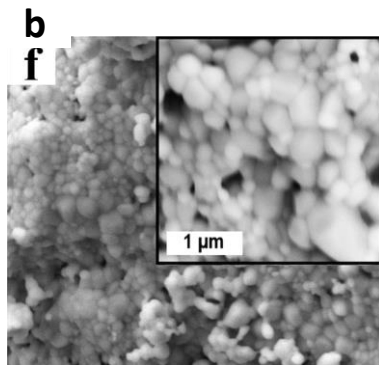
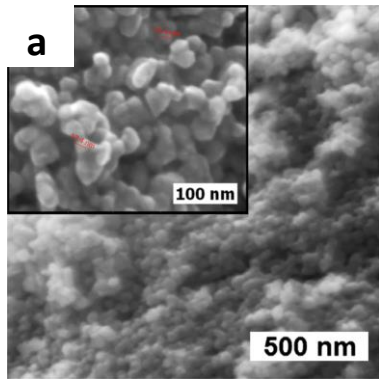


Fig. 3 SEM images for the (a) p400 and (b) p600 powders.

Fig. 4 The TEM images for (a) p400 and (b) p470 and XRTEM images for (c) p400 and (d) p470. Black arrows-GBs, interfaces; white arrows-dislocations. Inset of Fig. 7c: XRTEM image of a portion of a grain in p400 showing a distorted lattice and a dens concentration of dislocations

All the samples show room temperature ferromagnetism (RTFM) with M_s between 12×10^{-3} and 0.092×10^{-3} emu/g (**Fig. 1, Table 1**).

400 °C–800 °C annealed samples show a broad visible and/or a prominent violet-blue PL emission and, two narrow $g = 2.0065$, and $g = 1.9632$ EPR signals; 800 °C–970 °C annealed samples exhibit very intense green-yellow photoluminescence (**Fig. 2, Fig. 5, Table1**).

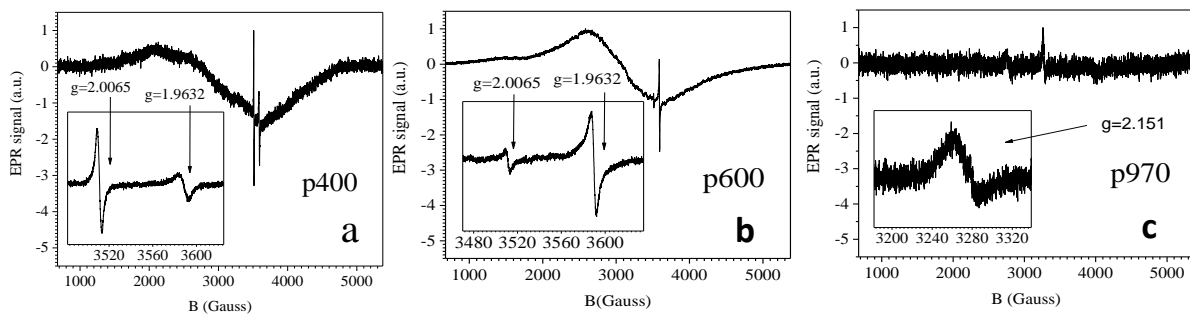


Fig. 5 Room-temperature EPR spectra of ZnO samples: (a) as-prepared p400, (b) p600 and (c) p970

The as-prepared sample (p400) is characterized by (i) a highest c/a ratio, c -axis constant and microstrain and (ii) a broad defect-related PL emission and two narrow $g = 2.0065$ and $g = 1.9632$ EPR signals consistent with the presence of V_{O^-} and Zn_i^- related defects (Table 1) (see also [2]). After PPMS heating above RT the M_s of the as-prepared sample increased from 7.0×10^{-3} emu/g to

22.0×10^{-3} emu/g. This, together with a T_C higher than 700°C , verifies the ferromagnetism stability for applications in spintronic devices operating at room temperature.

The samples annealed above 400°C exhibit primarily a prominent violet-blue emission and the $g = 1.9632$ (along with $g = 2.0065$) EPR signals associated with the presence of Zn_i (along with V_o) related defects at the GBs/interfaces.

ZnO annealed at 970°C in oxygen flow has the most relaxed structural parameters among all samples, a broad and very intense defect-related PL emission, consistent with the presence of V_O (and O_i)-type defects.

In conclusion, more insights were provided into the origin of RTFM: the coexistence of a non-equilibrium concentration of (V_O and/or Zn_i – type) native defects with a deformed and strained lattice (in the samples annealed at low temperatures) and/or pinned by GBs/dislocations/interfaces (in the samples annealed at high temperatures.) can generate RTFM and Curie temperature exceeding 700°C in undoped ZnO.

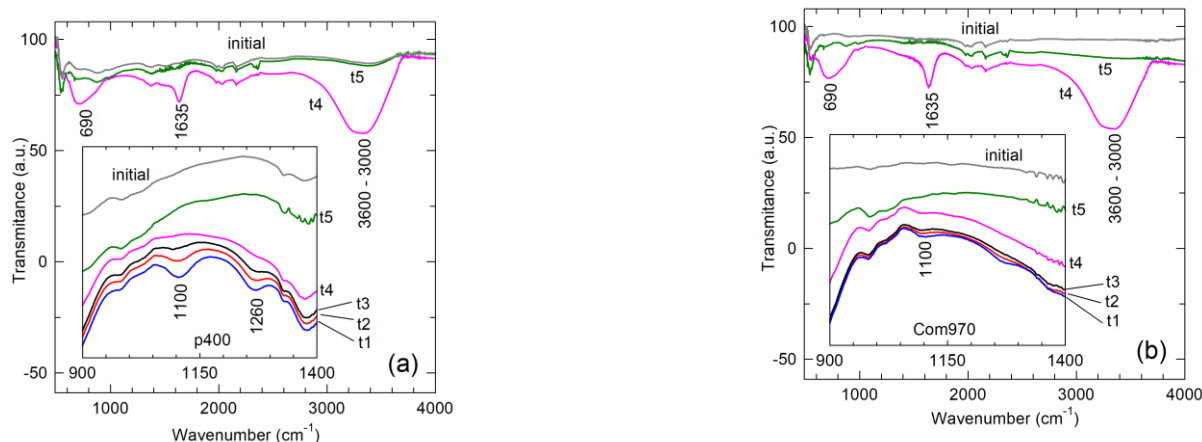


Fig. 6 FTIR-ATR spectra of the (a) p400 and (b) Com970 samples exposed to ammonia vapours. Insets: spectra after exposure to ammonia vapour and subsequently recorded in air at: $t_1 = 0$ sec, $t_2 = 60$ sec, $t_3 = 120$ sec, $t_4 = 240$ sec and $t_5 = 850$ sec. Shown are also the spectra for the initial unexposed samples.

Finally, the superior ammonia adsorption capacity (**Fig. 6**) of the as-prepared sample together with the presence of a large amount of donor intrinsic defects are essential for the performance of ammonia gas sensors.

References

1. V. Mihalache, M. Secu, C. Negrila, V. Bercu, I. Mercioniu, and A. Leca, *Temperature dependence and defect related structure, photoluminescence, (ferro)magnetism and ammonia sensitivity of undoped nanocrystalline ZnO*, *Materials Science and Engineering: B* **262** (2020) 114748
2. V. Mihalache, C. Negrila, V. Bercu, M. Secu, E. Vasile, and G.E. Stan, *Effect of dilute doping and non-equilibrium synthesis on the structural, luminescent and magnetic properties of nanocrystalline $\text{Zn}_{1-x}\text{Ni}_x\text{O}$ ($x = 0.0025 - 0.03$)*, *Materials Research Bulletin* **115** (2019) 37–48